The Dissertation Committee for Lokendra Jain Certifies that this is the approved version of the following dissertation:

Global Upscaling of Secondary and Tertiary Displacements

Committee:

Larry W Lake, Supervisor

Kamy Sepehrnoori

Steven Bryant

Sanjay Srinivasan

Todd Arbogast

Global Upscaling of Secondary and Tertiary Displacements

by

Lokendra Jain, B.Tech; M.S.

Dissertation

Presented to the Faculty of the Graduate School of
The University of Texas at Austin
in Partial Fulfillment
of the Requirements
for the Degree of

Doctor of Philosophy

The University of Texas at Austin
May 2014

“Imagination is more important than knowledge”

-Albert Einstein.

Acknowledgements

I would like to express my gratitude to Dr. Larry W Lake for his invaluable guidance and support. Working under his supervision was a learning experience which made me think critically. I am thankful to get into Dr. Lake's reservoir of insights in the subject matter and hope to learn from it in the future as well. I learned to look at the bigger picture while solving technical problems with him. He has helped me directly and indirectly in my academic research, professional and personal development. I am thankful for his continued support during the difficult phases of my research.

I am also thankful to Dr. Steven Bryant, Dr. Sanjay Srinivasan, Dr. Kamy Sephernoori and Dr. Todd Arbogast for their support while I was writing this dissertation. I would like to thank Mike Shook and Morteza Sayarpour for their timely help with my research. I would like to thank Dr. Roger Terzian and Ms. Joanna Castillo for their help with the computers and the software packages. I would also like to thank Ms. Frankie Hart and Ms. Heather Felauer for helping me in administrative matters.

Most importantly, I am thankful to Dr. Lake and Dr. Bryant because they taught me to talk slowly while communicating though it is still a work in progress.

I would like to extend my special thanks to my friends Ashwin, Rouzbeh, Fei, Ola, Gurpreet, Femi and Behzad for helping me understand concepts through thoughtful discussions and providing me with moral support when it was needed. I would like to thank my friends Mayank, Ankesh, Sayantan, Ashwin, Gurpreet, Hari and Chris for keeping my spirits up during the difficult times.

I would like to attribute this success to my parents and my sister in India. I would like to thank my mother Suman, for all the hard work and faith she had in me when I started my PhD. This would not have been possible without their continuous support and unconditional love.

I also thank my only love, my wife Purva, for her unwavering support and belief in me during the most difficult time of my research work. She provided me with a pillar of support and I hope could do the same for her.

I am grateful to our sponsors Chevron, ADNOC and CCP3 at The University of Texas at Austin for making this work possible.

Global Upscaling of Secondary and Tertiary Displacements

Lokendra Jain, Ph.D.

The University of Texas at Austin, 2014

Supervisor: Larry W Lake

Fluids injected during secondary and tertiary floods often leave parts of the reservoir unswept mostly because of large heterogeneity and mobility ratio. Several applications require an analytical scheme that could predict production with as few parameters possible. We develop such an analytical model of volumetric sweep that aims to apply an extension of Koval's theory where flow is assumed to be segregated under vertical equilibrium conditions for secondary and tertiary displacements. The unified theory for vertical equilibrium (viscous and dispersive) is also derived as a precursor to model development.

The original Koval factor is applicable for upscaling secondary miscible floods. The new analytical model for secondary and tertiary floods is applied to provide quick estimates of oil recovery of miscible as well as immiscible displacements, which is then calibrated against field data. The model parameters, Koval factor, sweep efficiency and pore volume, estimated after history matching could be used to make reservoir management decisions. The model is very simple; history matching can be done in a spreadsheet.

Single-front, gravity-free, displacements can be modeled using Koval factors. Two-front, gravity-free, displacements can also be modeled using Koval-type factors for both the fronts. These Koval-type factors, coupled with laboratory scale relative permeabilities, allows for scaling the displacement to a larger reservoir system. The new method incorporates by-passed pore volume as a parameter, a difference between this work and that of Molleai, along with Koval factors and local front velocities. For two front displacements, it also accounts for the interaction between the fronts which honors correct mass conservation, another difference with the work of Molleai. The results from new models for secondary and tertiary displacements were verified by comparing them against numerical simulations. The application was also demonstrated on actual field examples.

Current techniques for reservoir surveillance rely on numerical models. The parameters on which these numerical models depend on are very large in number, introducing large uncertainty. This technique provides a way to predict performance without the use of computationally expensive fine scale simulation models, which could be used for reservoir management while reducing the uncertainty.

Table of Contents

List of Tables xiv

List of Figures xviii

CHAPTER 1 1

Introduction...1

1.1 PROBLEM DESCRIPTION 1

1.2 RESEARCH OBJECTIVES: 4

Hypothesis: 4

1.3 Dissertation Outline: 5

CHAPTER 2 6

Literature review 6

2.1 RECOVERY STAGES 7

2.1.1 Primary recovery...8

2.1.2 Secondary recovery...8

2.1.3 Tertiary recovery...8

2.1.3.1 Trapped oil..9

2.1.3.2 Bypassed oil 10

2.2 OIL RECOVERY PREDICTION..10

2.3 UPSCALING OF SECONDARY AND TERTIARY DISPLACEMENTS 11

2.3.1 Waterflood upscaling 12

2.3.2 Chemical flood upscaling 13

2.3.2.1 Polymer flooding...13

2.3.2.2 Surfactant-Polymer floods 14

2.3.2.3 Alkaline-Surfactant Polymer Floods.................................14

2.3.2.4 Upscaling methods...14

2.3.3 Gas (solvent) flood upscaling 15

2.4 COHERENCE THEORY 20

2.5 VERTICAL EQUILIBRIUM 21

CHAPTER 3 24

Unified Analysis of Transverse Flow Equilibrium 24

  3.1 VERTICAL EQUILIBRIUM ANALYSIS 26

CHAPTER 4 41

Upscaling of Miscible Floods: An Extension to Koval’s Method 41

  4.1 ASSUMPTIONS 44
  4.2 THEORETICAL DEVELOPMENT 46
  4.3 GOVERNING EQUATIONS 47
  4.4 INITIAL AND BOUNDARY CONDITIONS 53
  4.5 METHOD OF SOLUTION 54
  4.6 COMPARISON BETWEEN THE NEW MODEL WITH MOLLAEI’S MODEL 59
    4.6.1 Case 1, (H_k=1.1) 60
    4.6.2 Case 2, (H_k=5) 62
    4.6.3 Case 3, (H_k=20) 63
  4.7 RESULTS AND VERIFICATION 65
    4.7.1 Continuous solvent injection 67
    4.7.2 Simultaneous Water- Solvent injection 70
      4.7.2.1 Low WAG ratio case 70
    4.7.2.2 Intermediate WAG ratio case 72
    4.7.2.3 High WAG ratio case 73
  4.8 OPTIMAL WAG RATIO 75
  4.9 SECONDARY FLOOD: HIGH WAG RATIO CASE 77
  4.10 OTHER APPLICATIONS 80
  4.11 CONCLUSIONS 81

CHAPTER 5 82

Lost Pore Volume: Secondary and Tertiary Floods 82

  5.1 Model development for secondary displacements 84
    5.1.1 Assumptions 85
  5.2 Model extension and verification for true reservoirs 96

    - 5.2.1 Verification steps 97
- 5.3 Results for water floods 102
    - 5.3.1 Line Drive pattern 103
    - 5.3.2 Quarter five-spot 110
- 5.4 Model development for tertiary two front displacements 118
    - 5.4.1 Assumptions 119
        - Miscible WAG floods, ...121
        - Polymer floods 122
- 5.5 Model extension and verification for true reservoirs 124
    - 5.5.1 Verification 126
- 5.6 Results 129
    - 5.6.1 Polymer floods 129
        - 5.6.1.1 Line drive pattern 129
        - 5.6.1.2 Quarter 5 spot 132
    - 5.6.2 Miscible gas flood 137
        - 5.6.2.1 Line drive pattern 138
        - 5.6.2.2 Quarter five-spot 139
- 5.7 Model Validation 144
    - 5.7.1 Model Validation steps 145
        - 5.7.1.1 Field data 145
        - 5.7.1.2 Field data preparation 146
    - 5.7.2 Water flooding history matching 147
    - 5.7.3 EOR history matching 155
        - 5.7.3.1 Polymer floods 155
        - Daqing field pilot PO 156
        - Limitations of Mollaei’s model 159
    - 5.7.4 Solvent gas/WAG flood 161
        - Slaughter WAG pilot 161
        - Rangely Field 163
- 5.8 Summary 166

CHAPTER 6 167
Conclusions and Future Work 167
6.1 CONCLUSIONS 167
6.1.1 Upscaling of miscible floods 167
6.1.2 Lost pore volume: Secondary and tertiary floods 168
6.1.3 Unified vertical equilibrium analysis.....................................169
6.2 FUTURE WORK...170
Appendix A..172
A.1 DERIVATION OF MASS CONSERVATION EQUATIONS 172
Appendix B..175
B.1 DEFINING FRACTIONAL FLOW IN EACH REGION (J, B AND I).................175
Appendix C..179
Automatic History Matching Algorithm...179
Miscible WAG floods 179
Polymer floods..180
Algorithm steps...182
Appendix D..185
Waterflood History matches 185
Reservoir Sand C4 185
Reservoir Sand C5 188
Reservoir Sand C6 189
Reservoir Sand C7 191
Polymer flood history matches 192
Chateaurenard field pilot..192
Marmul field pilot...193
North Burbank unit pilot...194
Sleepy Hollow pilot 195
Courtenay field..196
Miscible WAG/CO_2 history matches...197

  Twofreds WAG project....197
  Lost Soldier pilot....198
  Rangely Field....199

Nomenclature....201
  Greek symbols....203
  Subscripts....203

References....205

List of Tables

Table 1-1. Summary of various existing EOR processes. 9

Table 3-1. Summary of the conditions under which different forces contribute to transverse flow in a reservoir. 39

Table 4-1. a) Initial and injection conditions b) Calculated parameters from pixel scale fractional flow theory (Walsh and Lake, 1988) based on initial and injection conditions given in a). 57

Table 4-2. a) Initial and injection conditions b) Calculated parameters from pixel scale fractional flow theory (Walsh and Lake, 1988) based on initial and injection conditions given in a). 60

Table 4-3. a) Initial and injection conditions for continuous solvent injection b) Calculated parameters from pixel scale fractional flow theory (Walsh and Lake, 1988) based on initial and injection conditions given in a).68

Table 4-4. a) Initial and injection conditions for a flood with WR=0.42 b) Calculated parameters from pixel scale fractional flow theory (Walsh and Lake, 1988) based on initial and injection conditions given in a). 71

Table 4-5. a) Initial and injection conditions for a flood with WR=1.0 b) Calculated parameters from pixel scale fractional flow theory (Walsh and Lake, 1988) based on initial and injection conditions given in a). 72

Table 4-6. a) Initial and injection conditions for a flood with WR=2.7 b) Calculated parameters from pixel scale fractional flow theory (Walsh and Lake, 1988) based on initial and injection conditions given in a). 74

Table 4-7. a) Initial and injection conditions for a secondary flood with WR=2.7 b) Calculated parameters from pixel scale fractional flow theory (Walsh and Lake, 1988) based on initial and injection conditions given in a).78

Table 5-1. a) Initial and injection conditions b) Calculated parameters from pixel scale fractional flow theory (Buckley-Leverret, 1942) based on the initial and injection conditions given in a).......................................94

Table 5-2. Different combinations of autocorrelation correlation lengths in *x*, *y* and *z* direction for generation of permeability fields 98

Table 5-3. Simulation parameters for line drive pattern and quarter five spot pattern

Table 5-4. Permeability field correlation lengths for the history matched case in Figure 5-9..104

Table 5-5. History matched parameters for the case shown in Figure 5-9. The comparison between the simulation and model is also shown for ultimate sweep efficiency and average water saturation..............................105

Table 5-6. Permeability field correlation lengths for the history matched case in Figure 5-12..107

Table 5-7. History matched parameters for the case shown in Figure 5-12. The comparison between the simulation and model is also shown for ultimate sweep efficiency and average water saturation..............................107

Table 5-8. Permeability field correlation lengths for the history matched case in Figure 5-15..110

Table 5-9. History matched parameters for the case shown in Figure 5-15. The comparison between the simulation and model is also shown for ultimate sweep efficiency and average water saturation..............................110

Table 5-10. Permeability field correlation lengths for the history matched case in Figure 5-18 114
Table 5-11. History matched parameters for the case shown in Figure 5-18. The comparison between the simulation and model is also shown for ultimate sweep efficiency and average water saturation. 114
Table 5-12. Permeability field correlation lengths for the history matched case in Figure 5-26. 130
Table 5-13. History match parameters for water flood and tertiary polymer flood for line drive pattern in Figure 5-26. 131
Table 5-14. Permeability field autocorrelation lengths for the history matched case in Figure 5-28. 132
Table 5-15. History match parameters for water flood and tertiary polymer flood for quarter five-spot pattern in Figure 5-28. 133
Table 5-16. Permeability field autocorrelation lengths for the history matched case in Figure 5-34. 138
Table 5-17.History match parameters for water flood and tertiary SWAG flood.139
Table 5-18. Permeability field autocorrelation lengths for the history matched case in Figure 5-36. 140
Table 5-19. History match parameters for water flood and tertiary SWAG flood.141
. ……………………………………………………………143
Table 5-20. Summary of history matched parameters for all field waterflooding cases 150
Table 5-21. Summary and comparison of the cumulative oil produced and total pore volume for each well and the whole reservoir. 152
Table 5-22. Summary of all polymer history match parameters. 158

Table 5-23. Non-unique history matched parameters from Mollaei's model for Sleepy Hollow pilot shown in Figure 5-42. 160

Table 5-24. Summary of field/pilot/well history match parameters for CO_2/WAG floods...164

Table B.1. Saturation distribution in the three regions defined by fractional flow theory. 175

List of Figures

Figure 1-1. US oil production supply and consumption forecast (EIA, 2012). 6

Figure 1-2. US EOR production since 1986 (OGJ biennial survey, 2012).............7

Figure 2-3. Schematic capillary desaturation curves (Lake, 1989) 10

Figure 3-1. Schematic of a reservoir with heterogeneity for vertical equilibrium (Yortsos,1995) 24

Figure 3-2. Effects of only viscous forces on displacements, viscous fingering (Yortsos, 1995) 25

Figure 4-1. Fractional flow curves for a first-contact miscible SWAG flood showing the formation of an oil bank (*B*) with two fronts separating it from the initial (*I*) and injection (*J*) condition..47

Figure 4-2. a) Layer arrangement in the order of increasing interstitial velocity from top to bottom. The heterogeneous system represented by a uniformly layered system (infinite autocorrelation length in the x-direction). b) Dimensionless representation of the same layered system based on definitions below...49

Figure 4-3. Static *F-C* curves relating flow capacity to storage capacity for different heterogeneity factors. The greater the heterogeneity, the more flow capacity in smaller fraction of the pore volume..............................51

Figure 4-4 a) Schematic showing dimensionless representation of a layered medium. b) Schematic representation of the formation of oil bank and solvent flow in a layered medium. Injected solvent wave travels fastest in the bottommost layer with the highest interstitial velocity and slowest at the top with smallest interstitial velocity. 52

Figure 4-5. Schematic showing the physical end points. Upstream of the oil bank, the entire cross-section is flooded by injected solvent and C_J =1. Downstream of oil bank, the entire cross section is at initial condition and C_I = 1. 56

Figure 4-6. Ternary diagram showing all the points mathematically satisfying the system of conservation equations as slow σ- and fast σ+ paths. The correct physical solution plotted in red is the path originating from C_J = 1, i.e left bottom corner on the triangle and ending at C_I = 1. The paths transition from slow to fast at the red point shown on the plot. Path based on Mollaei solution is plotted in black. Each point on the path travels with a specific velocity (σ). 58

Figure 4-7. a) Pixel scale fractional flow curve for the application with W_R=2.3. b) Physical path from Figure 4-6 converted to flow profile in the reservoir. Each point on the path travels with a velocity (σ) which is used to plot the profile. The profile is converted to effluent history that shows oil cut as well as solvent cut. c) Oil bank breaks through at t_D=0.36 and solvent breaks through after the oil bank break through. Peak oil cut coincides with solvent breakthrough. d) Recovery of 0.3 i.e total remaining oil is recovered at injected pore volumes of 4. 59

Figure 4-8. Ternary diagram (Case 1) showing the correct physical solution plotted in red is the path originating from C_J = 1, i.e left bottom corner on the triangle and ending at C_I = 1. The paths transition from slow to fast at C_B = 1. Path based on Mollaei solution is plotted in black. Each point on the path travels with a specific velocity (σ) 60

Figure 4-9. a) Profiles match perfectly for case 1 between new model and Mollaei model. b) The effluent history match between the new model and Mollaei model is perfect for case 1. 61

Figure 4-10. Ternary diagram (case 2) showing the correct physical solution plotted in red is the path originating from $C_J = 1$, i.e left bottom corner on the triangle and ending at $C_I = 1$. The paths transition from slow to fast at the red point shown on the plot. Path based on Mollaei solution is plotted in black. Each point on the path travels with a specific velocity (σ) 62

Figure 4-11. a) Profiles mismatch when all three regions J, B and I coexist. b) The mismatch in the profile doesn't affect the solvent and oil bank breakthrough in current case. Oil cut peak from Mollaei's model is predicted to be smaller than the new model (case 2). 63

Figure 4-12. Ternary diagram (case 3) showing the correct physical solution plotted in red is the path originating from $C_J = 1$, i.e left bottom corner on the triangle and ending at $C_I = 1$. The paths transition from slow to fast at the red point shown on the plot. Path based on Mollaei solution is plotted in black. Each point on the path travels with a specific velocity (σ). 63

Figure 4-13. a) Profiles mismatch when all three regions J, B and I coexist. b) The mismatch in the profile doesn't affect the solvent and oil bank breakthrough in current case. Oil cut peak from Mollaei's model is predicted to be smaller than the new model (case 3). 64

Figure 4-14. Pixel scale fractional flow curves for the verification cases. 66

Figure 4-15. Two immiscible spreading waves form at the pixel scale for continuous solvent injection case. 68

Figure 4-16. a) Pixel scale fractional flow conditions shown for continuous solvent injection. b) Flow profile for continuous tertiary solvent flood. The solvent wave travels very fast because of high solvent mobility. c) Oil bank and solvent breakthrough right at the start and oil cut falls off after that. Solvent cut jumps to a very high value of 0.8 to 0.9 very early. The model solution compares well with the numerical simulation. d) High solvent cut in the later part of production causes 16 injected pore volumes for complete oil recovery. 69

Figure 4-17. a) Pixel scale fractional flow conditions shown for W_R=0.42. b) Flow profile for tertiary small WAG solvent flood. The solvent wave travels slowly because of lowered mobility at the back of the oil bank. c) The oil bank breaks through at the start with high oil cut and then falls off. The delayed solvent breakthrough results in a larger peak oil cut. d) Ultimate oil recovery is faster compared to continuous solvent injection addition of water and improved mobility ratio. Numerical fluctuations lead to inexact match between model and simulation. 71

Figure 4-18. a) Pixel scale fractional flow conditions shown for W_R=1. b) Flow profile for tertiary intermediate WAG solvent flood. The solvent wave travels slowly because of the smaller mobility at the back of the oil bank. c) Oil bank breaks through at the start with large oil cut of 26% and then falls off. The solvent breakthrough is delayed resulting in a higher peak oil cut value. The peak oil cut coincides with solvent breakthrough. d) Ultimate recovery takes about 4.8 injected pore volumes which is larger than for low WAG ratio case. 73

Figure 4-19. a) Pixel scale fractional flow information for W_R=2.7. b) Flow profile for tertiary high WAG ratio solvent flood. The solvent wave travels very slowly because of small total mobility at the back of the oil bank. c) Oil bank breaks through after some delay and solvent breakthrough is delayed further. The peak oil cut coincides with the solvent breakthrough. Oil cut falls off after solvent breaks through. d) The ultimate recovery takes a lot longer in this case compared to previous WAG cases because of smaller front velocities at pixel scale. 75

Figure 4-20. Pixel scale fractional flow curves showing the optimal injection WAG ratio W_R=0.38. 76

Figure 4-21. The optimal WAG ratio from the above plot falls close to W_R of 0.4. At this WAG ratio, peak oil cut is the highest and recovery time is the lowest. 77

Figure 4-22. Flow profile between the boundary points show multiple velocities for one (C_J, C_I) point. This is unphysical. This is because of very small mobility ratio of 0.1 at the front of the oil bank for this case. A correct profile is obtained by placing a shock and determining the shock velocity. This is a result of a change in pixel scale initial condition.79

Figure 4-23. a) Flow profile for secondary high WAG ratio W_R=2.7 solvent flood. b) The solvent wave is spreading and travels very slowly because of low total mobility at the back of the oil bank. The oil bank travels as a shock because the mobility ratio ahead of the oil bank is very small. c) The oil cut profile shows an initial plateau and falls off when solvent breaksthrough. The ultimate recovery takes much longer in this case because of smaller front velocities at pixel scale. d) The recovery efficiency is high on account of secondary miscible displacement. The results match the simulation very well..80

Figure 5-1. Schematic showing window scale flow behavior for secondary floods such as water and gas floods. Segregated flow is represented as a single front in the reservoir separating region J from I. 83

Figure 5-2. Schematic showing window scale flow behavior for tertiary floods such as miscible WAG, polymer, surfactant and ASP floods. Segregated flow is represented as two fronts in the reservoir separating Region B from Regions J and I...84

Figure 5-3. Fluid distribution in the two regions based on pixel scale fractional flow theory for water floods (Buckley-Leverett, 1942). The average water saturation in region J is S_{1J} and water saturation in region I is S_{1i}. The local front velocity is $v_{\Delta S}$...86

Figure 5-4. Static *F-C* curves relating flow capacity to storage capacity for different heterogeneity factors. The greater the heterogeneity, the more flow capacity in smaller fraction of the pore volume...............................88

Figure 5-5. Representation of a layered reservoir (a) dimensional and (b) dimensionless for model development. The layers are arranged in the order of decreasing interstitial velocity from bottom to top. The heterogeneous system represented by a uniformly layered system (infinite autocorrelation length in the x-direction)...........................88

Figure 5-6. Schematic representation of single front displacement in a layered reservoir (dimensionless) (Figure 5-4) with a fraction of reservoir never swept (lost pore volume)..89

a) b) 94

Figure 5-7. a) Pixel scale fractional flow curve for the application b) Physical flow profile in the reservoir. Each point on the path travels with a velocity that is used to calculate effluent history. c) Effluent history shows oil and water cut. Water breaks through at $t_D = 0.02$ after which the oil cut drops from unity to small values as the flood progresses. d) Recovery of 0.2 i.e total movable oil is recovered at the injected pore volume of 1.9. 95

Figure 5-8. Pixel scale fractional flow curves for the verification cases. The fractional flow curves shift towards the left (water more mobile) with increasing mobility ratios. 102

Figure 5-9. History match between simulation and model for the cumulative oil produced in a) and oil cut in b) show good matches. The oil cut in b) falls sharply from the beginning with start of injection.................104

Figure 5-10. The permeability distribution in the *x*-*y* plane with large scale correlation features in the *x*-direction (channels). 105

Figure 5-11. Water saturation distribution in the reservoir in an *x*-*y* plane at the end of simulation. The water saturation becomes progressively smaller (as shown by the two red ellipses) in grid blocks away from the line joining the injector and the producer. This spreading of water is caused by heterogeneity. 106

Figure 5-12. History match between simulation and model for the cumulative oil produced in a) and oil cut in b) show reasonably good matches. The oil cut in b) stays at a plateau in the beginning and falls sharply from the time breakthrough happens. 107

Figure 5-13. The permeability distribution in the x-y plane with large scale correlation features in the y-direction (channels). 108

Figure 5-14. Water saturation distribution in the reservoir in an *x*-*y* plane at the end of simulation (t_D = 4.96). The water saturation is uniformly high across the total pore volume because of uniform spreading due to heterogeneity structure...109

Figure 5-15. History match between simulation and model for the cumulative oil produced in a) and oil cut in b) show good matches. The oil cut in b) falls sharply from the beginning with start of injection. 110

Figure 5-16. The permeability distribution in the *x*-*y* plane with large scale correlation features in the *x*-direction (channels). 111

Figure 5-17. Water saturation distribution in the reservoir in an *x*-*y* plane at the end of simulation. The water saturation gets progressively smaller (as shown by the two red ellipses) in grid blocks away from the line joining the injector and the producer. This spreading of water is caused by heterogeneity. 112

Figure 5-18. History match between simulation and model for the cumulative oil produced in a) and oil cut in b) show reasonably good matches. The oil cut in b) stays at a plateau in the beginning and falls sharply after breakthrough. 113

Figure 5-19. The permeability distribution in the *x*-*y* plane with large scale correlation features in the *y*-direction (channels). 115

Figure 5-20. Water saturation distribution in the reservoir in an *x*-*y* plane at the end of simulation ($t_D = 4.96$). The water saturation is uniformly high across the total pore volume because of uniform spreading because of heterogeneity structure. 116

Figure 5-21. a) Ultimate volumetric sweep from the model compares very well with the simulation. b) Average water saturation in the swept regions from model also compares very well against the simulation. The results for all the verification cases from line drive and quarter five spot are shown here. 117

Figure 5-22. Ultimate volumetric sweep efficiency decreases as the Koval factor increases. The results for all the verification cases for line drive and quarter five spot pattern are plotted here. 117

Figure 5-23. Schematic representation of two front displacement into a layered reservoir (dimensionless) with a fraction of reservoir never swept (Lost pore volume) 120

Figure 5-24. a) Pixel scale fractional flow schematic for miscible WAG flood. b) Pixel scale flow schematic for polymer floods. Regions *J*, *B* and *I* are marked on both the fractional flow curves. 121

Figure 5-25. Pixel scale fractional flow curves for tertiary polymer flood. 129

Figure 5-26. Polymer flood (tertiary displacement) often follows water flood (secondary displacement). a) Water flood history match is shown using the new model for secondary floods. b) Oil cut history match between simulation and model is good. The oil cut initially increases with polymer injection. The oil cut reaches a peak value and falls off thereafter. 130

Figure 5-27. a) Water saturation map at the end of waterflooding and beginning of polymer injection (Water cut, 95%). b) Water saturation map at the end of polymer injection phase (Water cut, 95%) for line drive pattern.131

Figure 5-28. Polymer flood (tertiary displacement) following water flood (secondary displacement). a) Water flood history match is shown using the new model for secondary floods. b) Oil cut history match between simulation and model is good. The oil cut initially increases with polymer injection. The oil cut reaches a peak value and falls off thereafter................133

Figure 5-29. a) Water saturation map at the end of water flooding and beginning of polymer injection (Water cut, 95%). b) Water saturation map at the end of polymer injection phase (Water cut, 95%) for quarter five-spot pattern. 134

Figure 5-30. Koval factors for both the polymer bank and oil bank decrease as ultimate volumetric sweep increases for a) Line drive pattern and b) Quarter five-spot pattern. Koval factors for oil bank are also higher compared to polymer bank for both the patterns. 135

Figure 5-31. Koval factors for polymer bank and oil bank increase monotonically with increasing water flood Koval factors for a) Line drive pattern and b) Quarter five-spot pattern. Koval factors obtained during polymer floods are also well correlated with the water flood Koval factors for both patterns. 135

Figure 5-32. Ultimate volumetric sweep from the new model compares well with the simulation for polymer floods for a) Line drive pattern and b) Quarter five-spot pattern. 136

Figure 5-33.Pixel scale fractional flow curves for tertiary SWAG flood. 137

Figure 5-34. SWAG/CO_2 flood (tertiary displacement) follows water flood (secondary displacement). a) Water flood history match is shown using the new model for secondary floods. b) Oil cut history match between simulation and model is good. The oil cut initially increases with gas injection. The oil cut reaches a peak value and falls off thereafter.138

Figure 5-35. a) Water saturation map at the end of water flooding and beginning of SWAG injection (Water cut, 95%) b) Gas saturation map at the end of SWAG injection phase (Water cut, 95%) for line drive case. 139

Figure 5-36. SWAG/CO_2 flood (tertiary displacement) follows water flood (secondary displacement). a) Water flood history match is shown using the new model for secondary floods. b) Oil cut history match between simulation and model is good. The oil cut initially increases with gas injection. The oil cut reaches a peak value and falls off thereafter. 140

Figure 5-37. a) Water saturation map at the end of water flooding and beginning of SWAG injection (Water cut, 95%). b) Gas saturation map at the end of SWAG injection phase (Water cut, 95%) for quarter five-spot case. 141

Figure 5-38. Koval factors for both the solvent bank and oil bank decrease as ultimate volumetric sweep increases for a) Line drive pattern and b) Quarter five-spot pattern. Koval factors for oil bank are also higher compared to solvent bank for both the patterns. 142

Figure 5-39. Koval factors for solvent bank and oil bank increase monotonically with increasing water flood Koval factors for a) Line drive pattern and b) Quarter five-spot pattern. Koval factors obtained during solvent floods are also well correlated with the water flood Koval factors for both patterns. 143

Figure 5-40. Ultimate volumetric sweep from the model compares very well with the simulation for miscible SWAG floods for a) Line drive pattern and b) Quarter five-spot pattern. 143

Figure 5-41. Water flood history match for the whole reservoir (Sand-C4) 148

Figure 5-42. Water flood history match for a single well (Well 1) in the reservoir (Sand-C4) 149

Figure 5-43. Waterflood history match comparison between (a) Mollaei's and (b) the new model for cumulative oil produced for Well 1 (Sand C4).......149

Figure 5-44. Field and single well ultimate volumetric sweep decreases with increasing Koval factors. 153

Figure 5-45. The Koval factors from new model show an increasing trend with the Koval factors obtained from Mollaei model. 154

Figure 5-46. Koval factor comparison between the new model and Mollaei's model 154

Figure 5-47. Location of polymer flood pilots and wells for the Daqing field. (Wang et al., 1993). 156

Figure 5-48. Polymer flooding history match of Daqing PO pilot. The pilot data is from Wang et al. 1993. 157

Figure 5-49. Ultimate volumetric sweep efficiency decreases with increase in Koval factors for polymer and oil bank. 159

Figure 5-50. Polymer and oil bank Koval factors from a) new model and b) Mollaei's model. The polymer bank Koval factors from the new model are smaller than the oil bank Koval factors. 159

Figure 5-51. Non-unique solutions from Mollaei's model demonstrated using Sleepy Hollow pilot data...160

Figure 5-52. CO_2 WAG flood history match for Slaughter pilot (Rowe et al., 1982). 162

Figure 5-53. Waterflood and CO_2/WAG flood history matches for Well 1 in Rangely field. 163

Figure 5-54. Field Koval factors for solvent bank and oil bank decrease with increasing ultimate volumetric sweep. 165

Figure D.1. Waterflood history match for a single well (Well 2) in the reservoir (Sand- C4) 185

Figure D.2. Waterflood history match for a single well (Well 3) in the reservoir (Sand-C4). 185
Figure D.3. Waterflood history match for a single well (Well 4) in the reservoir (Sand-C4). 186
Figure D.4. Waterflood history match for a single well (Well 5) in the reservoir (Sand-C4). 186
Figure D.5. Water lood history match for a single well (Well 6) in the reservoir (Sand-C4). 187
Figure D.6. Waterflood history match for a single well (Well 7) in the reservoir (Sand-C4). The oil cut never starts to decline after the plateau for this well so the parameters estimated from history matching are unreliable. 187
Figure D.7. Waterflood history match for the whole reservoir sand C5.............188
Figure D.8. Waterflood history match for a single well (Well 1) in the reservoir (Sand C5)..188
Figure D.9. Waterflood history match for a single well (Well 2) in the reservoir (Sand C5)..189
Figure D.10. Waterflood history match for the whole reservoir sand C6...........189
Figure D.11. Waterflood history match for a single well (Well 1) in the reservoir (Sand C6). 190
Figure D.12. Waterflood history match for a single well (Well 2) in the reservoir (Sand C6). 190
Figure D.13. Waterflood history match for the whole reservoir sand C7...........191
Figure D.14. Waterflood history match for a single well (Well 1) in the reservoir (Sand C7). 191

Figure D.15. Waterflood history match for a single well (Well 2) in the reservoir (Sand C7). 192
Figure D.16. Polymer flooding history match of Chateaurenard polymer flood (Takaqi et al., 1992) 193
Figure D.17. Polymer flooding history match of Marmul polymer flood. (Koning et al., 1988) 194
Figure D.18.Polymer flooding history match of North Burbank polymer flood. (Zornes et al., 1986) 195
Figure D.19. Polymer flooding history match of Sleepy Hollow polymer flood.(Christopher et al., 1988) 196
Figure D.20. Polymer flooding history match of Courtenay polymer flood. (Putz et al., 1994) 197
Figure D.21. CO_2 WAG flood history match for Twofreds pilot (Flanders et al., 1993). 198
Figure D.22. CO_2 WAG flood history match for Lost Soldier pilot (Brokmeyer et al., 1996). 199
Figure D.23. Waterflood and CO_2/WAG flood history matches for Well 2 in Rangely field. 199
Figure D.24. Waterflood and CO2/WAG flood history matches for Well 3 in Rangely field. 200
Figure D.25. Waterflood and CO_2/WAG flood history matches for Well 4 in Rangely field. 200

CHAPTER 1

Introduction

Oil recovery efficiency in the primary phase of production life of any field is limited. Thus to improve oil recovery, a variety of supplemental techniques have been used. Water flooding generally governs the secondary phase of field production life and recovery techniques like gas flooding (miscible) and chemical flooding govern the tertiary phase. Other recovery techniques like steam flooding are also used to increase production from heavy oil fields.

1.1 PROBLEM DESCRIPTION

In waterflooding, injected water pushes the resident oil out of the reservoir. The water is immiscible with the reservoir oil and for many cases water is more mobile than the oil. Reservoir heterogeneity and large water mobility cause water to sweep the reservoir non-uniformly. Polymer floods are meant to increase the reservoir sweep because they reduce the water mobility.

In miscible flooding, injected solvent forms a single phase with the resident oil and thus helps push out otherwise trapped oil. The solvent generally is made of light hydrocarbons like liquidified petroleum gas and intermediates (C_2-C_6). The primary purpose of solvent flooding is to increase microscopic displacement efficiency but the non-uniform flow of solvent in the reservoir causes low sweep efficiency. Solvent fingers and channels in the reservoir often because of the low viscosity and leaves parts of the reservoir unswept.

The degree of solvent miscibility in the oil also governs the displacement efficiency. Under the conditions (pressure, temperature and compositions) when total miscibility is achievable, the displacement is called first-contact miscible. Displacements where miscibility is developed (condensing drive or vaporizing drive) are called multi-contact miscible floods. In multi-contact miscible floods the continuous component transfer between solvent and oil establishes a transition zone. In this transition zone all the compositions are contiguously miscible. The minimum pressure at the reservoir temperature when the multi-contact miscibility develops is called minimum miscibility pressure.

Numerical simulation is used to model mass, momentum and energy transport at coarse scales. Numerical simulation is a way to extend experimental results to large scales. Numerical models are also required to predict and optimize the oil recoveries by understanding flow behavior in the reservoirs. Predicting the oil recovery in waterfloods, polymer floods and miscible floods requires accurate representative coarse scale flow models. The accurate coarse scale models should be built on the basis of correct understanding of parameters affecting transport processes at a fine scale. The objective of reservoir simulation is to infer the behavior of hydrocarbon bearing petroleum systems using numerical models. Reservoir simulation not only models the hydrodynamics of flow in the reservoir but also accounts for injection, production wells along with the surface controls that dictate the flow.

The principle of reservoir simulation is to numerically solve the governing transport differential equations at the specified scale. The governing equations are solved for the variables like pressure, saturations and component concentrations by discretizing them in space and time. The numerical techniques allow for representation of the original differential equations in the form of set of algebraic equations to express fundamental laws of mass, energy and momentum conservation.

Waterfloods and polymer floods can be simulated using black-oil simulators. First contact, multi-contact and near miscible floods in hydrocarbon bearing zones need to be simulated using compositional simulators because oil and gas are mixtures of a number of components. In such displacements, viscous fingering and channeling leads to change in oil and solvent saturations as well as pressures at a scale smaller than the grid scale. These displacements are also adverse mobility ratio floods that leave bypassed hydrocarbon zones. Past simulation efforts directed towards solving the equations that govern miscible floods have met with limited success. The major obstacle faced by the simulation models is the mixing cell effect. This significantly dampens the flow instabilities that are induced because of unfavorable mobility ratio and heterogeneities. Thus the predicted recovery from such models is greater than the actual oil recovery. Effective modeling of viscous instabilities and channeling would need models at centimeter or millimeter scale. A fine scale model can represent the details of adverse mobility ratio floods.

The representation of reservoir systems with fine scale reservoir models and running dynamic simulations on them places prohibitive demands on computational resources. Thus coarse scale reservoir models are built for flow simulations. The fine scale or coarse scale simulation models still have substantial uncertainty associated with them because of large number of input parameters. The input parameters for the simulation models are not known apriori and slight change in the parameters changes the simulation output.

It is a challenge to develop simple upscaled models that predict the reservoir performance using only a few input parameters and represent all the variables that affect flow in the reservoir. The variables include reservoir heterogeneity, mobility ratios, volumetric sweep, phase behavior for miscible floods and initial and final saturations in the swept regions. Various upscaled models have been developed for performance prediction of secondary and tertiary floods as discussed in chapter 2. It is challenging to develop such models that also honor fine scale physics and account for heterogeneity and mobility ratio effects at reservoir scale.

1.2 RESEARCH OBJECTIVES:

Hypothesis:

If the field scale heterogeneity in reservoirs can be defined using a single parameter then it can be coupled with the information obtained from fine scale physics such as mobility ratio and local velocities for various flow processes in the reservoirs (immiscible and miscible) to predict average performance at field scale.

The main idea of this work is to construct an upscaled scheme for waterfloods and tertiary floods (miscible gas and polymer floods) that can address the important issues such as:

- Assess if the effects of heterogeneity and mobility ratio can be decoupled on the convective flow.
- Develop an upscaling technique that accurately represents the flow behavior from fine scale onto field scale models.
- Decouple the effects of convective mixing (sweep) from dispersive mixing on sweep efficiency (displacement and volumetric).
- Develop fast analytical models that predict field scale volumetric sweep efficiency and allows for estimating lost pore volume (fraction of total pore volume that always stays unswept) explicitly.
- Prove analytically the conditions for existence of vertical equilibrium under the presence of viscous and dispersive flow in heterogeneous reservoirs.

1.3 DISSERTATION OUTLINE:

- Chapter 2 of the dissertation has a commentary on the historical work done on various models developed to predict oil recovery for waterfloods, polymer floods and miscible WAG floods.
- Chapter 3 of the dissertation shows the analytical derivation of conditions for total transverse equilibrium. The proof was done because the models developed in the dissertation are based on transverse equilibrium assumption.
- Chapter 4 of the dissertation shows the formulation of a model for upscaling of tertiary miscible floods which are two front displacements.
- Chapter 5 of the dissertation shows the development, verification and field application of the models for predicting oil recovery for secondary and tertiary floods.
- Chapter 6 of the dissertation finally concludes the research presented in dissertation. Few recommendations for future work are also presented in the chapter.

CHAPTER 2

Literature review

Increasing oil prices and concerns about meeting energy demands have led to renewed focus on enhanced oil recovery (EOR). 7 million b/d of additional capacity would be needed by the year 2040 just in the US (Figure 1-1). EOR can help recover a significant portion of the remaining oil in discovered reservoirs. Advancements in technology have made the application of EOR economically attractive.

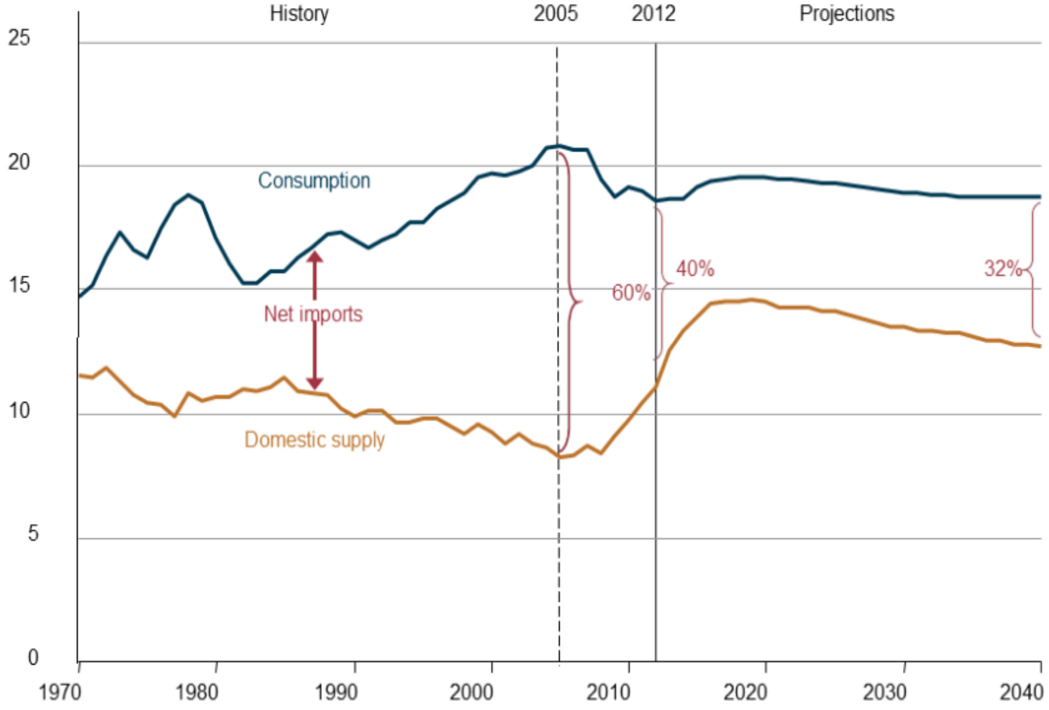

Figure 1-1. US oil production supply and consumption forecast (EIA, 2012).

In the United States, since 1986 6.4 billion barrels of oil has been recovered through various EOR technologies (Figure 1-2). Two EOR techniques, thermal recovery using steam injection and CO_2 miscible oil recovery are the most widely used because of their economic feasibility.

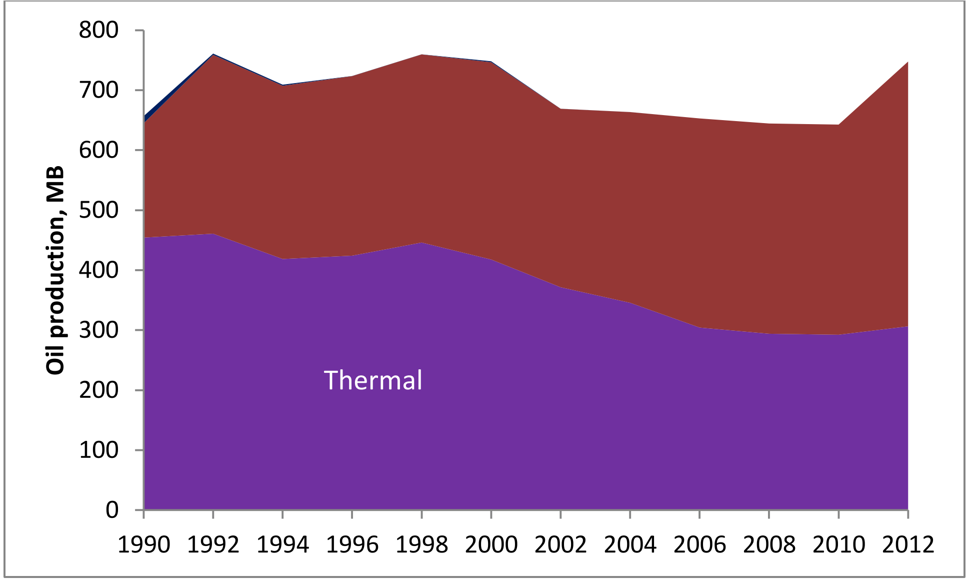

Figure 1-2. US EOR production since 1986 (OGJ biennial survey, 2012).

In this chapter, a brief description of the various recovery stages for an oil field is provided first.

The main objective of the dissertation is to develop upscaling models for predicting oil recovery in secondary and tertiary recovery stages. Second, upscaling is defined briefly followed by an overview of upscaling techniques for secondary floods (waterflood) and tertiary floods (polymer, WAG) that have been developed over the years. The upscaling models developed in the dissertation are based on vertical equilibrium (VE) assumption so the concept of VE is described finally.

2.1 RECOVERY STAGES

There are typically three recovery stages in the operating life of an oil field. The three recovery stages are briefly described below.

2.1.1 Primary recovery

The primary recovery from an oil reservoir is through one or more recovery mechanisms listed below (Walsh and Lake, 2003):

a) Water drive

b) Gas cap drive

c) Solution gas drive

d) Expansion drive

e) Gravity drainage

Recovery during this phase stops when the reservoir energy to expel the hydrocarbon is depleted or the economic limit is reached. The range of oil recovery from primary phase is between 5 to 15% (Dake, 1978).

2.1.2 Secondary recovery

The stage following primary recovery is called secondary recovery. The reservoir is supplied with the required energy for pressure support to produce more oil by injecting fluids such as brine or gas during secondary recovery. Recovery during this phase stops when the injected fluids recycle at an uneconomical rate. The current research focuses on developing upscaling method for waterfloods.

2.1.3 Tertiary recovery

The stage following secondary recovery is called tertiary recovery. The oil recovery is increased by either increasing the volumetric and/or displacement sweep efficiencies during the tertiary injection phase. When a fluid not normally present in the reservoir is injected in the reservoir to increase oil recovery the corresponding process is classified as an EOR process. There are mainly three types of EOR processes in tertiary recovery phase as shown in Table 1.

Gas flooding	**Chemical flooding**	**Thermal recovery**
CO_2/Nitrogen/flue gases/ hydrocarbon enriched gas	Polymer/ Alkali- Surfactant/Alkali- Surfactant-Polymer	Steam/ Cyclic steam stimulation/ Hot water/ Downhole steam generation/ In-situ combustion

Table 1-1. Summary of various existing EOR processes.

The EOR processes listed above (Table 1-1) target the oil either trapped by capillary forces in pores connected to small throats or the bypassed oil in unswept parts of the reservoir from secondary recovery stage.

2.1.3.1 Trapped oil

The amount of trapped oil is inversely proportional to the capillary number even though the relationship is strictly monotonic as shown in Figure 2-3. The capillary number (N_{CD}) (Lake, 1989) which is the ratio of viscous force to capillary forces, controls the amount of oil being trapped.

$$N_{CD} = \frac{\mu u}{\sigma}$$

(2.1)

where σ is the interfacial tension between flowing phases, μ is the viscosity of displacing fluid and u is the superficial injection velocity. The capillary number increases when injection velocity and viscosity increase and/or the interfacial tension decreases. The increase in capillary number required to cross the critical value to mobilize the trapped oil is a few order of magnitudes (Figure 2-3); thus increasing the injection velocity or viscosity is impractical compared to decreasing the interfacial tension.

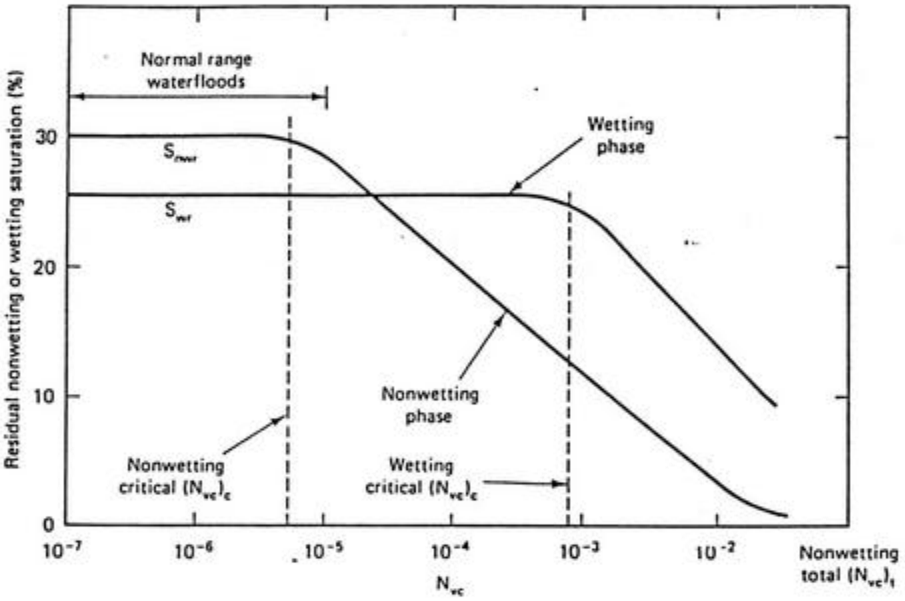

Figure 2-3. Schematic capillary desaturation curves (Lake, 1989)

2.1.3.2 Bypassed oil

The amount of bypassed oil depends on field heterogeneity and mobility ratio. Mobility ratio is defined as the ratio of injected fluid mobility to displaced fluid mobility. Since the field heterogeneity cannot be changed, mobility ratio reduction allows the injected fluid to move to previously unswept reservoir volume and recover more oil.

2.2 OIL RECOVERY PREDICTION

Oil recovery prediction for different recovery stages discussed above is important for economic analysis. For primary recovery, a special class of numerical simulators called tank models can be used to predict oil recovery (Walsh and Lake, 2003). As more data is gathered with production, for secondary and tertiary recovery stages, tools like reservoir simulators are used to predict oil recovery. The reservoir simulation models at a fine scale are computationally taxing, so such models are upscaled to provide reasonable estimates of oil recovery quickly. The upscaling for secondary and tertiary floods is described below in detail.

2.3 UPSCALING OF SECONDARY AND TERTIARY DISPLACEMENTS

Upscaling in reservoir simulation is a process where a detail-oriented model, called a fine scale model, is replaced by a representative model with equivalent properties that gives same predictions (Christie, 2001). Upscaling is a problem that is best addressed as depending on the production mechanism and the level of physical detail required to be accommodated to make predictons. Upscaling thus can be classified in terms of the type of parameters being upscaled (single or multi-phase flow parameter upscaling) (Durlofsky, 2003). Single-phase flow upscaling produces effective permeabilities for coarse scale models whereas two phase flow requires upscaling of capillary pressure as well as relative permeability parameters (Barker and Thibeau, 1997).

The second type of classification is related to the way the upscaled parameters are calculated. Upscaled parameters to replace the fine scale model can be calculated locally or globally. Locally the parameters are calculated by targeting the corresponding region from the fine scaled model. In global upscaling technique, the entire fine scale model is simulated to calculate coarse scale parameters with the assumption that these calculated parameters will be representative of all the similar flow scenarios (Durlofsky and Behrens, 1996).

Several researchers (Koval, 1963, Patton, 1969; Paul, 1982 and 1984; Lake, 1978; Sayarpour, 2008; Shook, 2009, Mollaei, 2011) have developed fast global upscaling models to predict waterflood and EOR flood performances. Upscaled models are developed analytically by incorporating the impact of various parameters such as reservoir heterogeneity, mobility ratios, reservoir mixing, etc., for each displacement process. The globally upscaled models are much faster and need fewer input parameters compared to the numerical simulation models. The globally upscaled models also provide quick quantitative estimates of recovery efficiency and production rates for economic evaluation and decision making.

2.3.1 Waterflood upscaling

Water injection in an oil reservoir is primarily performed to increase the oil production rate and ultimate oil recovery. The oil is recovered through "voidage replacement" – injection of water to increase the reservoir pressure and maintain it at a level below the fracture pressure of the reservoir (Craig, 1971). The oil is displaced from the pores by water, but recovery efficiency for waterfloods depends mainly on oil to water mobility ratio and rock heterogeneity.

Models to predict waterflood performance at different scales have been developed by several authors. The first analytical model to predict waterflood performance was developed by Buckley-Leverett (1942) using frontal advance theory for homogeneous one dimensional linear porous media.

Stiles (1949) developed an upscaled model to predict waterflood performance by using permeability variation and the vertical productive capacity distribution. The model was mainly developed to predict flood performance in depleted or nearly depleted oil fields at the reservoir scale. Dykstra and Parsons (1950) also developed a model to predict waterflood performance for a reservoir with vertically non-communicating layers. They identified mobility ratio, initial oil saturation and degree of permeability variation as the parameters influencing effluent history at reservoir scale. Craig (1955) performed a series of pattern waterfloods in the laboratory to study oil recovery performance. The model floods were scaled to reproduce field performance and a method was developed for applying mobility ratio concept to estimate areal and vertical sweep efficiency at reservoir scale.

Albertoni (2003) developed a model called the “Capacitance-Resistance model” that just uses the injection/production data for performance evaluation at the reservoir scale for waterfloods. Mollaei (2011) also developed a reservoir scale model to predict waterflood performance. The relationship between flow capacity and storage capacity as identified by (Koval, 1963 and Lake, 1989) forms the basis for Mollaei’s model. The model also uses injection/production data for evaluation of flood performance. Shook et al. (2009) also used the relationship between the flow capacity and storage capacity to evaluate the reservoir performance by analyzing tracer data.

2.3.2 Chemical flood upscaling

Chemical EOR is used to increase oil recovery either by injecting polymer (mobility control to increase volumetric sweep efficiency) or surface active agents such as surfactants (increase capillary number to decrease the residual oil saturation). The various chemical EOR methods as listed in Table 1 are polymer, surfactant-polymer (SP) and alkaline-surfactant-polymer (ASP) flooding.

2.3.2.1 Polymer flooding

Fingering and channeling for unfavourable mobility ratio waterfloods in heterogeneous reservoirs leads to small volumetric sweep efficiency. Sorbie, 1991 noted that channeling is prominent in waterfloods with mobility ratio greater than five.

Polymers are injected to decrease mobility ratios and increase volumetric sweep. Polymers are effective in highly heterogeneous reservoirs and high water-oil mobility ratio displacements. Polymer injection also delays the breakthrough while increasing sweep efficiency which also helps make the process economical. The injected polymer also helps recover oil from previously water swept zones by forming an oil bank (Patton, 1971) thus helping recover more oil. In some cases polymer might also help in reducing the residual oil saturation if increase in water viscosity is sufficient to increase the capillary number above the critical capillary number (Chen et al., 2011).

2.3.2.2 Surfactant-Polymer floods

Low tension flooding that involves injection of surface-active agents (surfactants) to lower the interfacial tension between water and oil phases and recover the trapped oil is called surfactant-polymer (SP) flooding (Lake , 1989). Polymer is also injected with the surfactant to increase displacement sweep (E_D) and volumetric sweep (E_V). Thus SP floods are expected to perform better than polymer floods. The SP flood is a multi-step process.

2.3.2.3 Alkaline-Surfactant Polymer Floods

The alkaline-surfactant-polymer (ASP) flood is very similar to surfactant-polymer (SP) flood. The main difference between ASP and SP floods is injection of alkaline in ASP floods along with surfactant and polymer to generate in-situ surfactant. The alkali reacts with the organic acids present in resident crude oil to produce surfactant.

2.3.2.4 Upscaling methods

The upscaling methods at global scale for chemical floods are fewer in number compared to waterfloods because of higher level of complexity associated with chemical floods.

Jones et al. (1984) developed a model for predicting oil rate versus time for polymer floods by combining a two-dimensional cross-sectional model using vertical equilibrium with areal sweep correlations and injectivity functions. The model is very fast compared to numerical simulation and is suitable for quick economic analysis. Paul et al. (1982) developed a model for evaluating performance of surfactant-polymer floods. The model correlates the factors impacting oil recovery to reservoir and flow properties such as permeability, depth of the reservoir, well spacing, heterogeneity (Dykstra-Parsons coefficient), crossflow, clay fraction and relative permeability. The effluent history is estimated from fractional flow theory, augmented with an effective mobility ratio to represent heterogeneity. Giordano (1987) developed a model to determine field scale performance as a function of field scale capillary number and Dykstra-Parsons coefficient for micellar/polymer floods.

Mollaei (2011) developed a model to capture the initial increase in oil cut that reaches a peak value and falls off thereafter for tertiary chemical floods. The model is based on the theory developed by Koval (1963) that captures the effects of heterogeneity and mobility ratio on the chemical flood performance. The model assumes that flow is segregated into different regions as observed from fractional flow theory for tertiary chemical floods.

2.3.3 Gas (solvent) flood upscaling

Solvent flooding is an EOR technique that recovers oil through vaporization, extraction, solubilization, condensation or dissolution. Sometimes viscosity reduction, oil swelling and solution gas drive also helps in oil recovery but the primary mechanism must be miscibility (Lake, 1989). Various fluids such as condensed petroleum gas, natural gas, carbon dioxide, air, nitrogen, flue gas and others are used to attain miscibility with the oil. The miscibility between the injected solvent with oil reduces the interfacial tension and helps recover more oil.

The volumetric sweep for a miscible gas flood depends on mobility ratio, gravity number, dispersive mixing (transverse and longitudinal) and heterogeneity (Doa, 2005).

CO_2 and hydrocarbon gases suffer from low volumetric sweep efficiency because of their high mobility. Miscible gases have been injected alternately with water to control the mobility ratio and improve the volumetric sweep efficiency successfully in the fields.

Walsh and Lake, 1988 studied miscible flooding in the presence of mobile water saturation. Their work is limited to one-dimensional displacements of oil by solvent without dispersion. Their work also applies to multi-contact miscible floods a well as first contact miscible floods because the displacements are assumed to be free of dispersion (Helfferich, 1981 and Hirasaki, 1981). The three component problem (solvent, water and oil) is solved using method of characterstics, which is discussed later in the chapter.

For gas flooding, the upscaled coarse grid simulators must characterize changes in phase behavior, changes in oil and gas compositions as the displacement progresses. Field data and scaled down lab experiments suggest that the miscible floods are unstable (Haberman, 1960). Unstable floods lead to fingering and intrinsic heterogeneity at large scale accentuates the problem further by causing channeling. Most proposals to simulate first-contact miscible floods effectively suggest empirical models to represent viscous fingering and channeling. One such proposal was made by Koval (1963) in which a factor (*K*) was introduced to represent the combined effect of longitudinal dispersion and mobility ratio on oil recovery.

$$F_s = \frac{1}{1+\frac{(1-S)}{KS}} \tag{2.2}$$

where, F_S is the average cross-sectional fractional flow of solvent, *S* is the average cross-sectional saturation of the solvent. Koval's theory is based on the premise that both dispersion and channeling are a result of heterogeneity, and it is difficult to decouple one from the other. In a strongly heterogeneous system, F_S is large even when the average cross-sectional saturation of the solvent (*S*) is small. Dougherty (1963) constructed a flow model akin to Koval's approach accounting for mixing. Dougherty's (1963) model uses four empirical parameters to define mixing between oil and the solvent caused by dispersion. He also proposed the use of heterogeneity factor defined by Koval (1963) to define fingering. Paul et al., 1984 developed a model that modified one-dimensional fractional flow theory to account for the effects of viscous fingering, reservoir heterogeneity and gravity segregation and combine it with areal sweep calculations for performance evaluation for miscible CO_2 floods.

Work done in the early 70's by Lantz (1970) and Todd and Longstaff (1972) used modified two and three phase immiscible simulators to simulate miscible floods. Lantz (1970) defined a method which required modification of relative permeability and capillary pressures to be special functions of saturation. The proper choice of these functions rendered the partial differential equations governing immiscible displacement completely analogous to miscible displacement.

Todd and Longstaff (1972) developed a method to modify existing three phase simulators to model miscible flood performance. They observed that the effect of dispersion on fluid properties can be effectively represented by an empirical model. The use of the empirical fluid model suggested by Lee and Claridge (1968) to calculate the effective viscosities and densities of oil and gas because of partial mixing made the mathematical solution to the problem very easy.

$$\mu_{oe} = \mu_o^{1-w} \mu_m^{w} \tag{2.3}$$

$$\mu_{ge} = \mu_g^{1-w} \mu_m^{w} \tag{2.4}$$

where, μ_{oe} and μ_{ge} are effective oil and gas viscosities respectively, μ_o and μ_g are the oil and gas viscosities without any mixing respectively, μ_m is the mixture viscosity and w is the mixing parameter which determines the amount of mixing and governs prediction power of the model. The mixture viscosity was determined by assuming ideal mixing and applying quarter power mixing rule.

Fayers (1988) described unstable displacement by suggesting the use of a fingering relationship

$$\Lambda = a + bC_f^{\alpha} \tag{2.5}$$

where, Λ is the fraction of cross-section occupied by fingers, C_f is the solvent saturation in the fingers, a is the initial finger width and $(a+b)$ is the fraction of the cross section occupied by fingers when $C_f = 1$. In a 2-D system Equation 2.5 relates the fraction of cross section invaded by the finger to the initial width by using an empirical parameter α. The fraction invaded by the fingers is used to define the upscaled mobilities for solvent and oil. Fayers and Newley (1988) also suggested a way to empirically extend this model to 2-D and 3-D flow systems by defining the average upscaled mobilities in the direction of finger propagation and in the direction transverse to it. The mobility functions depend upon the invaded fraction of the finger as their previous model suggested for 1-D displacement. The advantage of the approach suggested by Fayer and Newely (1988) was that it suggested a way to model miscible floods in multiple dimensions. Even though this was an advantage, the limitation of the model by Fayer and Newely was that the parameter α could not be easily correlated to any of the physical properties of the reservoir.

Mollaei (2011) also proposed the use of a model based on Koval's approach for miscible floods. The model for miscible floods is similar to the model proposed for chemical floods because tertiary solvent floods also form an oil bank thus leading to two travelling fronts in the reservoir (Walsh and Lake, 1988). The detailed description of Mollaei's model is provided in chapter 4 because it is the starting point of this research work.

The models described above are all suitable for first contact miscible floods. But none of the models above are suitable for multi-contact miscible floods i.e. the models are not equipped to handle the impact of phase behavior on mixing and vice versa. Todd and Chase (1979) suggested a model that used Todd and Longstaff model to account for viscous fingering under multi-contact miscible conditions. Ypma and Gardner (1984) demonstrated the importance of accounting for the interaction between phase behavior and fingering for multiple contact miscible floods. In 1-D systems viscous fingering has been observed to cause initial rapid growth of mixing zone which stabilizes at longer times. Young (1990) tried to solve this problem by using 1-D C-D equation and using dispersivity as a function of the gradient of viscosity ratio. This leads to larger dispersivities for floods with adverse mobility ratios. Crump (1988) suggested use of modified T-L model to account for phase behavior in multi-contact miscible floods. By using mixing parameter model dependent on mobility ratio and heterogeneity. Barker and Fayers (1994) proposed a new technique to upscale multi-contact miscible floods by introducing parameters which related flow rate of individual component at the boundary to the average mole fraction of the component in the desired upscaled volume. This averaging scheme requires rigorous fine scale simulations to get reliable correlating parameters for upscaling multi-contact miscible floods.

Nghiem and Agarwal (1989) proposed a two region model that suggested division of each grid block into two regions: a region with mixing between oil and solvent and a bypassed region. They suggested use of a transfer function allowing for mass transfer between these two regions. Their mass transfer model was based on two empirical parameters that are not effectively correlated to fine scale properties. Fayers et al. (1992) also proposed a similar approach of dividing each grid block into two regions and allowing mass transfer between the regions. These models in particular use empirical parameters for modeling that are not easily relatable to fine scale parameters that govern the physics of the flow. Huh et al. (2006) also proposed the use of two region model for upscaling of miscible floods. They used percolation theory (Kirkpatrik, 1973) and effective medium theory for an uncorrelated medium to define mobilities of fluids in the two regions. The channeling depends on the heterogeneity structure of the field and for statistically correlated geological fields the mobility model developed by Huh et al. (2006) becomes empirical in nature.

2.4 COHERENCE THEORY

The multi-component material balance equations developed in this dissertation are posed as hyperbolic equations with Riemann boundary conditions. Hyperbolic partial differential equations mathematically are *n* order partial differential equation that has a well-posed intial value problem for the first *n*-1 derivatives (Evans, 1998). For such problems Helfferich and Klein, 1970, Pope et al., 1978 and Walsh and Lake, 1988 show that the multicomponent wave is "coherent". Coherence dictates that all the components (dependent variables) travel with the same velocity at any point in space and time.

Consider a system with N components that is defined as:

$$\frac{\partial C_i}{\partial t} + \frac{\partial F_i}{\partial x} = 0 \qquad i = 1 \text{ to } N \tag{2.6}$$

$$F_i = f_i(C_1, C_2, C_3, ...C_N) \tag{2.7}$$

where, C_i is the concentration of i^{th} component and F_i is the flux term for i^{th} component and is a function of all the other component concentrations (equation 2.7). For such a system it can be proven using the method of characteristics (MOC) that at any given point in space and time (Helfferich, 1981) all concentrations have the same velocity,

$$\frac{dF_1}{dC_1} = \frac{dF_2}{dC_2} = \frac{dF_3}{dC_3} = ... = \frac{dF_N}{dC_N} = \eta \tag{2.8}$$

where, η is the velocity of the concentration waves. Equation 2.8 also shows that the number of waves equal the number of dependent variables (number of components).

Method of characteristics is a technique to solve hyperbolic partial differential equations. The method reduces the partial differential equations to a system of ordinary differential equations (Courant and Hilbert, 1962). The system of equations developed in chapter 4 present as a two component MOC problem. The method identifies the solution of the problem as two waves that travel in the system. These waves can be used to construct the flow profile for tertiary floods and used to generate recovery curves.

2.5 VERTICAL EQUILIBRIUM

The models developed in the dissertation are based on the vertical equilibrium assumption so we describe it in some detail here. The concept of vertical equilibrium can be easily explained using heat flow analogy in a metal plate (Coats, 1971). The metal plate with its thickness very small compared to its areal dimensions during heat flow can be assumed to have uniform temperature vertically. The uniform temperature vertically signifies thermal equilibrium but it not equivalent to zero heat flow vertically. The metal plate reaches thermal equilibrium vertically instantaneously with finite heat flow in the vertical direction.

The analogy can be extended to mass flow in thin reservoirs with large areal dimensions. For flow in such reservoirs the flow potential vertically can be assumed to be uniform. The uniform flow potential vertically signifies equilibrium but is not equivalent to zero flow vertically and any perturbation in the vertical direction diffuses and equilibrium fluid distribution is achieved instantaneously. Coats (1971), Yokoyama and Lake (1981), Zapata and Lake (1981), Yortsos (1991) and Shook et al. (1992) showed that VE applies in reservoirs where the vertical perturbations dissipate faster than the rate of flow in areal direction for immiscible two-phase flow. Mathematically they showed that the vertical equilibrium applies in the reservoirs with large R_L for immiscible displacement which is defined as,

$$R_L = \frac{L}{H}\sqrt{\frac{k_V}{k_H}} \tag{2.9}$$

where, L is the reservoir length, H is the reservoir thickness, k_V is the vertical permeability and k_H is the horizontal permeability. Zapata and Lake (1981) showed that under the VE assumption viscous cross-flow is maximum and, in a stratified reservoir, the mixing zone develops between the fastest and slowest front for displacements with mobility ratio higher than one. The development of mixing zone causes the vertical sweep to be higher than the corresponding segregated case. Oil displacement in a stratified reservoir (2-D) can be modelled using 1-D equations under the VE assumption (Coats, 1971). Thus, vertical equilibrium not only impacts the way flow process is modelled, it also impacts the oil recovery from a reservoir.

For miscible flow, the theory of equilibrium in the vertical direction was first used by Taylor (1953, 1954) for flow in a pipe. He showed that for a long pipe with small diameter the concentration variation vertically dissipates quickly and will manifest itself as a longitudinal diffusion. The flow in the two dimensional pipeline than can be solved as a one-dimensional flow with equivalent longitudinal diffusion. Lake and Hirasaki (1981) and Yortsos (1991) using the similar analyses for flow in stratified porous media, showed that transverse velocity profile in the reservoir along with the transverse dispersion can be represented by an equivalent longitudinal dispersion when, N_{TD} is large

$$N_{TD} = \frac{L\alpha_T}{H^2} \tag{2.10}$$

where, L is the reservoir length, H is reservoir thickness and α_T is the transverse dispersivity.

VE conditions for immiscible and miscible displacements have been derived analytically separately as discussed above. For displacements such as miscible water alternating gas flooding where viscous and dispersive forces impact the flow together, the analytical conditions required for total vertical equilibrium have not been derived. In this dissertation since models for miscible WAG floods are discussed, the unified vertical equilibrium theory is also developed.

CHAPTER 3

Unified Analysis of Transverse Flow Equilibrium

The description of flow during displacements in a reservoir that is long and narrow can be often simplified when flow is almost parallel. Various approximations have been identified by different researchers for such flow processes. The assumption of vertical equilibrium (VE) is typically one of them (Figure 3-1).

Depending on the fluid properties, the various approaches can be classified into two categories: one in which fluids are immiscible and flow is dominated by viscous, capillary and gravity forces, and another in which fluids are miscible and flow is also dominated by dispersive forces.

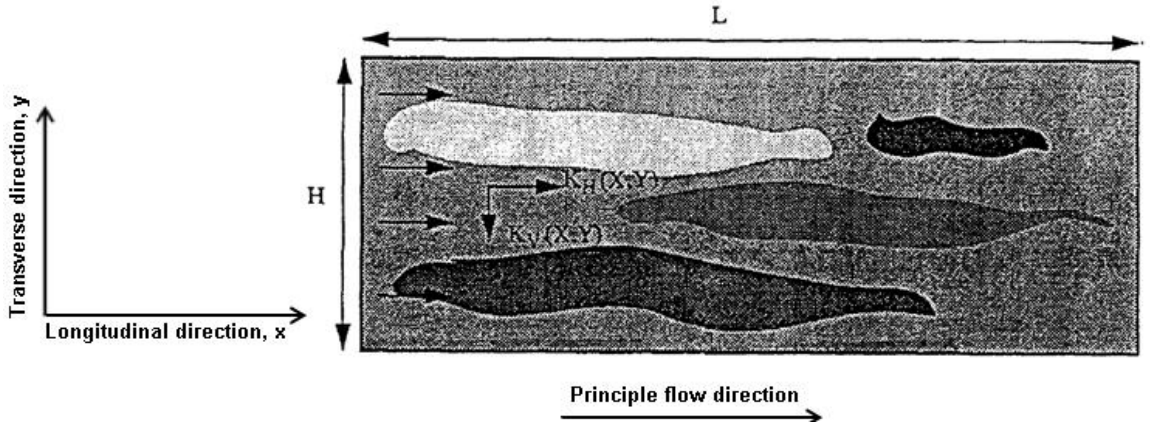

Figure 3-1. Schematic of a reservoir with heterogeneity for vertical equilibrium (Yortsos,1995)

The first category has been studied by several authors including Coats et al. (1971), Yokoyama and Lake (1981), Zapata and Lake (1981), Pande and Orr (1989), Lake et al (1990) and most recently by Yortsos (1995). A physical description of this category of vertical equilibrium can be found in Lake (1989). The term vertical in vertical equilibrium (VE) denotes the direction along the transverse coordinate. In the first category, most of the authors primarily capture the effects of interaction of heterogeneity with viscous forces while limiting the impact of gravity and capillary forces (Figure 3-2). The applicability of the dimensionless parameter $R_L=L/H(k_V/k_H)^{1/2}$ to characterize condition for vertical equilibrium has been verified by various authors numerically and has been analytically proven by Yortsos (1994) using asymptotic expansions. R_L has to take sufficiently large values for VE to be applicable.

The addition of gravity along with the viscous forces is an extension to VE where immiscible phases are assumed to be completely segregated. Dietz (1953) studied such segregated flow first followed by Le Fur et al. (1963), Beckers (1965), Fayers and Muggeridge (1990) and most recently by Shook et al. (1992) and Yortsos (1995).

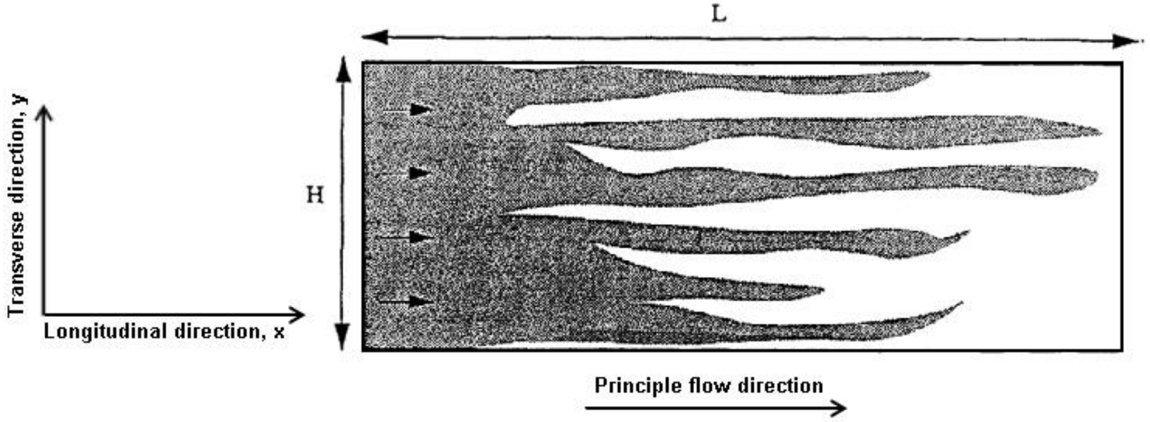

Figure 3-2. Effects of only viscous forces on displacements, viscous fingering (Yortsos, 1995)

The second category emphasizes the effects of dispersive forces for miscible flows in a porous media. The original contributions in this direction were made by Taylor (1953) and Aris (1956) in connection with flow of a dispersive tracer in a tube. Lake and Hirasaki (1981) worked on tracer dispersion in stratified media and identified that the dimensionless number $N_{TD}=L\alpha_T/H^2$ must be large enough for the stratified media to act as a single layer. Various phenomenological viscous fingering models, such as Koval (1963), Todd and Longstaff (1972) and Fayers (1984) follow along the same lines.

While the two categories of flow seem to derive from analogous conditions, no effort has been taken to treat them in a unified fashion. Most of the EOR processes have miscible and immiscible fluids flowing simultaneously in the heterogeneous reservoirs, thus necessitating a unified vertical equilibrium theory. The objective of this chapter is to provide a unified approach based on rigorous two variable power series expansion of the flow equations in systems where VE is expected to apply. This includes anisotropic and heterogeneous reservoirs which are long and narrow with large k_v/k_H ratios and large transverse dispersivity (α_T). The analysis is also aimed at analytically identifying the VE conditions for multi-component systems without the incompressibility assumption. First, the general material balance equations are laid out for each flowing component in two-phase multi-component flow system. The variables in the equations are expressed in terms of power series to identify vertical equillibrium conditions. The effects of gravity and capillarity are accounted for later to capture the impact on cross-flow terms.

3.1 VERTICAL EQUILIBRIUM ANALYSIS

Consider a constant rate displacement with two flowing phases and multiple components in a two- dimensional reservoir of thickness H and length L. For simplicity, the reservoir has no dip. An anisotropic, heterogeneous reservoir, with different permeabilities and component dispersitivities in the principle directions that are taken to coincide with the 'horizontal' (x) and the 'vertical' (y) directions, respectively, is taken for the analysis.

$$K_H = k_H \kappa_H(X,Y); \quad K_V = k_V \kappa_V(X,Y); \quad \phi = \bar{\phi}\varphi(X,Y) \tag{3.1}$$

$$\alpha_{L,j} = \overline{\alpha_L}\alpha_{L,j}(X,Y); \quad \alpha_{T,j} = \overline{\alpha_T}\alpha_{T,j}(X,Y) \tag{3.2}$$

where, K_H and K_V denote the two permeabilities, which can be further normalized by their arithmetic mean values k_H and k_V, respectively. The spatial dependence is thus on the normalized permeabilities $\kappa_i > 0$, ($i = H, V$) which are dimensionless and such that $\int_0^H \kappa_i \, dY = H$, when the x-dependence is neglected. $\alpha_{L,j}$ and $\alpha_{T,j}$ denote the two directional dispersivities for phase j ($j = 1,2$), which can be further normalized by their mean values $\bar{\alpha}_L$ and $\bar{\alpha}_T$, respectively. The spatial dependence is thus on the normalized dispersitivities $\alpha_{L,j} > 0$ and $\alpha_{T,j} > 0$, ($j = 1, 2$) which are dimensionless and subscript L refers to the longitudinal direction and T refers to the transverse direction. ϕ denotes the porosity, that is normalized by the arithmetic mean value $\bar{\phi}$. The spatial dependence is thus on the normalized porosity $\varphi > 0$, which is also dimensionless. We also normalize 'horizontal' and 'vertical' scales, X and Y, by the reservoir length (L) and height (H), respectively:

$$x_D = \frac{x}{L}; \quad y_D = \frac{y}{H}, \tag{3.3}$$

and scale all the velocities by the total injection flux q, time by $L\bar{\phi}/q$, and the fluid pressure by $Lq\mu_2^o/k_H$. If S_j denotes the saturation of phase j and $w_{i,j}$ denotes the mass fraction of component i in phase j, the strong form of dimensionless mass balance for a component i becomes

$$\frac{d}{dt_D}\left(\varphi(x_D,y_D)(\bar{\rho}_1 S_1 w_{i,1} + \bar{\rho}_2 S_2 w_{i,2})\right) + \frac{d}{dx_D}\left(N_{Di,x}\right) + \frac{L}{H}\frac{d}{dy_D}\left(N_{Di,y}\right) = 0; \quad \text{i=1 to N}_\text{c} \tag{3.4}$$

$$\bar{\rho}_j = \frac{\rho_j}{\rho_1^o - \rho_2^o}; \quad \text{j = 1, 2} \tag{3.5}$$

$$N_{Di,x} = \bar{\rho}_1 w_{i,1} u_{1x_D} + \bar{\rho}_2 w_{i,2} u_{2x_D} - \frac{\bar{\rho}_1 \alpha_{L,1} u_{1x_D}}{L}\frac{\partial w_{i,1}}{\partial x_D} - \frac{\bar{\rho}_2 \alpha_{L,2} u_{2x_D}}{L}\frac{\partial w_{i,2}}{\partial x_D}; \quad \text{i=1 to N}_\text{c} \tag{3.6}$$

$$N_{Di,y} = \bar{\rho}_1 w_{i,1} u_{1y_D} + \bar{\rho}_2 w_{i,2} u_{2y_D} - \frac{\bar{\rho}_1 \alpha_{T,1} u_{1x_D}}{H}\frac{\partial w_{i,1}}{\partial y_D} - \frac{\bar{\rho}_2 \alpha_{T,2} u_{2x_D}}{H}\frac{\partial w_{i,2}}{\partial y_D}; \quad \text{i=1 to N}_\text{c} \tag{3.7}$$

$$u_{jx_D} = -\lambda_j \mu_2^o \kappa_H (x_D, y_D)\frac{\partial P_{jD}}{\partial x_D}; \quad \text{j = 1, 2} \tag{3.8}$$

$$u_{jy_D} = -\frac{L}{H}\frac{k_V}{k_H}\lambda_j \mu_2^o \kappa_V (x_D, y_D)\left[\frac{\partial P_{jD}}{\partial y_D} + \frac{\rho_j g k_H H}{Lq\mu_2^o}\right]; \quad \text{j = 1, 2} \tag{3.9}$$

$$S_1 + S_2 = 1 \tag{3.10}$$

$$\frac{w_{i,1}}{w_{i,2}} = k_i; \quad \text{i=1 to N}_\text{c} \tag{3.11}$$

where, ρ_j^o is the density of phase *j* at a reference pressure and phase composition, μ_2^o is the viscosity of phase 2 at a reference pressure and phase composition. P_{jD} is the dimensionless pressure of phase *j*. λ_j is the mobility of phase *j*.

The further substitution $N_{Di,y}^{'} = \frac{L}{H} N_{Di,y}$ in equation 3.4 yields,

$$\frac{d}{dt_D}\left(\varphi(x_D, y_D)(\bar{\rho}_1 S_1 w_{i,1} + \bar{\rho}_2 S_2 w_{i,2})\right) + \frac{d}{dx_D}\left(N_{Di,x}\right) + \frac{d}{dy_D}\left(N_{Di,y}^{'}\right) = 0; \quad \text{i=1 to N} \tag{3.12}$$

$$\bar{\rho}_j = \frac{\rho_j}{\rho_1^o - \rho_2^o}; \quad \text{j = 1, 2} \tag{3.13}$$

Substituting for velocities in Equations 3.6 and 3.7 yields,

$$N_{Di,x} = -\bar{\rho}_1 w_{i,1}\lambda_1 \mu_2^o \kappa_H (x_D, y_D)\frac{\partial P_{1D}}{\partial x_D} - \bar{\rho}_2 w_{i,2}\lambda_2 \mu_2^o \kappa_H (x_D, y_D)\frac{\partial P_{2D}}{\partial x_D} +$$
$$\frac{\overline{\alpha_L}}{L}\bar{\rho}_1 \alpha_{L,1}(x_D, y_D)\lambda_1 \mu_2^o \kappa_H (x_D, y_D)\frac{\partial P_{1D}}{\partial x_D}\frac{\partial w_{i,1}}{\partial x_D} + \frac{\overline{\alpha_L}}{L}\bar{\rho}_2 \alpha_{L,2}(x_D, y_D)\lambda_2 \mu_2^o \kappa_H (x_D, y_D)\frac{\partial P_{2D}}{\partial x_D}\frac{\partial w_{i,2}}{\partial x_D}$$

(3.14)

$$\begin{aligned} N_{Di,\mathrm{y}}^{'} = {} & -\bar{\rho}_1 w_{i,1}\frac{L^2}{H^2}\frac{k_V}{k_H}\lambda_1 \mu_2^o \kappa_V (x_D, y_D)\left[\frac{\partial P_{1D}}{\partial y_D} + \frac{\rho_1 g k_H H}{Lq\mu_2^o}\right] - \\ & \bar{\rho}_2 w_{i,2}\frac{L^2}{H^2}\frac{k_V}{k_H}\lambda_2 \mu_2^o \kappa_V (x_D, y_D)\left[\frac{\partial P_{2D}}{\partial y_D} + \frac{\rho_2 g k_H H}{Lq\mu_2^o}\right] + \\ & \frac{L\overline{\alpha_T}}{H^2}\bar{\rho}_1 \alpha_{T,1}(x_D, y_D)\lambda_1 \mu_2^o \kappa_H (x_D, y_D)\frac{\partial P_{1D}}{\partial x_D}\frac{\partial w_{i,1}}{\partial y_D} + \\ & \frac{L\overline{\alpha_T}}{H^2}\bar{\rho}_2 \alpha_{T,2}(x_D, y_D)\lambda_2 \mu_2^o \kappa_H (x_D, y_D)\frac{\partial P_{2D}}{\partial x_D}\frac{\partial w_{i,2}}{\partial y_D} \end{aligned} \tag{3.15}$$

$$S_1 + S_2 = 1 \tag{3.16}$$

$$\frac{w_{i,1}}{w_{i,2}} = k_i; \quad \text{i=1 to N}_\text{c} \tag{3.17}$$

It follows from equation 3.15 that the relevant dimensionless groups are R_L^2 and N_{TD}, defined as

$$R_L^2 = \frac{L^2}{H^2}\frac{K_V}{K_H}; \quad N_{TD} = \frac{L\overline{\alpha_T}}{H^2} \tag{3.18}$$

The dimensionless parameter R_L^2 is precisely the parameter used in justifying viscous crossflow (Zapata and Lake, 1981; Lake, 1989) whereas N_{TD} is the dimensionless parameter used in justifying dispersive crossflow (Lake and Hirasaki, 1981). Equation 3.15 also suggests that the solutions to all the dependent variables in equation 3.19 are function of R_L^2 and N_{TD} at any given position and time.

$$N_{Di,x}, N^{'}_{Di,y}, P_{1D}, P_{2D}, S_1, S_2, w_{i,1}, w_{i,1} = f(x_D, y_D, t_D; R_L^2, N_{TD}) \tag{3.19}$$

Thus to obtain the appropriate transverse equilibrium (TE) model, we expand all the dependent parameters shown in equation 3.19 in a regular power series expansion using R_L^2 and N_{TD} as the variables,

$$N_{Di,x} = N_{Di,x,0} + \frac{N_{Di,x,1}}{R_L^2} + \frac{N_{Di,x,2}}{N_{TD}} + \frac{N_{Di,x,3}}{R_L^4} + \frac{N_{Di,x,4}}{R_L^2 N_{TD}} + \frac{N_{Di,x,5}}{N_{TD}^2} + \dots \tag{3.20}$$

$$N^{'}_{Di,y} = N^{'}_{Di,y,0} + \frac{N^{'}_{Di,y,1}}{R_L^2} + \frac{N^{'}_{Di,y,2}}{N_{TD}} + \frac{N^{'}_{Di,y,3}}{R_L^4} + \frac{N^{'}_{Di,y,4}}{R_L^2 N_{TD}} + \frac{N^{'}_{Di,y,5}}{N_{TD}^2} + \dots \tag{3.21}$$

$$P_{1D} = P_{1D,0} + \frac{P_{1D,1}}{R_L^2} + \frac{P_{1D,2}}{N_{TD}} + \frac{P_{1D,3}}{R_L^4} + \frac{P_{1D,4}}{R_L^2 N_{TD}} + \frac{P_{1D,5}}{N_{TD}^2} + \dots \tag{3.22}$$

$$P_{2D} = P_{2D,0} + \frac{P_{2D,1}}{R_L^2} + \frac{P_{2D,2}}{N_{TD}} + \frac{P_{2D,3}}{R_L^4} + \frac{P_{2D,4}}{R_L^2 N_{TD}} + \frac{P_{2D,5}}{N_{TD}^2} + \dots \tag{3.23}$$

$$S_1 = S_{1,0} + \frac{S_{1,1}}{R_L^2} + \frac{S_{1,2}}{N_{TD}} + \frac{S_{1,3}}{R_L^4} + \frac{S_{1,4}}{R_L^2 N_{TD}} + \frac{S_{1,5}}{N_{TD}^2} + \dots \tag{3.24}$$

$$S_2 = S_{2,0} + \frac{S_{2,1}}{R_L^2} + \frac{S_{2,2}}{N_{TD}} + \frac{S_{2,3}}{R_L^4} + \frac{S_{2,4}}{R_L^2 N_{TD}} + \frac{S_{2,5}}{N_{TD}^2} + \dots \tag{3.25}$$

$$w_{i,1} = w_{i,1,0} + \frac{w_{i,1,1}}{R_L^2} + \frac{w_{i,1,2}}{N_{TD}} + \frac{w_{i,1,3}}{R_L^4} + \frac{w_{i,1,4}}{R_L^2 N_{TD}} + \frac{w_{i,1,5}}{N_{TD}^2} + \dots \tag{3.26}$$

$$w_{i,2} = w_{i,2,0} + \frac{w_{i,2,1}}{R_L^2} + \frac{w_{i,2,2}}{N_{TD}} + \frac{w_{i,2,3}}{R_L^4} + \frac{w_{i,2,4}}{R_L^2 N_{TD}} + \frac{w_{i,2,5}}{N_{TD}^2} + \ldots \qquad (3.27)$$

Zapata and Lake, 1981 proved that viscous crossflow is maximum when $R_L^2 \gg 1$ for immiscible floods with no dispersive mixing. Lake and Hirasaki, 1981 showed that dispersive crossflow is maximum when $N_{TD} \gg 1$ for miscible floods with no viscous mixing. The aim of the chapter is to understand the behavior of viscous and dispersive crossflow in the reservoirs in the limits when $R_L^2 \gg 1$and $N_{TD} \gg 1$ together. So substituting equations 3.20 to 3.27 in equations 3.12 to 3.17 and taking limits of $R_L^2 \gg$ 1and $N_{TD} \gg 1$ yields the following leading order terms,

$$\frac{d}{dt_D}\left(\varphi(x_D, y_D)(\bar{\rho}_1 S_{1,0} w_{i,1,0} + \bar{\rho}_2 S_{2,0} w_{i,2,0})\right) + \frac{d}{dx_D}\left(N_{Di,x,0}\right) + \frac{d}{dy_D}\left(N'_{Di,y,0}\right) = 0; \quad \text{i=1 to } N_c$$

(3.28)

$$\bar{\rho}_j = \frac{\rho_j}{\rho_1^o - \rho_2^o}; \quad \text{j = 1, 2} \qquad (3.29)$$

$$\begin{aligned} N_{Di,x,0} = {} & -\bar{\rho}_1 w_{i,1,0} \lambda_1 \mu_2^o \kappa_H(x_D, y_D) \frac{\partial P_{1D,0}}{\partial x_D} - \bar{\rho}_2 w_{i,2,0} \lambda_2 \mu_2^o \kappa_H(x_D, y_D) \frac{\partial P_{2D,0}}{\partial x_D} + \\ & \frac{\overline{\alpha_L}}{L} \bar{\rho}_1 \alpha_{L,1}(x_D, y_D) \lambda_1 \mu_2^o \kappa_H(x_D, y_D) \frac{\partial P_{1D,0}}{\partial x_D} \frac{\partial w_{i,1,0}}{\partial x_D} + \\ & \frac{\overline{\alpha_L}}{L} \bar{\rho}_2 \alpha_{L,2}(x_D, y_D) \lambda_2 \mu_2^o \kappa_H(x_D, y_D) \frac{\partial P_{2D,0}}{\partial x_D} \frac{\partial w_{i,2,0}}{\partial x_D} \end{aligned} \qquad (3.30)$$

$$\bar{\rho}_1 w_{i,1,0} \lambda_1 \mu_2^o \kappa_V(x_D, y_D)\left[\frac{\partial P_{1D,0}}{\partial y_D} + \frac{\rho_1 g k_H H}{Lq\mu_2^o}\right] + \bar{\rho}_2 w_{i,2,0} \lambda_2 \mu_2^o \kappa_V(x_D, y_D)\left[\frac{\partial P_{2D,0}}{\partial y_D} + \frac{\rho_2 g k_H H}{Lq\mu_2^o}\right] = 0$$

(3.31)

$$\bar{\rho}_1 \alpha_{T,1}(x_D, y_D) \lambda_1 \mu_2^o \kappa_H(x_D, y_D) \frac{\partial P_{1D,0}}{\partial x_D} \frac{\partial w_{i,1,0}}{\partial y_D} + \bar{\rho}_2 \alpha_{T,2}(x_D, y_D) \lambda_2 \mu_2^o \kappa_H(x_D, y_D) \frac{\partial P_{2D,0}}{\partial x_D} \frac{\partial w_{i,2,0}}{\partial y_D} = 0$$

(3.32)

$$S_{1,0} + S_{2,0} = 1 \qquad (3.33)$$

$$\frac{w_{i,1,0}}{w_{i,2,0}} = k_i; \quad \text{i=1 to N}_\text{c} \qquad (3.34)$$

Equation 3.31 governs the way pressure varies in the transverse direction. Equation 3.31 when written for all N_c components yields the following system of equations in matrix form,

$$\mu_2^o \kappa_V(x_D, y_D)\begin{bmatrix} w_{1,1,0} & w_{1,2,0} \\ w_{2,1,0} & w_{2,2,0} \\ . & . \\ . & . \\ . & . \\ w_{N_c,1,0} & w_{N_c,2,0} \end{bmatrix}\begin{bmatrix} \overline{\rho}_1\lambda_1\left(\dfrac{\partial P_{1D,0}}{\partial y_D} + \dfrac{\rho_1 g k_H H}{Lq\mu_2^o}\right) \\ \overline{\rho}_2\lambda_2\left(\dfrac{\partial P_{2D,0}}{\partial y_D} + \dfrac{\rho_2 g k_H H}{Lq\mu_2^o}\right) \end{bmatrix} = 0 \tag{3.35}$$

Equation 3.34 when written for all N_c components yields the following system of equations in matrix form,

$$\begin{bmatrix} w_{1,1,0} \\ w_{2,1,0} \\ . \\ . \\ . \\ w_{N_C,1,0} \end{bmatrix} = \begin{bmatrix} w_{1,2,0} \\ w_{2,2,0} \\ . \\ . \\ . \\ w_{N_C,2,0} \end{bmatrix}\begin{bmatrix} k_1 \\ k_2 \\ . \\ . \\ . \\ k_{N_c} \end{bmatrix} \tag{3.36}$$

Equation 3.36 shows that the two vectors in the component concentration matrix in equation 3.35 are independent of each other. Linear independence of vectors $[w_{i,1,0}]$ and $[w_{i,2,0}]$ (Eq. 3.36) results in new conclusions derived from equation 3.35,

$$\frac{\partial P_{1D,0}}{\partial y_D} + \frac{\rho_1 g k_H H}{Lq\mu_2^o} = 0; \qquad \frac{\partial P_{2D,0}}{\partial y_D} + \frac{\rho_2 g k_H H}{Lq\mu_2^o} = 0 \tag{3.37}$$

Using relationship specified in equation 3.34, equation 3.32 can be written as

$$\left[\overline{\rho}_1 \alpha_{T,1}(x_D, y_D)\lambda_1 \mu_2^o \kappa_H(x_D, y_D)\frac{\partial P_{1D,0}}{\partial x_D} k_i + \overline{\rho}_2 \alpha_{T,2}(x_D, y_D)\lambda_2 \mu_2^o \kappa_H(x_D, y_D)\frac{\partial P_{2D,0}}{\partial x_D}\right]\frac{\partial w_{i,2,0}}{\partial y_D} = 0 \tag{3.38}$$

Thus,

$$\frac{\partial w_{i,2,0}}{\partial y_D}=0; \quad \frac{\partial w_{i,1,0}}{\partial y_D}=0; \quad \text{i=1 to Nc} \tag{3.39}$$

Equation 3.37 says that the phase pressure varies as a function of phase density in the transverse direction, whereas Equation 3.39 dictates $w_{i,1,0}= w_{i,1,0}(x_D,t_D)$ and $w_{i,2,0}= w_{i,2,0}(x_D,t_D)$, i.e., the component concentrations are independent of the transverse coordinate. Equations 3.37 and 3.39 are the fundamental assumptions of transverse equilibrium (viscous and dispersive), rigorously derived here in the limit $R_L^2 \gg 1$ and $N_{TD} \gg 1$. Numerical evidence suggests that TE is satisfied quite well when $R_L > 10$, and $N_{TD} > 5$ (Lake, 1991 and Lake and Hirasaki, 1981). This is consistent with our power series expansions (equations 3.20 to 3.27), where the next order enters at $O(1/N_{TD})$ and $O(1/R_L^2)$. The dispersive crossflow error from the next order term $O(1/N_{TD})$ in equations 3.20 to 3.27 is of the order of 20% (when N_{TD}=5). The viscous crossflow error from the next order term $O(1/R_L^2)$ in equations 3.20 to 3.27 is of the order of 1% (when R_L=10). The total error that is the sum of dispersive and viscous terms is of the order of 21%. If the dimensionless number $N_{TD} > 10$ and R_L=10, the error reduces to the order of 11%. The rigorous analytical identification of the parameters R_L^2 and N_{TD} as the relevant variables for the validity of TE represents the first result of this dissertation.

Unless otherwise noted, subscript 0 shall be omitted in the further analysis for convenience. The next step is to write the continuity equation

$$\frac{d}{dt_D}\left(\varphi(x_D,y_D)(\overline{\rho}_1 S_1+\overline{\rho}_2 S_2)\right)+\frac{d}{dx_D}\left(\sum_{i=1}^{N} N_{Di,x}\right)+\frac{d}{dy_D}\left(\sum_{i=1}^{N} N'_{Di,y,0}\right)=0 \tag{3.40}$$

$$N_{D,x}=\sum_{i=1}^{N} N_{Di,x}=\overline{\rho_1 u_{1x_D}}+\overline{\rho_2 u_{2x_D}} \tag{3.41}$$

$$N'_{D,y}=\sum_{i=1}^{N} N'_{Di,y}=\overline{\rho_1 u'_{1y_D}}+\overline{\rho_2 u'_{2y_D}} \tag{3.42}$$

The dispersive flux in the above equations is also defined as mass flux of any species relative to mass average velocity, thus the dispersive flux terms add to zero (Lake, 1989). The total velocity in longitudinal and transverse directions are given by

$$u_{tx_D} = -\lambda_1 \mu_2^o \kappa_H (x_D, y_D) \frac{\partial P_{1D}}{\partial x_D} - \lambda_2 \mu_2^o \kappa_H (x_D, y_D) \frac{\partial P_{2D}}{\partial x_D} \tag{3.43}$$

$$u'_{ty_D} = -R_L^2 \left\{ \lambda_1 \mu_2^o \kappa_V (x_D, y_D) \left[\frac{\partial P_{1D}}{\partial y_D} + \frac{\rho_2 g K_H H}{Lq\mu_2^o} \right] + \lambda_2 \mu_2^o \kappa_V (x_D, y_D) \left[\frac{\partial P_{2D}}{\partial y_D} + \frac{\rho_2 g K_H H}{Lq\mu_2^o} \right] \right\}$$

(3.44)

Capillary pressure, P_c is defined as the difference in phase pressures

$$P_c = P_2 - P_1 \tag{3.45}$$

Dimensionless capillary pressure is defined as

$$P_{cD} = \frac{k_H P_c}{L\mu_2^o q} = \frac{k_H P_2}{L\mu_2^o q} - \frac{k_H P_1}{L\mu_2^o q} = P_{2D} - P_{1D} \tag{3.46}$$

The dimensionless capillary pressure can also be expressed in terms of a J-function representation

$$P_c = J(S_1)\gamma \sqrt{\frac{\bar{\phi}\varphi(x_D, y_D)}{k_H \kappa_H (x_D, y_D)}} \tag{3.47}$$

Substituting P$_c$ from Eq. (47) to Eq. (46) yields

$$P_{cD} = \frac{k_H \gamma}{L\mu_2^o q} J(S_1) \sqrt{\frac{\bar{\phi}\varphi(x_D, y_D)}{k_H \kappa_H (x_D, y_D)}} = \frac{\sqrt{k_H \bar{\phi}}\gamma}{L\mu_2^o q} J(S_1) \sqrt{\frac{\varphi(x_D, y_D)}{\kappa_H (x_D, y_D)}} = P_{2D} - P_{1D} \tag{3.48}$$

where, γ is the interfacial tension. Interfacial tension is assumed to be constant over the range of variation in pressure and compositions. Substituting for P_{2D} in Equations 3.43 and 3.44 can be used to solve for phase pressure gradients in x and y coordinates

$$\frac{\partial P_{1D}}{\partial x_D} = -\frac{u_{tx_D}}{\kappa_H (x_D, y_D) \lambda_t \mu_2^o} - \frac{\lambda_2}{\lambda_t} N_{CD} \frac{\partial}{\partial x_D} \left(J(S_1) \sqrt{\frac{\varphi(x_D, y_D)}{\kappa_H (x_D, y_D)}} \right) \tag{3.49}$$

$$\frac{\partial P_{1D}}{\partial y_D} = -\frac{u'_{ty_D}}{R_L^2 \kappa_V(x_D, y_D)\lambda_t \mu_2^o} - \frac{\lambda_2}{\lambda_t} N_{CD} \frac{\partial}{\partial y_D} J(S_1)\sqrt{\frac{\varphi(x_D, y_D)}{\kappa_H(x_D, y_D)}} - \frac{\lambda_1 \overline{\rho_1} + \lambda_2 \overline{\rho_2}}{\lambda_t} N_g \tag{3.50}$$

$$N_{CD} = \frac{\sqrt{k_H \overline{\phi}}\gamma}{L\mu_2^o q}; \qquad N_g = \frac{k_H(\rho_1^o - \rho_2^o)gH}{L\mu_2^o q} \tag{3.51}$$

where, N_{CD} is the dimensionless capillary number and N_g is the dimensionless gravity number. Using the pressure gradients for flux terms (Equations 3.41 and 3.42) in continuity equation 3.40 yields

$$N_{D,x} = \frac{\lambda_1 \overline{\rho_1} + \lambda_2 \overline{\rho_2}}{\lambda_t} u_{tx_D} + \frac{\lambda_1 \lambda_2 \mu_2^o (\overline{\rho_1} - \overline{\rho_2})\kappa_H(x_D, y_D)}{\lambda_t} N_{CD} \frac{\partial}{\partial x_D}\left(J(S_1)\sqrt{\frac{\varphi(x_D, y_D)}{\kappa_H(x_D, y_D)}} \right) \tag{3.52}$$

$$N'_{D,y} = \frac{\lambda_1 \overline{\rho_1} + \lambda_2 \overline{\rho_2}}{\lambda_t} u'_{ty_D} + \frac{\lambda_1 \lambda_2 \mu_2^o (\overline{\rho_1} - \overline{\rho_2})\kappa_V(x_D, y_D)}{\lambda_t} R_L^2 N_{CD} \frac{\partial}{\partial y_D}\left(J(S_1)\sqrt{\frac{\varphi(x_D, y_D)}{\kappa_H(x_D, y_D)}} \right) + \frac{\lambda_1 \lambda_2 \mu_2^o (\overline{\rho_1} - \overline{\rho_2})\kappa_V(x_D, y_D)}{\lambda_t} R_L^2 N_g$$

(3.53)

The pressure gradients are also eliminated from the component flux equations 3.14 and 3.15

$$N_{Di,x} = \frac{\overline{\rho_1} w_{i,1}\lambda_1 + \overline{\rho_2} w_{i,2}\lambda_2}{\lambda_t} u_{tx_D} - \frac{\lambda_1\lambda_2\mu_2^o}{\lambda_t}(\overline{\rho_2} w_{i,2} - \overline{\rho_1} w_{i,1})\mathrm{K}_{\mathrm{H}}(x_D, y_D) N_{CD} \frac{\partial}{\partial x_D}\left(J(S_1)\sqrt{\frac{\varphi(x_D, y_D)}{\mathrm{K}_{\mathrm{H}}(x_D, y_D)}} \right) - N_{LD}\left(\frac{\lambda_1}{\lambda_t}\overline{\rho_1}\alpha_{L,1}(x_D, y_D)\frac{\partial w_{i,1}}{\partial x_D} + \frac{\lambda_2}{\lambda_t}\overline{\rho_2}\alpha_{L,2}(x_D, y_D)\frac{\partial w_{i,2}}{\partial x_D} \right) u_{tx_D} - N_{LD}\frac{\lambda_1\lambda_2\mu_2^o}{\lambda_t}\mathrm{K}_{\mathrm{H}}(x_D, y_D) N_{CD}\left(\overline{\rho_1}\alpha_{L,1}(x_D, y_D)\frac{\partial w_{i,1}}{\partial x_D} - \overline{\rho_2}\alpha_{L,2}(x_D, y_D)\frac{\partial w_{i,2}}{\partial x_D} \right)\frac{\partial}{\partial x_D}\left(J(S_1)\sqrt{\frac{\varphi(x_D, y_D)}{\mathrm{K}_{\mathrm{H}}(x_D, y_D)}} \right)$$

(3.54)

where, $N_{LD} = \frac{\overline{\alpha_L}}{L}$ (3.55)

N_{LD} is the dimensionless number that controls dispersive flow. It is also the inverse of Peclet number.

$$N'_{Di,y} = \frac{\overline{\rho_1} w_{i,1}\lambda_1 + \overline{\rho_2} w_{i,2}\lambda_2}{\lambda_t} u'_{ty_D} - \frac{\lambda_1\lambda_2\mu_2^o}{\lambda_t}(\overline{\rho_2} w_{i,2} - \overline{\rho_1} w_{i,1})\kappa_V(x_D, y_D) R_L^2 N_{CD} \frac{\partial}{\partial y_D}\left(J(S_1)\sqrt{\frac{\varphi(x_D, y_D)}{\kappa_H(x_D, y_D)}} \right) -$$

$$\frac{\lambda_1\lambda_2\mu_2^o}{\lambda_t}(\overline{\rho_2} w_{i,2} - \overline{\rho_1} w_{i,1})\kappa_V(x_D, y_D) R_L^2 N_g -$$

$$N_{TD}\left(\frac{\lambda_1}{\lambda_t}\overline{\rho_1}\alpha_{T,1}(x_D, y_D)\frac{\partial w_{i,1}}{\partial y_D} + \frac{\lambda_2}{\lambda_t}\overline{\rho_2}\alpha_{T,2}(x_D, y_D)\frac{\partial w_{i,2}}{\partial y_D} \right) u_{tx_D} -$$

$$\frac{\lambda_1\lambda_2\mu_2^o}{\lambda_t}\kappa_H(x_D, y_D) N_{TD} N_{CD}\left(\overline{\rho_1}\alpha_{T,1}(x_D, y_D)\frac{\partial w_{i,1}}{\partial y_D} - \overline{\rho_2}\alpha_{T,2}(x_D, y_D)\frac{\partial w_{i,2}}{\partial y_D} \right)\frac{\partial}{\partial x_D}\left(J(S_1)\sqrt{\frac{\varphi(x_D, y_D)}{\kappa_H(x_D, y_D)}} \right)$$

(3.56)

Subsequently, substituting Equation 3.41 into 3.40 and then integrating from 0 to y_D yields the transverse flux u'_{ty_D}

$$u'_{ty_D} = \frac{\lambda_t}{\lambda_1\overline{\rho_1} + \lambda_2\overline{\rho_2}}\left[\begin{array}{l} -\frac{\partial}{\partial t_D}\left(\int_0^{y_D} (\overline{\rho_1} S_1 + \overline{\rho_2} S_2) dy_D \right) - \frac{\partial}{\partial x_D}\left(\int_0^{y_D} \left(\frac{\overline{\rho_1}\lambda_1 + \overline{\rho_2}\lambda_2}{\lambda_t} \right) u_{tx_D} dy_D \right) - \\ \frac{\partial}{\partial x_D}\left(\int_0^{y_D} \left(\frac{\lambda_1\lambda_2\mu_2^o(\overline{\rho_1} - \overline{\rho_2})\kappa_H(x_D, y_D)}{\lambda_t} N_{CD}\frac{\partial}{\partial x_D}\left(J(S_1)\sqrt{\frac{\varphi(x_D, y_D)}{\kappa_H(x_D, y_D)}} \right) \right) dy_D \right) - \\ \frac{\lambda_1\lambda_2\mu_2^o(\overline{\rho_1} - \overline{\rho_2})\kappa_V(x_D, y_D)}{\lambda_t} R_L^2 N_{CD}\frac{\partial}{\partial y_D}\left(J(S_1)\sqrt{\frac{\varphi(x_D, y_D)}{\kappa_H(x_D, y_D)}} \right) - \\ \frac{\lambda_1\lambda_2\mu_2^o(\overline{\rho_1} - \overline{\rho_2})\kappa_V(x_D, y_D)}{\lambda_t} R_L^2 N_g \end{array} \right]$$

(3.57)

where no-flow boundary conditions at y_D=0, 1 were used. Substitution of u'_{ty_D} from equation 3.57 into flux term $N'_{Di,y}$ of equation 3.56 yields the final form of the material balance equation for component *i,*

$$
\begin{aligned}
&\frac{\partial}{\partial t_D}\Big(\varphi(x_D,y_D)(\overline{\rho}_1 S_1 w_{i,1}+\overline{\rho}_2 S_2 w_{i,2})\Big)-\frac{\overline{\rho}_1\lambda_1 w_{i,1}+\overline{\rho}_2\lambda_2 w_{i,2}}{\overline{\rho}_1\lambda_1+\overline{\rho}_2\lambda_2}\frac{\partial}{\partial t_D}\Big(\varphi(x_D,y_D)(\overline{\rho}_1 S_1+\overline{\rho}_2 S_2)\Big)+\\
&\frac{\overline{\rho}_1\lambda_1+\overline{\rho}_2\lambda_2}{\lambda_t}u_{tx_D}\frac{\partial}{\partial x_D}\left(\frac{\overline{\rho}_1\lambda_1 w_{i,1}+\overline{\rho}_2\lambda_2 w_{i,2}}{\overline{\rho}_1\lambda_1+\overline{\rho}_2\lambda_2}\right)-\\
&N_{LD}\frac{\partial}{\partial x_D}\left(\left(\frac{\overline{\rho}_1\lambda_1\alpha_{L,1}(x_D,y_D)}{\lambda_t}\frac{\partial w_{i,1}}{\partial x_D}+\frac{\overline{\rho}_2\lambda_2\alpha_{L,2}(x_D,y_D)}{\lambda_t}\frac{\partial w_{i,2}}{\partial x_D}\right)u_{tx_D}\right)-\\
&N_{CD}\frac{\partial}{\partial x_D}\left(\frac{\lambda_1\lambda_2\mu_2^o}{\lambda_t}(\overline{\rho_2}w_{i,2}-\overline{\rho_1}w_{i,1})\mathrm{K}_{\mathrm{H}}(x_D,y_D)\frac{\partial}{\partial x_D}\left(J(S_1)\sqrt{\frac{\varphi(x_D,y_D)}{\mathrm{K}_{\mathrm{H}}(x_D,y_D)}}\right)\right)-\\
&N_{LD}N_{CD}\frac{\partial}{\partial x_D}\left(\frac{\lambda_1\lambda_2\mu_2^o}{\lambda_t}\mathrm{K}_{\mathrm{H}}(x_D,y_D)\left(\overline{\rho_1}\alpha_{L,1}(x_D,y_D)\frac{\partial w_{i,1}}{\partial x_D}-\overline{\rho_2}\alpha_{L,2}(x_D,y_D)\frac{\partial w_{i,2}}{\partial x_D}\right)\frac{\partial}{\partial x_D}\left(J(S_1)\sqrt{\frac{\varphi(x_D,y_D)}{\mathrm{K}_{\mathrm{H}}(x_D,y_D)}}\right)\right)-\\
&\left[\begin{array}{l}\dfrac{\partial}{\partial t_D}\left(\displaystyle\int_0^{y_D}\varphi(x_D,y_D)(\overline{\rho}_1 S_1+\overline{\rho}_2 S_2)\,\mathrm{dy_D}\right)+\dfrac{\partial}{\partial x_D}\left(\displaystyle\int_0^{y_D}\frac{\overline{\rho}_1\lambda_1+\overline{\rho}_2\lambda_2}{\lambda_t}u_{tx_D}\,\mathrm{dy_D}\right)+\\ N_{CD}\dfrac{\partial}{\partial x_D}\left(\displaystyle\int_0^{y_D}\frac{\lambda_1\lambda_2\mu_2^o}{\lambda_t}(\overline{\rho_2}-\overline{\rho_1})\mathrm{K}_{\mathrm{H}}(x_D,y_D)\frac{\partial}{\partial x_D}\left(J(S_1)\sqrt{\frac{\varphi(x_D,y_D)}{\mathrm{K}_{\mathrm{H}}(x_D,y_D)}}\right)dy_D\right)\end{array}\right]\frac{\partial}{\partial y_D}\left(\frac{\overline{\rho}_1\lambda_1 w_{i,1}+\overline{\rho}_2\lambda_2 w_{i,2}}{\overline{\rho}_1\lambda_1+\overline{\rho}_2\lambda_2}\right)+\\
&\frac{\partial}{\partial y_D}\left(\frac{\lambda_1\lambda_2\mu_2^o}{\overline{\rho}_1\lambda_1+\overline{\rho}_2\lambda_2}\overline{\rho}_1\overline{\rho}_2(w_{i,2}-w_{i,1})\mathrm{K}_V(x_D,y_D)\left(R_L^2N_g-R_L^2N_{CD}\frac{\partial}{\partial y_D}\left(J(S_1)\sqrt{\frac{\varphi(x_D,y_D)}{\mathrm{K}_{\mathrm{H}}(x_D,y_D)}}\right)\right)\right)-\\
&N_{TD}\frac{\partial}{\partial y_D}\left(\left(\frac{\overline{\rho}_1\lambda_1\alpha_{\mathrm{T},1}(x_D,y_D)}{\lambda_t}\frac{\partial w_{i,1}}{\partial y_D}+\frac{\overline{\rho}_2\lambda_2\alpha_{\mathrm{T},2}(x_D,y_D)}{\lambda_t}\frac{\partial w_{i,2}}{\partial y_D}\right)u_{tx_D}\right)-\\
&N_{TD}N_{CD}\frac{\partial}{\partial y_D}\left(\frac{\lambda_1\lambda_2\mu_2^o}{\lambda_t}\mathrm{K}_{\mathrm{H}}(x_D,y_D)\left(\overline{\rho_1}\alpha_{\mathrm{T},1}(x_D,y_D)\frac{\partial w_{i,1}}{\partial y_D}-\overline{\rho_2}\alpha_{\mathrm{T},2}(x_D,y_D)\frac{\partial w_{i,2}}{\partial y_D}\right)\frac{\partial}{\partial y_D}\left(J(S_1)\sqrt{\frac{\varphi(x_D,y_D)}{\mathrm{K}_{\mathrm{H}}(x_D,y_D)}}\right)\right)=0
\end{aligned}
$$

(3.58)

Before we proceed, let us recall the conditions for the validity of the transverse equilibrium TE. It was derived in the limit R_L>>1 and N_{TD}>>1. In order for gravity and capillarity to be absent from equation 3.58, the strong constraints below are needed

$$N_{CD} << \frac{1}{N_{TD}} \text{ and } N_{CD} << \frac{1}{N_{LD}} \text{ and } N_{CD} << \frac{1}{R_L^2} \text{ and } N_g << \frac{1}{R_L^2} \tag{3.59}$$

The conditions in equation 3.59 can also be represented in terms of the original reservoir variables as

$$\frac{\sqrt{k_H \overline{\phi} \gamma}}{L \mu_2^o q} \ll \frac{H^2}{L \overline{\overline{\alpha_T}}} \quad \text{and} \quad \frac{\sqrt{k_H \overline{\phi} \gamma}}{L \mu_2^o q} \ll \frac{L}{\overline{\overline{\alpha_L}}} \quad \text{and} \quad \frac{\sqrt{k_H \overline{\phi} \gamma}}{L \mu_2^o q} \ll \frac{H^2 k_H}{L^2 k_V} \tag{3.60}$$

$$\frac{k_V (\rho_1^o - \rho_2^o) g}{\mu_2^o q} \ll \frac{H}{L} \tag{3.61}$$

where the capillary number N_{CD} defined is the same as by Yokoyama and Lake, (1981). Under the conditions in equation 3.59, equation 3.58 is transformed into a form where transverse equilibrium emphasizes viscous as well as dispersive crossflow because of heterogeneity.

$$\begin{aligned}
&\frac{\partial}{\partial t_D}\Big(\varphi(x_D, y_D)(\overline{\rho}_1 S_1 w_{i,1} + \overline{\rho}_2 S_2 w_{i,2})\Big) - \frac{\overline{\rho}_1 \lambda_1 w_{i,1} + \overline{\rho}_2 \lambda_2 w_{i,2}}{\overline{\rho}_1 \lambda_1 + \overline{\rho}_2 \lambda_2} \frac{\partial}{\partial t_D}\Big(\varphi(x_D, y_D)(\overline{\rho}_1 S_1 + \overline{\rho}_2 S_2)\Big) + \\
&\frac{\overline{\rho}_1 \lambda_1 + \overline{\rho}_2 \lambda_2}{\lambda_t} u_{tx_D} \frac{\partial}{\partial x_D}\left(\frac{\overline{\rho}_1 \lambda_1 w_{i,1} + \overline{\rho}_2 \lambda_2 w_{i,2}}{\overline{\rho}_1 \lambda_1 + \overline{\rho}_2 \lambda_2}\right) - \\
&N_{LD} \frac{\partial}{\partial x_D}\left(\left(\frac{\overline{\rho}_1 \lambda_1 \alpha_{L,1}(x_D, y_D)}{\lambda_t} \frac{\partial w_{i,1}}{\partial x_D} + \frac{\overline{\rho}_2 \lambda_2 \alpha_{L,2}(x_D, y_D)}{\lambda_t} \frac{\partial w_{i,2}}{\partial x_D}\right) u_{tx_D}\right) - \\
&\left[\frac{\partial}{\partial t_D}\left(\int_0^{y_D} \varphi(x_D, y_D)(\overline{\rho}_1 S_1 + \overline{\rho}_2 S_2)\,\mathrm{dy_D}\right) + \frac{\partial}{\partial x_D}\left(\int_0^{y_D} \frac{\overline{\rho}_1 \lambda_1 + \overline{\rho}_2 \lambda_2}{\lambda_t} u_{tx_D}\,\mathrm{dy_D}\right)\right] \frac{\partial}{\partial y_D}\left(\frac{\overline{\rho}_1 \lambda_1 w_{i,1} + \overline{\rho}_2 \lambda_2 w_{i,2}}{\overline{\rho}_1 \lambda_1 + \overline{\rho}_2 \lambda_2}\right) - \\
&N_{TD} \frac{\partial}{\partial y_D}\left(\left(\frac{\overline{\rho}_1 \lambda_1 \alpha_{\mathrm{T},1}(x_D, y_D)}{\lambda_t} \frac{\partial w_{i,1}}{\partial y_D} + \frac{\overline{\rho}_2 \lambda_2 \alpha_{\mathrm{T},2}(x_D, y_D)}{\lambda_t} \frac{\partial w_{i,2}}{\partial y_D}\right) u_{tx_D}\right) = 0
\end{aligned} \tag{3.62}$$

If the densities of the two phases are almost constant i.e. the pressure and component concentration variation do not affect the density too much

$$\frac{\partial \overline{\rho_j}}{\partial P_{1D}} << 1; \quad \frac{\partial \overline{\rho_j}}{\partial w_{i,j}} << 1; \quad j = 1, 2 \text{ and } i = 1 \text{ to } \mathrm{N_c} \tag{3.63}$$

Under the above assumption, the pressure gradient in the x direction could be eliminated

$$u_{tx_D} = \frac{\kappa_H(x_D, y_D)\lambda_t}{\int_0^1 \kappa_H(x_D, y_D)\lambda_t dy_D}\,\overline{u}_{tx_D}; \quad \text{and} \quad \overline{u}_{tx_D} = 1 \tag{3.64}$$

Substitution of the total velocity u_{tx_D} from equation 3.64 to equation 3.62 yields the final result

$$\begin{aligned}
&\frac{\partial}{\partial t_D}\Big(\varphi(x_D, y_D)(\overline{\rho}_1 S_1 w_{i,1} + \overline{\rho}_2 S_2 w_{i,2})\Big) - \frac{\overline{\rho}_1\lambda_1 w_{i,1} + \overline{\rho}_2\lambda_2 w_{i,2}}{\overline{\rho}_1\lambda_1 + \overline{\rho}_2\lambda_2}\frac{\partial}{\partial t_D}\Big(\varphi(x_D, y_D)(\overline{\rho}_1 S_1 + \overline{\rho}_2 S_2)\Big) + \\
&\frac{\overline{\rho}_1\lambda_1 + \overline{\rho}_2\lambda_2}{\lambda_t}\frac{\kappa_H(x_D, y_D)\lambda_t}{\int_0^1 \kappa_H(x_D, y_D)\lambda_t dy_D}\frac{\partial}{\partial x_D}\left(\frac{\overline{\rho}_1\lambda_1 w_{i,1} + \overline{\rho}_2\lambda_2 w_{i,2}}{\overline{\rho}_1\lambda_1 + \overline{\rho}_2\lambda_2}\right) - \\
&N_{LD}\frac{\partial}{\partial x_D}\left(\left(\frac{\overline{\rho}_1\lambda_1\alpha_{L,1}(x_D, y_D)}{\lambda_t}\frac{\partial w_{i,1}}{\partial x_D} + \frac{\overline{\rho}_2\lambda_2\alpha_{L,2}(x_D, y_D)}{\lambda_t}\frac{\partial w_{i,2}}{\partial x_D}\right)\frac{\kappa_H(x_D, y_D)\lambda_t}{\int_0^1 \kappa_H(x_D, y_D)\lambda_t dy_D}\right) - \\
&\left[\frac{\partial}{\partial t_D}\left(\int_0^{y_D} \varphi(x_D, y_D)(\overline{\rho}_1 S_1 + \overline{\rho}_2 S_2)\,\mathrm{dy_D}\right) + \frac{\partial}{\partial x_D}\left(\frac{\int_0^{y_D} (\overline{\rho}_1\lambda_1 + \overline{\rho}_2\lambda_2)\kappa_H(x_D, y_D)\,\mathrm{dy_D}}{\int_0^1 \kappa_H(x_D, y_D)\lambda_t dy_D}\right)\right]\frac{\partial}{\partial y_D}\left(\frac{\overline{\rho}_1\lambda_1 w_{i,1} + \overline{\rho}_2\lambda_2 w_{i,2}}{\overline{\rho}_1\lambda_1 + \overline{\rho}_2\lambda_2}\right) - \\
&N_{TD}\frac{\partial}{\partial y_D}\left(\left(\frac{\overline{\rho}_1\lambda_1\alpha_{\mathrm{T},1}(x_D, y_D)}{\lambda_t}\frac{\partial w_{i,1}}{\partial y_D} + \frac{\overline{\rho}_2\lambda_2\alpha_{\mathrm{T},2}(x_D, y_D)}{\lambda_t}\frac{\partial w_{i,2}}{\partial y_D}\right)\frac{\kappa_H(x_D, y_D)\lambda_t}{\int_0^1 \kappa_H(x_D, y_D)\lambda_t dy_D}\right) = 0
\end{aligned}$$

(3.65)

This equation represents the second result of this chapter. It is a second order PDE in two spatial dimensions (x, y), that contains saturation and component concentration as dependent variables. More importantly, equation 3.62 contains a viscous crossflow term (fifth term on the LS) and dispersive crossflow term (sixth term on the LS), both of which arise from transverse equilibrium in absence of gravity and capillarity.

In this chapter, a formal approach was used to derive rigorously the conditions for Transverse Equilibrium. The identification of R_L and N_{TD} as the key parameters for power series expansion was a key to the analysis. The analysis conforms to previously known numerical results and, for the first time, rigorously establishes the validity for two phase multicomponent compressible miscible flow in the limit of large R_L^2 and N_{TD}. The conditions developed depend on the geometry of the porous media as well as the static petrophysical properties.

The conditions for TE should ideally lead to a reduction in dimensionality of the problem but the inter-dependence of viscous and dispersive flow prevents us from attaining that result. Heterogeneity of the reservoir is also accounted for in the analysis. The relative strength of viscous to other forces (gravity and capillary) dictates the flow regime in the reservoir.

$N_g << \frac{1}{R_L^2}$	Gravity not dominant but capillary forces contribute to transverse flow
$N_{CD} << \frac{1}{N_{TD}}$ & $N_{CD} << \frac{1}{R_L^2}$	Capillary forces not dominant but gravity contributes to transverse flow
$N_{CD} << \frac{1}{N_{TD}}$ & $N_{CD} << \frac{1}{R_L^2}$ and $N_g << \frac{1}{R_L^2}$	Capillary and gravity are both not dominant. Maximum crossflow caused by viscous and dispersive forces

Table 3-1. Summary of the conditions under which different forces contribute to transverse flow in a reservoir.

The typical values of reservoir properties are: length L = 1000 ft, thickness H = 30, kv/kh = 0.1, longitudinal dispersivity α_L = 0.032 ft and transverse dispersivity α_T = 0.0032 ft. The relevant dimensionless parameter for such reservoir are R_L^2 =110, N_{TD} = 0.0035 and N_{LD} = 0.000035. For typical reservoirs the state of total transverse equilibrium is not achieved because N_{TD} stays smaller than one. The gravity number must be smaller than N_g = 0.01 for gravity to be negligible. This condition is not fulfilled very often and gravity plays a significant role in displacements. The capillary number must be smaller than N_{CD} = 0.01 for capillaity to be negligible. This condition is fulfilled sometimes depending on the interfacial tension between the two phases.

CHAPTER 4

Upscaling of Miscible Floods: An Extension to Koval's Method

Solvents, such as carbon dioxide, are shown to be cause unstable displacement of oil (Perrine, 1961) in theory and (Blackwell, 1959) experimentally. Field data and scaled down lab experiments also suggest that such floods are unstable (Haberman, 1960). These instabilities in the displacement leaves some parts of the reservoir unswept, causes early breakthrough of solvent and reduced oil cut. Unstable floods lead to fingering and intrinsic heterogeneity at large scale exacerbates the problem further by causing channeling.

The problem of solvent fingering is also accentuated by channeling, longitudinal dispersion, viscosity and gravity differences (Perrine, 1961). Longitudinal dispersion in a porous media is caused by mechanical spreading because of random grain scale inhomogeneities. Viscosity differences lead to faster growth of the fingers as solvent tries to follow the path of least resistance. Gravity differences causes solvent to override and leads to fast growth of the ensuing tongues. Miller 1966 showed that gravity can cause segregation of injected miscible gas and water. It was also showed by Miller, 1966 that the oil bank that forms ahead of an over-riding miscible fluid is forced down below solvent tongue and moves slowly towards producing well. The oil bank is slowly recovered immiscibly at a very slow rate by injected water along with the gas. Thus a significant amount of oil displaced by miscible fluid is left unswept in the reservoir. The effect of gravity can be significant for floods with low gravity number but incorporating gravity complicates the model formulation. For this reason model and results reported herein are for matched density fluids.

Much research effort has been spent on ways to accurately predict the performance of unstable miscible displacements in heterogeneous media. Most proposals to simulate miscible floods effectively suggest empirical models to represent viscous fingering and channeling.

Dougherty (1963) constructed a flow model akin to Koval's approach accounting for mixing. Some work was done in the 70's by Lantz (1970) and Todd and Longstaff (T-L) (1972) to use existing two and three phase immiscible simulators and modify them to simulate miscible floods. Fayers (1988) described unstable displacements by suggesting the use of a fingering function.

$$\Lambda = a + bC_f^{\alpha} \tag{4.1}$$

where, Λ is the fraction of cross-section occupied by fingers, C_f is the solvent saturation in the fingers, a is the initial finger width and $(a+b)$ is the fraction of the cross section occupied by fingers when $C_f = 1$. Fayers and Newley (1988) also empirically extended this model to 3-D flow systems. Todd and Chase (1979) suggested a model based on the T-L model to account for viscous fingering under multi-contact miscible conditions. Crump (1988) applied a modified T-L model using mobility ratio dependent mixing model along with Koval heterogeneity factor H_k determined from unit mobility ratio displacements. Nghiem and Agarwal (1989), Fayers et al. (1992) and Huh et al. (2006) proposed use of two region models for upscaling of miscible floods. The modeling of viscous instabilities and channeling requires models at centimeter or millimeter scale (Gardner and Ypma, 1984). All the above models, requiring numerical simulation, and are time consuming.

The scale of reservoirs compared to the scale of the instabilities established a need for an upscaling scheme that could predict production with as few parameters as possible. Therefore, using fast and accurate analytical techniques, which represent the underlying physical phenomena is important. One of the earliest models for this purpose was developed by Koval (1963).

Koval introduced a factor (*K*) to represent the effects of fingering and channeling combined on oil recovery by a miscible solvent.

$$F_s = \frac{1}{1 + \frac{(1-S)}{KS}} \tag{4.2}$$

where, F_s is the fractional flow of solvent, S is the saturation of the solvent along the cross-section. Koval's theory is based on the premise that both dispersion and channeling are a result of heterogeneity and it is difficult to decouple one from the other. Patton (1971) presented a predictive model for polymer floods, Paul et al. developed a model to predict surfactant-polymer floods in 1982 and a similar model for CO_2 flood evaluation in 1984. Genrich (1987) studied the effects of heterogeneity on WAG performance and developed a steady-state, analytical model to predict production. Molleai (2011) developed a more rigorous model based on the Koval method for displacements. His model accounts for the two fronts at global scale by defining separate Koval factors for both. The models developed so far either do not work for two front displacements or do not account for the interactions between them at large scale for heterogeneous fields.

The contributions of this work are (a) to formally and rigorously introduce the mobility ratio correction term in the Koval theory, and (b) to decouple the local and global problem while accounting for interaction between the two fronts at reservoir scale. The local problem is the pixel scale problem solved using fractional flow theory and global problem represents the effects of large scale heterogeneity at window scale. The definition of the scales and the nature of local and the global problem are discussed below in detail.

4.1 ASSUMPTIONS

Before going further, we define a few terms related to upscaling. The pixel scale (Li, 1995) is the scale below which no information is assumed to be available. In context of the chapter, the pixel scale is the fractional flow scale (fine scale) or the information that we obtain from core scale (relative permeabilities). The window scale is the scale beyond which no information is evident. In the context of the chapter, the window scale is the reservoir or interwell scale.

The section itemizes the set of simplifying assumptions and their impact on the study.

1. Just for model development and verification, we restrict ourselves to a 2-D linear and isothermal reservoir. Multidimensional flow does not rule out viscous instabilities. The isothermal assumption simplifies the problem because only mass conservation equations must be solved.
2. For miscible floods, pressure, temperature and solvent compositions influence miscibility development. For WAG floods where miscibility develops, the pixel scale problem is then governed by the fractional flow theory (Walsh and Lake, 1988).
3. The rock and fluid properties are assumed to be independent of pressure. This assumption is valid for most of the cases we deal in the paper. Polymer and ASP floods with two fronts at the pixel scale pose no controversy related to this assumption. Miscible floods with gas as a solvent on the other hand do, because gases are compressible. Fractional flow theory was developed for incompressible fluids and it governs flow physics in our models at the pixel scale. For gases like CO_2 which are fairly incompressible at high pressures, this assumption is

reasonable. In cases where the pressure gradients developed during flow are small the assumptions holds.

4. Spreading because of capillary forces for immiscible fluids is negligible. Spreading caused by dispersion of components in miscible fluids is negligible (high Peclet numbers). In other words the mixing zone developed is very small compared to the window scale. This reduces mass conservation equations to first-order hyperbolic equations and the method of characteristics can be used to solve them and gain useful insights.
5. Initial conditions assume uniform oil and water saturation in the whole reservoir. Different initial saturation distributions give different flow conditions at the pixel scale and add a layer of complexity.
6. We assume that we have at most three components, oil, water and a displacing agent (solvents, surfactant solutions or polymer solutions), in the reservoir at any time. There is at most two phases in the system, an aqueous phase that contains water and an oleic phase that contains solvent and oil. Insight from pixel scale fractional flow theory for floods that form two fronts suggests segregated regions of flow.
7. Effects of gravity were ignored in the reservoir which is taken to be in vertical equilibrium throughout. This assumption is essential to the model development.
8. The reservoir scale problem depends on pixel scale (local scale) problem. The local scale problem is largely piston like for miscible WAG floods (Walsh and Lake, 1988) as shown in Figure 4-1.

The assumptions 1 to 8 give a set of hyperbolic mass conservation equations that can be solved using the method of characteristics so that coherent wave theory applies (Hilbert and Courant, 1962; Lake, 1989).

4.2 THEORETICAL DEVELOPMENT

The Buckley-Leverett method (1942) is a very useful tool to predict oil recovery for immiscible oil and gas displacements. It was based on simplifying assumptions but gave insights that were consistent with the physical observations. The Koval (1963) theory for miscible floods helped predict oil recovery while accounting for heterogeneity and adverse mobility ratio.

Walsh and Lake (1988) also made simplifying assumptions and built on extensions to the Buckley-Leverett theory to predict oil recovery for first-contact miscible water-alternating-gas (SWAG) floods under varying injection and initial conditions for homogeneous systems.

The two important relationships were developed in the above theories.

The frontal advance formula,

$$\frac{dx_D}{dt_D} = \frac{\partial F_i}{\partial C_i} \tag{4.3}$$

And the fractional flow equation,

$$F_i = f(C_i\text{'}s, \mathrm{H_k}, MR) \tag{4.4}$$

where F_i stands for fractional flow of the component i, C_i*'s* are the concentrations of all the components from $i = 1$ to N in the reservoir, H_k stands for heterogeneity factor and MR is the mobility ratio. The frontal advance formula in other words is the velocity at which that component travels in the system. Coherence or simple wave theory stipulates that all the components present in the reservoir travel with the same wave velocity. We also develop similar relationships for upscaled systems where the fractional flow equation would depend on pixel scale information as well as window scale information.

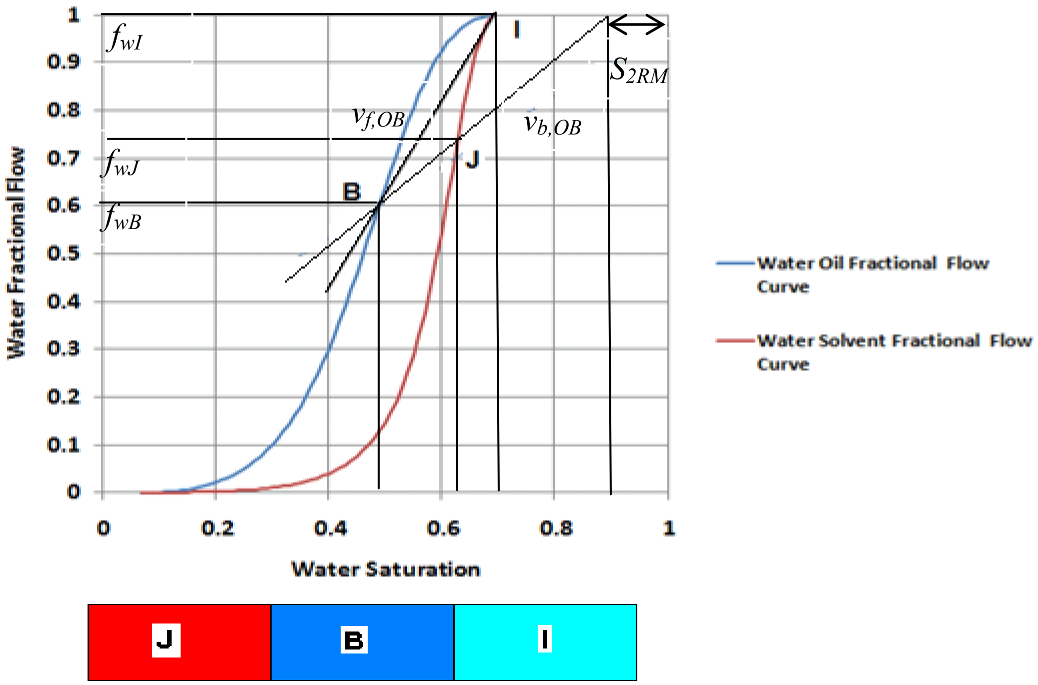

Figure 4-1. Fractional flow curves for a first-contact miscible SWAG flood showing the formation of an oil bank (*B*) with two fronts separating it from the initial (*I*) and injection (*J*) condition

4.3 GOVERNING EQUATIONS

Subject to the assumptions listed above, the cross-sectionally averaged conservation equations yield a set of hyperbolic equations that are to be solved using the methods of characteristics (referred to as MOC from now on in the chapter):

Water mass balance yields:

$$f_{1,J}\frac{\partial F_J}{\partial X_D}+f_{1,B}\frac{\partial F_B}{\partial X_D}+f_{1,I}\frac{\partial F_I}{\partial X_D}+S_{1,J}\frac{\partial C_J}{\partial t_D}+S_{1,B}\frac{\partial C_B}{\partial t_D}+S_{1,I}\frac{\partial C_I}{\partial t_D}=0 \tag{4.5}$$

Solvent mass balance yields:

$$(1-f_{1,J})\frac{\partial F_J}{\partial X_D}+(1-S_{1,J}-S_{2RM})\frac{\partial C_J}{\partial t_D}=0 \tag{4.6}$$

$$F_J+F_B+F_I=1 \tag{4.7}$$

$$C_J+C_B+C_I=1 \tag{4.8}$$

where J is the region in the reservoir being occupied by solvent, B is the region where oil banks and I is the region with initial reservoir conditions. $f_{1,J}$, $f_{1,B}$ and $f_{1,I}$ is the water fractional flow in regions J, B and I respectively, at the pixel scale. $S_{1,J}$, $S_{1,B}$ and $S_{1,I}$ are the water saturation in regions J, B and I respectively, at the pixel scale. S_{2RM} is the residual oil to miscible floods. The residual oil to miscible floods could result from local heterogeneity in permeable medium or dispersion and its interaction with phase behavior (Gardner et al., 1981). This information is derived from pixel scale fractional flow theory as shown in Fig. 4-1. Subscripts 1, 2 and 3 refer to brine, oil and solvent respectively in the paper. At the window scale shown in Fig. 4-4b, $f_{1,J}$, $f_{1,B}$, $f_{1,I}$, $S_{1,J}$, $S_{1,B,}$ $S_{1,I}$ and S_{2RM} are assumed to be constant. This assumption is valid because of the formation of three distinct flow regions at pixel scale (Fig. 4-1).

C_J is the fraction of total cross-section swept by the injected fluid, C_B is the fraction of the total cross-section swept by the oil bank and C_I is the fraction of total cross-section occupied by initial oil at any given position and time as shown in Figure 4-4b. F_J is the fraction of total flow in the region defined by C_J, F_B is the fraction of total flow in the region defined by C_B, and F_I is the fraction of total flow in the region defined by C_I as shown in Figure 4-4. Eqs. 4-9 and 4-10 are simplified and compact forms of Eqs. 4-5 and 4-6 respectively and their detailed derivation is shown in Appendix A.

$$v_{f,OB}\frac{\partial F_I}{\partial X_D}+\frac{\partial C_I}{\partial t_D}=0 \tag{4.9}$$

$$v_{b,OB}\frac{\partial F_J}{\partial X_D}+\frac{\partial C_J}{\partial t_D}=0 \tag{4.10}$$

$$v_{f,OB}=\frac{f_{1,I}-f_{1,B}}{S_{1,I}-S_{1,B}} \tag{4.11}$$

$$v_{b,OB}=\frac{f_{1,J}-f_{1,B}}{S_{1,J}-S_{1,B}}=\frac{1-f_{1,J}}{1-S_{1,J}-S_{2RM}} \tag{4.12}$$

where $v_{f,OB}$ is the pixel scale velocity at the front of the oil bank and $v_{b,OB}$ is the pixel scale velocity at the back of the oil bank as shown in Figure 4-1. The independent variables in Eq. 4-5 and Eq. 4-6 are dimensionless time and position:

$$t_D = \frac{\int_0^t u\,dt}{\phi L}, \quad x_D = \frac{\int_0^x dx}{L} \tag{4.13}$$

The dimensionless time (t_D) defined above is the cumulative fluid injected per unit pore volume and the dimensionless position (x_D) is distance away from injection well divided by the distance between the injector and the producer (L). The velocity of the flowing fluids in the reservoir is invariable with position on account of constant cross sectional area as well as incompressibility of the fluids, but it can change with time. The detailed derivation of the mass conservation equations is in Appendix A.

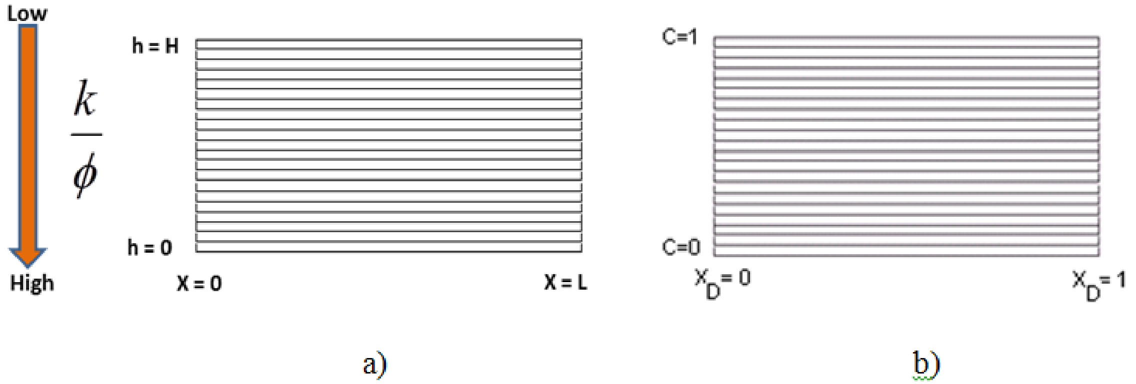

Figure 4-2. a) Layer arrangement in the order of increasing interstitial velocity from top to bottom. The heterogeneous system represented by a uniformly layered system (infinite autocorrelation length in the x-direction). b) Dimensionless representation of the same layered system based on definitions below.

Now consider a layered reservoir with infinite correlation length in the flow direction (x direction) and correlation length in the direction perpendicular to bulk flow (z direction) is limited by layer thickness. The layers are arranged in the order of their interstitial velocities (r_n) i.e the layer with largest interstitial velocity is at the bottom and that with the least interstitial velocity at the top (Figure 4-2a). The interstitial velocity (r_n) is defined as:

$$r_n = \frac{k_n}{\phi_n} \tag{4.14}$$

The dimensionless representation (Figure 4-2b) of the layered media shown in Figure 4-2a is needed for general solutions. The dimensionless variables are as follows:

$$C = \frac{\sum_{i=1}^{n} \phi_i h_i}{\sum_{i=1}^{N} \phi_i h_i}, \text{ discrete or } C = \frac{\int_0^h \phi dh}{\int_0^H \phi dh}, \text{continuous} \tag{4.15}$$

where ø$_i$ is the porosity of ith layer and *H* is the total thickness of the reservoir, *C* is the dimensionless thickness or cumulative storage capacity up to any height (*h*). We also define the cumulative flow capacity (*F*) contained in layers upto height (*h*) as:

$$F = \frac{\sum_{i=1}^{n} k_i h_i}{\sum_{i=1}^{N} k_i h_i}, \text{ discrete or } F = \frac{\int_0^h k dh}{\int_0^H k dh}, \text{continuous} \tag{4.16}$$

where k_i is the permeability of ith layer. *F*, the cumulative flow capacity, can also be thought of as fraction of total flow in single phase unit mobility ratio flow regime through region *C*. The cumulative flow capacity (*F*) and cumulative storage capacity (*C*) relate to each other based on Koval theory (Figure 4-3).

$$F = \frac{1}{1 + \frac{(1-C)}{H_k C}} \tag{4.17}$$

where H_k is defined as the heterogeneity factor.

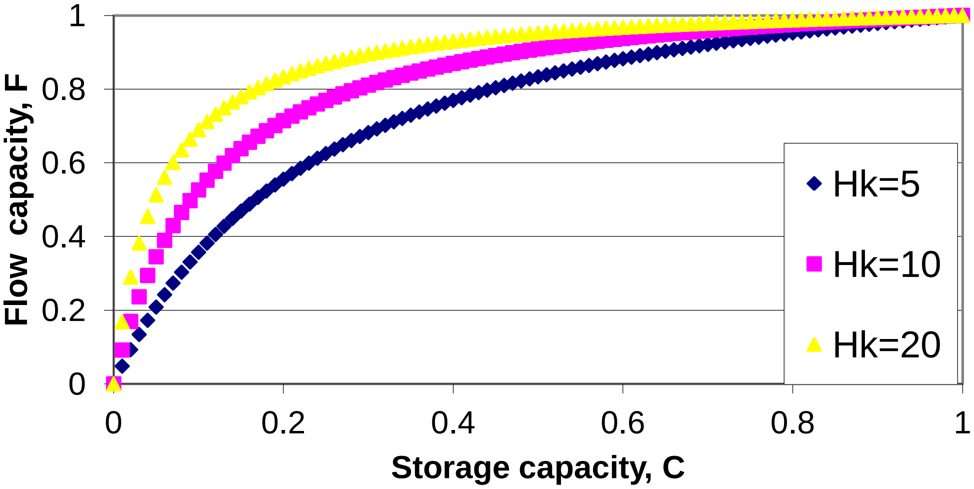

Figure 4-3. Static *F-C* curves relating flow capacity to storage capacity for different heterogeneity factors. The greater the heterogeneity, the more flow capacity in smaller fraction of the pore volume.

One main contribution of this work is the use of relationship in Eq. 4-17 to reduce the degrees of freedom of this problem from N (number of layers) to one thereby reducing the dimensionality of the problem from 2-D to 1-D in space. The important thing in Eq. 4-17 is that the effects of mobility ratio are not included so far in the relationship, the F-C curves are, thus far, statistical representations of heterogeneity or normalized distribution functions. Although Koval added mobility contract effects heuristically, in this work we do so more rigorously. And we do it for more general cases.

The layered reservoir in Figure 4-2 is being flooded with the solvent through a vertical injector located at $x = 0$. The vertical production well is at $x = L$. Both wells are completed across all layers. Figure 4-4 illustrates the schematic representation of solvent and oil bank distribution in such reservoir after injection.

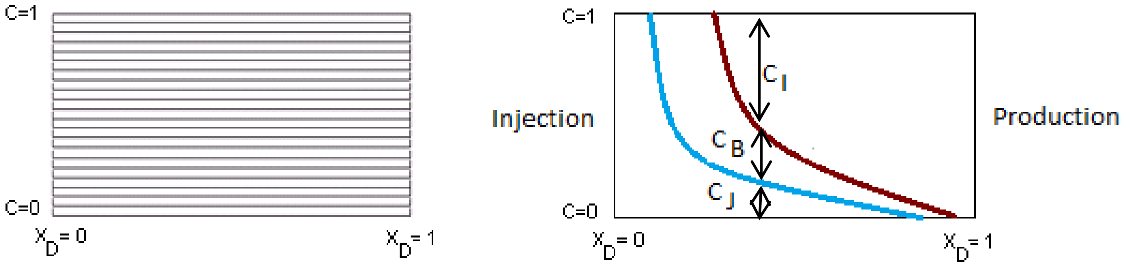

Figure 4-4 a) Schematic showing dimensionless representation of a layered medium. b) Schematic representation of the formation of oil bank and solvent flow in a layered medium. Injected solvent wave travels fastest in the bottommost layer with the highest interstitial velocity and slowest at the top with smallest interstitial velocity.

The fractional flow relationships at the window scale (F_J, F_I) for such a displacement used in governing Eqs. 4-5 and 4-6 are in Eqs. 4-18 and 4-19. F_J and F_I are related to C_J, C_B and C_I as (Appendix B):

$$F_J = \frac{C_J}{C_J + \left[\frac{1}{MR_b}\right]\left[\frac{1}{1+(H_k-1)(C_J+C_B)}\right]C_B + \left[\frac{1}{MR_b MR_f}\right]\left[\frac{1+(H_k-1)C_J}{1+(H_k-1)(C_J+C_B)}\right]\left[\frac{1}{H_k}\right]C_I}$$

(4.18)

$$F_I = \frac{C_I}{\left[MR_b MR_f\right]\left[\frac{1+(H_k-1)(C_J+C_B)}{1+(H_k-1)C_J}\right]\left[H_k\right]C_J + \left[MR_f\right]\left[\frac{H_k}{1+(H_k-1)C_J}\right]C_B + C_I} \qquad (4.19)$$

Conservation Eqs. 4-9 and 4-10 are solved for C_J and C_I using the relationships defined in Eqs. 4-18 and 4-19. F_J and F_I depend on reservoir heterogeneity factor (H_k), mobility ratio (MR_b) at the back of the oil bank and mobility ratio (MR_f) at the front of the oil bank. The reservoir heterogeneity factor is a window scale parameter whereas mobility ratios are pixel scale parameters that depend on saturation distributions in the regions (*J*, *B* and *I*). These relationships have been explicitly derived and illustrated in Appendix B.

The effects of mixing because of solvent dispersion into the oil changes the mobility ratio at the solvent front. As listed in the assumptions, for high Peclet numbers, there is no mixing between oil and solvent at the solvent front. Thus, note that the solvent viscosity used in calculating the total mobility ratio at the back of the oil bank (MR_b) does not assume quarter power mixing rule as was used by Koval (1963) to account for the mixing effects. Molleai (2011) also defined the window scale fractional flow functions F_J and F_I based on Koval theory as shown in Eqs. 4-20 and 4-21.

$$F_J = \frac{C_J}{C_J + \left[\frac{1}{H_k MR_b}\right](1 - C_J)} \tag{4.20}$$

$$F_I = \frac{C_I}{C_I + \left[MR_f H_k\right](1 - C_I)} \tag{4.21}$$

Eqs. 4-20 and 4-21 suggest that the window scale fractional flow in region *J* only depends on C_J and in region *I* only depends on C_I. This suggests that the two fronts in such displacements (Figure 4-4) at window scale travel independent of each other. Fractional flow theory (Walsh and Lake, 1988) shows that the fronts interact at the pixel scale. Since these fronts interact at the pixel scale, they should interact at window scale too. Another significant contribution of this work is that it accounts for the interactions between these fronts at window scale (Eqs. 4-18 and 4-19).

4.4 INITIAL AND BOUNDARY CONDITIONS

The initial condition (t_D=0), referred to by script *I*, is uniform water saturation $S_{1,I}$ based on assumption 5. Initially, there is no solvent in the reservoir. The injected condition at (x_D = 0) is a two-phase mixture of solvent and water for miscible WAG floods and the injection condition is specified by the water-solvent fractional flow $f_{1,J}$.

We assume that water and solvent are injected simultaneously though small deviations between simultaneous and alternating solvent-water injection have been suggested by Dai and Orr (1987).

4.5 METHOD OF SOLUTION

The Method of Characteristics or MOC solves for the velocities with which C_J and C_I travel based on simple wave theory at all points in the system. This velocity (σ) is derived as:

$$v_{f,OB}\frac{dF_I}{dC_I} = v_{\mathrm{b},OB}\frac{dF_J}{dC_J} = \sigma = \frac{x_D}{t_D} \tag{4.22}$$

The derivatives in Eq. (4-22) are total derivatives and coherence or simple wave theory suggests a relation $C_I = C_I(C_J)$ found by expanding the derivatives in Eq. 4-22 and writing them in matrix form yields:

$$\begin{bmatrix} v_{f,OB}\dfrac{\partial F_I}{\partial C_I} & v_{f,OB}\dfrac{\partial F_I}{\partial C_J} \\ v_{b,OB}\dfrac{\partial F_J}{\partial C_I} & v_{b,OB}\dfrac{\partial F_J}{\partial C_J} \end{bmatrix} \begin{bmatrix} dC_I \\ dC_J \end{bmatrix} = \sigma \begin{bmatrix} dC_I \\ dC_J \end{bmatrix} \tag{4.23}$$

Solving Eq. (4-23) for the eigenvalues, σ^+ and σ^-

$$\sigma^+,\sigma^- = \frac{1}{2}\left\{\left(v_{f,OB}\frac{\partial F_I}{\partial C_I} + v_{b,OB}\frac{\partial F_J}{\partial C_J}\right) \pm \left[\left(v_{f,OB}\frac{\partial F_I}{\partial C_I} - v_{b,OB}\frac{\partial F_J}{\partial C_J}\right)^2 + 4v_{f,OB}v_{b,OB}\frac{\partial F_I}{\partial C_J}\frac{\partial F_J}{\partial C_I}\right]^{½}\right\}$$

(4.24)

Both the eigenvalues are presumed to be real and $\sigma^+ > \sigma^-$. These eigenvalues are only functions of C_I and C_J. The eigenvalues also relate C_I and C_J as:

$$\frac{dC_I}{dC_J}=\frac{v_{f,OB}\dfrac{\partial F_I}{\partial C_J}}{\sigma-v_{f,OB}\dfrac{\partial F_I}{\partial C_I}}=\frac{\sigma-v_{b,OB}\dfrac{\partial F_J}{\partial C_J}}{v_{b,OB}\dfrac{\partial F_J}{\partial C_I}} \tag{4.25}$$

The interpretation of Eq. 4-24 suggests that each point (C_I, C_J) has two travel velocities and the relationship between C_I and C_J depends on the chosen velocity. In a physical system, each point (C_I, C_J) only travels with one velocity. Using appropriate end points and Lax's condition, 1) $C_J = 1$ and $C_I = 0$ on the upstream end and $C_J = 0$ and $C_I = 1$ on the downstream end as shown in Fig. 4-5 and 4-4, 2) The velocity (σ) should increase downstream; the correct physical solution is obtained.

After the physical solution is identified, the correct velocity (σ) of each point (C_I, C_J) is known. The oilcut and cumulative oil produced are calculated using the correct velocity from the physical solution. Each point $(C_I, C_J)^*$ breaks through at x_D=1 when,

$$t_D^*=\frac{1}{\sigma(C_J,C_I)^*} \tag{4.26}$$

The fraction of total flow in region J and I at x_D=1 and t_D^* is

$$F_J(t_D^*)=\frac{C_J^*}{C_J^*+\left[\dfrac{1}{MR_b}\right]\left[\dfrac{1}{1+(H_k-1)(C_J^*+C_B^*)}\right]C_B^*+\left[\dfrac{1}{MR_bMR_f}\right]\left[\dfrac{1+(H_k-1)C_J^*}{1+(H_k-1)(C_J^*+C_B^*)}\right]\left[\dfrac{1}{H_k}\right]C_I^*} \tag{4.27}$$

$$F_I(t_D^*)=\frac{C_I^*}{\left[MR_bMR_f\right]\left[\dfrac{1+(H_k-1)(C_J^*+C_B^*)}{1+(H_k-1)C_J^*}\right]\left[H_k\right]C_J^*+\left[MR_f\right]\left[\dfrac{H_k}{1+(H_k-1)C_J^*}\right]C_B^*+C_I^*} \tag{4.28}$$

$$F_B(t_D^*)=1-F_J(t_D^*)-F_I(t_D^*) \tag{4.29}$$

The oil cut equation then is:

$$Oilcut(t_D^*)=(1-f_{1,B})F_B(t_D^*)+(1-f_{1,I})F_I(t_D^*) \tag{4.30}$$

Since solvent only flows in region *J*, solvent cut equation then is:

$$Solvent\ cut(t_D^*) = (1 - f_{1,J})F_J(t_D^*) \tag{4.31}$$

The recovery efficiency (N_{PD}) is:

$$N_{PD}(t_D^*) = \int_0^{t_D^*} Oilcut(t_D)dt_D \tag{4.32}$$

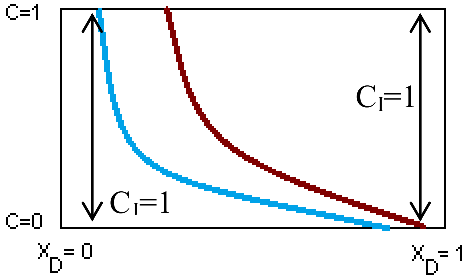

Figure 4-5. Schematic showing the physical end points. Upstream of the oil bank, the entire cross-section is flooded by injected solvent and C_J =1. Downstream of oil bank, the entire cross section is at initial condition and C_I = 1.

The mathematical solution for the problem can be represented graphically on a ternary diagram, which greatly simplifies interpretation of the displacement. Figure 4-6 illustrates the application of the method of solving Eqs. 4-9 and 4-10 for a tertiary first-contact water alternating gas miscible flood. The input parameters required for solving system of Eqs. 4-9 to 4-12, 4-18 and 4-19 for example application are given in Table 4-1a.

Initial condition		Injection condition		
S_{1I}	f_{1I}	S_{1J}	f_{1J}	*WAG ratio* (W_R)
0.7	*1.0*	*0.62*	*0.7*	*2.3*

a)

	Parameters derived from pixel scale fractional flow theory				
H_k	MR_b	MR_f	S_{1B}	f_{1B}	S_{2RM}
2	1.52	0.76	0.49	0.6	0

b)

Table 4-1. a) Initial and injection conditions b) Calculated parameters from pixel scale fractional flow theory (Walsh and Lake, 1988) based on initial and injection conditions given in a).

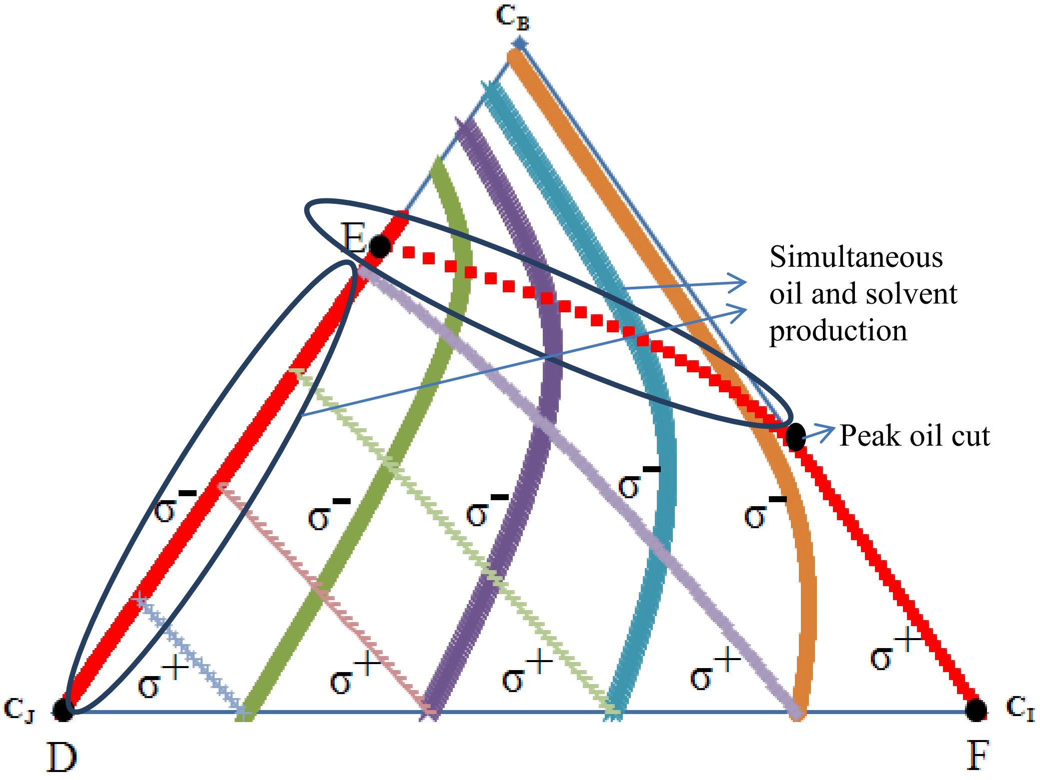

Figure 4-6. Ternary diagram showing all the points mathematically satisfying the system of conservation equations as slow σ- and fast σ+ paths. The correct physical solution plotted in red is the path originating from $C_J = 1$, i.e left bottom corner on the triangle and ending at $C_I = 1$. The paths transition from slow to fast at the red point shown on the plot. Path based on Mollaei solution is plotted in black. Each point on the path travels with a specific velocity (σ).

The results are shown in Fig. 4-7, which is similar to Walsh and Lake diagrams (Walsh and Lake, 1988). Although there are many possibilities, the Fig. 4-7 results are qualitatively similar to field-scale solvent flood behavior (a) peak oil cuts is in the 10-20% range, (b) the peak oil cut coincides with solvent breakthrough, and (c) prolonged simultaneous production of solvent and oil (Haberman, 1960).

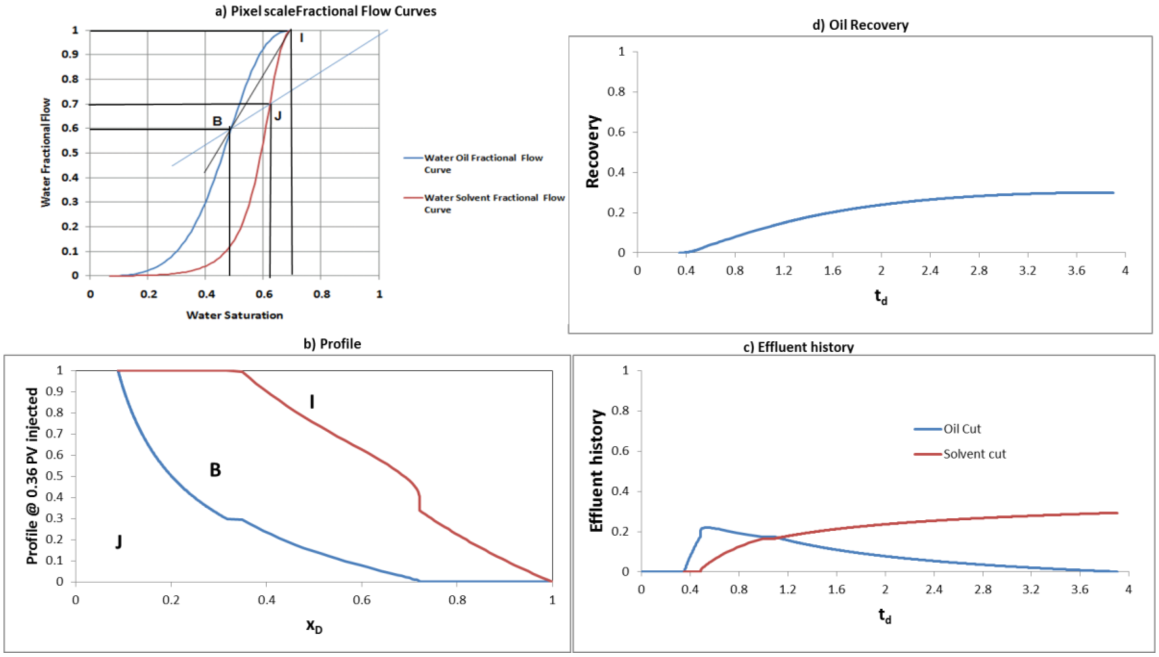

Figure 4-7. a) Pixel scale fractional flow curve for the application with W_R=2.3. b) Physical path from Figure 4-6 converted to flow profile in the reservoir. Each point on the path travels with a velocity (σ) which is used to plot the profile. The profile is converted to effluent history that shows oil cut as well as solvent cut. c) Oil bank breaks through at t_D=0.36 and solvent breaks through after the oil bank break through. Peak oil cut coincides with solvent breakthrough. d) Recovery of 0.3 i.e total remaining oil is recovered at injected pore volumes of 4.

4.6 COMPARISON BETWEEN THE NEW MODEL WITH MOLLAEI'S MODEL

The results from the model are compared to model developed by Mollaei, 2011. Eqs. 4-20 and 4-21 based on his model are used to generate the flow profile and effluent history results for the application case discussed above. Comparison of results with the new model is illustrated by two examples shown from Fig. 4-8 through Fig. 4-11.

Initial condition		Injection condition		
S_{1I}	f_{1I}	S_{1J}	f_{1J}	*WAG ratio* (W_R)
0.7	*1.0*	*0.62*	*0.7*	*2.3*

a)

Heterogeneity factor, H_k			Parameters derived from pixel scale fractional flow theory				
Cases			MR_b	MR_f	S_{1B}	f_{1B}	S_{2RM}
1	**2**	**3**					
1.1	5	20	1.52	0.76	0.49	0.6	0

b)

Table 4-2. a) Initial and injection conditions b) Calculated parameters from pixel scale fractional flow theory (Walsh and Lake, 1988) based on initial and injection conditions given in a).

4.6.1 Case 1, (H_k=1.1)

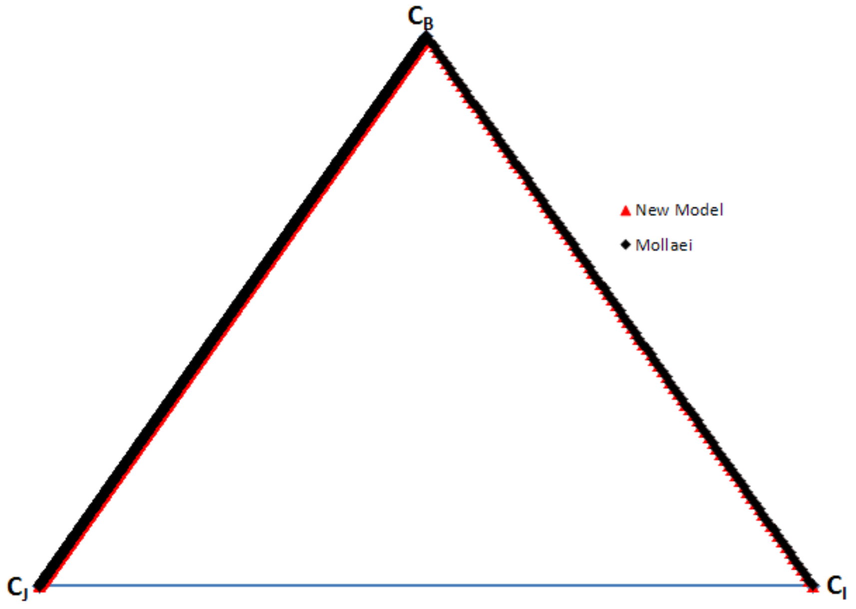

Figure 4-8. Ternary diagram (Case 1) showing the correct physical solution plotted in red is the path originating from $C_J = 1$, i.e left bottom corner on the triangle and ending at $C_I = 1$. The paths transition from slow to fast at $C_B = 1$. Path based on Mollaei solution is plotted in black. Each point on the path travels with a specific velocity (σ)

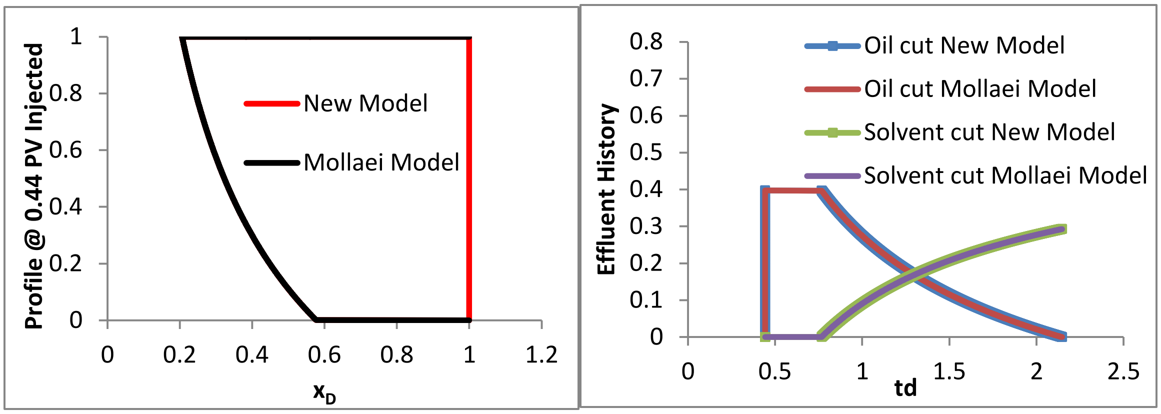

a)

b)

Figure 4-9. a) Profiles match perfectly for case 1 between new model and Mollaei model. b) The effluent history match between the new model and Mollaei model is perfect for case 1.

The pixel scale and window scale parameters for case 1 are given in Table 4-2. Heterogeneity factor (H_k) for case 1 has a value of 1.1 that is very small and the representative reservoir is essentially homogeneous. Figure 4-8 and 4-9a show the wave profile in the reservoir. The wave profiles obtained from the new model and Mollaei model match perfectly and lead to perfect match for effluent history from the two models. Figure 4-8 and 4-9a suggest that regions *J*, *B* and *I* do not coexist together at any location between $x_D = 0$ and $x_D = 1$ and the new model reduces to Mollaei model because the interactions between two fronts at the window scale are insignificant. The solvent front travels as a spreading wave despite small heterogeneity because the mobility ratio at the chemical bank is greater than unity ($MR_b = 1.52$). The oil bank front travels as a shock at window scale because the mobility ratio is smaller than unity ($MR_f = 0.76$).

4.6.2 Case 2, (H_k=5)

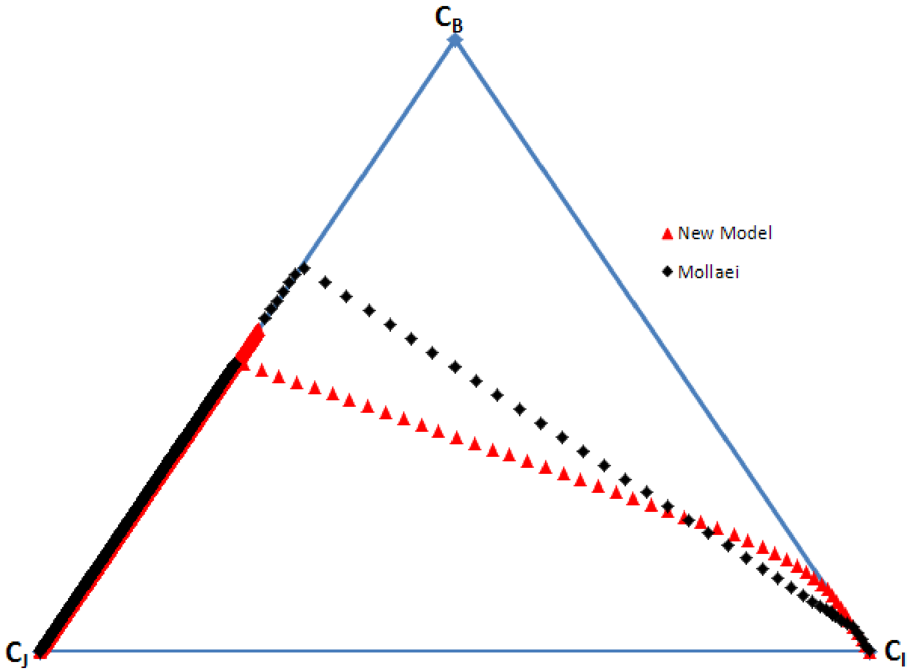

Figure 4-10. Ternary diagram (case 2) showing the correct physical solution plotted in red is the path originating from $C_J = 1$, i.e left bottom corner on the triangle and ending at $C_I = 1$. The paths transition from slow to fast at the red point shown on the plot. Path based on Mollaei solution is plotted in black. Each point on the path travels with a specific velocity (σ)

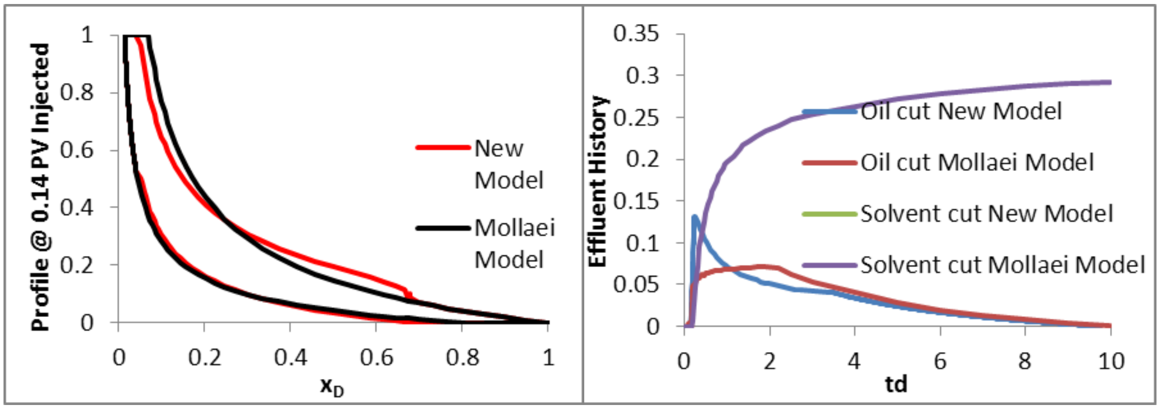

a) b)

Figure 4-11. a) Profiles mismatch when all three regions J, B and I coexist. b) The mismatch in the profile doesn't affect the solvent and oil bank breakthrough in current case. Oil cut peak from Mollaei's model is predicted to be smaller than the new model (case 2).

4.6.3 Case 3, (H_k=20)

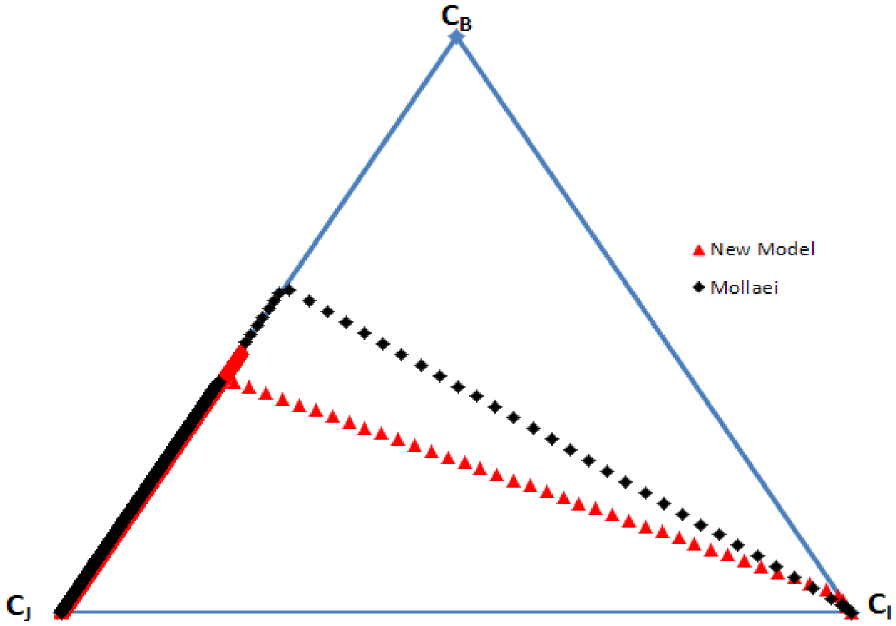

Figure 4-12. Ternary diagram (case 3) showing the correct physical solution plotted in red is the path originating from $C_J = 1$, i.e left bottom corner on the triangle and ending at $C_I = 1$. The paths transition from slow to fast at the red point shown on the plot. Path based on Mollaei solution is plotted in black. Each point on the path travels with a specific velocity (σ).

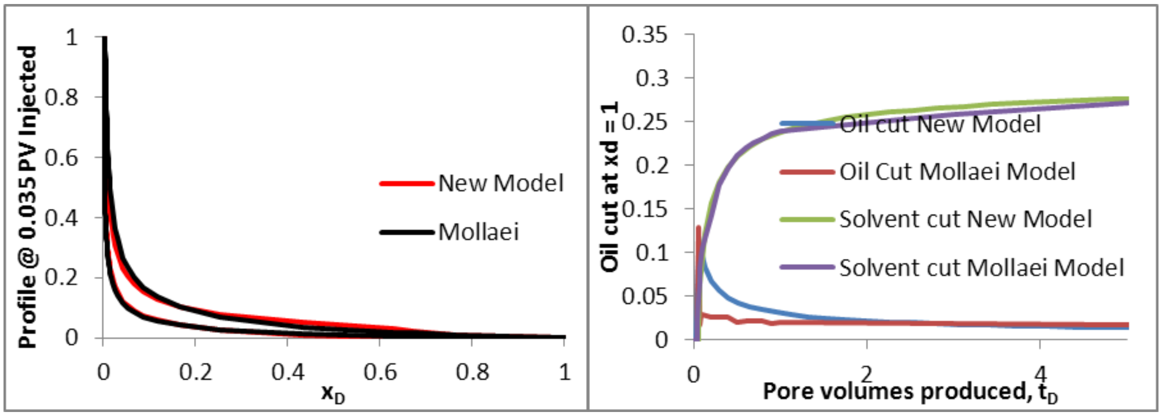

a) b)

Figure 4-13. a) Profiles mismatch when all three regions J, B and I coexist. b) The mismatch in the profile doesn't affect the solvent and oil bank breakthrough in current case. Oil cut peak from Mollaei's model is predicted to be smaller than the new model (case 3).

The pixel and window scale parameters for cases 2 and 3 are also given in Table 4-2. Regions *J*, *B* and *I* coexist for cases 2 and 3 as shown in ternary diagrams (Figure 4-10 and 12). When regions *J*, *B* and *I* coexist the coupled hyperbolic mass balance equations in the new model dictate that the two fronts cannot travel independent of each other. That Mollaei, 2011 does not account for the coupling of the mass balance equations leads to mismatch in solvent and oil bank wave profiles (Fig. 4-8 and 4-10) and results in erroneous oil cut prediction as shown in Figures 4-11b and 4-13b. The oil cut from Mollaei's model is estimated at a lower value compared to the new model for the cases with H_k greater than unity (Fig. 4-11b and 4-13b).

Layered reservoirs used in cases 2 and 3 are more heterogeneous than the reservoir used in case 1. It can be seen that as heterogeneity increases from case 1 to 3, solutions from Mollaei's model increasingly deviate from the new model. Mollaei's model is accurate when the mobility ratios of the two fronts and heterogeneity of the reservoirs is small. Smaller heterogeneity as well as mobility ratios for solvent and oil bank reduces the coupling between the mass balance equations and that makes Mollaei's model accurate. The degree of coupling between the mass balance equations increases as the heterogeneity of the reservoirs increase and that makes Mollaei's model inaccurate.

4.7 RESULTS AND VERIFICATION

Ternary plot in Figure 4-6 is the culmination of the mathematical development of the model; the rest of this section deals with the New model verification and application. Pixel scale information varies from case to case, being derived from fractional flow theory (Walsh and Lake, 1988). Miscible waves at the pixel scale are indifferent but at the window scale could be spreading waves because of heterogeneity. These are to be demonstrated in the examples.

We present several cases with varying heterogeneity and different injection and initial conditions. The main challenge of this work is to show all the diverse solutions without obfuscating complexity. The results in this section would be presented as illustrated in Fig. 4-7 (Walsh diagram) for various cases.

In this section, the results from the model will be verified against numerical simulation. The heterogeneity defined by H_k in the model (simulation model must use discrete layers) is required to be used to generate permeability field for the simulation. This ensures consistent heterogeneity for the model and simulation. If permeability field for the simulations is assumed to be log-normal then variance (v_{ln}) for such fields is directly related to Dykstra-Parsons coefficient (V_{DP}) and heterogeneity factor (H_k). These relationships are defined as (Paul et al., 1982 and Lake, 1989):

$$V_{DP}=1-\exp(-\sqrt{v_{ln}} \qquad (4.29)$$

$$\ln(H_k) = \frac{V_{DP}}{\left(1 - V_{DP}\right)^{0.2}} \tag{4.30}$$

The porosity and thickness for all the layers in the simulations are constant. The porosity and thickness could be treated as varying from layer to layer but this introduces a layer of complexity without any additional benefits.

To make verification straightforward, simulations were run first with a set of pixel scale parameters as input. The same parameters were then used in the model to calculate effluent histories for comparison. All the cases represented in this section are for heterogeneity factor H_k of 5 or equivalent V_{DP} of 0.59. At reservoir conditions the water (μ_1) and oil viscosities (μ_2) are 0.71 and 0.18 cp, respectively, and the solvent viscosity (μ_3) is 0.12 cp. These viscosities are used to calculate the pixel-scale fractional flow curves (Fig. 4-14).

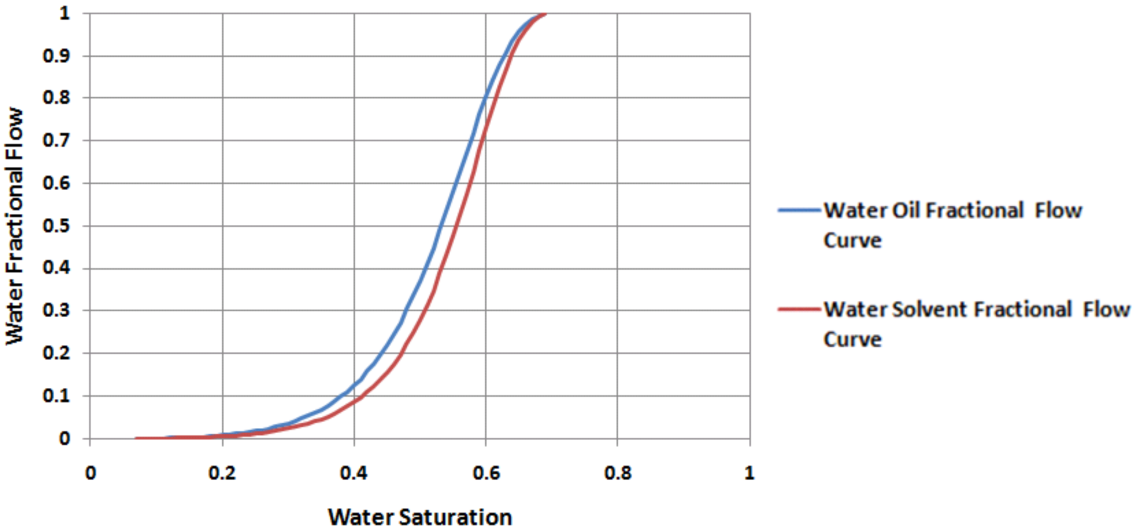

Figure 4-14. Pixel scale fractional flow curves for the verification cases.

The fact that the two fractional flow curves are close to each other does not affect the verification because the pixel scale conditions in the regions *J*, *B* and *I* are well defined as shown in the individual cases below.

4.7.1 Continuous solvent injection

Figure 4-16 shows results for a tertiary displacement case using continuous solvent injection and $f_{1J} = 0$. The initial and injection conditions are in Table 4-3 as are the mobility ratios at the back and front of the oil bank. The method to calculate the mobility ratios at the back and front of the oil bank is shown in Appendix-B. The appropriate saturation at the pixel scale for the oil bank is derived from method proposed by Walsh and Lake, 1988. Continuous tertiary miscible solvent injection causes two immiscible spreading waves at the pixel scale (Walsh and Lake, 1988). First spreading immiscible wave forms ahead of miscible wave as shown on water-oil fractional flow curve between points B and C in Fig. 4-15. Second small immiscible wave forms behind miscible wave as shown on water-solvent fractional flow curve between points J and A in Fig. 4-15. These immiscible spreading waves suggest varying saturations in the injection region (*J*) and oil bank region (*B*). Since the immiscible spreading wave in injection region (*J*) travels slowly compared to the miscible wave the saturation in region (*J*) can be assumed to be constant. On the other hand, immiscible spreading wave in the oil bank region has small variation in the saturations and thus an average constant value is chosen. This is necessary for the mass conservation equations at the window scale, which are derived assuming that there are three distinct regions of flow (*J*, *B* and *I*) with constant pixel scale saturations in each.

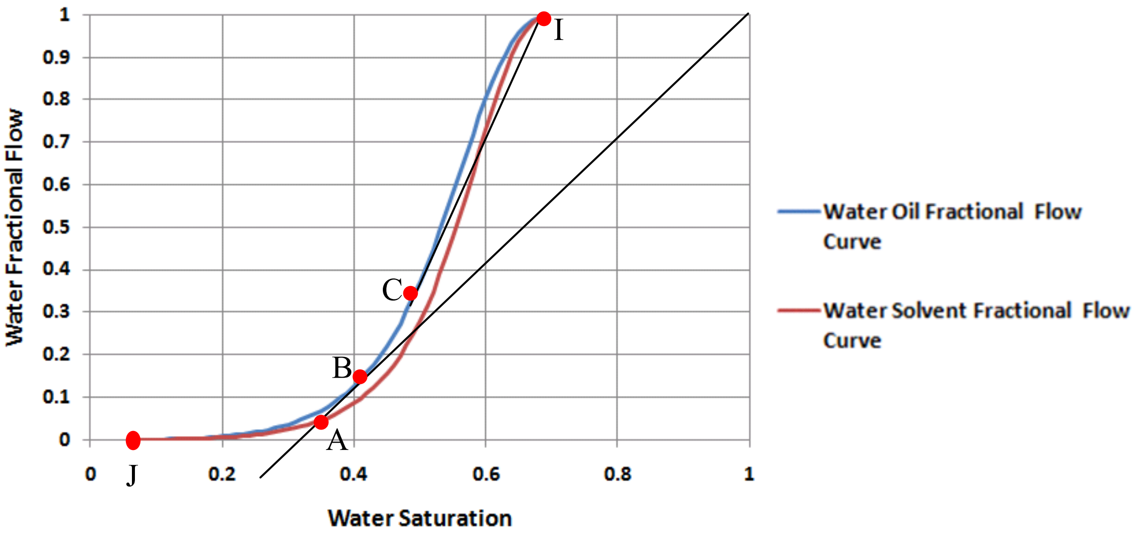

Figure 4-15. Two immiscible spreading waves form at the pixel scale for continuous solvent injection case.

Initial condition		Injection condition		
S_{1I}	f_{1I}	S_{1J}	f_{1J}	*WAG ratio* *(W_R)*
0.7	1.0	0.26	0.01	2.3

a)

	Parameters derived from pixel scale fractional flow theory				
H_k	MR_b	MR_f	S_{1B}	f_{1B}	S_{2RM}
5	3.90	1.71	0.43	0.2	0

b)

Table 4-3. a) Initial and injection conditions for continuous solvent injection b) Calculated parameters from pixel scale fractional flow theory (Walsh and Lake, 1988) based on initial and injection conditions given in a).

Figure 4-16b shows the flow profile of solvent and oil bank in the reservoir. The solvent wave given by C_J travels very fast and breaks through almost as soon as oil production starts (Fig. 4-16c) because of the high mobility ratio at the back of the oil bank. Large oil cut (about 10%) is also seen in the effluent history as soon as production starts but oil cut wanes after that significantly. This is because of the large amount of solvent production. High solvent production (Fig. 4-13c) is caused by the propensity of high mobility fluids following the path of least resistance. In turn recovering all the remaining oil from the reservoir takes many pore volumes of solvent which could render the process uneconomic (Fig. 4-16d).

The effluent history in Fig. 4-16c and 4-16d also show very good comparison between the solution obtained from the model versus numerical solution.

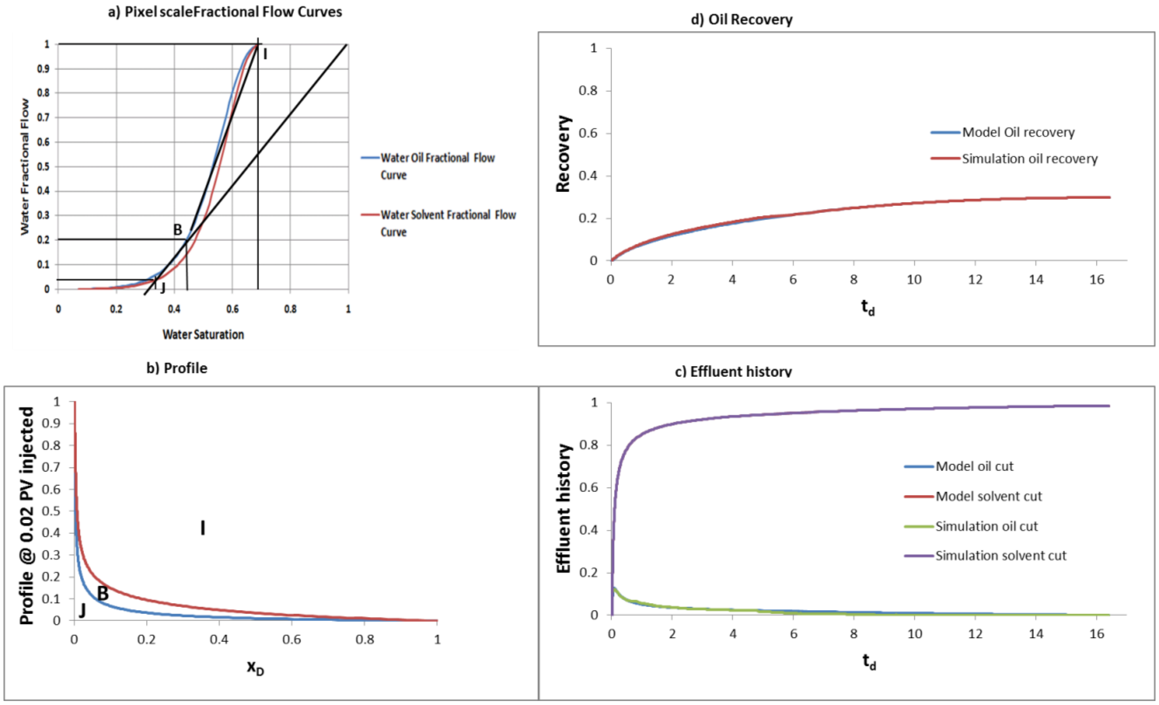

Figure 4-16. a) Pixel scale fractional flow conditions shown for continuous solvent injection. b) Flow profile for continuous tertiary solvent flood. The solvent wave travels very fast because of high solvent mobility. c) Oil bank and solvent breakthrough right at the start and oil cut falls off after that. Solvent cut jumps to a very high value of 0.8 to 0.9 very early. The model solution compares well with the numerical simulation. d) High solvent cut in the later part of production causes 16 injected pore volumes for complete oil recovery.

4.7.2 Simultaneous Water- Solvent injection

Water injection along with the solvent (SWAG) is a preferred practice as a means to lower adverse mobility ratio between the solvent and the oil. Pure solvent injection is a highly adverse mobility ratio flood but simultaneous water-solvent injection improves the mobility ratio and thus in turn increases sweep. We define a term called WAG ratio (W_R) here:

$$W_R = \frac{f_{1J}}{1 - f_{1J}} \tag{4.31}$$

4.7.2.1 Low WAG ratio case

In this case, the WAG ratio is 0.42. The mobility ratio improvement is obtained by injecting a small fraction of water with the solvent stream. This is evident if the mobility ratio values are compared for the current case (Table 4-4) vs continuous solvent injection case (Table 4-3). The mobility ratio at the back of the bank is not very adverse on account of the high solvent viscosity (0.12 cp) at reservoir conditions in this particular case. The injected pore volumes of solvent required to recover all the oil in the current case is 3.8 (Fig. 4-17d) compared to 16 for the continuous solvent injection case (Fig. 4-16d). This shows the direct impact of improving the mobility ratio even when the heterogeneity of the reservoir (H_k = 5) is same for the current case as well as the continuous solvent injection case. The comparison between simulation and the model is fairly good in this case. Small fluctuations in the solution from the numerical simulation are attributed to numerical instabilities in the solution.

Initial condition		Injection condition		
S_{1I}	f_{1I}	S_{1J}	f_{1J}	*WAG ratio* (W_R)
0.7	1.0	0.51	0.3	0.42

a)

	Parameters derived from pixel scale fractional flow theory				
H_k	MR_b	MR_f	S_{1B}	f_{1B}	S_{2RM}
5	1.05	1.51	0.47	0.23	0

b)

Table 4-4. a) Initial and injection conditions for a flood with WR=0.42 b) Calculated parameters from pixel scale fractional flow theory (Walsh and Lake, 1988) based on initial and injection conditions given in a).

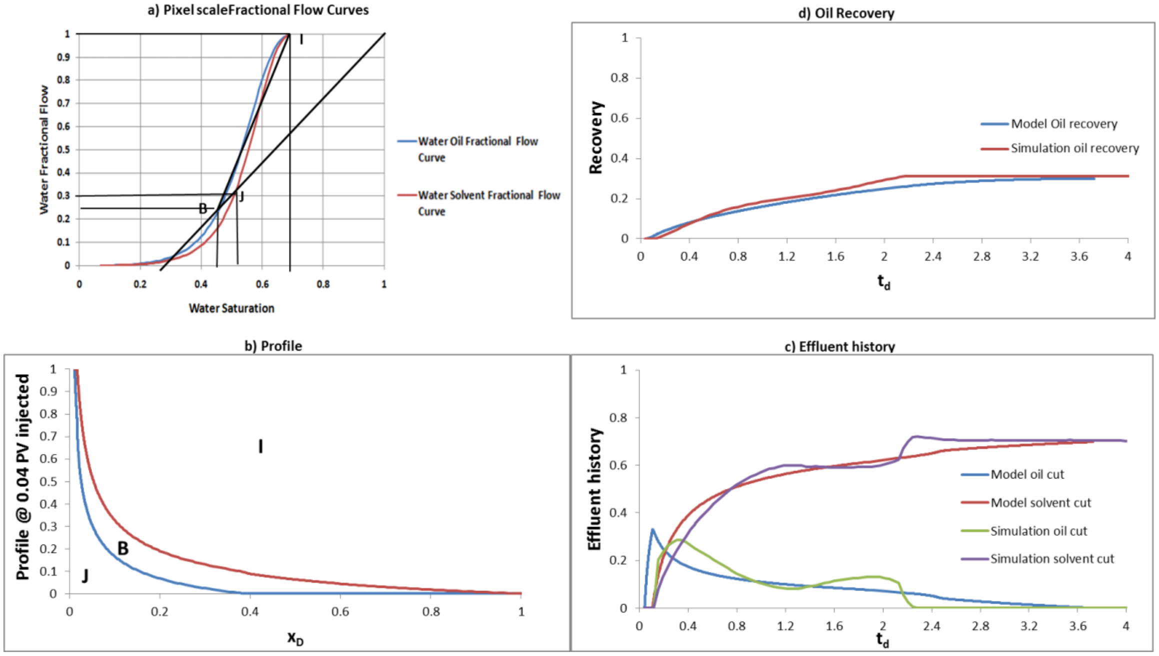

Figure 4-17. a) Pixel scale fractional flow conditions shown for W_R=0.42. b) Flow profile for tertiary small WAG solvent flood. The solvent wave travels slowly because of lowered mobility at the back of the oil bank. c) The oil bank breaks through at the start with high oil cut and then falls off. The delayed solvent breakthrough results in a larger peak oil cut. d) Ultimate oil recovery is faster compared to continuous solvent injection addition of water and improved mobility ratio. Numerical fluctuations lead to inexact match between model and simulation.

4.7.2.2 Intermediate WAG ratio case

In this case W_R is unity. Increasing the WAG ratio compared to previous case of W_R = 0.42 delays solvent breakthrough. This maybe an economic advantage because recycling of the injected solvent is delayed. Limitation of increasing the WAG ratio is evident when total pore volumes injected is compared for recovering all the oil. Current case requires 4.8 pore volumes of total injection (Fig. 4-18) compared to previous case of low WAG ratio case which required 3.8 pore volumes of total injection (Fig. 4-17).

The solution obtained from numerical simulation compares well with the model solution.

Initial condition		Injection condition		
S_{1I}	f_{1I}	S_{1J}	f_{1J}	WAG ratio (W_R)
0.7	1.0	0.56	0.5	1.0

a)

	Parameters derived from pixel scale fractional flow theory				
H_k	MR_b	MR_f	S_{1B}	f_{1B}	S_{2RM}
5	1.06	1.11	0.53	0.47	0

b)

Table 4-5. a) Initial and injection conditions for a flood with WR=1.0 b) Calculated parameters from pixel scale fractional flow theory (Walsh and Lake, 1988) based on initial and injection conditions given in a).

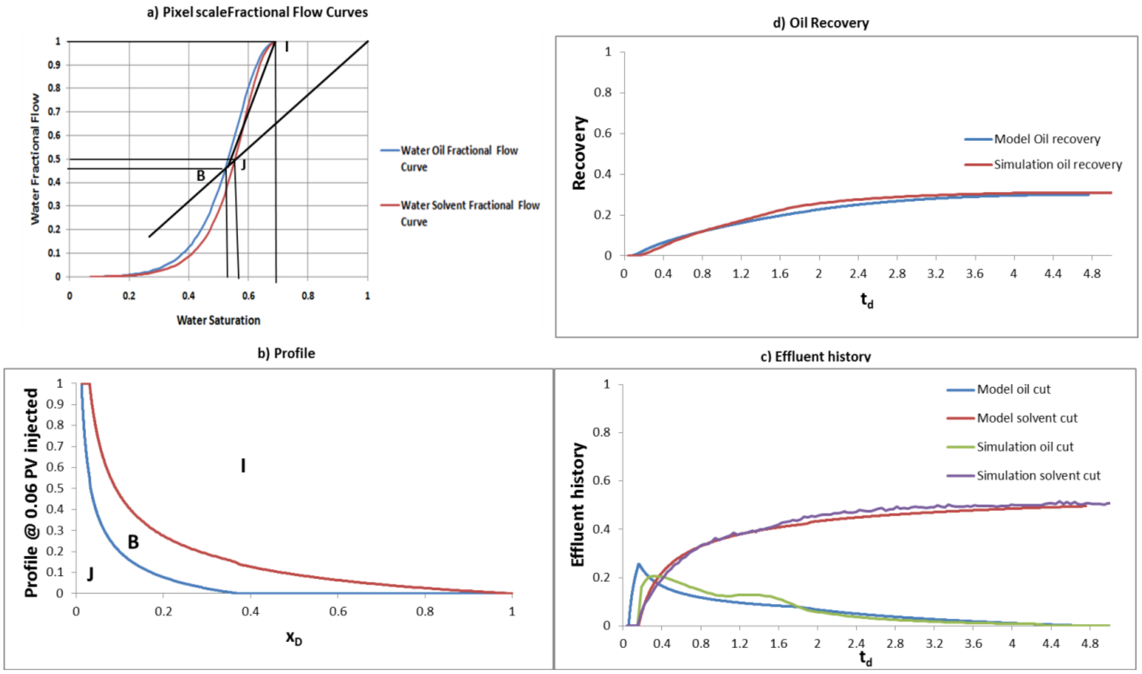

Figure 4-18. a) Pixel scale fractional flow conditions shown for W_R=1. b) Flow profile for tertiary intermediate WAG solvent flood. The solvent wave travels slowly because of the smaller mobility at the back of the oil bank. c) Oil bank breaks through at the start with large oil cut of 26% and then falls off. The solvent breakthrough is delayed resulting in a higher peak oil cut value. The peak oil cut coincides with solvent breakthrough. d) Ultimate recovery takes about 4.8 injected pore volumes which is larger than for low WAG ratio case.

4.7.2.3 High WAG ratio case

The WAG ratio (W_R) in this case is 2.7. Large WAG ratios are also detrimental to recovery because ultimate recovery takes a long time (Fig. 4-19). This effect is because the pixel scale velocity of the front and the back of the oil bank is reduced greatly (Walsh and Lake, 1988). Reduction in pixel scale velocity also leads to later breakthrough of the solvent so the optimal WAG ratio is an important aspect of the WAG flood design (Walsh and Lake, 1988). As WAG ratios increase, the peak oil cut also decreases (Fig. 4-21) because of an increase in total recovery time and waning of the oil cut tail. The model captures the simulated effluent history very well for this case too.

In all the cases shown above, the oil cut from numerical solution slightly lags the simulation solution. This slight discrepancy is because the miscible flood effects of gravity were not eliminated completely in the simulation.

Initial condition		Injection condition		
S_{1I}	f_{1I}	S_{1J}	f_{1J}	*WAG ratio* (W_R)
0.7	1.0	0.6	0.73	2.7

a)

	Parameters derived from pixel scale fractional flow theory				
H_k	MR_b	MR_f	S_{1B}	f_{1B}	S_{2RM}
5	1.06	0.91	0.58	0.71	0

b)

Table 4-6. a) Initial and injection conditions for a flood with WR=2.7 b) Calculated parameters from pixel scale fractional flow theory (Walsh and Lake, 1988) based on initial and injection conditions given in a).

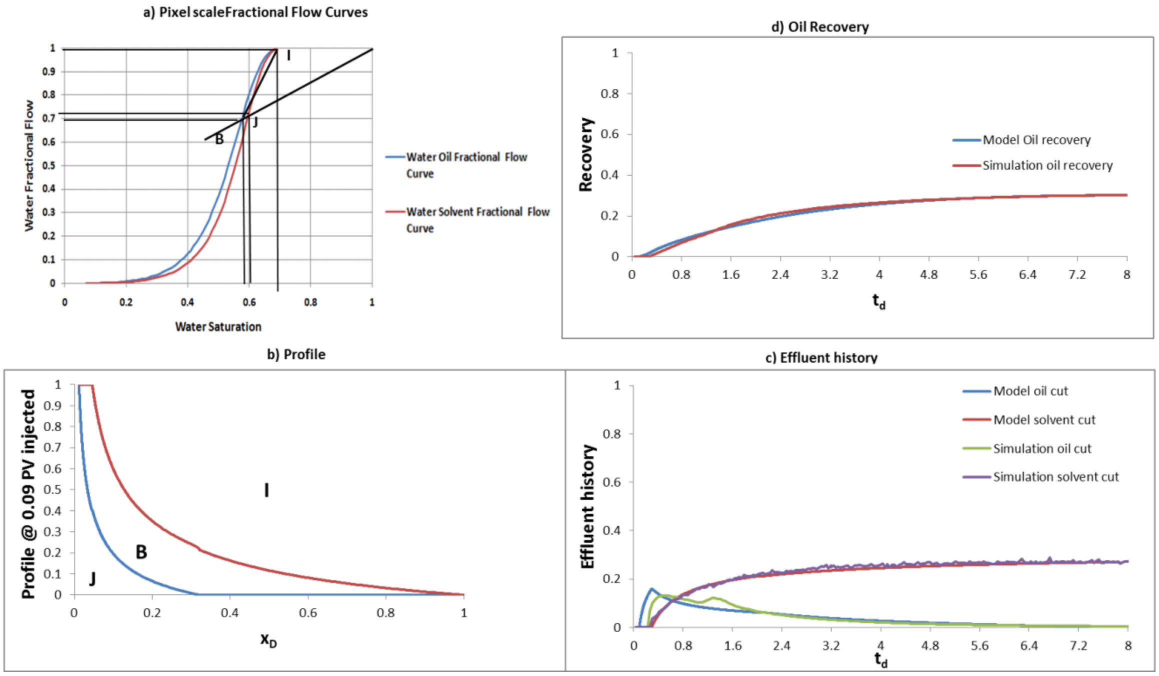

Figure 4-19. a) Pixel scale fractional flow information for W_R=2.7. b) Flow profile for tertiary high WAG ratio solvent flood. The solvent wave travels very slowly because of small total mobility at the back of the oil bank. c) Oil bank breaks through after some delay and solvent breakthrough is delayed further. The peak oil cut coincides with the solvent breakthrough. Oil cut falls off after solvent breaks through. d) The ultimate recovery takes a lot longer in this case compared to previous WAG cases because of smaller front velocities at pixel scale.

4.8 OPTIMAL WAG RATIO

Walsh and Lake (1988) define an optimal WAG ratio as the injection condition when fractional flow of oil is the highest with quick oil recovery. Ghanbarnezhad and Lake, 2010 also proved that the optimal WAG ratio from Walsh and Lake, 1988 for a homogeneous reservoir is also the same for a layered reservoir.

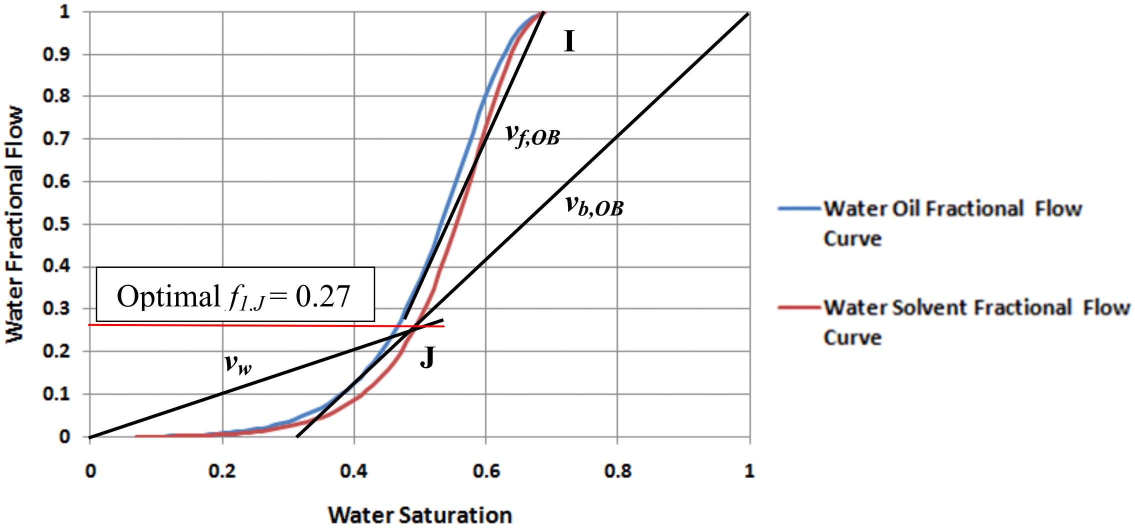

Figure 4-20. Pixel scale fractional flow curves showing the optimal injection WAG ratio W_R=0.38.

For a tertiary displacements, the optimal W_R is given by the point of intersection of miscible wave line ($v_{b,OB}$) with the water solvent fractional flow curve when it is drawn as a tangent to water oil fractional flow curve (Walsh and Lake, 1988). Based on the construction shown in Fig. 4-20 the optimal W_R = 0.39. Figure 4-21 shows a plot of peak oil cut as well as total pore volumes injected for ultimate recovery for all the tertiary flood cases discussed above.

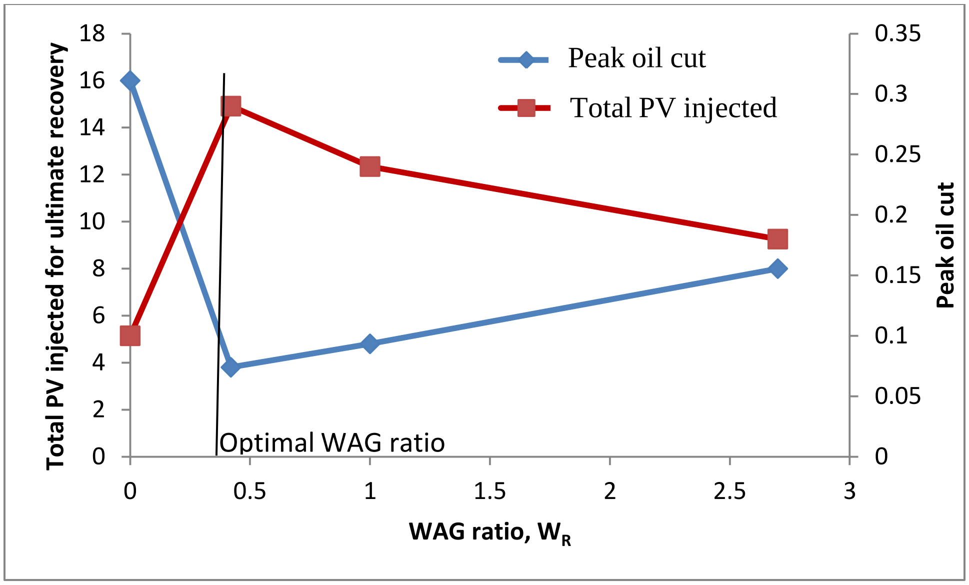

Figure 4-21. The optimal WAG ratio from the above plot falls close to W_R of 0.4. At this WAG ratio, peak oil cut is the highest and recovery time is the lowest.

The optimal W_R of 0.4 is almost equal to the optimal WAG ratio of 0.39 suggested by pixel scale fractional flow theory. The slight mismatch is because of the frequency of points on the Fig. 4-21. Thus pixel scale analysis is very robust when it comes to deciding for optimal WAG ratio for large scale reservoirs.

4.9 SECONDARY FLOOD: HIGH WAG RATIO CASE

This case demonstrates a high WAG ratio (W_R=2.7), secondary flood. Initial condition in this case differs from all the previous tertiary flood cases. The initial oil saturation is at residual water saturation of 7%. In all the tertiary flood cases the profile waves for C_I and C_J were spreading. Changing the initial condition at the pixel scale changes the nature of wave profile completely (Fig. 4-22).

Initial condition		Injection condition		
S_{1I}	f_{1I}	S_{1J}	f_{1J}	*WAG ratio (W_R)*
0.7	1.0	0.07	0.0	2.7

a)

	Parameters derived from pixel scale fractional flow theory				
H_k	MR_b	MR_f	S_{1B}	f_{1B}	S_{2RM}
5	1.06	0.1	0.58	0.71	0

b)

Table 4-7. a) Initial and injection conditions for a secondary flood with WR=2.7 b) Calculated parameters from pixel scale fractional flow theory (Walsh and Lake, 1988) based on initial and injection conditions given in a).

This case shows a combination of spreading as well as shock waves (Fig. 4-19). The mathematical solution is depicted in Fig. 4-19. It shows two velocities for one (C_I, C_J) point. Lax's condition dictates an increase in velocities downstream. Thus a shock formation is the only way a physical solution could be obtained. The shock velocity is determined by applying mass balance for either of the components i.e. solvent, oil or water.

Applying material balance across the shock for solvent, the shock velocity is given by:

$$\sigma = \frac{f_{3J}F_J|^{+} - f_{3J}F_J|^{-}}{S_{3J}C_J|^{+} - S_{3J}C_J|^{-}} \tag{4.32}$$

Physical flow profile (Fig. 4-23b) is obtained by placing the shock for the current problem. The effluent history, calculated after obtaining the physical flow profile, is compared to the solution obtained by numerical solution. Numerical simulation shows a dispersed front across the shock obtained from the model. The results match each other very well in this case too.

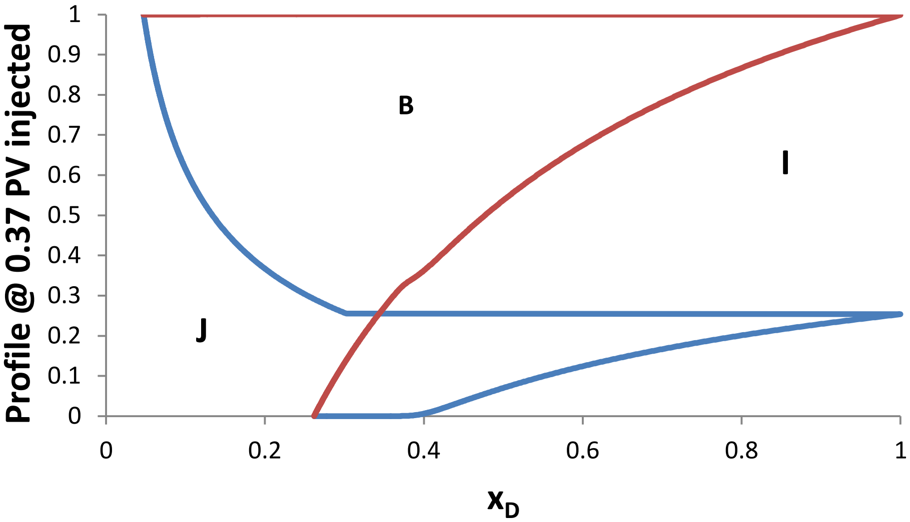

Figure 4-22. Flow profile between the boundary points show multiple velocities for one (C_J, C_I) point. This is unphysical. This is because of very small mobility ratio of 0.1 at the front of the oil bank for this case. A correct profile is obtained by placing a shock and determining the shock velocity. This is a result of a change in pixel scale initial condition.

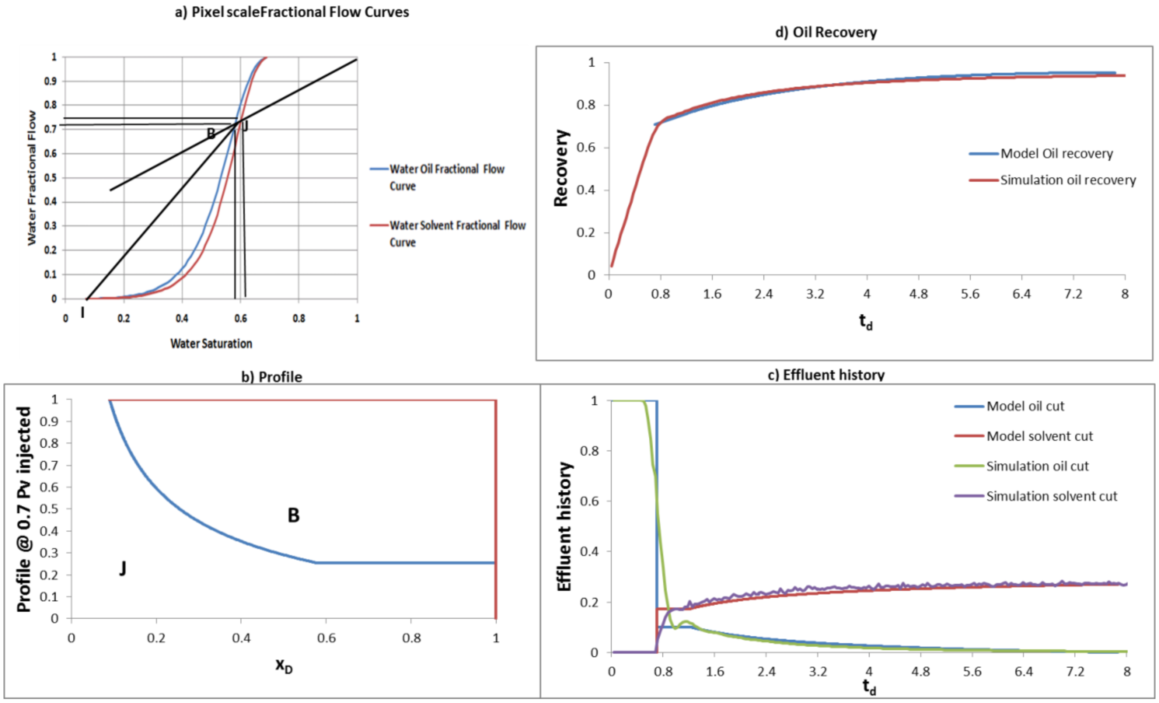

Figure 4-23. a) Flow profile for secondary high WAG ratio W_R=2.7 solvent flood. b) The solvent wave is spreading and travels very slowly because of low total mobility at the back of the oil bank. The oil bank travels as a shock because the mobility ratio ahead of the oil bank is very small. c) The oil cut profile shows an initial plateau and falls off when solvent breakesthrough. The ultimate recovery takes much longer in this case because of smaller front velocities at pixel scale. d) The recovery efficiency is high on account of secondary miscible displacement. The results match the simulation very well.

4.10 OTHER APPLICATIONS

The upscaling method outlined in this paper for miscible floods based on certain assumptions is derived by first principles. The pixel scale flow is governed by fractional flow theory for WAG floods, which suggests formation of three distinct regions of flow (Figure 4-1). Similar situation at the pixel scale is also observed for polymer as well as alkali surfactant polymer floods. Thus the method derived in this paper can be directly extended to such floods.

4.11 CONCLUSIONS

This work is primarily an exposition of a new method to predict miscible floods performance at field scale (window scale) using pixel scale fractional flow data which is one of the examples of two front displacements. The pixel scale information for upscaling depends on fractional flow theory; therefore, specific conclusions vary from case to case. The method described in the paper can be applied to a large variety of fractional flow curves attainable in practice coupled with heterogeneity. It will yield trends between reservoir performance and properties. The new model, when applied to predict and compare reservoir performance, will yield information about reservoir heterogeneity and mobility ratios. This information will yield quantitative reservoir sweep. This model thus can be used as a screening tool for predicting effectiveness of miscible floods.

This analyses when oil and solvent are miscible with each other without dispersion yield following novel contributions:

1) General method of characteristics honors all the pixel scale information obtained from fractional flow theory. It works for arbitrary fractional flow curves, WAG ratios and initial conditions.
2) The upscaling method couples reservoir heterogeneity with pixel scale information.
3) The method accounts for the interactions between the two fronts which form for tertiary and secondary miscible WAG displacements. This interaction thus far has not been accounted for at window scale.

CHAPTER 5

Lost Pore Volume: Secondary and Tertiary Floods

Primary recovery in oil fields is followed by secondary and tertiary recovery. Fluids, such as brine and gas, when injected push the remaining oil out of the reservoir during secondary recovery. Secondary recovery is followed by tertiary recovery phase where fluids, such as miscible gases (CO_2) and polymers are injected to increase the recovery efficiency. Fluids, such as brine and gas, finger and channel through the reservoir often because of their high mobility and reservoir heterogeneity that leaves parts of the reservoir unswept. Fluids like polymer solutions are often injected in the reservoir to decrease their mobility in turn displacing the oil from previously unswept parts of the reservoir. Even in such favorable displacements, reservoir heterogeneity leads to less than perfect ultimate sweep efficiency.

Secondary and tertiary floods are further classified as immiscible and miscible floods. Secondary immiscible displacement, such as waterfloods have been studied by Buckley-Leverett (1942) at pixel scale (fine scale) and at field scale using streamline simulation. Such displacements are characterized by saturation moving as spreading and shock waves, capillary pressure being neglected. The spreading wave part of the displacement travels slowly in comparison to the shock wave. Such displacements at the window scale (reservoir scale) can be treated as segregated flow with two regions. Region J is where injected water and Region I is where the resident oil flows (Figure 5-1). Such flow can be modeled (Mollaei, 2011) at the reservoir scale by extending Koval's theory (1963). Secondary miscible displacements, such as gas floods have been studied by Koval (1963) at the window scale. Koval (1963) model also assumes segregation between the two miscible components (oil and miscible solvent (gas)).

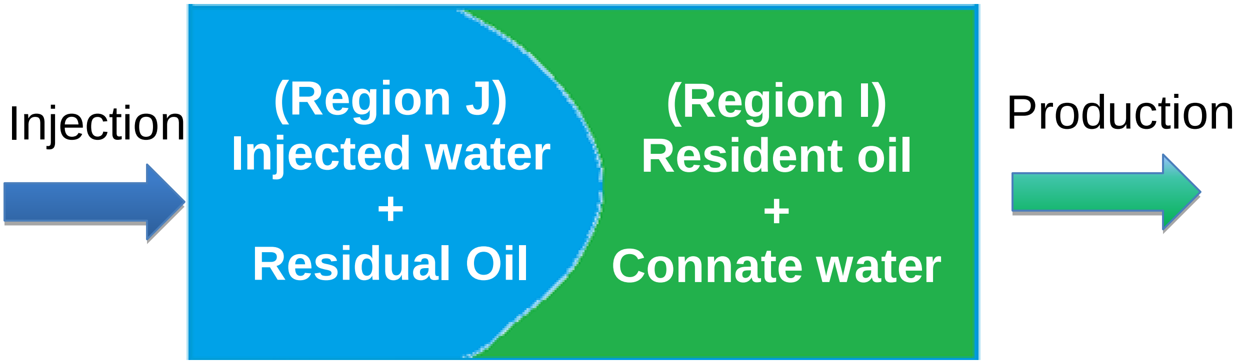

Figure 5-1. Schematic showing window scale flow behavior for secondary floods such as water and gas floods. Segregated flow is represented as a single front in the reservoir separating region J from I.

Tertiary displacements, such as polymer floods and water alternating gas floods (WAG) have been studied by several researchers at the pixel scale. A WAG flood at pixel scale is characterized by a combination of shock and spreading waves depending on water to gas ratios (Walsh and Lake, 1988). Polymer floods at the pixel scale are also characterized by a combination of shock and spreading waves (Patton et al., 1971). Such displacements at the window scale are treated as segregated flow with three regions (Figure 5-2). Region J is where injected solvent and water flows, Region B is where banked up oil and water flows while Region I is where water flows with remaining oil to secondary floods.

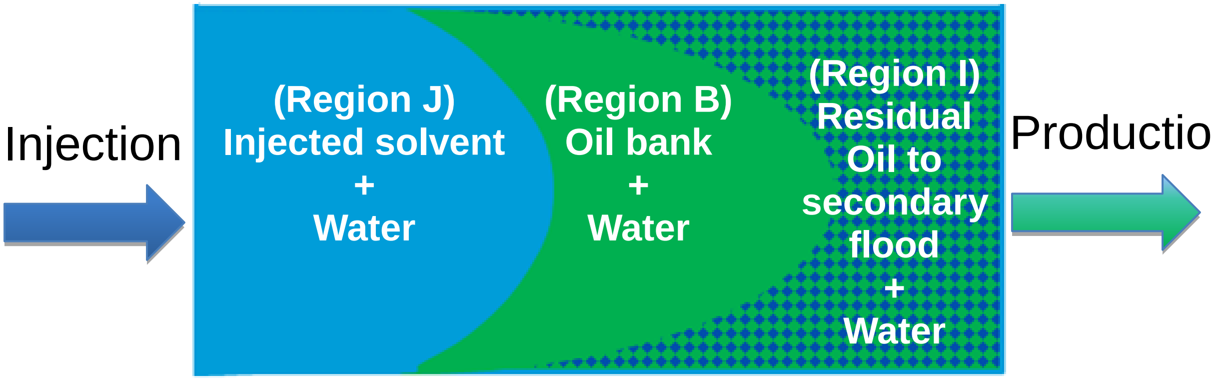

Figure 5-2. Schematic showing window scale flow behavior for tertiary floods such as miscible WAG, polymer, surfactant and ASP floods. Segregated flow is represented as two fronts in the reservoir separating Region B from Regions J and I.

While viscous fingering and channeling because of unfavorable mobility and heterogeneity during the two displacement phases (secondary and tertiary) in a field life can be upscaled by assuming flow to be segregated into different regions. None of the models so far try to incorporate the pore volume, which always stays unswept during displacement processes again because of unfavorable mobility ratio and heterogeneity. We call the unswept fraction of the total pore volume as lost pore volume (LPV). Inversely, this is also directly related to the ultimate volumetric sweep efficiency. Number of secondary and tertiary flood simulations performed during the research work shows existence of lost pore volume (LPV). This chapter deals with the formulation and real world applicability and use of the upscaling method under the segregated flow assumption that also incorporates the ultimate sweep efficiency as an additional parameter for both secondary and tertiary displacements.

5.1 MODEL DEVELOPMENT FOR SECONDARY DISPLACEMENTS

Secondary floods, such as waterfloods are single front displacements. Figure 5-3 shows the fluid distribution along with the front travelling at the pixel scale for such floods (Buckley-Leverett, 1942). The model integrates the local scale information (Mobility ratio (M) and local front velocity ($v_{\Delta S}$)) along with the heterogeneity factor (H_K) from window scale.

5.1.1 Assumptions

1. The model would be developed on a 2D layered reservoir (Figure 5-3 and 5-5) with infinite correlation length in flow direction (X), which would be later extended in its application to realistic reservoirs.
2. Vertical equilibrium applies throughout thus allowing for maximum cross flow in transverse direction (Y) The assumption is same as the one used in previous chapter.
3. The fluids are assumed to be incompressible (Such an assumption is reasonable for oil-water and CO_2-oil systems). The rock is also assumed to be incompressible. In cases where the pressure gradients during flow are small the assumption is most accurate.
4. The reservoir is isothermal thus eliminating the need to solve energy balance equation in conjunction with mass balance equation.
5. Gravity effects are neglected in the formulation along with the spreading caused by capillary pressure.
6. For adverse mobility ratio floods, the injected fluids (water) move into high permeability regions leaving the areas with highest resistance to flow unswept.
7. The spreading wave portion on the pixel scale fractional flow curve (Figure 5-3, shown in red) travels much slower than the shock, thus the assumption of flow being segregated within the flood holds.

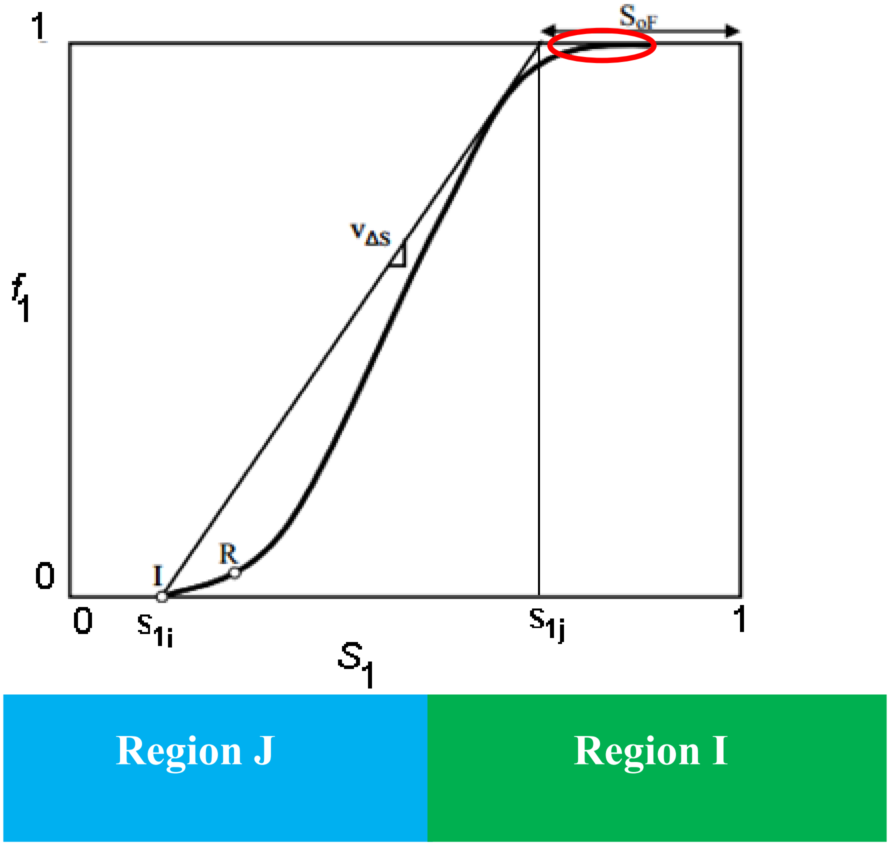

Figure 5-3. Fluid distribution in the two regions based on pixel scale fractional flow theory for water floods (Buckley-Leverett, 1942). The average water saturation in region J is S_{1J} and water saturation in region I is S_{1i}. The local front velocity is $v_{\Delta S}$.

Now consider a layered reservoir with infinite correlation length in the flow direction (x direction) and the correlation length in the direction perpendicular to bulk flow (z direction) is limited by layer thickness. The layers are arranged in the order of their interstitial velocities (r_n) i.e the layer with largest interstitial velocity is at the bottom and that with the least interstitial velocity is at the top (Figure 5-2a). The interstitial velocity (r_n) is defined as:

$$r_n = \frac{k_n}{\phi_n} \tag{5.1}$$

The dimensionless representation in terms of storage capacity(C) in Figure 5-4b is same as previous chapter. Storage capacity (C) is related to the thickness as

$$C = \frac{\sum_{i=1}^{n} \phi_i h_i}{\sum_{i=1}^{N} \phi_i h_i}, \text{ discrete or } C = \frac{\int_0^h \phi dh}{\int_0^H \phi dh}, \text{continuous} \tag{5.2}$$

where ϕ_i is the porosity and h_i is the thickness of the ith layer and H is the total thickness of the reservoir, C is the dimensionless thickness or cumulative storage capacity up to any height (h). We also define the cumulative flow capacity (F) contained in layers upto height (h) as:

$$F = \frac{\sum_{i=1}^{n} k_i h_i}{\sum_{i=1}^{N} k_i h_i}, \text{ discrete or } F = \frac{\int_0^h k dh}{\int_0^H k dh}, \text{continuous} \tag{5.3}$$

where k_i is the permeability of the ith layer. F, the cumulative flow capacity, can also be thought of as fraction of total flow in single phase unit mobility ratio flow regime through region C. The cumulative flow capacity (F) and cumulative storage capacity (C) relate to each other based on Koval theory (Figure 5-4).

$$F = \frac{1}{1 + \frac{(1-C)}{H_k C}} \tag{5.4}$$

where H_k is defined as the heterogeneity factor.

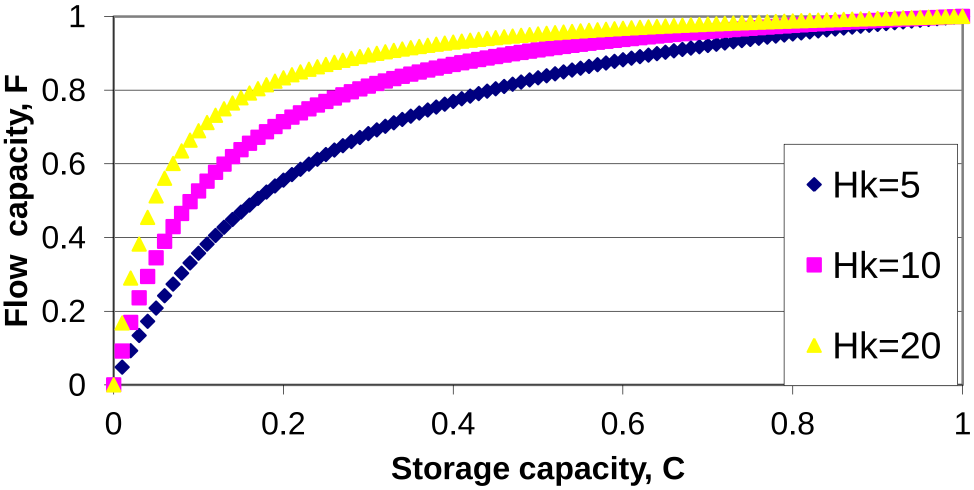

Figure 5-4. Static *F-C* curves relating flow capacity to storage capacity for different heterogeneity factors. The greater the heterogeneity, the more flow capacity in smaller fraction of the pore volume.

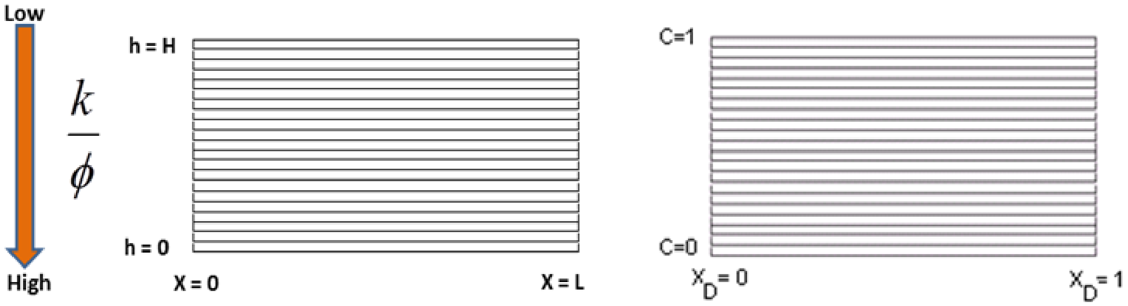

a)   b)

Figure 5-5. Representation of a layered reservoir (a) dimensional and (b) dimensionless for model development. The layers are arranged in the order of decreasing interstitial velocity from bottom to top. The heterogeneous system represented by a uniformly layered system (infinite autocorrelation length in the x-direction).

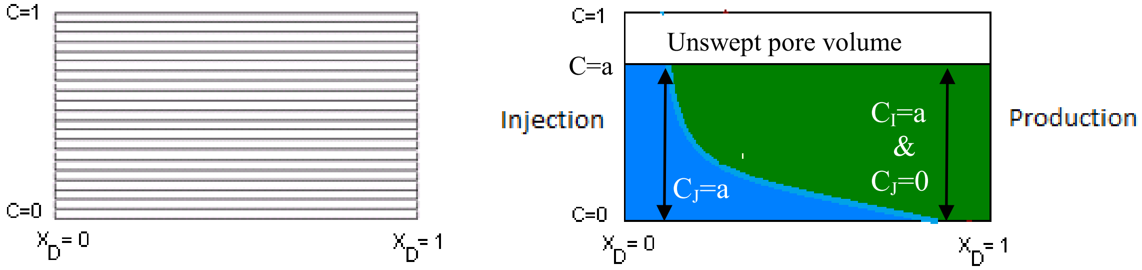

Figure 5-6. Schematic representation of single front displacement in a layered reservoir (dimensionless) (Figure 5-4) with a fraction of reservoir never swept (lost pore volume)

Figure 5-6 represents two distinct regions with different fluid flow configurations. Injected brine flows in Region *J* and resident oil flows along with the connate water in Region *I*. Oil saturation in the unswept region does not change. The pixel scale (local or fine scale) water saturation (S_{1J} and S_{1I}) and water fractional flow (f_{1J} and f_{1I}) values in regions (*J* and *I*) are marked on fractional flow curve in Figure 5-3.

Subject to above assumptions, the cross-sectionally averaged water conservation equation yields a hyperbolic equation

$$q\left(f_{1J}-f_{1I}\right)\frac{\partial F_J}{\partial X}+\bar{\phi}\left(S_{1J}-S_{1I}\right)\frac{\partial C_J}{\partial t}=0 \tag{5.5}$$

where q is the total injection rate, $\bar{\phi}$ is the average porosity of the reservoir, F_J is the fraction of the total flow in the flooded region (*J*) and C_J is the fraction of the flooded region (*J*). The dimensionless variables are

$$x_D=\frac{X}{L}; \qquad \mathrm{t_D}=\frac{qt}{\bar{\phi}L} \tag{5.6}$$

where, L is the distance between the injection and production faces. The local front velocity (Figure 5-3) from fractional flow theory is

$$v_{\Delta S}=\frac{f_{1J}-f_{1I}}{S_{1J}-S_{1I}} \tag{5.7}$$

Using the above definitions yields the dimensionless form of the water material balance equation is

$$v_{\Delta s}\frac{\partial F_J}{\partial x_D}+\frac{\partial C_J}{\partial t_D}=0 \tag{5.8}$$

Equation 5.8 is a hyperbolic mass conservation equation and could be solved using the method of characteristics if

$$F_J = f(C_J) \tag{5.9}$$

By definition

$$F_J=\frac{u_{tJ}}{u_{tJ}+u_{tI}} \tag{5.10}$$

where, u_{tJ} and u_{tI} are the total flowrates per unit width of the reservoir in regions *J* and *I* respectively. Darcy's law is applied to define these flowrates in terms of pressure gradient and fluid mobility.

$$u_{tJ}=\int_{0}^{h_J}\left(-k\left(\frac{k_{r1,J}}{\mu_1}+\frac{k_{r2,J}}{\mu_2}\right)\frac{dP}{dx}\right)\text{dh} \tag{5.11}$$

$$u_{tI}=\int_{h_J}^{h_J+h_B}\left(-k\left(\frac{k_{r1,\mathrm{I}}}{\mu_1}+\frac{k_{r2,\mathrm{I}}}{\mu_2}\right)\frac{dP}{dx}\right)\text{dh} \tag{5.12}$$

where *k* is the absolute permeability at the given point. The total fluid mobility in each region is defined as

$$\lambda_J=\frac{k_{r1,J}}{\mu_1}+\frac{k_{r2,J}}{\mu_2},\quad \text{Total fluid mobility in Region J} \tag{5.13}$$

$$\lambda_I=\frac{k_{r1,\mathrm{I}}}{\mu_1}+\frac{k_{r2,\mathrm{I}}}{\mu_2},\quad \text{Total fluid mobility in Region I} \tag{5.14}$$

Based on assumptions (2) and (5) listed above, the pressure gradient along the whole cross-section would be the same

$$\frac{\partial}{\partial y}\left(\frac{\partial P}{\partial x}\right)=0 \tag{5.15}$$

Thus the total fractional flow in region *J*, (F_J) would then be

$$F_J = \frac{u_{tJ}}{u_{tJ}+u_{tI}} = \frac{\int_0^{h_J} k\lambda_J dh}{\int_0^{h_J} k\lambda_J dh + \int_{h_J}^{h_J+h_I} k\lambda_I dh} = \frac{\lambda_J \int_0^{h_J} kdh}{\lambda_J \int_0^{h_J} kdh + \lambda_I \int_{h_J}^{h_J+h_I} kdh} \tag{5.16}$$

Equation 5.16 has two terms in the denominator compared to three for two front WAG displacements as derived in previous chapter. The total fluid mobilities in each region are constant because local saturations within each region are invariant. Thus the heterogeneity representative of the window scale is decoupled from the pixel scale mobility ratios. The individual integrals in the equation 5.16 are related to the cumulative flow capacity based on equations 5.2, 5.3 and 5.4:

$$\int_0^{h_J} kdh = \frac{\int_0^H kdh}{1+\frac{1-C_J}{H_k C_J}} \tag{5.17}$$

$$\int_{h_J}^{h_J+h_I} kdh = \int_0^H kdh \left(\frac{1}{1+\frac{1-(C_J+C_I)}{H_k(C_J+C_I)}} - \frac{1}{1+\frac{1-C_J}{H_k C_J}} \right) \tag{5.18}$$

The relationships in equation 5.17 and 5.18 are a result of relating flow capacity with storage capacity using heterogeneity factor (H_k). The relationship is described in detail in the previous chapter. Figure 5-6 depicts the ultimate volumetric sweep efficiency to be *a*, and the remaining fraction as the lost pore volume, then

$$C_J + C_I = a \tag{5.19}$$

Substitution of equation 5.19 reduces equation 5.18 to

$$\int_{h_J}^{h_J+h_I} kdh = \int_0^H kdh \left(\frac{1}{1+\frac{1-a}{H_k a}} - \frac{1}{1+\frac{1-C_J}{H_k C_J}} \right) = \int_0^H kdh \left(\frac{\frac{a-C_J}{H_k a C_J}}{\left(1+\frac{1-a}{H_k a}\right)\left(1+\frac{1-C_J}{H_k C_J}\right)} \right) \tag{5.20}$$

Substituting equations 5.17 and 5.20 into equation 5.16 would give:

$$F_J = \frac{1}{1 + \left[\frac{\lambda_I}{\lambda_J}\right]\left[\frac{1}{H_K a}\right]\left[\frac{a - C_J}{C_J}\right]\left[\frac{1}{1 + \frac{1}{H_K}\left(\frac{1}{a} - 1\right)}\right]} \tag{5.21}$$

Equation 5.21 is simplified to the following:

$$F_J = \frac{1}{1 + \left[\frac{\lambda_I}{\lambda_J}\right]\left[\frac{1}{H_K a}\right]\left[\frac{a - C_J}{C_J}\right]} \tag{5.22}$$

Simplification in equation 5.22 is accurate under the following condition:

$$\frac{1}{H_K}\left(\frac{1}{a} - 1\right) \ll 1 \tag{5.23}$$

The condition in equation 5.23 holds for the range of heterogeneity factors and ultimate sweep efficiency values. The following two conditions justify the use of condition in equation 5.23,

1. When H_K is small, the ultimate volumetric sweep would be high i.e. close to unity and assumption holds

   $$\text{when } H_K \text{ is small;} \quad a \simeq 1 \; or \; \left(\frac{1}{a} - 1\right) \simeq 0 \text{ and } \frac{1}{H_k}\left(\frac{1}{a} - 1\right) \simeq 0 \tag{5.24}$$

2. When H_K is high, the ultimate volumetric sweep would be small but the assumption still holds.

   $$\text{when } H_K \text{ is high;} \quad \frac{1}{H_k} \simeq 0 \text{ and } \frac{1}{H_k}\left(\frac{1}{a} - 1\right) \simeq 0 \tag{5.25}$$

$$M = \frac{\lambda_J}{\lambda_I} \tag{5.26}$$

where, M is the mobility ratio. The product of heterogeneity factor (H_K) and effective mobility ratio (M) by definition is called Koval factor (K).

$$K = H_k M \tag{5.27}$$

The final form for F_J in equation 5.22 using equation 5.27 is

$$F_J = \frac{1}{1+\left[\frac{1}{Ka}\right]\left[\frac{a-C_J}{C_J}\right]} \tag{5.28}$$

Equation 5.28 shows that the new model is a two parameter model that depends on Koval factor (*K*) and ultimate volumetric sweep efficiency (*a*). The model developed by Mollaei (2011) in comparison is a single parameter model that depends on Koval factor (*K*) alone (Equation 5.29).

$$F_J = \frac{1}{1+\left[\frac{1}{K}\right]\left[\frac{1-C_J}{C_J}\right]} \tag{5.29}$$

With the relationship established between F_J and C_J in equation 5.28 the water material balance shown in equation 5.8 can be solved using the method of characteristics

$$\frac{x_D}{t_D} = v_{\Delta S}\frac{dF_J}{dC_J} = v_{\Delta S}\frac{Ka^2}{\left(a+(Ka-1)C_J\right)^2} \tag{5.30}$$

The physical solution to the material balance equation depends on the appropriate end points i.e. $C_J = a$ on the upstream and $C_J = 0$ on the downstream (Figure 5-6). The velocity for each C_J can be calculated from equation 5.30. The interpretation of equation 5.30 between the appropriate end points suggests that the velocity increases from upstream to downstream thus satisfying Lax's condition. Since the velocity of each C_J is known F_J is calculated at x_D=1 for different times.

$$C_J(\mathrm{x_D}=1) = \frac{\sqrt{v_{\Delta S}Ka^2t_D}-a}{(Ka-1)} \tag{5.31}$$

$$F_J(x_D=1) = \frac{Ka}{Ka-1}\left(1-\frac{1}{\sqrt{v_{\Delta S}Kt_D}}\right) \tag{5.32}$$

The oil cut equation then is:

$$Oilcut(t_D) = (1-f_{1I})(1-F_J(x_D=1)) + \left(1-f_{1J}\right)F_J(x_D=1) \tag{5.33}$$

The recovery efficiency (N_{PD}) is:

$$N_{PD}(t_D) = \int_0^{t_D} Oilcut(t_D)dt_D \qquad (5.34)$$

The mathematical solution for the secondary flood with a single front displacement problem can be represented graphically. Such an example is shown in Figure 5-7. The input parameters required for solving the problem for the example application are given in Table 5-1a.

Initial condition		*Injection condition*	
S_{1I}	f_{1I}	S_{1J}	f_{1J}
0.3	*0.0*	*0.7*	*1.0*

a)

	Parameters derived from pixel scale fractional flow theory		
H_k	M	$v_{\Delta S}$	a
2	5	5.2	1.0

b)

Table 5-1. a) Initial and injection conditions b) Calculated parameters from pixel scale fractional flow theory (Buckley-Leverret, 1942) based on the initial and injection conditions given in a).

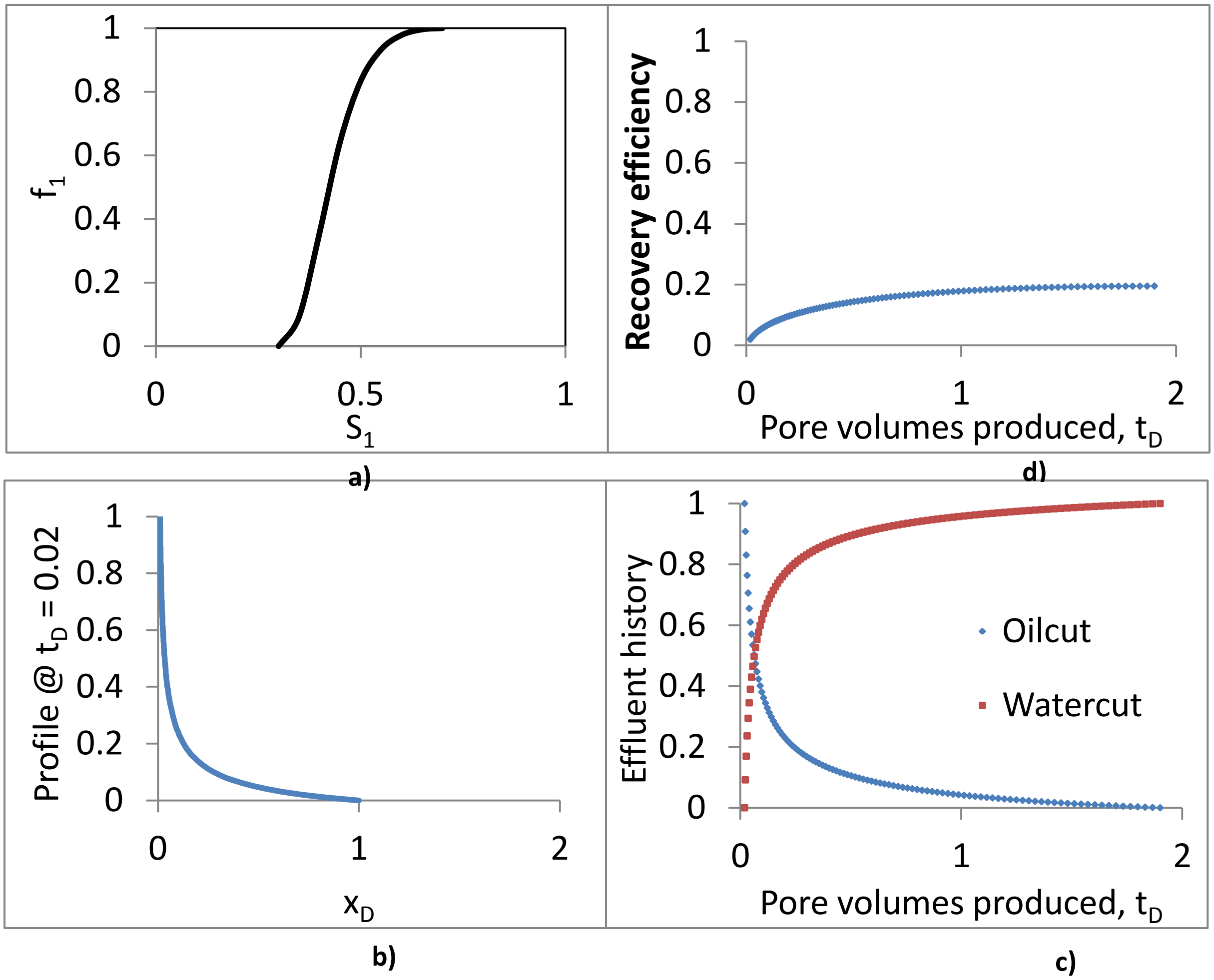

Figure 5-7. a) Pixel scale fractional flow curve for the application b) Physical flow profile in the reservoir. Each point on the path travels with a velocity that is used to calculate effluent history. c) Effluent history shows oil and water cut. Water breaks through at $t_D = 0.02$ after which the oil cut drops from unity to small values as the flood progresses. d) Recovery of 0.2 i.e total movable oil is recovered at the injected pore volume of 1.9.

Mollaei (2011) model would also give the same result for the example application as the new model. The similar solution is a result of assuming ultimate volumetric sweep efficiency to be perfect at unity. At unit ultimate volumetric sweep the new model reduces to Mollaei's (2011) model. The limitation of the new model in the current state is that it cannot be used in a predictive mode because the ultimate volumetric sweep for a reservoir is not known a priori. The heterogeneity factor for an oil reservoir is also an unknown until some displacement data (tracer data etc.) are collected. The questions then are twofold, 1) How can the new model be extended to realistic reservoirs and 2) How can the hypothesis behind the models be verified? The following section answers these questions.

5.2 MODEL EXTENSION AND VERIFICATION FOR TRUE RESERVOIRS

The model has been developed using a 2-D layered reservoir. We hypothesize that the model can still be extended to 3-D reservoir with varying degrees of heterogeneity. We also hypothesize that

1. The lost pore volume for closed patterns (Line drive, 5-spot) would decrease with time because the volumetric sweep eventually reaches the value of one. It is assumed that when oil cut reaches a plateau at small values, the time required to sweep the remaining unswept zones would be very large. Thus the sweep efficiency calculated at small oil cut can be assumed to be ultimate volumetric sweep.
2. The effects of the reservoir heterogeneity i.e. correlation structure of the permeability field corresponding to the flow direction on reservoir performance would be captured by Koval factor (*K*).
3. The effects of the well alignment in the reservoir (Line drive pattern, 5-spot pattern etc.) on reservoir performance would be captured by Koval factor and the ultimate volumetric sweep efficiency.
4. Each layer in a 2-D model can be thought of as a streamline in an equivalent 3-D model and the Koval factor allows for the flow to be distributed to each

streamline based on heterogeneity and mobility ratio. The local change in saturation along each streamline is captured by the parameter $v_{\Delta S}$, which is the local velocity derived from fractional flow theory.

5. The streamline profile for two phase flow varies with time. For 2-D layered reservoirs when each layer is treated equivalent to a streamline in a 3-D reservoir. For a layered reservoir the streamline profile does not vary with time, so in a 3-D reservoir the Koval factor indicates the average behavior over entire production life.

5.2.1 Verification steps

The outlined hypotheses are verified against various numerical simulations capturing different degrees of heterogeneity, well alignment and mobility ratios.

1. Design numerical simulation experiments with permeability field correlated in the *x*, *y* and *z* directions. Table 5-2 shows the different combinations of dimensionless correlation length combinations. Dimensionless correlation length is defined as the ratio of range of the permeability field and well spacing. The permeability field is generated using software called FFTSIM which is a stochastic generator developed by Dr. James W Jennings (Jennings et al., 2000).

	Autocorrelation lengths in different directions		
Serial No.	L_x	L_y	L_z
1	0	0	0
2	0.5	0	0
3	1	0	0
4	5	0	0
5	10	0	0

Table 5-2. continued

6	0	0.5	0
7	0	1	0
8	0	5	0
9	0	10	0
10	0.5	0.5	0
11	0.5	1	0
12	0.5	5	0
13	0.5	10	0
14	1	0.5	0
15	1	1	0
16	1	5	0
17	1	10	0
18	5	0.5	0
19	5	1	0
20	5	5	0
21	5	10	0
22	10	0.5	0
23	10	1	0
24	10	5	0
25	10	10	0

Table 5-2. Different combinations of autocorrelation correlation lengths in *x*, *y* and *z* direction for generation of permeability fields

2. The well spacing is chosen to be 1000 ft which is of the same order as often used in oil fields. The grid blocks are chosen to be at a fine scale for accurate estimation of ultimate volumetric sweep efficiency and saturation changes of the swept region.
3. The two most common well patterns (Line drive with L/D ratio of 1 and quarter five-spot) were chosen for the numerical simulation experiments. These two patterns allow the effects of flow geometry to be studied and verify if the Koval factor captures the effects of geometry on flow.
4. The end point mobility ratios are chosen to vary from 1 to 5. The mobility ratios are varied to capture the effects of local saturation changes through the pixel scale velocity parameter ($v_{\Delta S}$).
5. All simulations have the same initial irreducible water saturation. The water injection is initiated at the beginning at a constant rate. Water and oil in the simulation are incompressible and the effects of capillary spreading and gravity are neglected. All the simulations are stopped when the water cut reaches a value of 99%. At a high water cut of 99%, the volumetric sweep efficiency does not change any further.
6. The results are used at the end of simulation to calculate the ultimate volumetric sweep efficiency. The water saturation map is exported out of the simulator (CMG-IMEX). All the grid blocks with change in saturation values from the initial (upto three significant digits) are scanned. The pore volume associated with those grid blocks is calculated and called the ultimate swept pore volume.

$$Ultimate\ Swept\ Pore\ Volume = \sum_{i=1}^{Ns} PV_i \tag{5.35}$$

$$Total\ Pore\ Volume, V_p = \sum_{i=1}^{Nt} PV_i \tag{5.36}$$

$$Volumetric\ sweep\ efficiency\ (a) = \frac{Ultimate\ Swept\ Pore\ Volume}{Total\ Pore\ Volume} \tag{5.37}$$

$$Lost\ Pore\ Volume\ (LPV) = 1 - a \tag{5.38}$$

where, N_s is the number of swept grid blocks and N_t is the total number of grid blocks and PV_i is the pore volume of the i^{th} grid block. The average water saturation in the swept pore volume is also calculated

$$Average\ Water\ Saturation, S_{1_{avg}} = \frac{\sum_{i=1}^{Ns} S_{1_i} PV_i}{\sum_{i=1}^{Ns} PV_i} \tag{5.39}$$

7. The production data from the simulations is also an output for further analysis. The production data (Cumulative oil produced, water cut and total fluid production rate) is equivalent to what is available for analysis in oil fields. The new model is now applied on the production data for history matching. The oil cut is calculated from equations 5.32 and 5.33. The parameters for the history matching are shown in equation 5.40 for oil cut calculation,

$$f_o\big|_{x_D=1}(t_D) = f(t_D; K, v_{\Delta s}, a, V_p) \tag{5.40}$$

$$t_D = \frac{\int_o^t q\,dt}{V_p} \tag{5.41}$$

The history matching for water flood (single front displacement) can be performed in an excel sheet. The error is calculated at each time step and the total error is minimized to calculate optimized set of history matched parameters shown in equation 5.42.

$$\text{Total error} = \sum_{j=1}^{N} \beta_j \left(f_o(t_D)\big|_{x_D=1,\text{model}} - f_o(t_D)\big|_{x_D=1,simulation} \right)^2 = f(K, \Delta v_s, a, V_p) \quad (5.42)$$

where, N is the total time steps and β_j is the weight parameter for the j^{th} timestep. For all the history matches performed in this dissertation, $\beta_j = 1$ for all j's.

8. The parameter $v_{\Delta S}$ from fractional flow theory can be written as

$$v_{\Delta S} = \frac{1 - f_{1i}}{\overline{S}_1 - S_{1i}} \quad (5.43)$$

where, f_{1i} is the local fractional flow of water and S_{1i} is the local water saturation at $t = 0$ and $\overline{S}_1$ is the average water saturation from Welge construction.

$$\overline{S}_1 = S_{1i} + \frac{1 - f_{1i}}{v_{\Delta S}} \quad (5.44)$$

The results for average water saturation and ultimate volumetric sweep efficiency are compared between simulation and the history match from the new model. The unit slope line on the cross plots for the three parameters will verify the hypotheses made earlier in the section. The next section shows the results from the model verification analysis on all the numerical simulations.

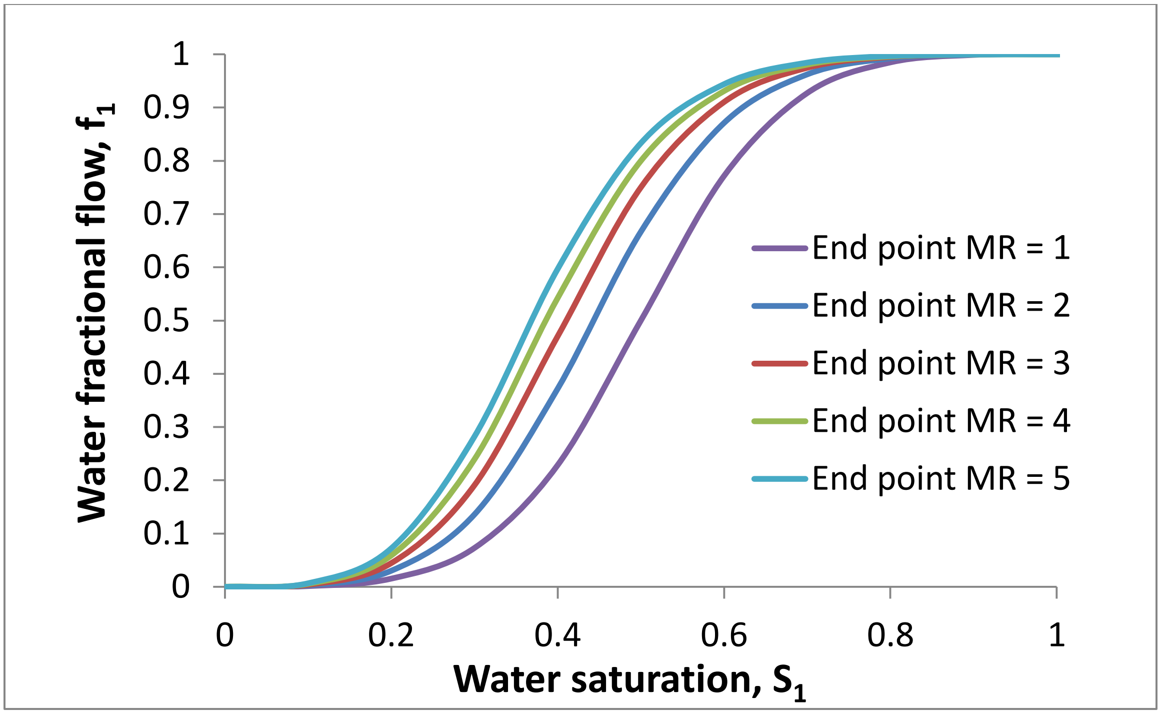

Figure 5-8. Pixel scale fractional flow curves for the verification cases. The fractional flow curves shift towards the left (water more mobile) with increasing mobility ratios.

5.3 RESULTS FOR WATER FLOODS

The main challenge of this work is to show all the solutions for varying degree of heterogeneity, mobility ratios and well patterns. The heterogeneity and saturation maps would be shown for only a few cases to explain the results. In this section, the applicability of the new model would be tested against numerical simulation.

At reservoir conditions the water viscosity is 1 cp and the oil viscosity varies from 1 to 5 cp. These viscosities were used to calculate the five pixel scale fractional flow curves (Figure 5-8). All the simulation parameters are defined below in Table 5-3.

	Well pattern	
	Line drive	Quarter five spot
Grid Size, N_x x N_y x N_z	64 x 64 x 16	128 x 128 x 16
Grid Dimensions, D_x x D_y x D_z (ft)	15.625 x 15.625 x 6.25	11.05 x 11.05 x 6.25
Porosity, ϕ	0.3	0.3
Average Permeability (*x*-direction), k_x (md)	100	100
Average Permeability (*y*-direction), k_y (md)	100	100
k_z/k_x ratio	1	1
Total Pore Volume, V_p, ft^3	30000000	29544894
Initial Reservoir Pressure, P_i , psi	4800	4800
Initial Water Saturation, S_{1i}	0	0
Injection rate, *q* (RB/day)	700	700
Production Well, BHP, psi	4000	4000

Table 5-3. Simulation parameters for line drive pattern and quarter five spot pattern

The total number of simulations based on the all the combinations of all the heterogeneous fields, mobility ratios and well patterns is 250.

5.3.1 Line Drive pattern

The first history matched case (Figure 5-9) is shown for a reservoir with high autocorrelation lengths in the flow direction (*x*-direction). The large correlation length in the flow direction along with no correlation in two other transverse directions mimics a reservoir with long channel like geologic features (Figure 5-10). The history match result (Table 5-5) shows a large Koval factor (*K*) indicating the presence of high permeability channels causing early break through.

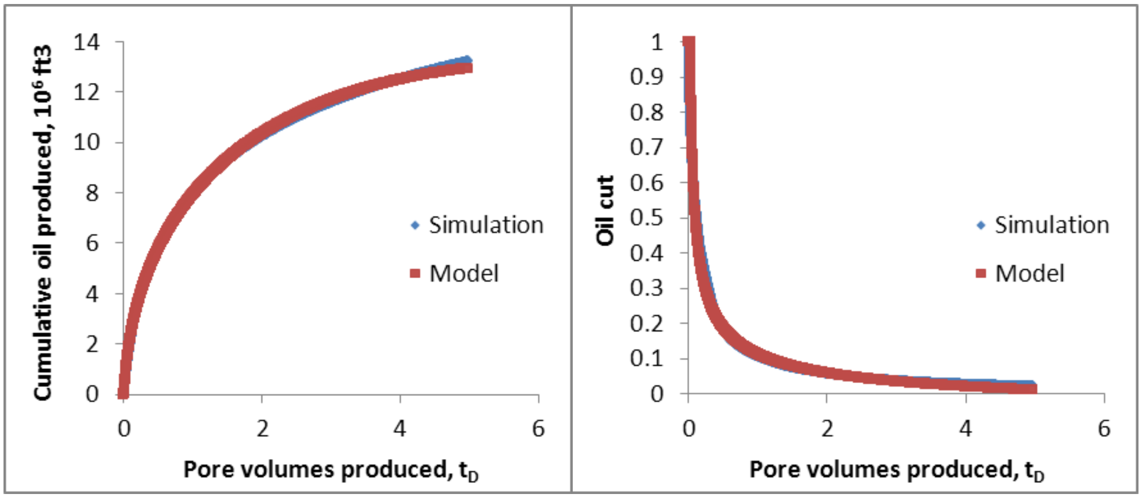

a) b)

Figure 5-9. History match between simulation and model for the cumulative oil produced in a) and oil cut in b) show good matches. The oil cut in b) falls sharply from the beginning with start of injection.

Autocorrelation length		
L_x	L_y	L_z
10	0	0

Table 5-4. Permeability field correlation lengths for the history matched case in Figure 5-9

The history matched ultimate volumetric sweep and average water saturation from the model also match the values estimated from the simulation. The pixel scale fractional flow theory suggests that the average water saturation in the swept region should be equal to ($\bar{S_1} = 1 - S_{OF}$). The average water saturation in the swept region is smaller than 0.6, which is the value calculated from fractional flow theory because of slow spreading of water into previously unswept areas (Figure 5-11).

End point mobility ratio	Koval factor, K	Ultimate sweep efficiency, a(model)	Ultimate sweep efficiency, a(simulation)	Average water saturation in the swept region, S_1(model)	Average water saturation in the swept region, S_1(simulation)	Average water saturation from fractional flow theory $(1-S_{oF})$
5	18.91	0.78	0.79	0.56	0.55	0.6

Table 5-5. History matched parameters for the case shown in Figure 5-9. The comparison between the simulation and model is also shown for ultimate sweep efficiency and average water saturation.

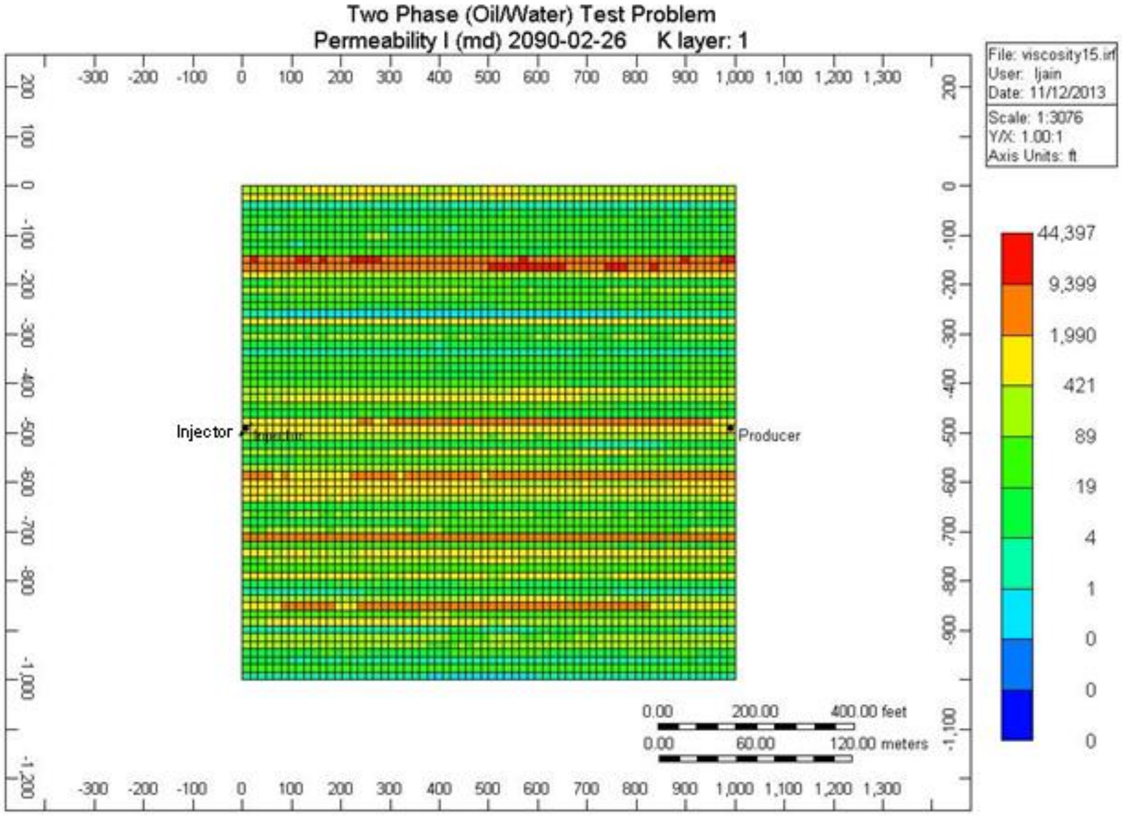

Figure 5-10. The permeability distribution in the x-y plane with large scale correlation features in the x-direction (channels).

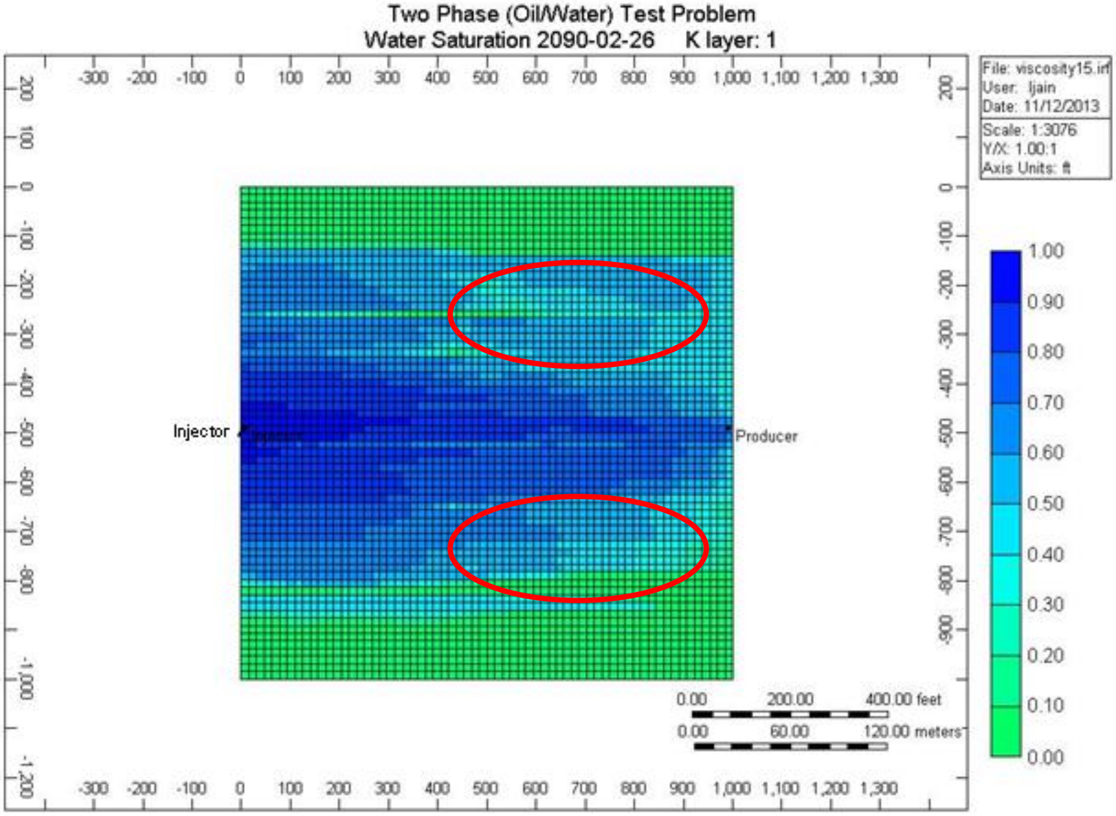

Figure 5-11. Water saturation distribution in the reservoir in an *x*-*y* plane at the end of simulation. The water saturation becomes progressively smaller (as shown by the two red ellipses) in grid blocks away from the line joining the injector and the producer. This spreading of water is caused by heterogeneity.

The second history matched case (Figure 5-12) is for a reservoir with high autocorrelation lengths in *y*-direction. The small correlation length in the flow direction along with large correlation in the other transverse direction (*y*) mimics a reservoir with long channel like geologic features (Figure 5-13) perpendicular to the principle flow direction. The history match results (Table 5-7) with small Koval factor (*K*) confirms the presence of geologic features that help spread water uniformly across the total pore volume and decelerates the water breakthrough. The history matched ultimate volumetric sweep and average water saturation from the model also match the values estimated from

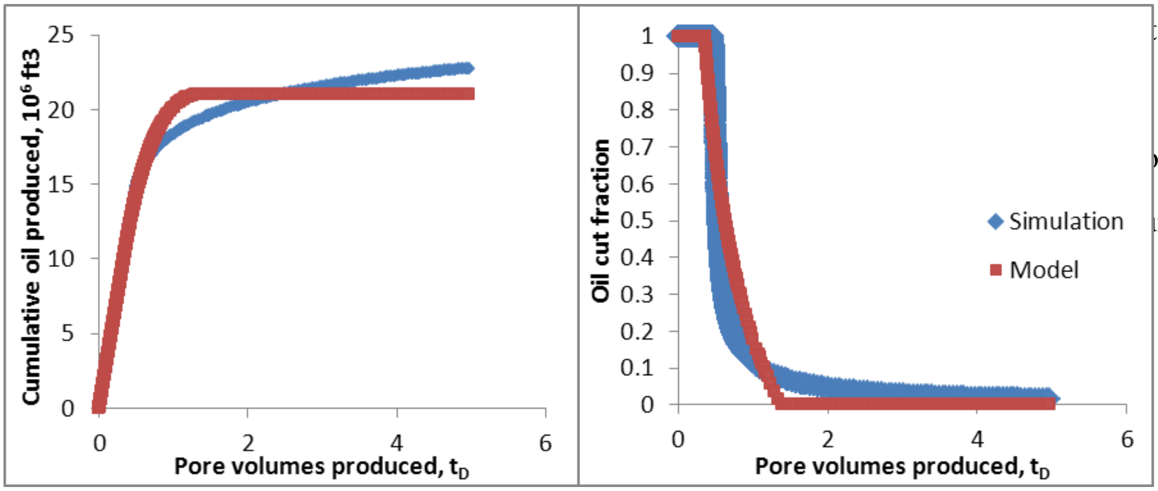

a)

b)

Figure 5-12. History match between simulation and model for the cumulative oil produced in a) and oil cut in b) show reasonably good matches. The oil cut in b) stays at a plateau in the beginning and falls sharply from the time breakthrough happens.

Autocorrelation length		
L_x	L_y	L_z
0	10	0

Table 5-6. Permeability field correlation lengths for the history matched case in Figure 5-12

End point mobility ratio	Koval factor, *K*	Ultimate sweep efficiency, a(model)	Ultimate sweep efficiency, a(simulation)	Average water saturation in the swept region, S_1(model)	Average water saturation in the swept region, S_1(simulation)	Average water saturation from fractional flow theory ($1-S_{oF}$)
5	1.96	1.0	1.0	0.71	0.76	0.6

Table 5-7. History matched parameters for the case shown in Figure 5-12. The comparison between the simulation and model is also shown for ultimate sweep efficiency and average water saturation.

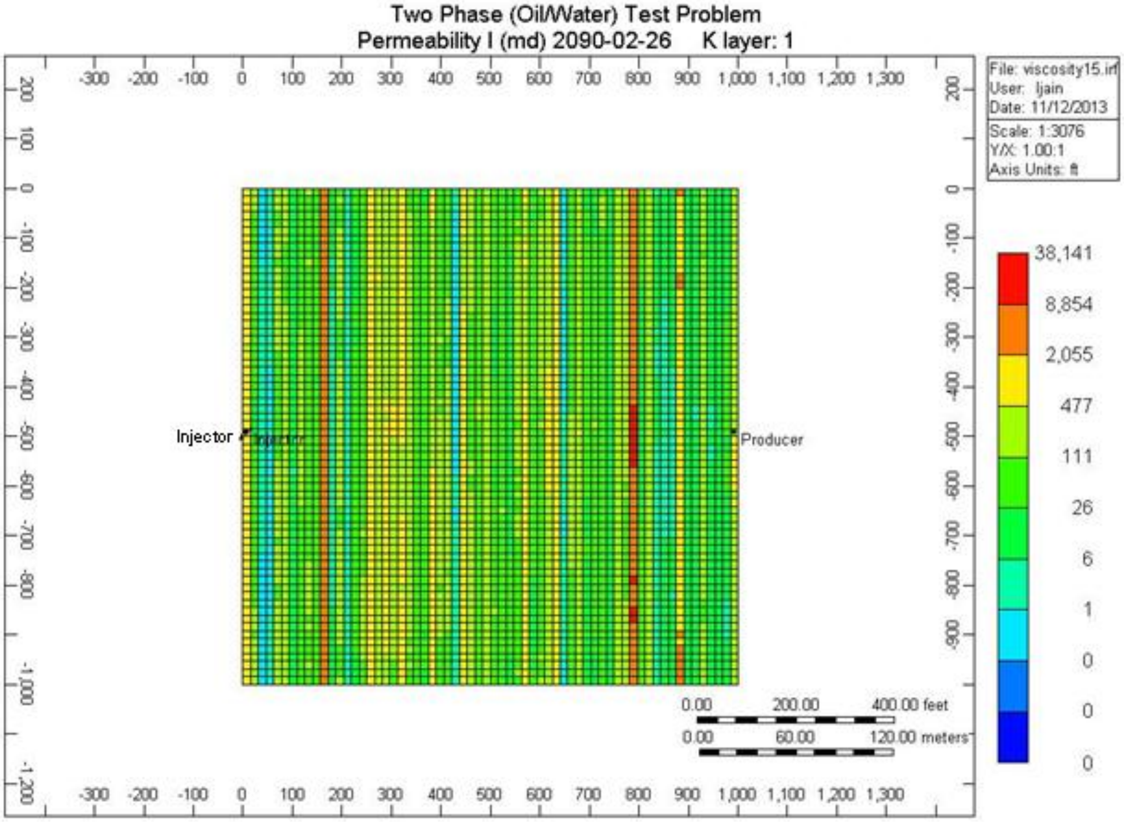

Figure 5-13. The permeability distribution in the x-y plane with large scale correlation features in the y-direction (channels).

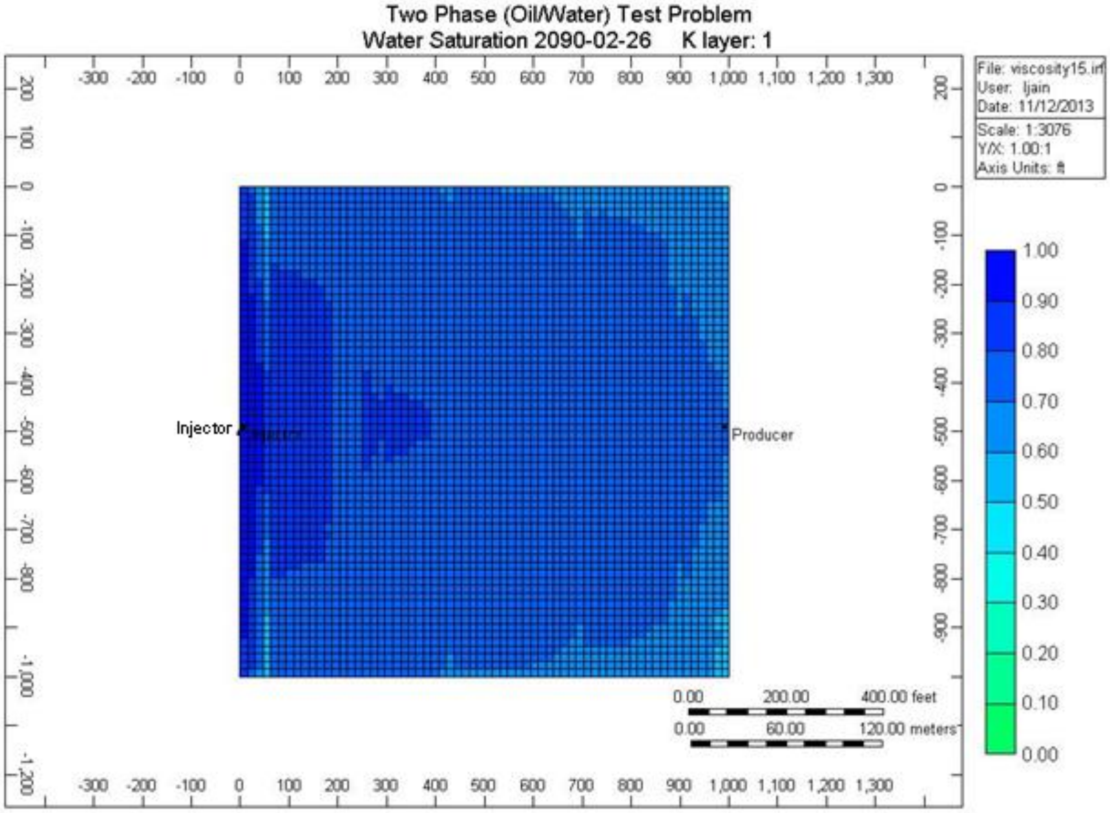

Figure 5-14. Water saturation distribution in the reservoir in an *x*-*y* plane at the end of simulation ($t_D = 4.96$). The water saturation is uniformly high across the total pore volume because of uniform spreading due to heterogeneity structure.

5.3.2 Quarter five-spot

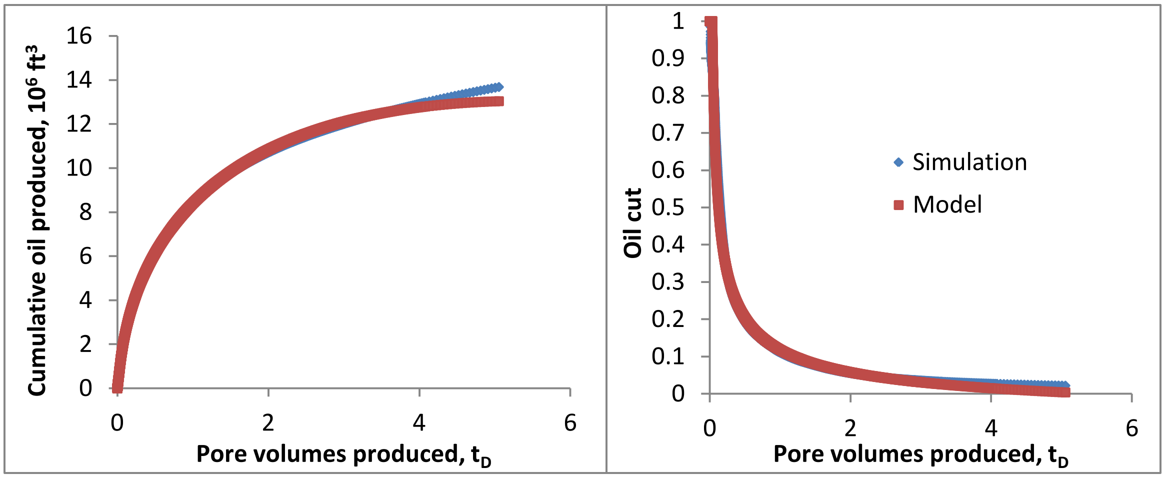

a) b)

Figure 5-15. History match between simulation and model for the cumulative oil produced in a) and oil cut in b) show good matches. The oil cut in b) falls sharply from the beginning with start of injection.

Autocorrelation length		
L_x	L_y	L_z
10	0	0

Table 5-8. Permeability field correlation lengths for the history matched case in Figure 5-15

End point mobility ratio	Koval factor, K	Ultimate sweep efficiency, a(model)	Ultimate sweep efficiency, a(simulation)	Average water saturation in the swept region, S_I(model)	Average water saturation in the swept region, S_I(simulation)	Average water saturation from fractional flow theory ($1-S_{oF}$)
5	16.18	0.76	0.78	0.58	0.57	0.6

Table 5-9. History matched parameters for the case shown in Figure 5-15. The comparison between the simulation and model is also shown for ultimate sweep efficiency and average water saturation.

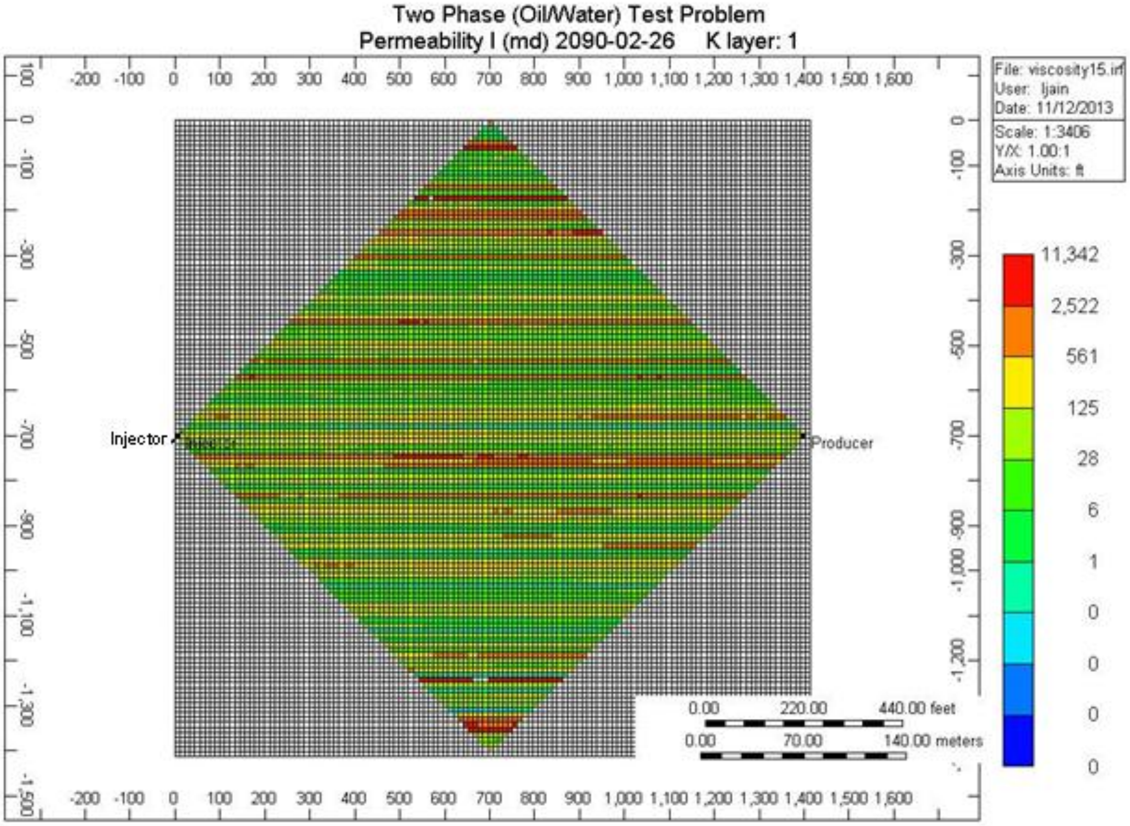

Figure 5-16. The permeability distribution in the *x*-*y* plane with large scale correlation features in the *x*-direction (channels).

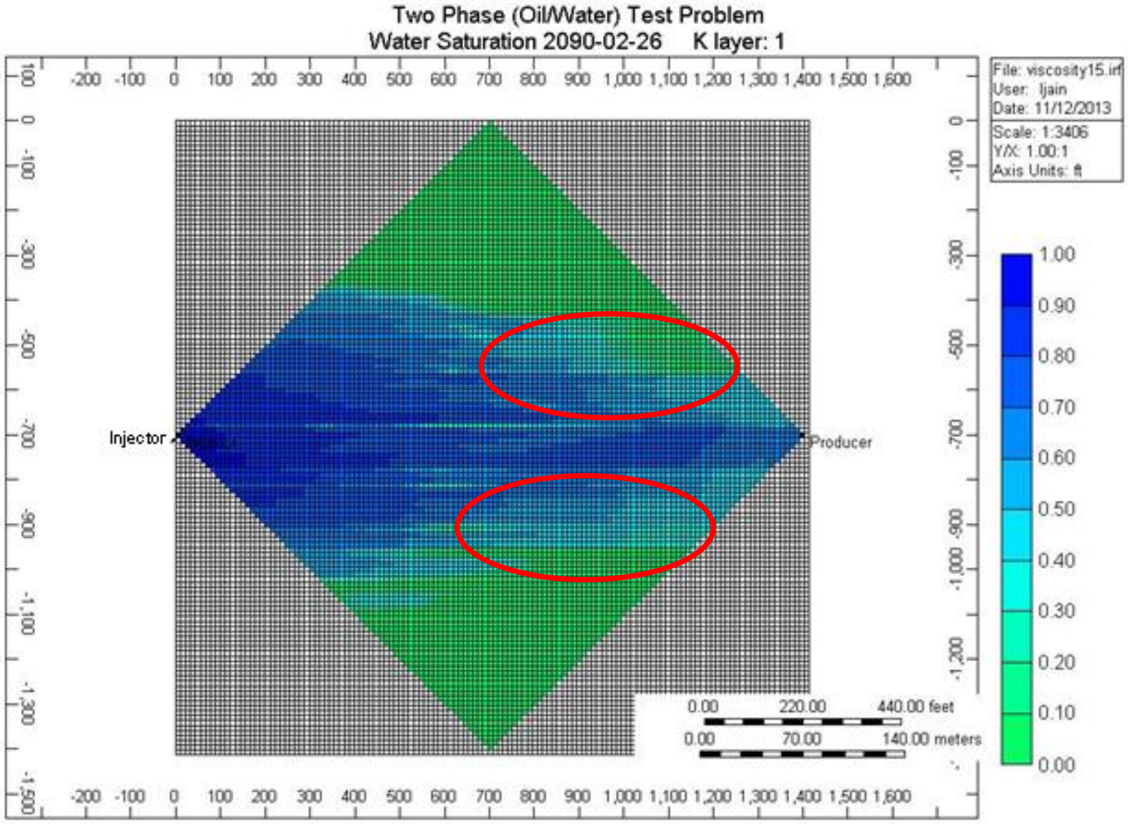

Figure 5-17. Water saturation distribution in the reservoir in an *x*-*y* plane at the end of simulation. The water saturation gets progressively smaller (as shown by the two red ellipses) in grid blocks away from the line joining the injector and the producer. This spreading of water is caused by heterogeneity.

The third history matched case for a quarter five-spot pattern (Figure 5-15) is shown for a reservoir with large autocorrelation length in flow direction (*x*-direction). The large correlation length in the flow direction along with no correlation in two other transverse directions mimics a reservoir with long channel like geologic features (Figure 5-16). Such The history match result in Table 5-9 showing large Koval factor (*K*) also confirms the presence of geological features with high permeability that would act as preferred conduit of flow for water and accelerate the water breakthrough. The history matched ultimate volumetric sweep and average water saturation from the model also match the values estimated from the simulation. The pixel scale fractional flow theory suggests that the average water saturation in the swept region should be equal to (1-S_{oF}). The average water saturation in the swept region is smaller than 0.6, which is the value calculated from fractional flow theory because of the slow spreading of water into previously unswept areas (Figure 5-17).

The difference between a line drive pattern and a five spot pattern is captured in Koval factors. The Koval factor for line drive pattern (K = 19) is larger than for the five spot pattern (K=16). The higher Koval factor for linear drive pattern means early water breakthrough in comparison to the quarter five spot pattern because breakthrough time is inversely proportional to the Koval factor. The total pore volumes for the two patterns is nearly equal so interwell distance for quarter five spot pattern is larger compared to line drive pattern. Thus, the fastest water stream would travel quicker to reach production well in the line drive pattern.

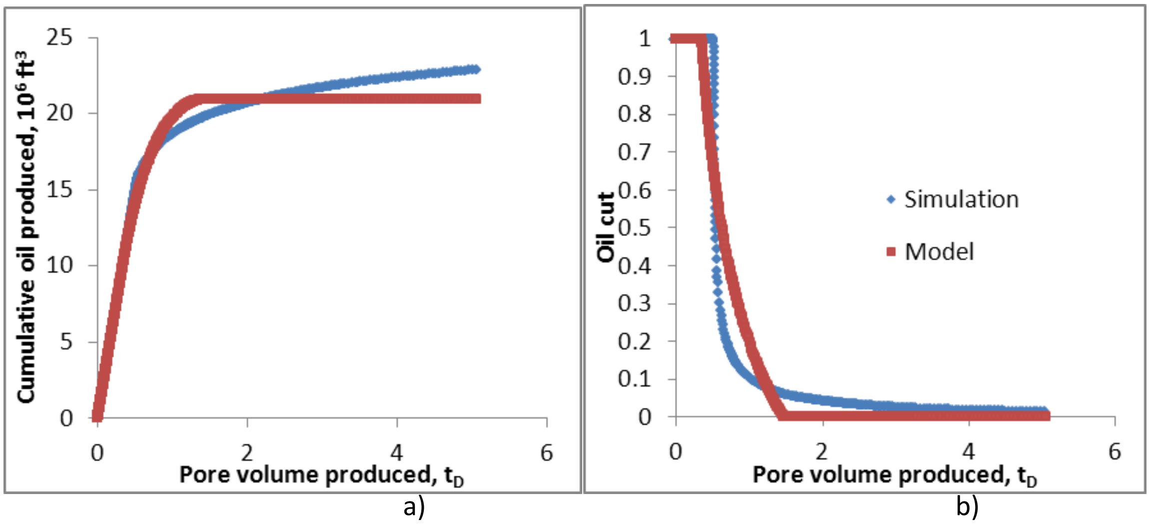

Figure 5-18. History match between simulation and model for the cumulative oil produced in a) and oil cut in b) show reasonably good matches. The oil cut in b) stays at a plateau in the beginning and falls sharply after breakthrough.

Autocorrelation length		
L_x	L_y	L_z
0	10	0

Table 5-10. Permeability field correlation lengths for the history matched case in Figure 5-18

End point mobility ratio	Koval factor, K	Ultimate sweep efficiency, a(model)	Ultimate sweep efficiency, a(simulation)	Average water saturation in the swept region, S_I(model)	Average water saturation in the swept region, S_I(simulation)	Average water saturation from fractional flow theory (1-S_{oF})
5	1.9	1.0	1.0	0.71	0.77	0.6

Table 5-11. History matched parameters for the case shown in Figure 5-18. The comparison between the simulation and model is also shown for ultimate sweep efficiency and average water saturation.

The fourth history matched case (Figure 5-18) is shown for a quarter five spot pattern reservoir with high dimensionless correlation lengths in *y*-direction. The history match result in Table 5-11 such as small Koval factor (*K*) verifies the fact that the injected water spreads perpendicular to principle flow direction (*x*). The history matched ultimate volumetric sweep and average water saturation from the model also match the values estimated from the simulation. The average water saturation in the swept region is higher than 0.6, which is the value calculated from fractional flow theory because of the uniform spreading of water into the whole pore volume (Figure 5-20).

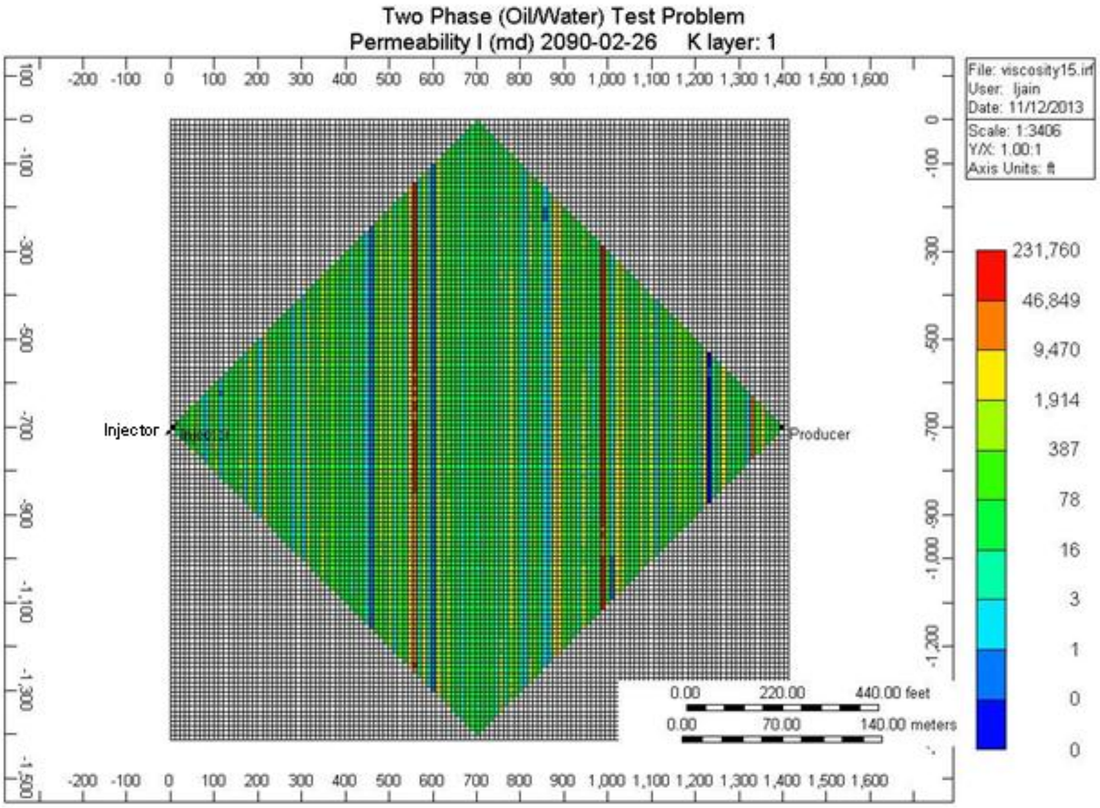

Figure 5-19. The permeability distribution in the *x*-*y* plane with large scale correlation features in the *y*-direction (channels).

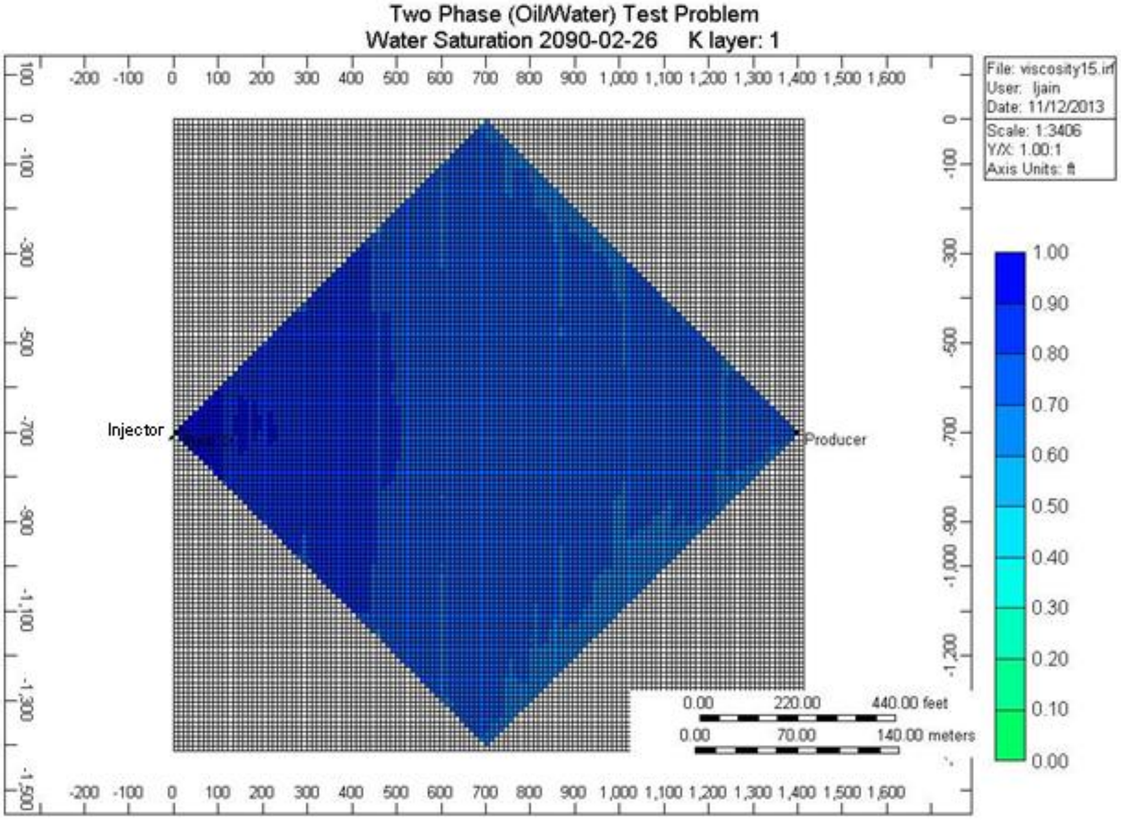

Figure 5-20. Water saturation distribution in the reservoir in an *x*-*y* plane at the end of simulation ($t_D = 4.96$). The water saturation is uniformly high across the total pore volume because of uniform spreading because of heterogeneity structure.

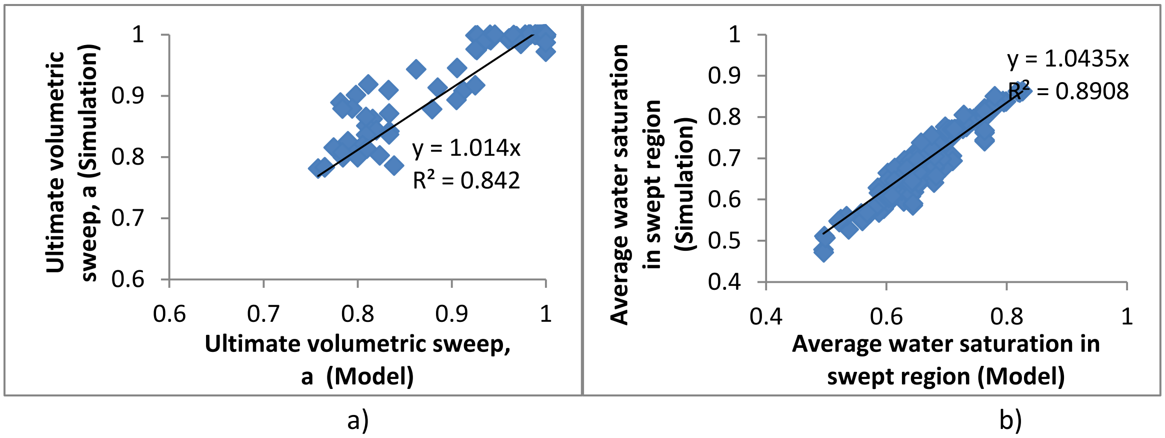

Figure 5-21. a) Ultimate volumetric sweep from the model compares very well with the simulation. b) Average water saturation in the swept regions from model also compares very well against the simulation. The results for all the verification cases from line drive and quarter five spot are shown here.

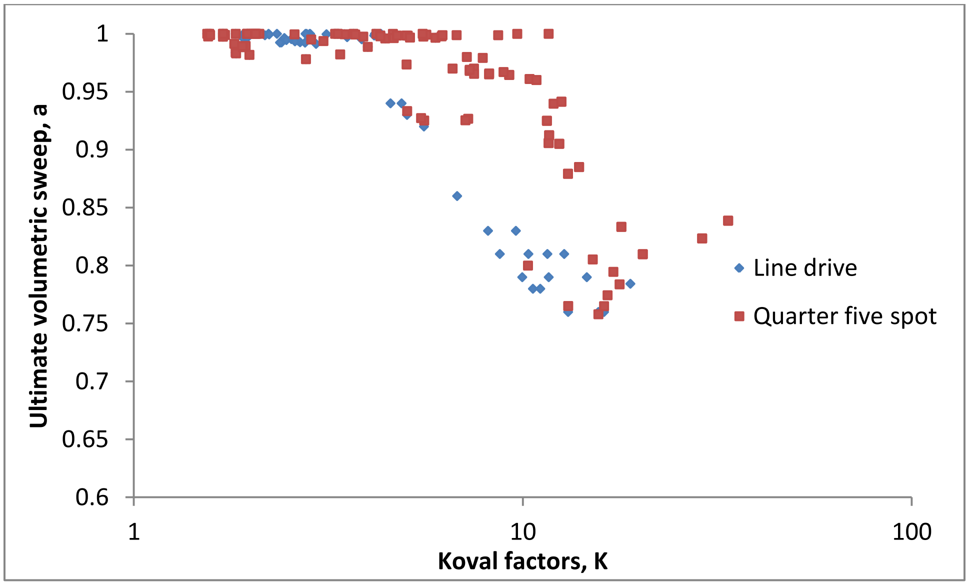

Figure 5-22. Ultimate volumetric sweep efficiency decreases as the Koval factor increases. The results for all the verification cases for line drive and quarter five spot pattern are plotted here.

The results for confined line drive and quarter five-spot patterns show that the new model with ultimate volumetric sweep is simple and effective for heterogeneous fields with varying mobility ratios. The comparison between simulation and history matched model parameters is in Figure 5-21. The ultimate volumetric sweep as well as average water saturation in the swept region matches well between simulation and the model. The ultimate volumetric sweep in all the cases never falls below 0.75 because the patterns used in the simulations are confined and the highest mobility ratio is 5. The ultimate volumetric sweep also decreases with an increase in Koval factor because it is an indicator of heterogeneity and mobility ratio (Figure 5-22). The relationship between the Koval factor and the ultimate volumetric sweep is also non-linear.

Thus we demonstrate that the Koval factor based approach combines the effects of vertical and areal sweep into one parameter called the ultimate volumetric sweep (a). The displacement sweep from relative permeability measurements is also retained in the model in the parameter called local scale fractional flow velocity ($v_{\Delta s}$). The complexity associated with the displacement sweep is reduced by treating the displacements as piston like locally. The average water saturation predicted from the model in the swept regions for the simulation cases is close to the real value because the new model accounts for the effects of lost pore volume separately. The key upgrade from the new Koval based model is replacement of a thickness with storage capacity and inclusion of the unswept pore volume.

5.4 MODEL DEVELOPMENT FOR TERTIARY TWO FRONT DISPLACEMENTS

Tertiary displacements, such as miscible water alternating gas (WAG) floods, polymer floods and ASP floods are examples of two front displacements. The theory for predicting oil recovery for isothermal two front displacements based on Koval's approach was developed by Mollaei (2011). Mollaei's (2011) model accounted for the heterogeneity as well as mobility ratio for both the fronts but not the interactions between the two fronts at reservoir scale. The interactions between the two fronts are accounted for in the new model developed in the previous chapter for WAG floods. The effects of heterogeneity and mobility ratio were also included in the model. The concept of lost pore volume would now be integrated into the model.

5.4.1 Assumptions

1. The model would be developed on a 2D layered reservoir with infinite correlation length in flow direction (*x*) which would be later extended in its application to realistic reservoirs.
2. Vertical equilibrium applies throughout thus allowing for maximum cross flow in transverse direction (*y*).
3. The fluids are assumed to be incompressible (Such an assumption is reasonable for CO_2-oil-water systems). Rock is also assumed to be incompressible. In cases where the pressure gradients during flow are small the assumption holds.
4. The reservoir is considered to be isothermal thus eliminating the need to solve energy balance equation in conjunction with mass balance equation.
5. Gravity effects are neglected in the formulation along with the spreading caused by capillary pressure.
6. For adverse mobility ratio floods, injected fluids (water or gas) move into high permeability regions leaving the areas with highest resistance to flow unswept. For tertiary gas floods with low WAG ratios (i.e. high gas content) and high mobility ratios the ultimate volumetric sweep is lower compared to polymer floods with good mobility control.

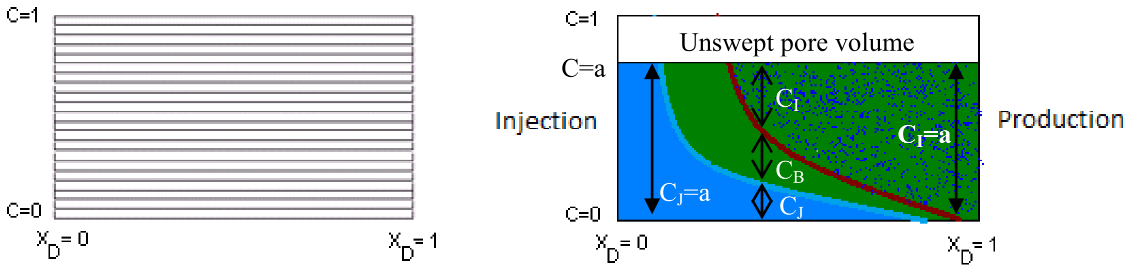

Figure 5-23. Schematic representation of two front displacement into a layered reservoir (dimensionless) with a fraction of reservoir never swept (Lost pore volume)

Figure 5-23 represents three distinct regions with different fluid flow configurations. Injected solvent flows in region *J* along with water and the residual oil, oil and water flows in region *B*, and residual oil to secondary flood and water flows in region *I*. The pixel scale (local or fine scale) water saturation (S_{1J}, S_{1B} and S_{1I}) and water fractional flow (f_{1J}, f_{1B} and f_{1I}) values correspond to regions (*J*, *B* and *I*) marked on fractional flow curves (Walsh and Lake, 1988) in Figure 5-24.

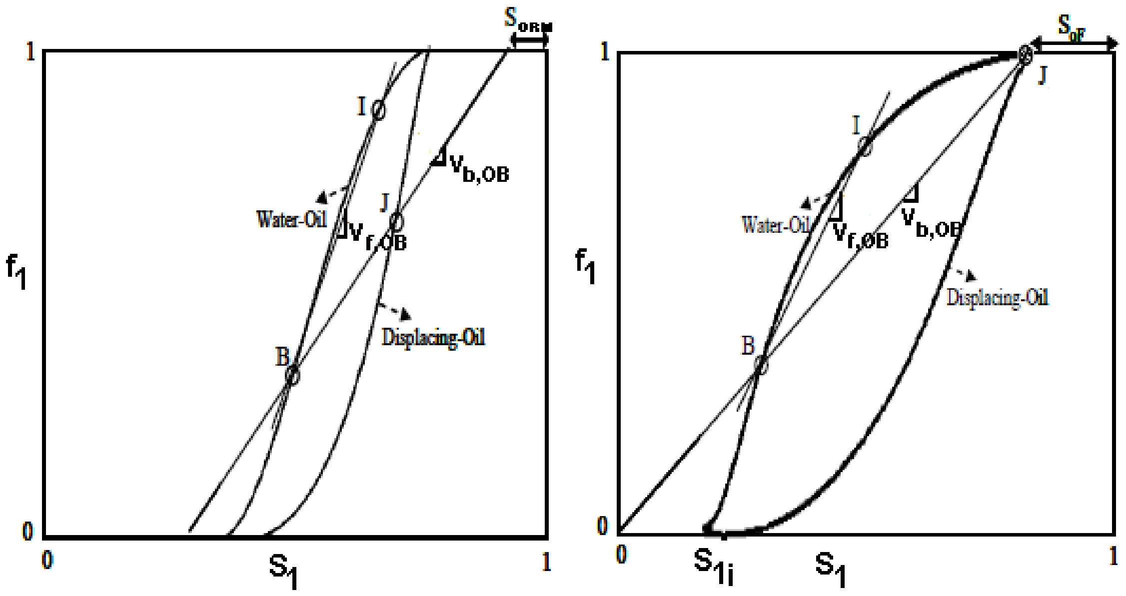

a)　　　　　　　　　　　　　　　　　　　　　　b)

Figure 5-24. a) Pixel scale fractional flow schematic for miscible WAG flood. b) Pixel scale flow schematic for polymer floods. Regions *J*, *B* and *I* are marked on both the fractional flow curves.

Subject to above assumptions, the cross-sectionally averaged mass conservations for two front displacements such as WAG and polymer floods yield a set of dimensionless hyperbolic equations (derived in Appendix-A).

$$v_{f,OB}\frac{\partial F_I}{\partial x_D}+\frac{\partial C_I}{\partial t_D}=0 \tag{5.45}$$

$$v_{b,OB}\frac{\partial F_J}{\partial x_D}+\frac{\partial C_J}{\partial t_D}=0 \tag{5.46}$$

The pixel scale velocities are defined for different floods as:

Miscible WAG floods,

$$v_{f,OB}=\frac{f_{1,I}-f_{1,B}}{S_{1,I}-S_{1,B}} \tag{5.47}$$

$$v_{b,OB}=\frac{f_{1,J}-f_{1,B}}{S_{1,J}-S_{1,B}}=\frac{1-f_{1,J}}{1-S_{1,J}-S_{ORM}}=\frac{1-f_{1,B}}{1-S_{1,B}-S_{ORM}} \tag{5.48}$$

Polymer floods

$$v_{f,OB} = \frac{f_{1,I} - f_{1,B}}{S_{1,I} - S_{1,B}} \tag{5.49}$$

$$v_{b,OB} = \frac{f_{1,B}}{S_{1,B}} = \frac{1}{1 - S_{OF}} \tag{5.50}$$

where, C_J is the fraction of total cross-section swept by injected fluid, C_B is the fraction of total cross-section swept by oil bank and C_I is the fraction of total cross-section occupied by initial oil at any given position and time as shown in Figure 5-23. F_J is the fraction of total flow in the region defined by C_J, F_B is the fraction of total flow in the region defined by C_B, and F_I is the fraction of total flow in the region defined by C_I as shown in Figure 5-23.

Subscripts 1, 2 and 3 refer to brine, oil and solvent, respectively. At the window scale shown in Fig. 4b, $f_{1,J}$, $f_{1,B}$, $f_{1,I}$, $S_{1,J}$, $S_{1,B}$ and $S_{1,I}$ are assumed to be constant. This assumption is valid because of the formation of three distinct flow regions at pixel scale (Figure 5-23). S_{ORM} is the residual oil to miscible floods (because dispersion and phase behavior) and S_{OF} is the residual oil to polymer flood. $v_{f,OB}$ is the pixel scale velocity at the front of the oil bank and $v_{b,OB}$ is the pixel scale velocity at the back of the oil bank as shown in Figure 5-23.

The equations 5.45 and 5.46 could be solved if the relationships in equation 5.51 could be defined

$$F_J, F_I = f(\mathrm{C}_{J,}\mathrm{C}_{B,}\mathrm{C}_I) \tag{5.51}$$

The similar relationships were derived in the previous chapter for a layered reservoir without incorporating the concept of lost pore volume. If the fraction (a) of the total pore volume is assumed to define the ultimate volumetric sweep efficiency (Figure 5-22) then

$$C_J + C_B + C_I = a \tag{5.52}$$

The relationships for a layered reservoir in equation 5.51 with lost pore volume incorporated are derived in Appendix-B. The fractional flow relationships at window scale used in governing equations 5.45 and 5.46 are

$$F_J = \frac{C_J}{C_J + \left[\frac{1}{MR_b}\right]\left[\frac{1}{1+(H_k-1)(C_J+C_B)}\right]C_B + \left[\frac{1}{MR_b MR_f}\right]\left[\frac{1+(H_k-1)C_J}{1+(H_k-1)(C_J+C_B)}\right]\left[\frac{1}{1+(H_k-1)a}\right]C_I} \tag{5.53}$$

$$F_I = \frac{C_I}{\left[MR_b MR_f\right]\left[\frac{1+(H_k-1)(C_J+C_B)}{1+(H_k-1)C_J}\right]\left[1+(H_k-1)\mathrm{a}\right]C_J + \left[MR_f\right]\left[\frac{1+(H_k-1)\mathrm{a}}{1+(H_k-1)C_J}\right]C_B + C_I} \tag{5.54}$$

The above relationships are further simplified by eliminating heterogeneity factor and mobility ratios because

1. The heterogeneity factor for a reservoir is a function of parameters such as, correlation structure of permeability field, well patterns and well spacing. Thus determination of heterogeneity factor which is an unknown is very difficult.
2. The mobility ratios for the two fronts are difficult to determine as the mixing of fluids in the reservoir because heterogeneity is also difficult to establish.

The simplified relationship for F_J and F_I are

$$F_J = \frac{C_J}{C_J + \frac{C_B}{K_b} + \frac{C_I}{K_f a}} \tag{5.55}$$

$$F_I = \frac{C_I}{K_f a C_J + \frac{K_f a}{K_b} C_B + C_I} \tag{5.56}$$

Mollaei's (2011) model defines F_J and F_I as

$$F_J = \frac{C_J}{C_J + \frac{(1-C_J)}{K_b}} \tag{5.57}$$

$$F_I = \frac{(1-C_I)}{(1-C_I) + K_f C_I} \tag{5.58}$$

where, K_b is the pseudo Koval factor for the chemical bank and K_f is the pseudo Koval factor for oil bank. The new model is a three parameter (Equations 5.55 and 5.56) as compared to Mollaei's model which is a two parameter model (Equations 5.57 and 5.58). The new simplified model still accounts for the interactions between the two fronts because coupling between material balance equations 5.45 and 5.46 is preserved whereas in Mollaei's model the two fronts are treated as independent. The set of material balance equations 5.45 and 5.46 can be solved using method of characteristics or MOC and the velocities for each (C_J, C_I) can be calculated based on simple wave theory.

$$v_{f,OB} \frac{dF_I}{dC_I} = v_{\mathrm{b},OB} \frac{dF_J}{dC_J} = \sigma \tag{5.59}$$

The solution method is exactly the same to that outlined in previous chapter. The limitation of the new model in the current state is that it cannot be used in a predictive mode because the ultimate volumetric sweep for a reservoir is not known a priori. The heterogeneity factor for an oil reservoir is also an unknown until some displacement data (tracer data etc.) is collected. The question then is how can the model be extended to real heterogeneous reservoirs?

5.5 MODEL EXTENSION AND VERIFICATION FOR TRUE RESERVOIRS

The model has been developed using a 2-D layered reservoir. We hypothesize that the model can still be extended to 3-D reservoir with varying degrees of heterogeneity. We also hypothesize that

1. The effects of reservoir heterogeneity i.e. autocorrelation structure of the permeability field corresponding to the flow direction on reservoir performance along with the mobility ratios would be captured by Koval factor (K_b and K_f).
2. The lost pore volume for closed patterns (Line drive, 5-spot) would decrease with time because the volumetric sweep eventually reaches the value of one. It is assumed that when oil cut reaches a plateau at small values, the time required to sweep the remaining unswept zones would be very large. Thus the sweep efficiency calculated at small oil cut can be assumed to be ultimate volumetric sweep.
3. The effects of the well alignment in the reservoir (Line drive pattern, five-spot pattern etc.) on reservoir performance would be captured by Koval factors and the ultimate volumetric sweep efficiency.
4. Each layer in a 2-D model can be thought of as a streamline in an equivalent 3-D model and Koval factor allows for the flow to be distributed to each streamline based on heterogeneity and mobility ratio. The local change in saturation along each streamline is captured by the parameters $v_{b,OB}$ and $v_{f,OB}$, which are the local front velocities derived from fractional flow theory (Walsh and Lake, 1988).
5. The streamline profile for two phase flow varies with time. For 2-D layered reservoirs when each layer is treated equivalent to a streamline in a 3-D reservoir. For a layered reservoir the streamline profile does not vary with time, so in a 3-D reservoir the Koval factor indicates the average behavior over entire production life.

5.5.1 Verification

The outlined hypotheses are verified against various numerical simulations capturing different degrees of heterogeneity, well alignment and mobility ratios for WAG and polymer floods.

1. Design numerical simulation experiments with permeability field correlated in *x*, *y* and *z* direction. Table 5-2 shows the different combinations of dimensionless correlation length combinations. Permeability field is generated using a software called FFTSIM which is a stochastic generator developed by Dr. James W Jennings (Jennings et al., 2000).
2. The well spacing is chosen to be 1000 ft which is of the same order as often used in the oil fields. The grid blocks are chosen to be at a fine scale for the accurate estimation of ultimate volumetric sweep efficiency and saturation changes of the swept region.
3. The two most common well patterns (Line drive with *L*/*D* ratio of 1 and quarter five-spot) were chosen for the numerical simulation experiments. These two patterns allow the effects of flow geometry to be studied and verify if the Koval factor captures the effects of geometry on flow.
4. All the simulations have the same initial irreducible water saturation. The tertiary displacement follows secondary displacement. Thus, the water injection is followed by tertiary gas flood or polymer flood. Water and oil in the simulation are incompressible and the effects of capillary spreading and gravity are neglected. WAG flood or polymer injection is initiated when the secondary phase water cut reaches 95% for all the simulations. The gas in all the simulations is CO_2, miscible with the oil. WAG and polymer injection cause an increase in oil cut in production stream. The oil cut increases and falls down after reaching a

peak value. It is a characteristic of tertiary WAG and polymer floods. All the simulations are stopped when oil cut drops to 1% during both types of tertiary displacements. At such low oil cut of 1%, the volumetric sweep efficiency does not change any further.

5. The results are used at the end of simulation to calculate the ultimate volumetric sweep efficiency to tertiary WAG and polymer floods. The gas saturation and polymer concentration maps are exported out of the simulator (CMG-GEM). All the grid blocks with any change in gas saturation or polymer concentration values from the initial are scanned. The pore volume associated with those grid blocks is calculated. It is called the swept pore volume for tertiary flood.

$$Swept\ Pore\ Volume\ (tertiary) = \sum_{i=1}^{Ntr} PV_i \tag{5.60}$$

$$Total\ Pore\ Volume, V_p = \sum_{i=1}^{Nt} PV_i \tag{5.61}$$

$$Volumetric\ sweep\ efficiency\ (a) = \frac{Swept\ Pore\ Volume\ (tertiary)}{Total\ Pore\ Volume} \tag{5.62}$$

$$Lost\ Pore\ Volume\ (tertiary), \left(LPV_{tertiary}\right) = 1 - a \tag{5.63}$$

where, N_{tr} is the number of swept grid blocks for tertiary flood and N_t is the total number of grid blocks and PV_i is the pore volume of i^{th} grid block.

6. The production data from the simulations is also an output for further analysis. The production data (Cumulative oil produced, oil cut and total fluid production rate) is equivalent to what is available for analysis in oil fields. The new model is now applied on the production data for history matching. The parameters for the history matching are shown in equation 5.64

$$f_o\big|_{x_D=1} = f(t_D : K_b, K_f, v_{b,OB}, v_{f,OB}, a, V_p) \tag{5.64}$$

$$t_D = \frac{\int_o^t q dt}{V_p} \tag{5.65}$$

The history matching for two-front displacements is difficult because the model requires solution to a system of hyperbolic material balance equations. An automatic history matching program was developed for tertiary floods. The error is calculated at each time step and the total error is minimized to calculate optimized set of history matched parameters shown in equation 5.66

$$Total\ error = \sum_{j=1}^{N} \beta_j \left(f_o(t_{D_j})\Big|_{\text{model}} - f_o(t_{D_j})\Big|_{\text{simulation}} \right)^2 = f(K_f, K_b, v_{b,OB}, v_{f,OB}, a, V_p)$$

(5.66)

where, N is the total number of time steps and β_j is the weight parameter for the j^{th} timestep. For all the history matches performed in this dissertation, $\beta_j = 1$ for all j's. The automatic history matching program algorithm is described in detail in Appendix C.

7. The average water saturation in the flooded region for polymer flood can be calculated from

$$v_{b,OB} = \frac{1}{\overline{S_1}} = \frac{1}{1 - S_{OF}} \tag{5.67}$$

where, $\overline{S}_1$ is the average water saturation after polymer flood. Equation 5.67 can be solved for $\overline{S}_1$

$$\overline{S_1} = \frac{1}{v_{b,OB}} \tag{5.68}$$

The results for ultimate volumetric sweep efficiency and total pore volume are compared between simulation and the history match from the new model for both the floods. The next section shows the results from the model verification analysis on all the numerical simulations.

5.6 RESULTS

The main challenge of this work is to show all the solutions for varying degree of heterogeneity, mobility ratios and well patterns. In this section, the verified of the new model would be tested against numerical simulations for polymer and WAG floods.

5.6.1 Polymer floods

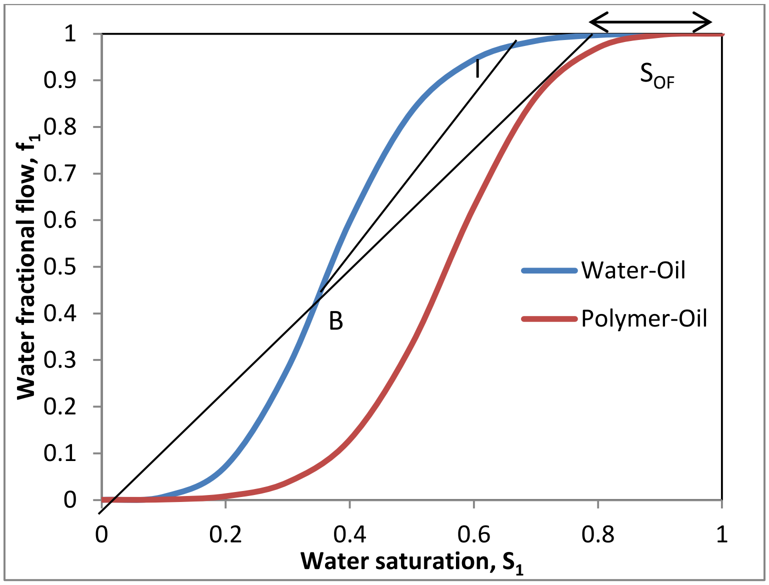

Figure 5-25. Pixel scale fractional flow curves for tertiary polymer flood.

Oil viscosity at reservoir conditions is 5 cp for all the simulated cases. The secondary flood water viscosity is 1 cp. The tertiary flood water viscosity is 10 cp (polymer injection). These viscosities were used to calculate the pixel scale fractional flow curves (Figure 5-25). The other simulation parameters are defined in Table 5-3.

5.6.1.1 Line drive pattern

The first case for a tertiary polymer flood history match is shown in Figure 5-26b. The water flood stops when the oil cut reaches 0.05 (water cut, $f_{1,I} = 0.95$) with 2.2 PV of total injection. The average water saturation in the flooded region at the end of water flood estimated from the new model for secondary flood is 0.56. Thus the initial condition before the polymer injection starts is $f_{1,I}$ = 0.95 and $S_{1,I}$ = 0.56. The oil bank forms in the reservoir because of polymer injection. Oil cut starts to increase and reaches a peak value of 0.18 after the oil bank breaks through. The oil cut then decreases as the injected polymer starts to recycle. The polymer injection is stopped after 2.8 PV of fluid is injected (Figure 5-26b).

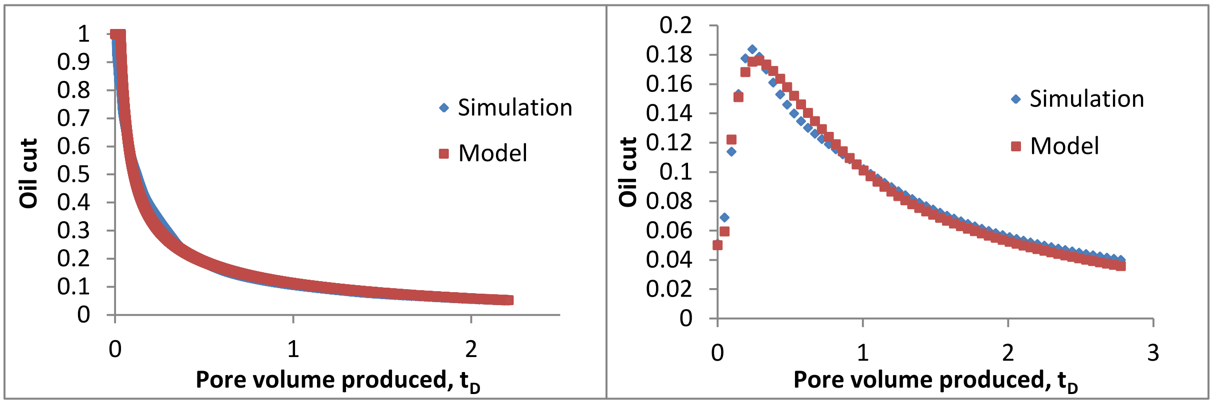

a)Waterflood b)Polymer flood

Figure 5-26. Polymer flood (tertiary displacement) often follows water flood (secondary displacement). a) Water flood history match is shown using the new model for secondary floods. b) Oil cut history match between simulation and model is good. The oil cut initially increases with polymer injection. The oil cut reaches a peak value and falls off thereafter.

Autocorrelation length		
L_x	L_y	L_z
10	0	0

Table 5-12. Permeability field correlation lengths for the history matched case in Figure 5-26.

Water flood	Koval factor	K	18.91	Polymer flood	Chemical bank Koval factor	K_b	3.65
					Oil bank Koval factor	K_f	5.48
	Ultimate volumetric sweep efficiency	a (model)	0.78		Ultimate volumetric sweep efficiency	a (model)	0.85
		a (simulation)	0.79			a (simulation)	0.86
	Average water saturation in swept area	S_{1avg} (model)	0.56		Average water saturation in polymer swept area	S_{1avg} (model)	0.91
		S_{1avg} (simulation)	0.55			S_{1avg} (simulation)	0.89

Table 5-13. History match parameters for water flood and tertiary polymer flood for line drive pattern in Figure 5-26.

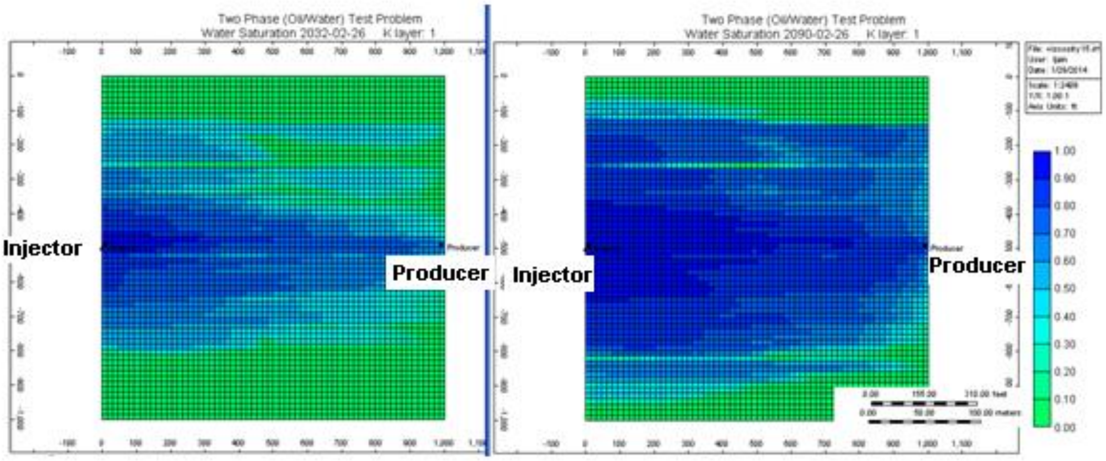

a) Waterflood b) Polymer flood

Figure 5-27. a) Water saturation map at the end of waterflooding and beginning of polymer injection (Water cut, 95%). b) Water saturation map at the end of polymer injection phase (Water cut, 95%) for line drive pattern.

5.6.1.2 Quarter 5 spot

The second case for tertiary polymer flood is in Figure 5-28b. The water flood stops when the oil cut reaches 0.05 at t_D = 2.2 PV of injection. The average water saturation in the flooded region at the end of water flood estimated from the model for secondary floods is 0.56. Thus the initial condition before the polymer injection starts is $f_{1,I}$ = 0.95 and $S_{1,I}$ = 0.56. The oil bank forms in the reservoir due to polymer injection. Oil cut starts to increase and reaches a peak value of 0.18 after the oil bank breaks through. The oil cut then decreases as the injected polymer starts to recycle. The polymer injection is stopped after 2.7 PV of fluid is injected (Figure 5-28b).

Autocorrelation length		
L_x	L_y	L_z
10	0	0

Table 5-14. Permeability field autocorrelation lengths for the history matched case in Figure 5-28.

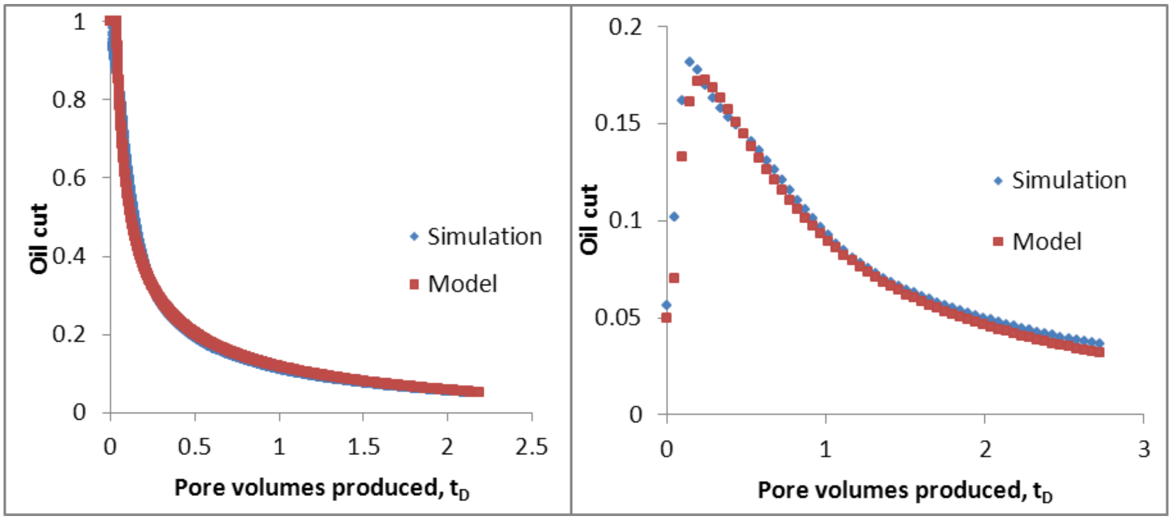

a) Waterflood

b) Polymer flood

Figure 5-28. Polymer flood (tertiary displacement) following water flood (secondary displacement). a) Water flood history match is shown using the new model for secondary floods. b) Oil cut history match between simulation and model is good. The oil cut initially increases with polymer injection. The oil cut reaches a peak value and falls off thereafter.

Water flood	Koval factor	K	16.18	Polymer flood	Polymer bank Koval factor	K_b	3.65
					Oil bank Koval factor	K_f	5.93
	Ultimate volumetric sweep efficiency	a (model)	0.76		Ultimate volumetric sweep efficiency	a (model)	0.83
		a (simulation)	0.78			a (simulation)	0.85
	Average water saturation in swept area	S_{1avg} (model)	0.56		Average water saturation in polymer swept area	S_{1avg} (model)	0.91
		S_{1avg} (simulation)	0.58			S_{1avg} (simulation)	0.92

Table 5-15. History match parameters for water flood and tertiary polymer flood for quarter five-spot pattern in Figure 5-28.

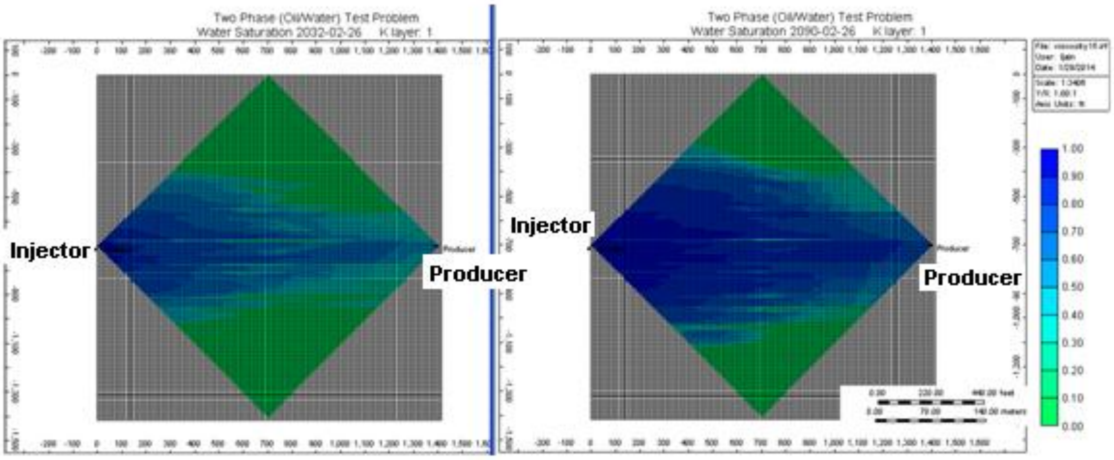

a) Waterflood b) Polymer flood

Figure 5-29. a) Water saturation map at the end of water flooding and beginning of polymer injection (Water cut, 95%). b) Water saturation map at the end of polymer injection phase (Water cut, 95%) for quarter five-spot pattern.

The end point mobility ratio decreases to 0.5 for polymer flood from 5 for water flood. The purpose of polymer flood is to increase the sweep efficiency by lowering the mobility ratio. The ultimate volumetric sweep efficiency increases by 7% for both the cases shown above (Table 5-13 and 5-15) when the injection shifts from water to polymer. The average water saturation in the zones flooded with polymer also increases by 35% from water flood for both the cases (Table 5-13 and 5-15). The increase in water saturation during polymer floods is also suggested by the pixel scale fractional flow theory for polymer floods (Figure 5-24). The Koval factors for polymer flood drop significantly compared to water flood (Table 5-13 and 5-15) because of decrease in the mobility ratio.

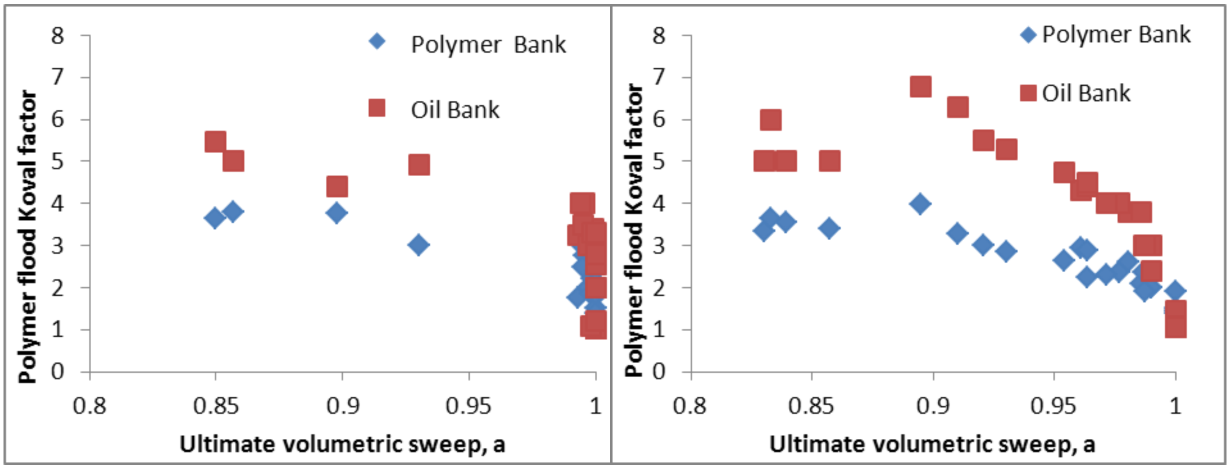

a) Line drive pattern

b) Quarter five-spot pattern

Figure 5-30. Koval factors for both the polymer bank and oil bank decrease as ultimate volumetric sweep increases for a) Line drive pattern and b) Quarter five-spot pattern. Koval factors for oil bank are also higher compared to polymer bank for both the patterns.

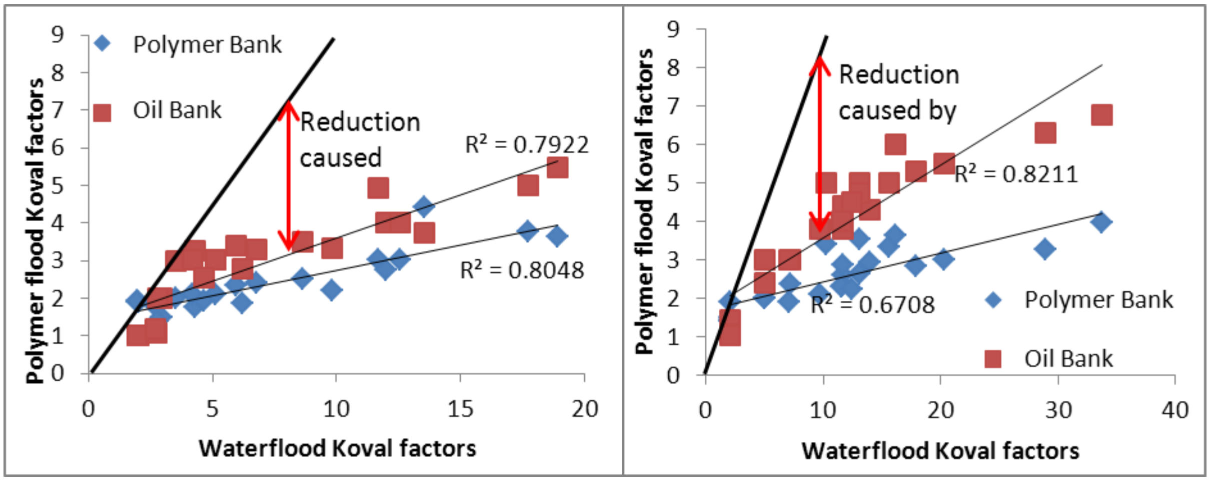

a) Line drive pattern

b) Quarter five-spot pattern

Figure 5-31. Koval factors for polymer bank and oil bank increase monotonically with increasing water flood Koval factors for a) Line drive pattern and b) Quarter five-spot pattern. Koval factors obtained during polymer floods are also well correlated with the water flood Koval factors for both patterns.

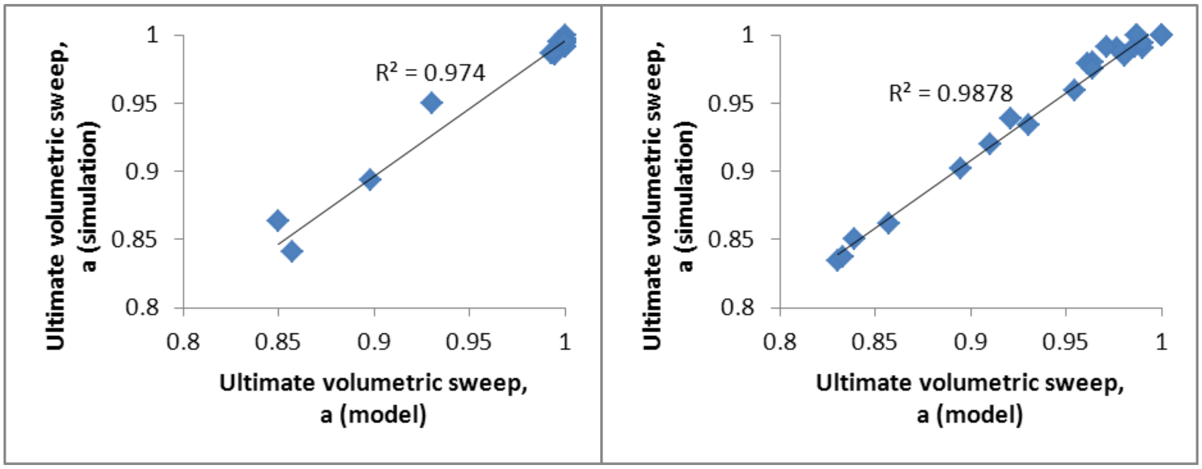

a) Line drive pattern

b) Quarter five-spot pattern

Figure 5-32. Ultimate volumetric sweep from the new model compares well with the simulation for polymer floods for a) Line drive pattern and b) Quarter five-spot pattern.

Higher ultimate volumetric sweep efficiency indicates more uniform displacement of oil in the drainage volume without fluid channeling. Favorable (low) mobility ratios and/or small heterogeneity are the main reasons for good volumetric sweep. Koval factors are direct measures of mobility ratio and heterogeneity so smaller values must indicate higher volumetric sweep (Figure 5-30). The inverse relationship between the Koval factor and volumetric sweep holds for both line drive and quarter five-spot pattern (Figure 5-30).

Under the following conditions, a relationship is expected between water flood Koval factors and polymer flood Koval factors:

- For all the simulation cases shown above, water viscosity changes from 1 cp for water flood phase to 10 cp for polymer flood phase while oil viscosity remains constant at 5 cp.

- Field heterogeneity is a static property and thus is invariable with time.

Figure 5-31 illustrates a good correlation between waterflood Koval factors and both the polymer flood Koval factors (polymer bank and oil bank). For the same change in water mobility, an increasing trend between water flood Koval factors and polymer flood Koval factors represent increasing heterogeneity.

The ultimate volumetric sweep obtained from the model matches well with the values estimated from the simulation grid at the end of polymer flood (Figure 5-32).

5.6.2 Miscible gas flood

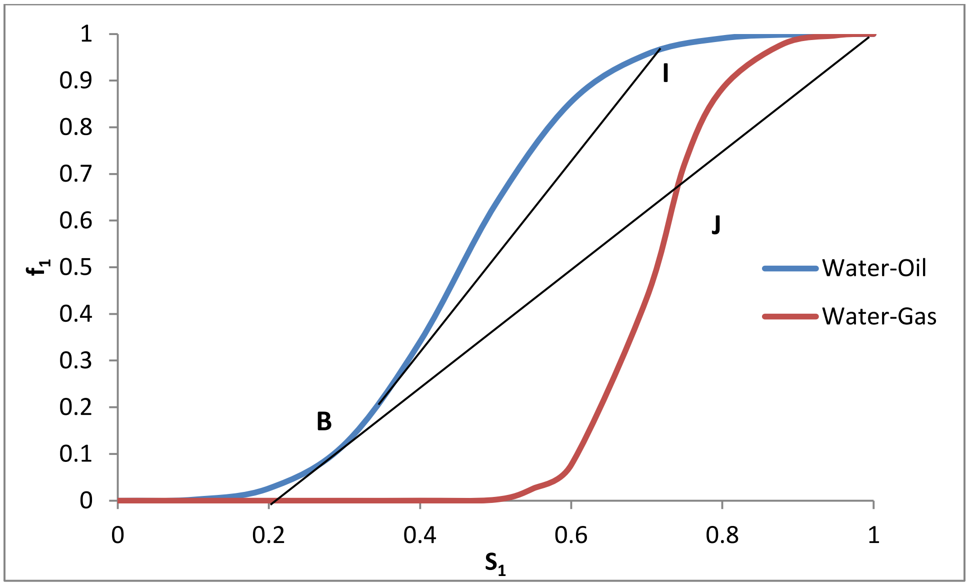

Figure 5-33.Pixel scale fractional flow curves for tertiary SWAG flood.

At reservoir conditions the oil viscosity is 3.5 cp for all the simulated cases. The secondary flood water viscosity is 0.7 cp. The tertiary flood gas viscosity is 0.2 cp. These viscosities were used to calculate the pixel scale fractional flow curves (Figure 5-33). All the simulations were performed at a fixed WAG ratio of 2.03. The other simulation parameters are defined in Table 5-3.

5.6.2.1 Line drive pattern

The first case for a tertiary SWAG flood history match is in Figure 5-34b. The waterflood stops when the oil cut reaches 0.05 with 2.2 PV of total injection. The average water saturation in the flooded region at the end of waterflood estimated from the model for secondary flood is 0.56. Thus the initial condition before the SWAG injection starts is $f_{1,I}$ = 0.95 and $S_{1,I}$ = 0.56. The oil bank forms in the reservoir because of miscible gas injection. Oil cut increases to a peak value of 0.21 after the oil bank breaks through. The oil cut then decreases quickly as the injected gas starts to be produced. The SWAG injection stops after 1.5 PV of fluid is injected (Figure 5-34b).

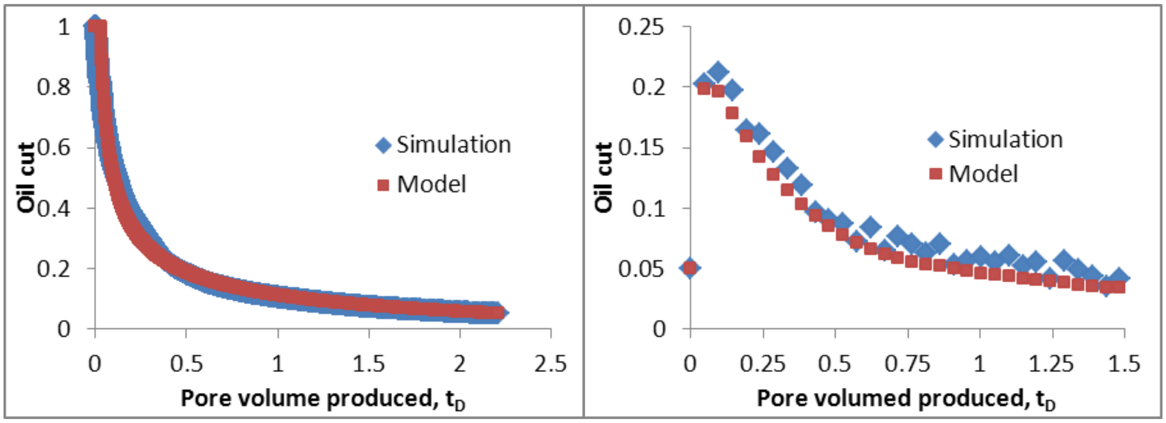

a)Waterflood b) SWAG flood

Figure 5-34. SWAG/CO_2 flood (tertiary displacement) follows water flood (secondary displacement). a) Water flood history match is shown using the new model for secondary floods. b) Oil cut history match between simulation and model is good. The oil cut initially increases with gas injection. The oil cut reaches a peak value and falls off thereafter.

Autocorrelation length		
L_x	L_y	L_z
10	0	0

Table 5-16. Permeability field autocorrelation lengths for the history matched case in Figure 5-34.

Water flood	Koval factor	K	18.01	SWAG/ CO_2 flood	Solvent bank Koval factor	K_b	17.2
					Oil bank Koval factor	K_f	21.0
	Ultimate volumetric sweep efficiency	a (model)	0.78		Ultimate volumetric sweep efficiency	A (model)	0.41
		a (simulation)	0.79			A (simulation)	0.42
	Average water saturation in swept area	S_{1avg} (model)	0.56		Average water saturation in solvent swept area	S_{1avg} (model)	0.75
		S_{1avg} (simulation)	0.55			S_{1avg} (simulation)	0.73

Table 5-17.History match parameters for water flood and tertiary SWAG flood.

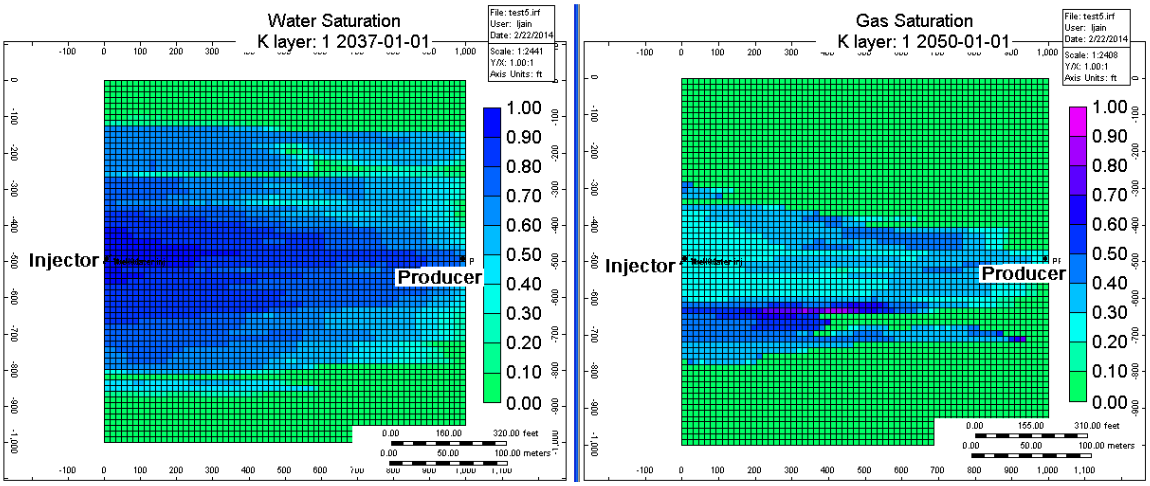

a) Waterflood b) SWAG flood

Figure 5-35. a) Water saturation map at the end of water flooding and beginning of SWAG injection (Water cut, 95%) b) Gas saturation map at the end of SWAG injection phase (Water cut, 95%) for line drive case.

5.6.2.2 Quarter five-spot

The second case for tertiary SWAG flood is shown in Figure 5-36b. The water flood stops when the oil cut reaches 0.05 with 2.2 PV of total injection. The average water saturation in the flooded region at the end of water flood is 0.56. Thus the initial condition before the SWAG injection starts is assumed to be $f_{1,I} = 0.95$ and $S_{1,I} = 0.56$. The oil bank forms in the reservoir because of gas/CO_2 injection. Oil cut starts to increase and reaches a peak value of 0.22 after the oil bank breaks through. The oil cut then decreases as the injected gas starts to recycle. The gas injection is stopped after 1.5 PV of fluid is injected (Figure 5-36b).

Autocorrelation length		
L_x	L_y	L_z
10	0	0

Table 5-18. Permeability field autocorrelation lengths for the history matched case in Figure 5-36.

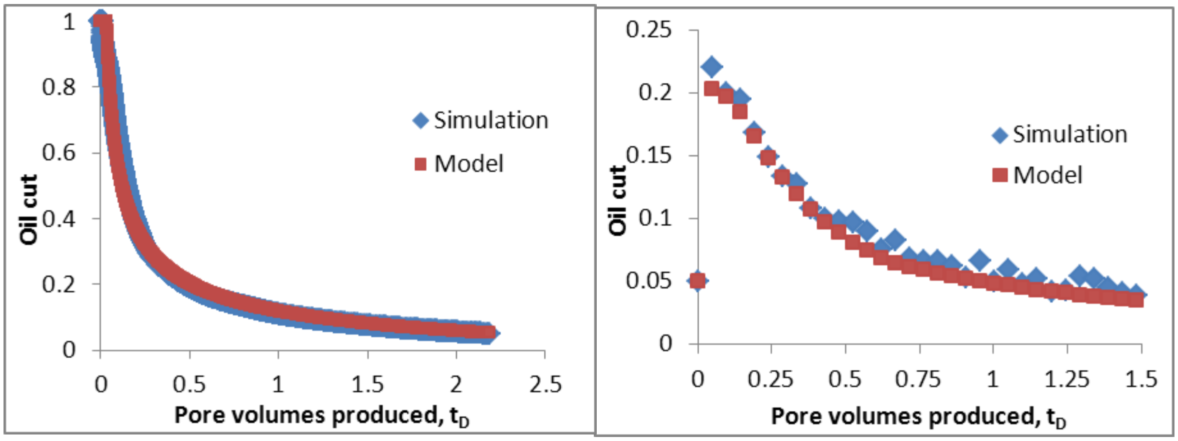

a) Waterflood

b) SWAG flood

Figure 5-36. SWAG/CO_2 flood (tertiary displacement) follows water flood (secondary displacement). a) Water flood history match is shown using the new model for secondary floods. b) Oil cut history match between simulation and model is good. The oil cut initially increases with gas injection. The oil cut reaches a peak value and falls off thereafter.

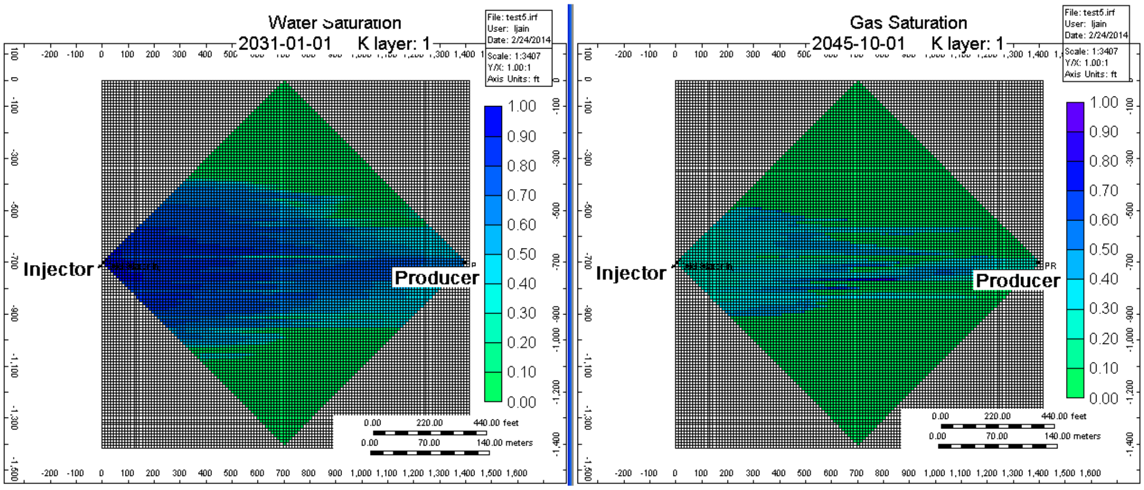

a) Waterflood

b) SWAG flood

Figure 5-37. a) Water saturation map at the end of water flooding and beginning of SWAG injection (Water cut, 95%). b) Gas saturation map at the end of SWAG injection phase (Water cut, 95%) for quarter five-spot case.

Water flood	Koval factor	K	15.43	SWAG/ CO_2 flood	Solvent bank Koval factor	K_b	18.2
					Oil bank Koval factor	K_f	25.4
	Ultimate volumetric sweep efficiency	a (model)	0.76		Ultimate volumetric sweep efficiency	a (model)	0.38
		a (simulation)	0.78			a (simulation)	0.40
	Average water saturation in swept area	S_{1avg} (model)	0.56		Average water saturation in solvent swept area	S_{1avg} (model)	0.77
		S_{1avg} (simulation)	0.58			S_{1avg} (simulation)	0.74

Table 5-19. History match parameters for water flood and tertiary SWAG flood.

The end point mobility ratio increases to 17.5 for the solvent flood from 5 for water flood. The purpose of the gas/solvent flood is to increase the displacement efficiency by inducing miscibility and reducing the solvent/oil interfacial tension. The ultimate volumetric sweep efficiency decreases by 35% for line drive case (Table 5-17) and by 37% for quarter five spot case (Table 5-19) from waterflood phase. The decrease in sweep efficiency results from solvent channeling through high permeability streaks (Figure 5-34b and 5-36b). The average gas saturation in the zones flooded with solvent is 75% which is approximately equal to 77% as estimated from fractional flow theory (Fig. 5-33). The average gas saturation in the flooded region is small because the injection WAG ratio is 2.03. The pixel scale fractional flow theory for miscible gas floods at WAG ratio of 2.03 also suggests small gas saturation in the flooded region (Figure 5-33). The Koval factors for gas flood increases significantly compared to water flood (Table 5-17 and 5-19) because of increase in the mobility ratio.

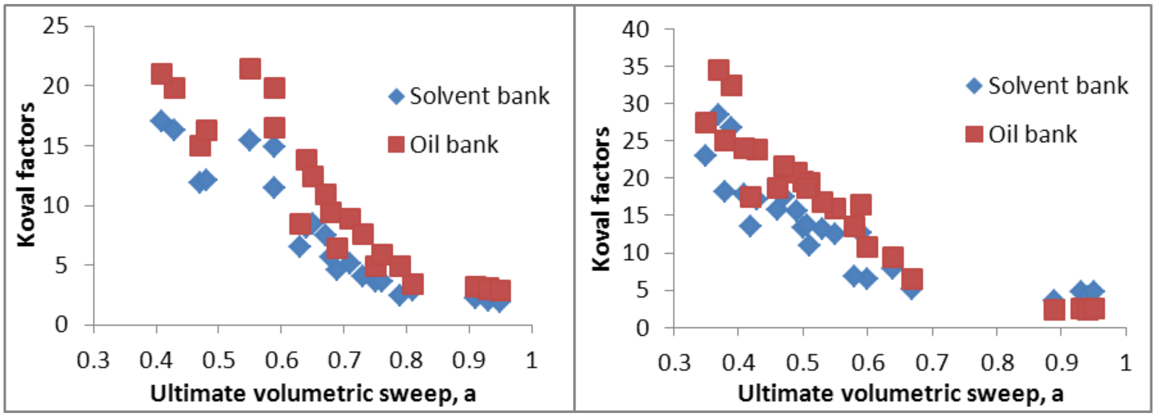

a) Line drive pattern

b) Quarter five-spot pattern

Figure 5-38. Koval factors for both the solvent bank and oil bank decrease as ultimate volumetric sweep increases for a) Line drive pattern and b) Quarter five-spot pattern. Koval factors for oil bank are also higher compared to solvent bank for both the patterns.

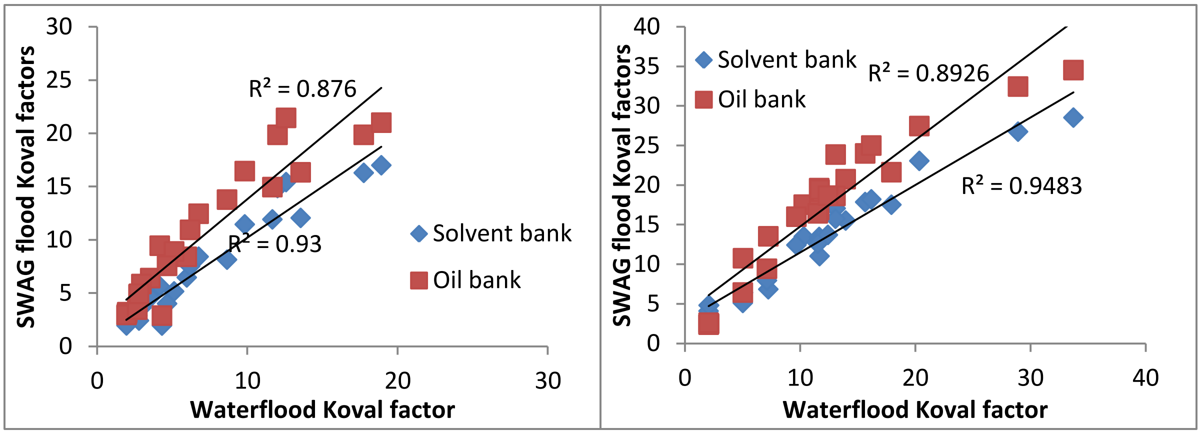

a) Line drive pattern

b) Quarter five-spot pattern

Figure 5-39. Koval factors for solvent bank and oil bank increase monotonically with increasing water flood Koval factors for a) Line drive pattern and b) Quarter five-spot pattern. Koval factors obtained during solvent floods are also well correlated with the water flood Koval factors for both patterns.

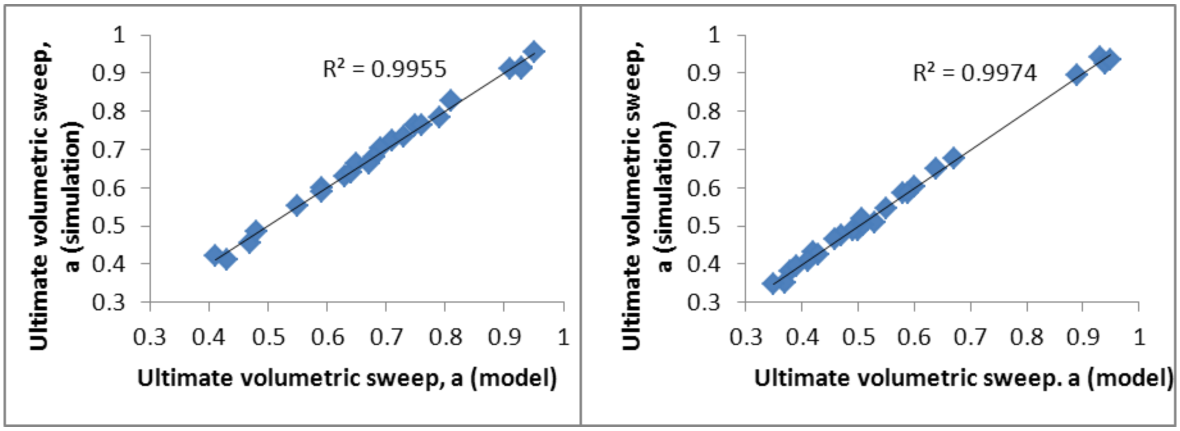

a) Line drive pattern

b) Quarter five-spot pattern

Figure 5-40. Ultimate volumetric sweep from the model compares very well with the simulation for miscible SWAG floods for a) Line drive pattern and b) Quarter five-spot pattern.

Small ultimate volumetric sweep efficiency indicates non-uniform displacement of the drainage volume because of fluid channeling. Unfavorable (high) mobility ratio is the main reason for poor ultimate volumetric sweep. Koval factors are direct measures of mobility ratio and heterogeneity so high values must indicate small volumetric sweep (Figure 5-38). The inverse relationship between the Koval factor and volumetric sweep holds for both line drive and quarter five-spot pattern (Figure 5-38).

Figure 5-39 illustrates a good correlation between water flood Koval factors and both the solvent flood Koval factors (solvent bank and oil bank). For the same change in water mobility, increasing trend between water flood Koval factors and polymer flood Koval factors represent increasing heterogeneity. The ultimate volumetric sweep obtained from the model matches well with the values estimated from the simulation grid at the end of solvent flood (Figure 5-40).

5.7 MODEL VALIDATION

The terms verification and validation differ in their meanings when it concerns new mathematical models. Verification is concerned with whether the model is error-free and well-engineered while validation is concerned with the real world applicability of the proposed mathematical model. Also, verification is the process of determining that a model implementation accurately represents the developer's conceptual description of the model and the solution to the model (AIAA, 1998). Validation, in context of the current work, is the process of determining the degree to which the proposed model is an accurate representation of the real world from the perspective of the intended uses of the model (AIAA, 1998). This definition of validation is to be distinguished from the use of the term in the scientific method sense of testing a prediction of a scientific model against experimentally obtained data.

A good scientific model satisfies two conditions: it describes a large class of observations by using only a few arbitrary parameters and it must be able to make definite predictions of future observations (Popper, 1935). The validity of the models developed in this research in the scientific sense is limited because they cannot be used to predict the performance of secondary and tertiary displacements. The intended use of the models developed in this chapter is to understand the efficiency of the secondary and tertiary displacements for real field cases. History matching the field data provides a set of parameters that can be used to understand the effectiveness of the displacements. The basic steps for history matching the field results are outlined briefly followed by few examples for each of the process.

5.7.1 Model Validation steps

The data is gathered for field waterflood, polymer floods and gas floods. The collected data is history matched with the model. Following are each of the validation steps outlined in detail.

5.7.1.1 Field data

Field data for water floods shown later was obtained through personal communication. Field data for polymer floods and WAG floods is collected through published resources and personal communication. Field data includes oil cut and/or cumulative oil recovery at reservoir conditions as well as total production rates and injection rates of the wells. This includes 15 single well waterfloods, 6 field polymer floods and 4 field solvent floods. It also includes 5 single well waterfloods which are followed by solvent floods for a Colorado oil field called Rangley. The number of field data used for model validation for each EOR process reflects the limited availability of the data for such analysis.

5.7.1.2 Field data preparation

In each case the reported production effluent history (oil cut or cumulative oil recovery) were used for history matching. The field effluent history before being fed to the model is converted to reservoir conditions. Phase behavior data such as fluid formation volume factors are required to convert data to the reservoir conditions. The models for waterflooding and polymer/solvent floods are different as detailed in earlier section on model development so the incremental results of EOR/waterflooding phases are required even when the reported results are continuous from primary to tertiary. So for cumulative oil recovered, the incremental must be extracted for each EOR stage. Oil cut data is at a point in time and not averaged over a given duration like cumulative oil recovered so only the initial oil cut at the start of each EOR phase is required.

The models for water/polymer/solvent flooding uses dimensionless time so the time scale on the field data is required to be converted to dimensionless using Equation 5.69:

$$t_D = \frac{\int_0^t q_{pro}(t)dt}{V_P} \tag{5.69}$$

where $q_{pro}(t)$ is the total production rate of all fluids at time t and V_P is the average pore volume associated with the drainage area. The total production rate is used for history matching because the model is applied at each production well and individual contributions from each injector towards production from each production well are hard to determine. Capacitance Resistance model has the capability to obtain the contribution of each injector towards each production well (Morteza, 2008). The only other information that is required at the start of each production phase (water/polymer or solvent flood) for history matching is:

- S_{1i}: The initial water saturation in the swept region at the start of each phase

- f_{1i}: The initial water cut at the start of each phase

The total production rate from the field is known but the associated drainage pore volume is an unknown so it is one of the history match parameters. The number of input parameters required is very basic and few in number compared to history matching with numerical simulation.

5.7.2 Water flooding history matching

The water flood history matching model and procedure is explained in detail in the previous chapter. The water flood history match procedure is simpler compared to other EOR processes because the water flood has two saturation regions compared to three for polymer and solvent floods. The matching parameters as stated in the verification section for waterflooding are the Koval factor (K), the local water front velocity ($v_{\Delta s}$) and the ultimate volumetric sweep efficiency (a). The water flood performance depends on the Koval factor (heterogeneity and mobility ratio), the local water front velocity (local change in saturation representative of the displacement sweep) and ultimate volumetric sweep. The total pore volume is also an unknown and treated as a history match parameter. History match is performed on oil cut for water floods,

$$f_o\big|_{x_D=1}(t_D) = f(t_D; K, v_{\Delta s}, a, V_p) \tag{5.70}$$

$$Total\ error = \sum_{j=1}^{N} \beta_j \left(f_o(t_{D_j})\Big|_{\text{model}} - f_o(t_{D_j})\Big|_{\text{field}} \right)^2 = f(K, v_{\Delta s}, a, V_p) \tag{5.71}$$

The solver in Microsoft excel was used to vary the history match parameters and obtain a good history match by minimizing the total error in equation 5.71. The history matching is a constrained optimization problem because the history match parameters have upper or lower limits based on physical arguments. The Koval factor as well as local front velocity cannot be less than unity whereas ultimate volumetric sweep efficiency has to be between zero and one. The ultimate volumetric sweep efficiency reaches the limit in one when the flood performs really well and sweep is uniform.

Figure 5-41 and 5-42 are examples of the water flood history matches for an actual reservoir and a single well in that reservoir.

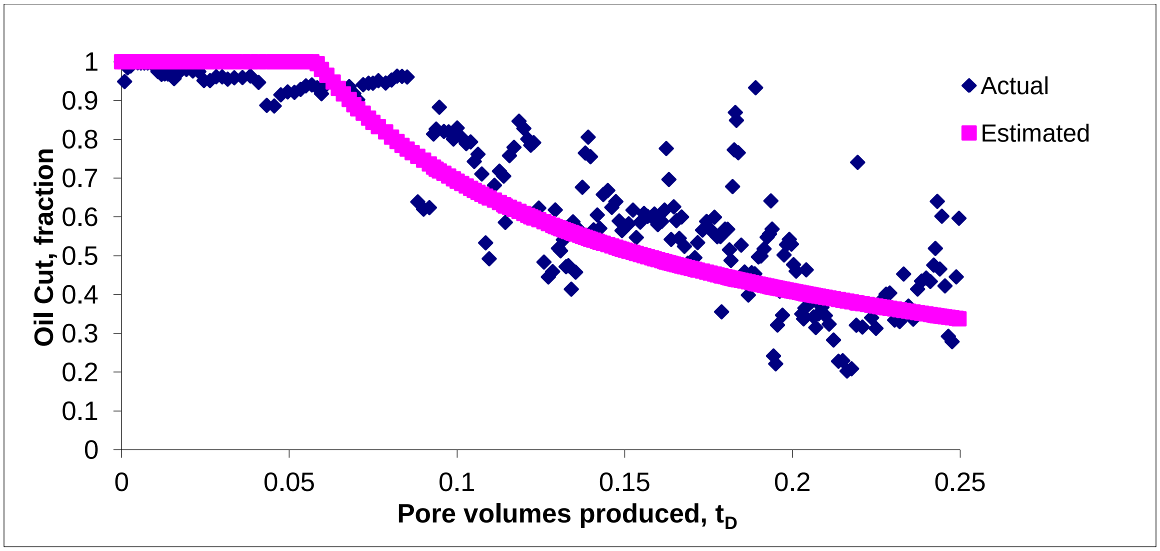

Figure 5-41. Water flood history match for the whole reservoir (Sand-C4)

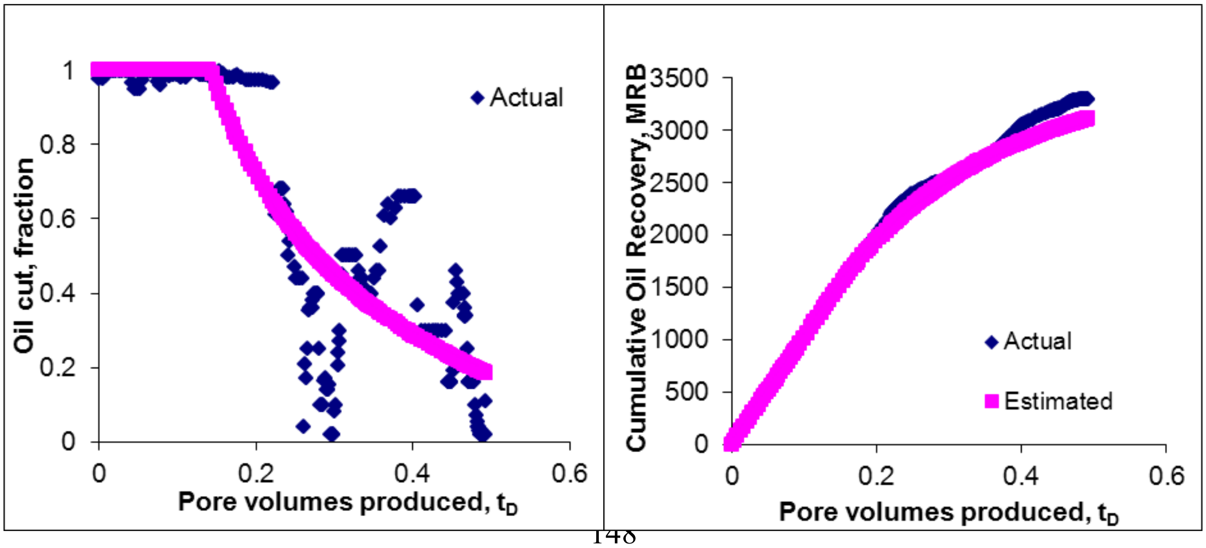

Figure 5-42. Water flood history match for a single well (Well 1) in the reservoir (Sand-C4)

The water flood history match for the whole reservoir Sand-C4 is shown in Figure 5-41. The actual oil cut data from the field has a lot of noise which results from various field operating conditions. The history match oil cut is smooth and matches the average behavior of oil cut from the field. The waterflood history match for a single well in reservoir sand C-4 is shown in Figure 5-42. The actual oil cut from the field for a single well also contains some noise (fluctuations) in the data, which could be attributed to changes in the well operating conditions. The average history match for the cumulative oil produced is very good. The total pore volume that of the whole reservoir sand is approximately 70 MMRB which is 7 times compared to the pore volume associated with the single well (10 MMRB) shown in Table 5-20.

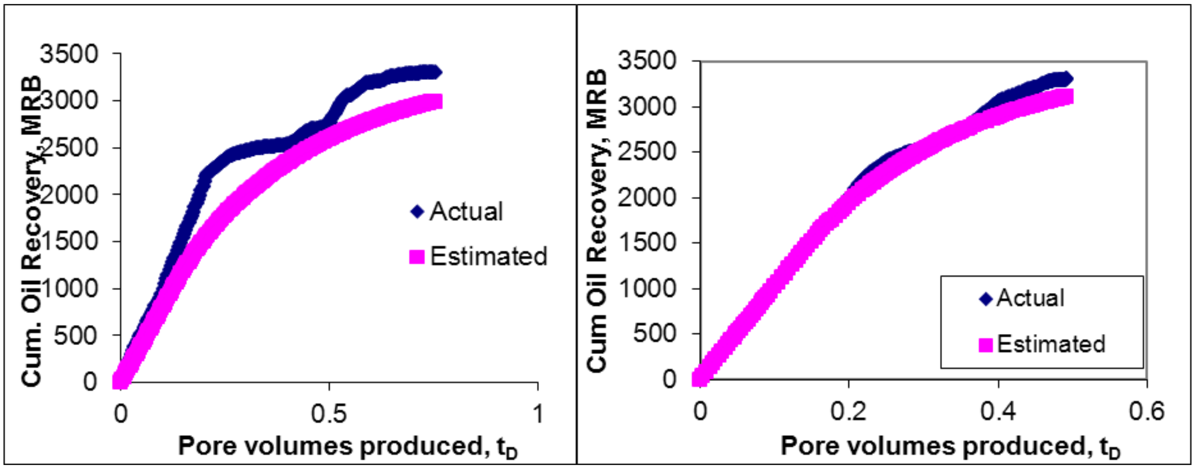

a) Mollaei's model

b) New model

Figure 5-43. Waterflood history match comparison between (a) Mollaei's and (b) the new model for cumulative oil produced for Well 1 (Sand C4).

The history match from the new model is much better compared to Mollaei's model as shown in Figure 5-43. The better history match from the new model could be attributed to the number of fitting parameters mathematically. The number of history match parameters for the new model is four compared to three for the Mollaei's model. The other physical reason for a better history match could be the differentiation between the unswept and swept zones in the new model.

Reservoir Name		**Koval factor, *K***		**Local front velocity, v_{AS}**	**Ultimate volumetric sweep, *a***	**Total pore volume V_p, (MMB)**
		New model	**Mollaei model**			
Sand C-4	**Whole reservoir**	**6.48**	**7.13**	**2.50**	**0.67**	**70.00**
	Well 1	2.84	3.00	2.12	0.82	10.18
	Well 2	2.45	5.48	2.34	0.99	6.37
	Well 3	1.81	2.54	2.49	0.93	9.91
	Well 4	7.92	8.37	2.27	0.50	12.18
	Well 5	10.07	3.50	2.78	0.40	4.46
	Well 6	12.68	4.75	2.42	0.63	5.11
	Well 7	1.001	12.98	2.71	1.00	2.00
Sand C-5	**Whole reservoir**	**3.36**	**3.74**	**2.53**	**0.91**	**69.92**
	Well 1	1.97	1.46	2.38	0.79	9.58
	Well 2	4.75	2.82	2.11	0.99	0.95
Sand C-6	**Whole reservoir**	**6.45**	**4.00**	**2.46**	**0.83**	**85.00**
	Well 1	10.98	6.87	2.31	0.37	17.82
	Well 2	2.03	1.50	2.65	0.75	5.12
Sand C-7	**Whole reservoir**	**4.59**	**4.58**	**2.82**	**0.99**	**137.00**
	Well 1	2.35	2.70	2.54	0.88	20.73
	Well 2	3.84	5.00	2.69	0.78	42.50

Table 5-20. Summary of history matched parameters for all field waterflooding cases

Table 5-20 summarizes waterflooding history match parameters for different reservoirs and the single wells in those reservoirs. Table 5-20 also summarizes the Koval factors obtained by Mollaei (2011) for the same water flood history matches. The obtained Koval factors and ultimate volumetric sweep efficiencies for the field history match are in between maximum and minimum of the same single well parameters for reservoir C-4 and C-5. The Koval factors and ultimate volumetric sweep for C-4 sand largely form two groups. Wells 1, 2 and 3 have small Koval factors wells 4, 5, 6 and 7 have large Koval factors. The variability can be speculated to be related to the geological factors such as permeability anisotropy, well spacing, etc. The Koval factors and ultimate volumetric sweep for the sands C-6 and C-7 are not equal to the average values from the wells. The estimated total pore volume associate with the individual wells also does not sum to the estimated total reservoir pore volume for all four reservoirs. The total production from sands C-4, C-5, C6 and C-7 also exceeds the cumulative production from individual wells for each reservoir (Table 5-21). This mismatch must be attributed to existence of more production wells in the reservoir than reported in Table 5-20 and 5-21.

Reservoir Name		**Cumulative oil produced, MRB**	**Total pore volume, V_p, (MMRB)**
Sand C-4	Well 1	3296.48	10.18
	Well 2	2442.55	6.37
	Well 3	3713.55	9.91
	Well 4	1905.04	12.18
	Well 5	697.18	4.46
	Well 6	790.70	5.11
	Well 7	621.70	2.00
	Well Total	**13467.20**	**50.21**
	Whole reservoir	**15011.43**	**70.00**
Sand C-5	Well 1	2806.26	9.58
	Well 2	380.05	0.95
	Well Total	**3186.31**	**10.53**
	Whole reservoir	**20399.47**	**69.92**
Sand C-6	Well 1	1548.35	17.82
	Well 2	1448.17	5.12
	Well Total	**2996.52**	**22.94**
	Whole reservoir	**21987.87**	**85.00**
Sand C-7	Well 1	5850.15	20.73
	Well 2	12352.08	42.50
	Well Total	**18202.23**	**63.23**
	Whole reservoir	**67496.46**	**137.00**

Table 5-21. Summary and comparison of the cumulative oil produced and total pore volume for each well and the whole reservoir.

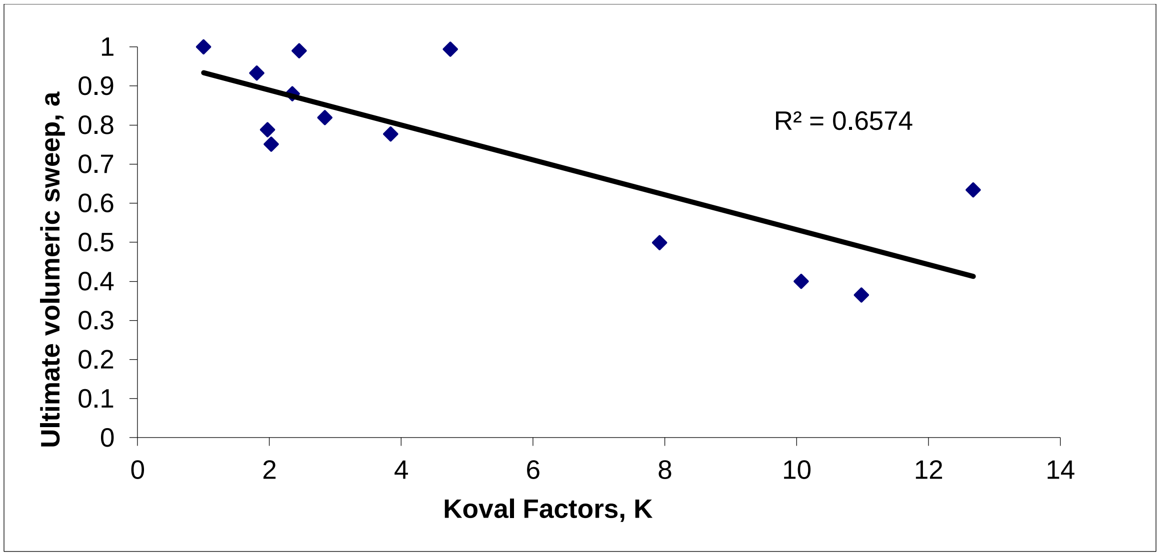

Figure 5-44. Field and single well ultimate volumetric sweep decreases with increasing Koval factors.

Figure 5-44 demonstrates the relationship between the ultimate volumetric sweep and the Koval factors for the four reservoirs analyzed above. The ultimate volumetric sweep decreases with an increase in Koval factors (representative of heterogeneity and mobility ratio) as expected.

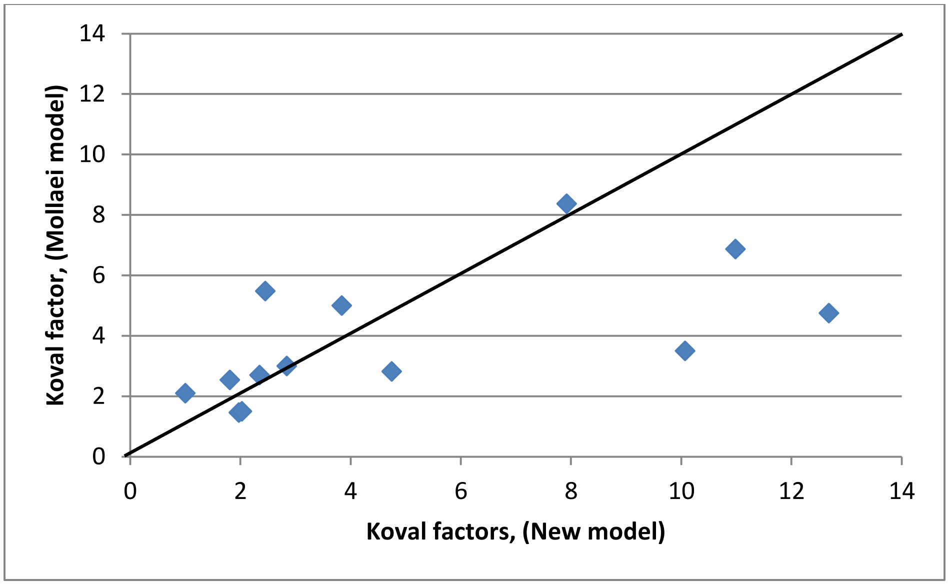

Figure 5-45. The Koval factors from new model show an increasing trend with the Koval factors obtained from Mollaei model.

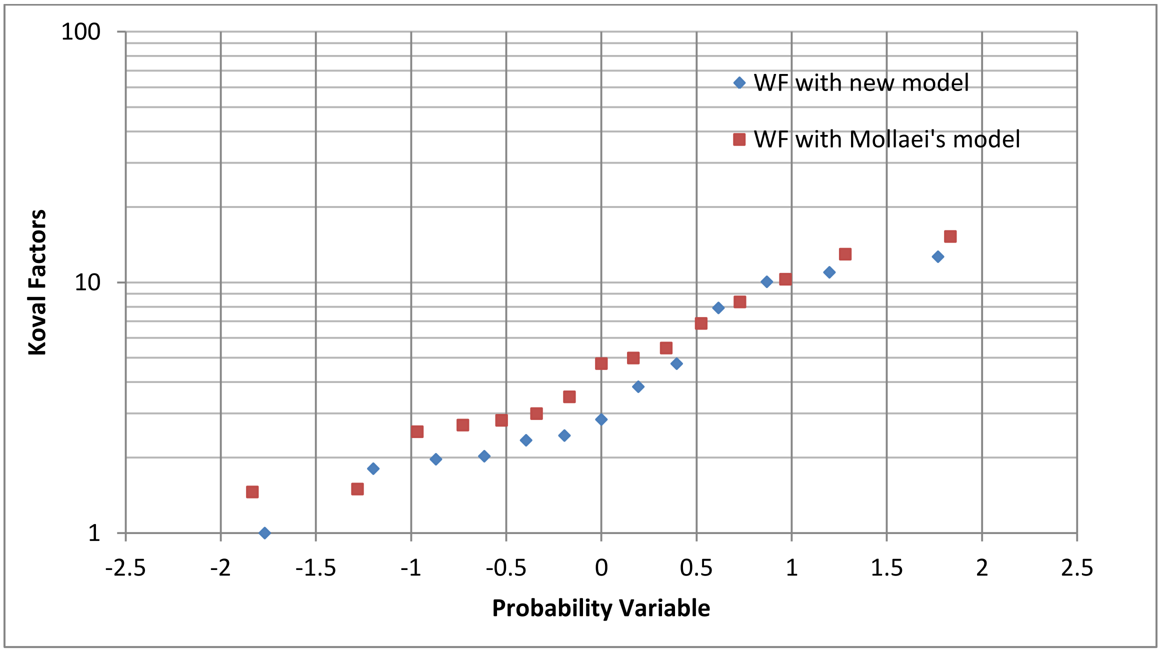

Figure 5-46. Koval factor comparison between the new model and Mollaei’s model

The comparison between the Koval factors from the new model with Mollaei's model shows an increasing trend (Figure 5-45). The Koval factors obtained from the new model are different than from the Mollaei's model because the new model is a two parameter model versus one parameter Mollaei model (Figure 5-45 and 5-46).

5.7.3 EOR history matching

The tertiary flood, two-front displacement models have been validated against two of isothermal EOR processes: polymer and solvent (gas) flooding. In the next few sections, validation examples for polymer and solvent history matching are shown.

5.7.3.1 Polymer floods

In chemical EOR polymer is injected for mobility ratio control between displacing and displaced fluids to bring about improved oil recovery and increase in volumetric sweep (Lake, 1989). The production history data (cumulative oil produced, oil cut and total production rate) of six pilot and field polymer floods is used for history matching of the model.

The history matching procedure for polymer floods is different than waterflooding. The polymer flood model has six history matching parameters, two additional to waterflooding because of existence of two displacing fronts: Polymer bank Koval factor (K_b), oil bank Koval factor (K_f), polymer bank local front velocity ($v_{b,OB}$), oil bank local front velocity ($v_{f,OB}$), ultimate volumetric sweep (a) and total pore volume (V_p) are adjusted to achieve a good history match.

Each history matching parameter represents some reservoir and/or process characteristics. Similar to waterflooding, the Koval factors describe the effect of heterogeneity and mobility ratio on performance curves (oil cut, cumulative recovery). Factors such as polymer adsorption and degradation and salinity can also influence the oil recovery. They mainly affect the viscosity and relative permeability of the injected polymer solution that are accounted for in the mobility ratio and local front velocities.

The six variables (K_b,K_f,$v_{b,OB}$,$v_{f,OB}$,a,V_p) are adjusted in the automatic history matching algorithm (explained in Appendix C) to match pilot and field oil cut.

$$f_o\big|_{x_D=1} = f(t_D : K_b, K_f, v_{\mathrm{b},OB}, v_{f,OB}, a, V_p) \tag{5.73}$$

The regression is performed to minimize the total error and achieve a good match between actual and predicted results.

$$\mathit{Total\ error} = \sum_{j=1}^{N} \beta_j \left(f_o(t_{D_j})\Big|_{\mathrm{model}} - f_o(t_{D_j})\Big|_{\mathit{field}} \right)^2 = f(K_b, K_f, v_{\mathrm{b},OB}, v_{f,OB}, a, V_p) \tag{5.74}$$

The Daqing pilot polymer floods history match is discussed below. The remaining five field polymer history matches are in Appendix D.

Daqing field pilot PO

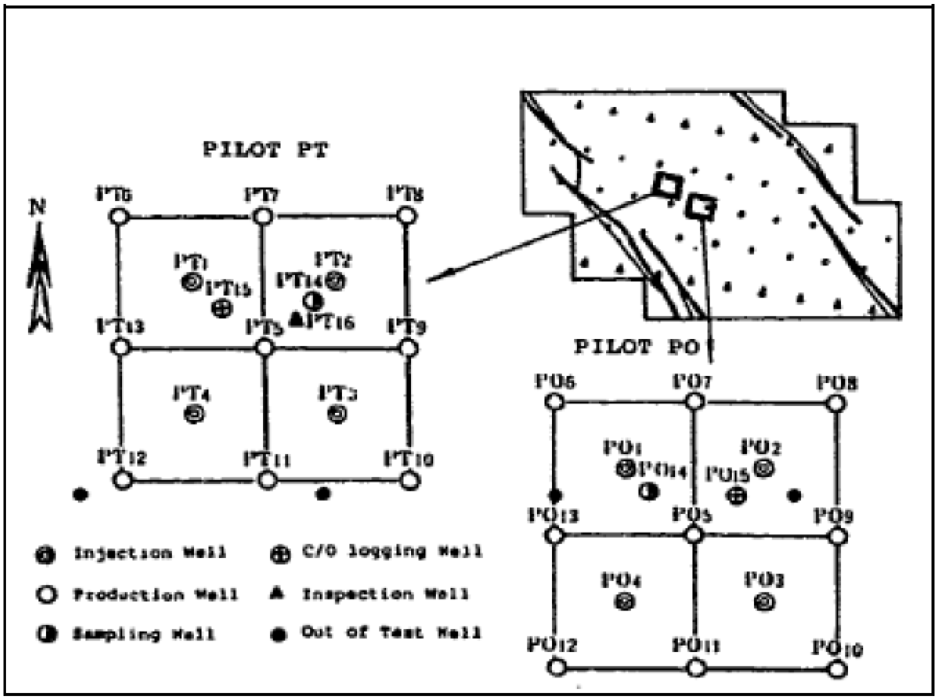

Figure 5-47. Location of polymer flood pilots and wells for the Daqing field. (Wang et al., 1993).

The Daqing field comprises of the Putaohua and Saertu sandstone formations. The average net thickness of the field ranges from 7 to 38 ft with the average thickness at 20 ft. The average oil viscosity in the reservoir is 9.5 cp. The field was discovered in 1959. Water injection in both the layers began in June of 1960. The adverse mobility ratio for water floods led to polymer demonstration projects to improve oil recovery. The pilot one (PO) polymer flood was initiated in 1990 and ended in 1992. The pilot resulted in decrease in water cut by 16% and increase in oil recovery by 14% of OOIP demonstrating the effectiveness of the polymer flood. Figure 5-47 shows the five spot pattern layout for the polymer pilot (PO). The excellent history match is shown in Figure 5-48.

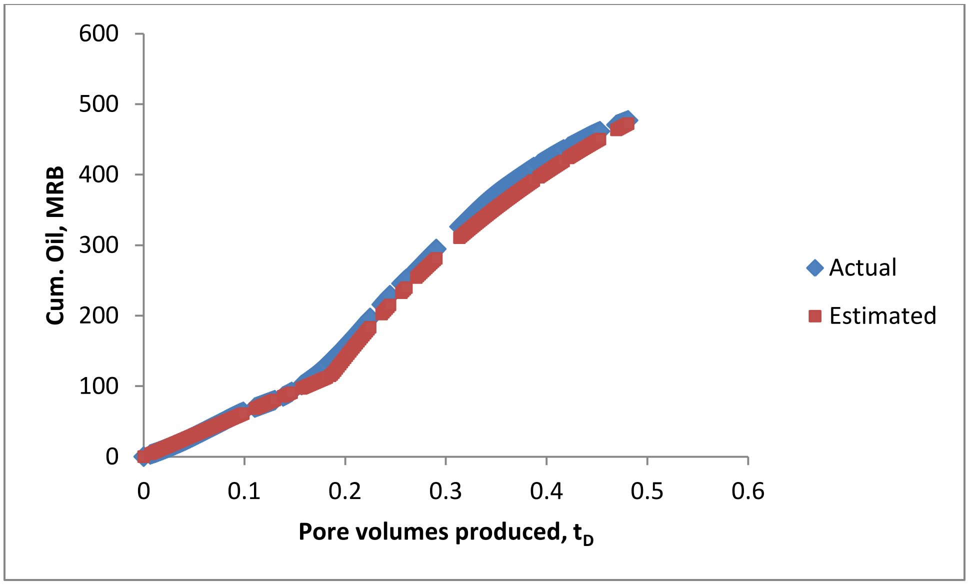

Figure 5-48. Polymer flooding history match of Daqing PO pilot. The pilot data is from Wang et al. 1993.

		Daqing PO	Chateaurenard	Marmul	North Burbank	Sleepy Hollow	Courtenay
Polymer bank Koval factor, K_b	New model	2.50	1.80	1.80	3.15	3.27	5.28
	Mollaei Model	1.85	4.53	3.53	2.29	2.87	4.60
Oil bank Koval factor, K_f	New model	3.88	3.51	2.88	13.09	16.37	9.8
	Mollaei model	1.75	1.08	1.03	5.01	2.10	2.07
Local front velocity, $v_{b,OB}$	New model	1.10	1.43	1.55	1.12	1.16	1.19
Local front velocity, $v_{f,OB}$	New model	2.98	2.72	2.95	3.86	2.40	3.13
Ultimate volumetric sweep, a	New model	0.55	0.65	0.66	0.54	0.51	0.50
Total pore volume, Vp (MMRB)	New model	3.10	0.87	4.99	23.00	70.00	16.93

Table 5-22. Summary of all polymer history match parameters.

The results of all the polymer history matches from the new model are summarized in Table 5-22. The estimated total pore volumes vary from 1 to 70 million reservoir barrels depending on the size of the pilot area. The ultimate volumetric sweep efficiencies vary from 0.5 to 0.7 for the pilots which are reasonable field estimates for the pilots. The ultimate volumetric sweep decreases with increasing Koval factors for the polymer bank as well as oil bank (Figure 5-49).

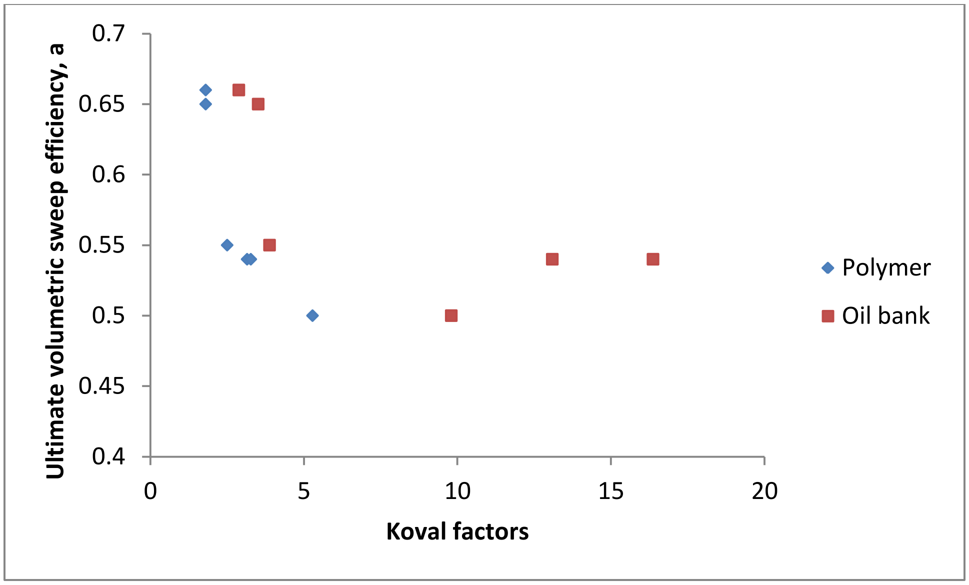

Figure 5-49. Ultimate volumetric sweep efficiency decreases with increase in Koval factors for polymer and oil bank.

Limitations of Mollaei's model

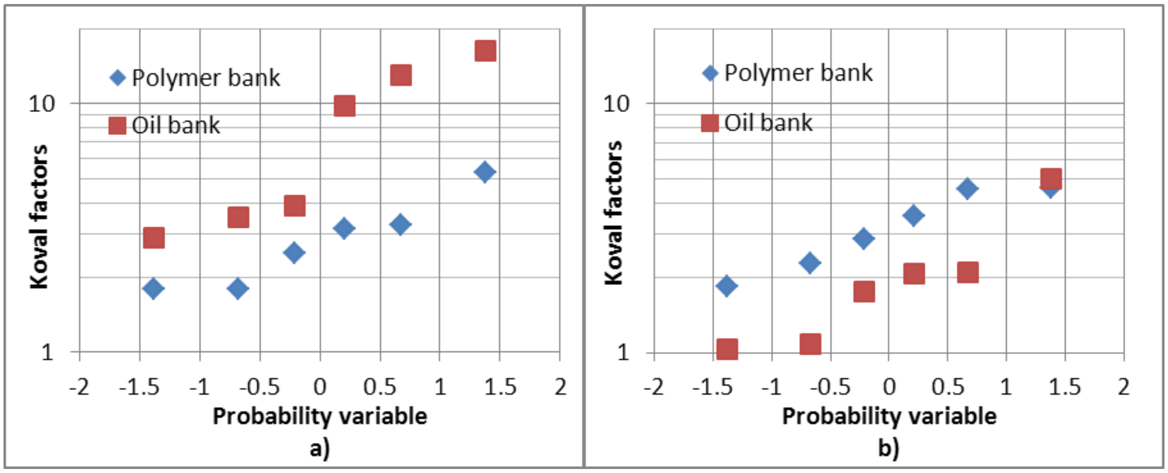

Figure 5-50. Polymer and oil bank Koval factors from a) new model and b) Mollaei's model. The polymer bank Koval factors from the new model are smaller than the oil bank Koval factors.

Polymers are injected to decrease the mobility ratio. Smaller mobility ratios at the polymer bank should result in smaller Koval factors compared to the oil bank Koval factors. The polymer bank Koval factors from the new model are smaller than the polymer bank Koval factors (Figure 5-50a) which is vice versa for Mollaei's model (Figure 5-50b). The limitation posed by Mollaei's model in capturing the physical impact of reduction in mobility ratio on polymer bank Koval factors is resolved in the new model.

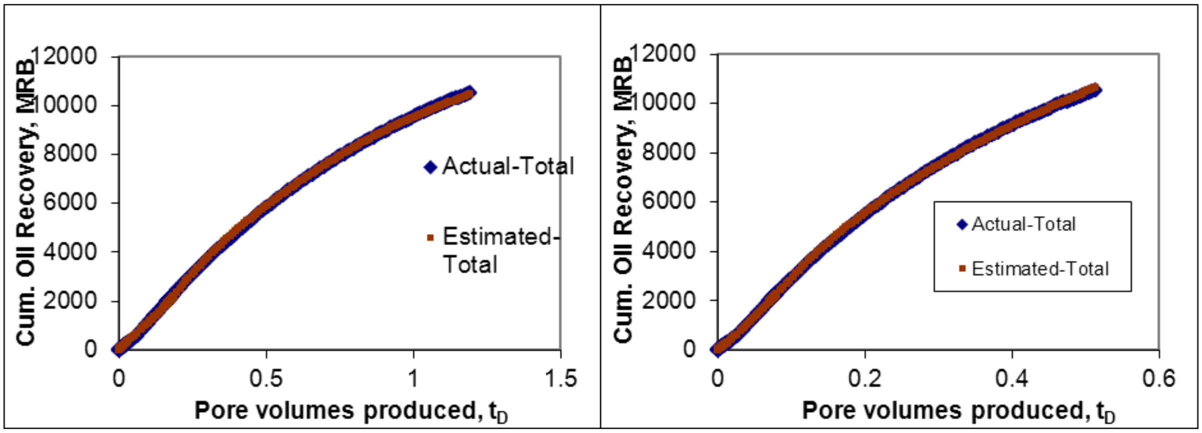

a) Solution 1 **b) Solution 2**

Figure 5-51. Non-unique solutions from Mollaei's model demonstrated using Sleepy Hollow pilot data.

	Mollaei's model		New model
	Solution 1 (a)	Solution 2 (b)	
Polymer bank Koval factor, K_b	3.77	7.59	3.27
Oil bank Koval factor, K_f	2.51	7.62	16.37
Local front velocity, v_b	1.27	1.27	1.16
Local front velocity v_f	3.32	12.22	2.40
Total pore volume, V_p (MMB)	**55.30**	**108.80**	70.00
Ultimate volumetric sweep, a	-	-	0.51

Table 5-23. Non-unique history matched parameters from Mollaei's model for Sleepy Hollow pilot shown in Figure 5-42.

Non-uniqueness is also a limitation with Mollaei's model. Figure 5-51 demonstrates the two history matched solutions for Sleepy Hollow polymer pilot. The two fronts for polymer floods in Mollaei's model are treated independently of each other thus resulting in non-unique solutions. The total pore volume estimates between Mollaei's solution 1 and solution 2 differ by a factor of 2 (Table 5-23). The Koval factors are very different for the two solutions along with the local front velocities. The non-uniqueness thus is a detriment if reservoir management decisions are to be made.

5.7.4 Solvent gas/WAG flood

Miscible water alternate gas (WAG) floods have been successfully implemented in the oil fields as an EOR technique. Miscible gas helps reduce the interfacial tension thereby decreasing the residual oil. The purpose of WAG injection is to increase sweep by reducing the effective mobility ratio between the injected gas and formation oil, which is a problem for miscible gas floods with early breakthrough and poor sweep (Mathiassen, 2003; Lake, 2008).

Several field cases for WAG floods are used for history matching of the model. The history matching procedure is the same as for polymer floods with the same number of matching parameters. The local scale front velocities are different for WAG floods (Walsh and Lake, 1989) compared to polymer floods (defined in the model development section for tertiary floods). Results of few published CO_2/WAG projects were history matched.

Slaughter WAG pilot

The Slaughter estate unit is located in Hockley County in the Permian basin of west Texas. The pilot area of the field contains continuous dense and permeable layers. The dense streaks also contain skeletal wackestones that are heterogeneous with various amounts of silt and organic material. The skeletal material has been replaced by anhydrite which results in lower peameability. The reservoir is approximately 4900 ft deep with net pay of 75 ft. The average formation permeability and porosity are 6.4 md and 0.12 respectively. The reservoir temperature is 105 F with average oil viscosity at 2 cp. Water injection in the pilot area with double five-spot pattern started in 1972. Water breakthrough occurred in six months after injection began and water cut increased to 80% in twelve months after water breakthrough. The water flood oil rate decline was very steep. The CO_2 WAG was started in 1976 in the pilot area with WAG ratio of 1:1 on a reservoir barrel basis. The tertiary oil production was first observed more than a year after solvent gas injection. The lengthy response time is because of thorough water flooding of the pilot. Tertiary incremental oil recovery was estimated to be 15% of OOIP. The history match between the field oil cut and model oil cut is good (Figure 5-52).

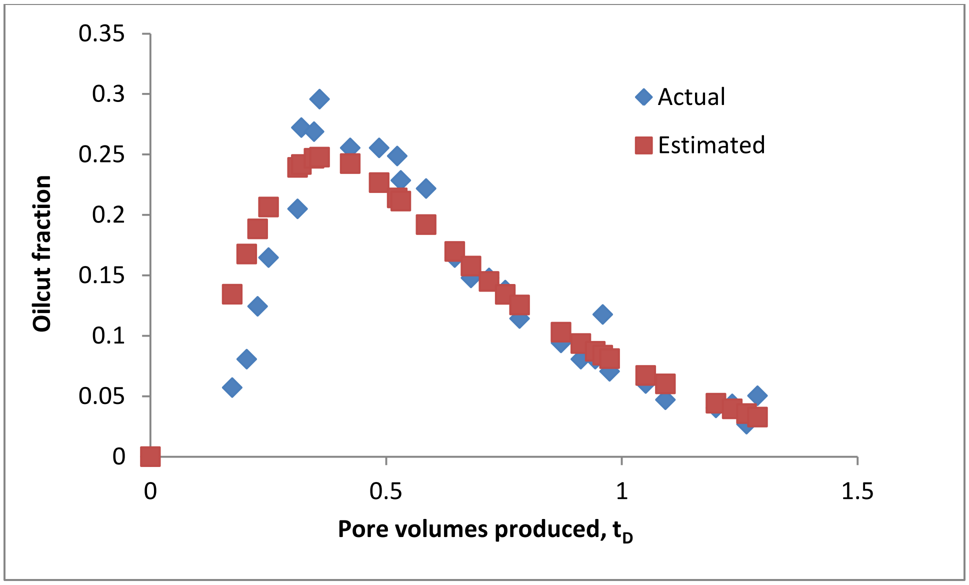

Figure 5-52. CO_2 WAG flood history match for Slaughter pilot (Rowe et al., 1982).

Rangely Field

The Rangely Weber Sand Unit is located in Rio Blanco County, Colorado. The field was discovered in 1933. The Rangely Weber formation consists of a series of interbedded eolian sandstones and fluvial siltstones at a depth between 5500 and 6500 ft. The average net thickness of the reservoir is 189 ft. The average porosity and permeability of the net sands is 0.12 and 8 md, respectively. The field started primary production in 1950 with primary drive mechanisms being fluid expansion and hydrocarbon gas reinjection for pressure maintenance. The peripheral water injection began in 1958 with field wide pattern water flood not starting until 1969. CO_2 injection started in 1986 at which time water cut from secondary recovery reached 95%.

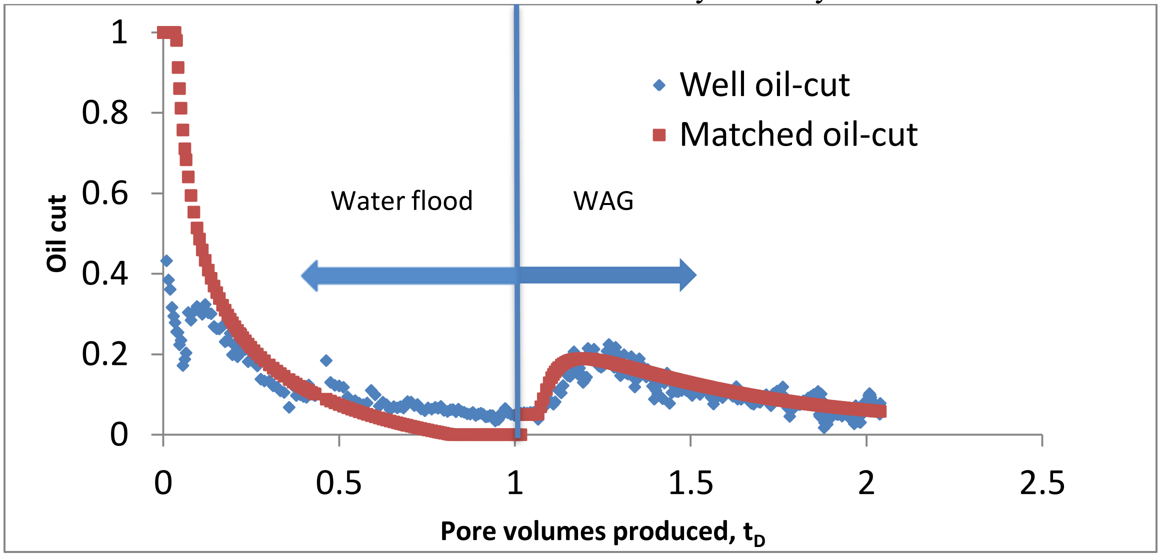

Figure 5-53. Waterflood and CO_2/WAG flood history matches for Well 1 in Rangely field.

		Slaughter	Twofreds	Lost Soldier	Rangely			
					Well 1	Well 2	Well 3	Well 4
Koval factor, K	Water flood	-	-	-	5.0	11.68	48.90	8.21
Solvent bank Koval factor, K_b	New model (WAG)	3.50	7.25	18.59	2.56	5.1	8.45	13.61
	Mollaei Model (WAG)	6.89	63.26	37.93	-	-	-	-
Oil bank Koval factor, K_f	New model (WAG)	5.25	14.59	51.07	5.79	10.1	19	27
	Mollaei Model (WAG)	3.04	5.56	6.05	-	-	-	-
Local front velocity , $v_{\Delta s}$	Water flood	-	-	-	5.5	2.28	2.08	5.0
Local front velocity, $v_{b,OB}$	New model (WAG)	1.88	1.7	1.33	1.34	1.34	1.14	1.15
Local front velocity, $v_{f,OB}$	New model (WAG)	3.8	3.34	4.64	2.64	1.65	2.67	2.39
Ultimate volumetric sweep, a	Water flood	-	-	-	0.95	0.91	0.63	0.7
	WAG	0.85	0.45	0.32	0.60	0.65	0.35	0.38
Total pore volume, Vp (MMRB)	Water flood	-	-	-	5.5	4.0	6.0	5.0
	WAG	1.25	33.7	299	5.26	4.09	5.8	5.1

Table 5-24. Summary of field/pilot/well history match parameters for CO_2/WAG floods.

Figure 5-53 shows the good history match for Well 1 in Rangely field. The waterflood oil cut drops drastically in the beginning to 0.2. Oil cut than shows an increase up to 0.3 followed by a gradual decrease (Figure 5-53). The trend is observed in the other three well history matches (Appendix D). The initial drop in oil cut may be attributed to some near wellbore problems during waterflooding. The history match for WAG flood shows a good match between the model and the field data. The ultimate volumetric sweep decreases by 35% when injection shifts from waterflood to WAG flood (Table 5-24). The total pore volume associated with Well 1 estimated from waterflood history match (5.5 MMRB) is very close to the value estimated from WAG flood history match (5.26 MMRB). The other history matches are shown in Appendix D.

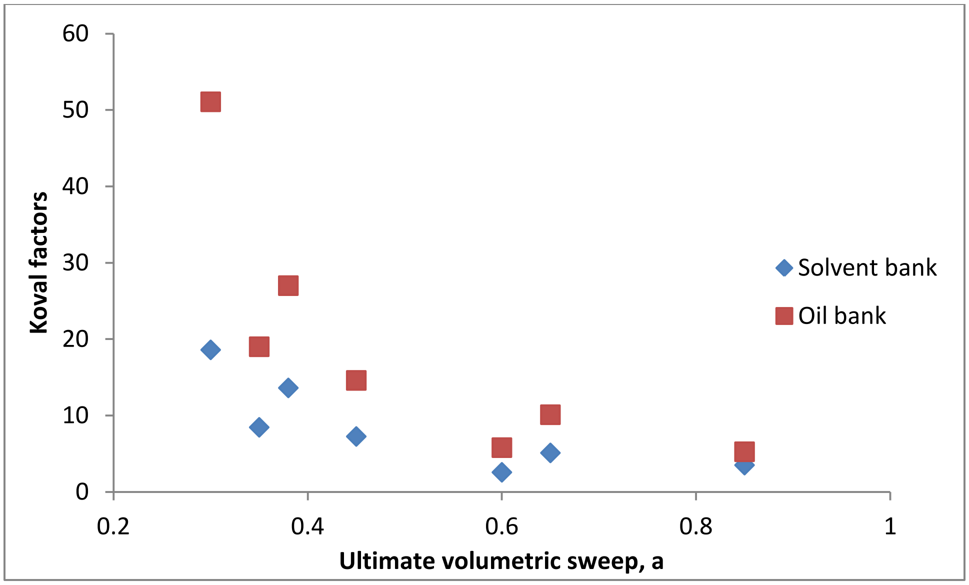

Figure 5-54. Field Koval factors for solvent bank and oil bank decrease with increasing ultimate volumetric sweep.

The results of all the WAG history matches from the new model are summarized in Table 5-23. The estimated total pore volumes vary from 1 to 5 million reservoir barrels depending on the size of the pilot area. The ultimate volumetric sweep efficiencies vary from 0.3 to 0.8 for the pilots which are reasonable field estimates for the pilots. The ultimate volumetric sweep decreases with increasing Koval factors for the solvent bank as well as oil bank (Figure 5-54).

5.8 SUMMARY

This work is primarily an exposition of a new method to upscale secondary and tertiary floods. The pixel scale information for upscaling depends on fractional flow theory therefore specific conclusions vary from case to case. The new models when applied to predict and compare reservoir performance will yield information about reservoir heterogeneity, mobility ratios, displacement sweep and ultimate volumetric sweep efficiency.

This analyses for secondary and tertiary floods leads to following novel contributions:

1) The new waterflood model when applied to field data yields information about average local displacement sweep, and ultimate volumetric sweep.
2) The method couples window scale reservoir heterogeneity with pixel scale information i.e local saturation changes.
3) The new tertiary flood model accounts for the interactions between the two fronts and can capture non-monotonous oil cut trend observed in the fields for tertiary floods. This interaction has never been accounted for at window scale.
4) The models are developed for secondary and tertiary displacements and can be used to make reservoir management decisions (displacement sweep and ultimate volumetric sweep efficiency).

CHAPTER 6

Conclusions and Future Work

6.1 CONCLUSIONS

6.1.1 Upscaling of miscible floods

The first objective of this research was to develop an upscaled model for tertiary miscible (WAG) flood performance evaluation. For tertiary WAG floods, the effects of long-range features such as channels or viscous fingering are captured through a heterogeneity factor and mobility ratios in the model. The effect of dispersion or short range heterogeneity on displacement is captured by the parameter called residual oil to miscible floods (S_{2RM}). The local change in saturation as predicted by local fractional flow theory is captured through the local front velocities in the model.

Few important contributions of the new model are:

- The upscaled model couples field scale heterogeneity with the mobility ratio and also honors the fine-scaled (local) information derived from fractional flow theory to predict reservoir effluent history.
- The new model, even though based on Koval's theory, captures the non-monotonic oil cut response at production wells because of oil bank formation for tertiary WAG floods.
- The fractional flow theory shows that the velocities of the two fronts depend on each other. This coupling between the two fronts is preserved at the reservoir scale in the new model. This coupling was neglected in the work by previous researchers.

- The effect of the coupling between the two fronts on effluent history is predominant in the reservoirs with large heterogeneity and large mobility ratios.
- The solvent bank front for small WAG ratio cases (high mobility ratio) moves fast and catches the oil bank front. It leads to instantaneous solvent breakthrough along with an immediate increase in oil cut. The solvent bank was never observed to overtake the oil bank for high heterogeneity and high mobility ratio cases.

6.1.2 Lost pore volume: Secondary and tertiary floods

The second objective of the research was to develop a fast and analytical upscaled model for secondary (waterflood) and tertiary (WAG and polymer) floods history matching and provide quantitative estimates of ultimate volumetric sweep. The upscaled models based on Koval's theory account for the effects of heterogeneity and mobility ratio on viscous instabilities that develop during secondary and tertiary floods. The new models also honor the impact of local saturation changes during waterfloods, polymer and WAG floods on recovery.

The secondary model for waterfloods depends on one Koval factor (K). The tertiary models for polymer and WAG floods depend on two Koval factors defined for two fronts (K_b and K_f).

Few important contributions of the new models are:

- Koval factors capture the effects of flow geometry or well ptterns on effluent history as demonstrated with line-drive and quarter five-spot patterns.
- The average oil saturations observed in the fields/pilots are larger than observed in the laboratory experiments. This observation suggests an existence of lost pore volume that would be inaccessible to the injected fluids. The swept and unswept parts of the reservoir were treated separately in the models. It also allowed for

integration of fine scale physics applicable for the flooded parts into the models for accurate history matching.

- The models for secondary and tertiary floods were able to successfully match field and numerical simulation results. The ultimate volumetric sweep estimated for tertiary polymer floods was higher than the ultimate waterflood volumetric sweep for all the simulation cases. Similarly, for WAG floods the ultimate volumetric sweep was estimated to be smaller than the waterflood ultimate volumetric sweep. The impact of mobility ratio on sweep was captured in the model.
- Ultimate volumetric sweep for waterfloods as well as tertiary polymer and WAG floods increases with decreasing Koval factors. Small Koval factors represent small heterogeneity and mobility ratio thus indicating uniform sweep.
- Koval factors obtained for waterfloods and tertiary floods (WAG and polymer floods) are directly proportional to each other for the same change in mobility ratios for all simulation cases. Polymer flood Koval factors were observed to be smaller than waterflood Koval factors on account of decrease in mobility ratio. WAG flood Koval factors were observed to be high compared to waterflood Koval factors on account of increase in mobility ratio.

6.1.3 Unified vertical equilibrium analysis

The models were developed under the vertical equilibrium assumption. The analytical proof of conditions required for total vertical equilibrium (viscous and dispersive) was derived for a two-dimensional, two phase, multicomponent compressible flow without neglecting gravity, the following conclusions were drawn:

- The dimensionless numbers R_L and N_{TD} must be larger than one for flow to achieve total equilibrium (viscous and dispersive) in transverse direction.
- The viscous and dispersive fluxs are additive so for total transverse equilibrium the potential gradient and concentration gradient must both be zero in vertical (transverse) direction.
- For gravity effects and capillary effects to be negligible, the gravity number (N_g) must be smaller than the inverse of R_L^2 and the capillary number (N_{CD}) must be smaller than the inverse of both R_L^2 and N_{TD}. These are stronger constraints than gravity number and capillary number being much smaller than unity as was previously known.

6.2 FUTURE WORK

- The model developed in this research can be extended to other displacements in porous media. The fractional flow theory (Noh et al., 2007) for CO_2 displacing brine suggests the formation of two travelling fronts in the porous media at the fine scale. The injected CO_2 creates a drying front (caused by mass transfer between CO_2 phase and aqueous phase) at the back and a Buckley-Levrett front ahead of it. The fine scale problem as posed above is similar to the tertiary two front displacements (WAG and polymer floods) studied in the research. The fine scale model can be applied to heterogeneous reservoirs and can be used to determine the time-weighted storage capacity for CO_2 storage in heterogeneous reservoirs similar to Jain and Bryant's, 2010 work on the subject for homogeneous reservoirs.
- The Koval factors obtained from the secondary flood model are correlated with the tertiary flood Koval factors as shown in chapter 5. The model can be extended

to generate a correlation surface to predict tertiary Koval factors for a given change in mobility ratio for polymer and WAG floods. The correlation between Koval factors between secondary and tertiary floods can be used to predict the tertiary flood performance. Koval factors are also inversely proportional to ultimate volumetric sweep. A correlation for the change in sweep efficiency can also be developed for changes in Koval factors between secondary and tertiary floods.

- The models developed are for isothermal displacements. The model can be extended to thermal floods (steam floods) by combining the heat loss models to predict performance.

Appendix A

A.1 DERIVATION OF MASS CONSERVATION EQUATIONS

Figure 4.5 shows the schematic of the fluid distribution in a layered reservoir at any given time.

We write the mass conservation equations averaged across the cross section shown in Figure 4-4b. The system shown in Figure 4-4 is 2-D but vertical equilibrium assumption allows for reduction in dimensionality of the equations to 1-D.

A water mass balance yields:

$$f_{1,J}\frac{\partial F_J}{\partial X_D}+f_{1,B}\frac{\partial F_B}{\partial X_D}+f_{1,I}\frac{\partial F_I}{\partial X_D}+S_{1,J}\frac{\partial C_J}{\partial t_D}+S_{1,B}\frac{\partial C_B}{\partial t_D}+S_{1,I}\frac{\partial C_I}{\partial t_D}=0 \tag{A.1}$$

A solvent mass balance yields:

$$(1-f_{1,J})\frac{\partial F_J}{\partial X_D}+(1-S_{1,J}-S_{2RM})\frac{\partial C_J}{\partial t_D}=0 \tag{A.2}$$

Other governing equations are:

$$F_J+F_B+F_I=1 \tag{A.3}$$

$$C_J+C_B+C_I=1 \tag{A.4}$$

where $f_{1,J}$, $f_{1,B}$ and $f_{1,I}$ is the brine fractional flow in Region *J*, *B* and *I* respectively at the pixel scale. $S_{1,J}$, $S_{1,B}$ and $S_{1,I}$ is the brine saturation in Region *J*, *B* and *I,* respectively, at the pixel scale. S_{2RM} is the residual oil to miscible floods in Region *J*. The parameters $f_{1,J}$, $f_{1,B}$, $f_{1,I}$, $S_{1,J}$, $S_{1,B}$, $S_{1,I}$ and S_{2RM} are constants from Walsh and Lake, 1988 and are derived from fractional flow theory as shown in Figure 4-1. Subscripts 1, 2 and 3 refer to brine, oil and solvent, respectively.

F_J is the fraction of total flow in the region containing C_J, F_B is the fraction of total flow in the region containing C_B, and F_I is the fraction of total flow in the region defined by C_I as shown in Figure A.1.

$$F_J, F_B \text{ and } F_I = f(C_J, C_B, C_I, H_k \text{ and Mobility Ratio}) \tag{A.5}$$

The detailed derivation of these terms are in Appendix B.

There are two degrees of freedom for the above defined system of equations at any given point in space and time. Thus the number of differential equations required to represent the system must be two. We combine equations A.1 to A.5 and derive a set of hyperbolic equations that are to be solved using the method of characteristics.

Substitute for F_B and C_B from equations A.3 and A.4 respectively into equation A.1.

$$(f_{1,J}-f_{1,B})\frac{\partial F_J}{\partial X_D}+(f_{1,I}-f_{1,B})\frac{\partial F_I}{\partial X_D}+(S_{1,J}-S_{1,B})\frac{\partial C_J}{\partial t_D}+(S_{1,I}-S_{1,B})\frac{\partial C_I}{\partial t_D}=0 \tag{A.6}$$

Rearranging equation A.6 gives,

$$(S_{1,J}-S_{1,B})\left[\frac{(f_{1,J}-f_{1,B})}{(S_{1,J}-S_{1,B})}\frac{\partial F_J}{\partial X_D}+\frac{\partial C_J}{\partial t_D}\right]+(S_{1,I}-S_{1,B})\left[\frac{(f_{1,I}-f_{1,B})}{(S_{1,I}-S_{1,B})}\frac{\partial F_I}{\partial X_D}+\frac{\partial C_I}{\partial t_D}\right]=0 \tag{A.7}$$

Rearranging equation A.2 gives,

$$(1-S_{1,J}-S_{2RM})\left[\frac{(1-f_{1,J})}{(1-S_{1,J}-S_{2RM})}\frac{\partial F_J}{\partial X_D}+\frac{\partial C_J}{\partial t_D}\right]=0 \tag{A.8}$$

The above equations can be simplified further by going back to the information available from the pixel scale. At the pixel scale, the fronts ahead and at the back of the oil bank have distinct velocities as shown in Figure 4-1. These pixel scale front velocities are defined as:

$$v_{f,OB}=\frac{f_{1,I}-f_{1,B}}{S_{1,I}-S_{1,B}},\ \text{Velocity at the front of the oil bank} \tag{A.9}$$

$$v_{b,OB}=\frac{f_{1,J}-f_{1,B}}{S_{1,J}-S_{1,B}}=\frac{1-f_{1,J}}{1-S_{1,J}-S_{2RM}},\ \text{Velocity at the back of the oil bank} \tag{A.10}$$

Using equations A.9 and A.10, a simplified version of equations A.7 and A.8 is written as:

$$(S_{1,J}-S_{1,B})\left[v_{b,OB}\frac{\partial F_J}{\partial X_D}+\frac{\partial C_J}{\partial t_D}\right]+(S_{1,I}-S_{1,B})\left[v_{f,OB}\frac{\partial F_I}{\partial X_D}+\frac{\partial C_I}{\partial t_D}\right]=0 \tag{A.11}$$

$$(1 - S_{1,J} - S_{2RM})\left[v_{b,OB} \frac{\partial F_J}{\partial X_D} + \frac{\partial C_J}{\partial t_D} \right] = 0 \tag{A.12}$$

Eq. A.12 is further reduced to:

$$v_{b,OB} \frac{\partial F_J}{\partial X_D} + \frac{\partial C_J}{\partial t_D} = 0 \tag{A.13}$$

Substituting A.13 in the R.H.S of equation A.11 would give,

$$(S_{1,I} - S_{1,B})\left[v_{f,OB} \frac{\partial F_I}{\partial X_D} + \frac{\partial C_I}{\partial t_D} \right] = 0 \tag{A.14}$$

Eq. A.14 yields:

$$v_{f,OB} \frac{\partial F_I}{\partial X_D} + \frac{\partial C_I}{\partial t_D} = 0 \tag{A.15}$$

Equations A.12 and A.14 shows an explicit coupling of pixel scale information ($v_{b,OB}$ and $v_{f,OB}$) with the reservoir scale information (F_J, F_I, C_J and C_I). The material balance for the upscaled system thus honors the information obtained at the pixel scale.

Appendix B

B.1 DEFINING FRACTIONAL FLOW IN EACH REGION (*J*, *B* AND *I*)

Table B.1 shows the fluid distribution along with the relative permeability information based on pixel scale information from fractional flow theory (Walsh and Lake, 1988).

Region	Oil saturation	Oil relative permeability	Water saturation	Water relative permeability	Solvent saturation	Solvent relative permeability
J	$S_{2,J}$	0	$S_{1,J}$	$k_{r1,J}$	$S_{3,J}$	$k_{r3,J}$
B	$S_{2,B}$	$k_{r2,B}$	$S_{1,B}$	$k_{r1,B}$	$S_{3,B}$	0
I	$S_{2,I}$	$k_{r2,I}$	$S_{1,I}$	$k_{r1,I}$	$S_{3,I}$	0

Table B.1. Saturation distribution in the three regions defined by fractional flow theory.

where subscript 1 refers to water, 2 refers to oil and 3 refers to solvent. Using Darcy's law, we can write the total fluid velocity in the three regions (*J*,*B* and *I*) at a point as:

$$u_{J,x} = -k\left(\frac{k_{r1,J}}{\mu_1} + \frac{k_{r3,J}}{\mu_3}\right)\frac{dP}{dx}, \qquad \text{velocity in region J} \tag{B.1}$$

$$u_{B,x} = -k\left(\frac{k_{r1,B}}{\mu_1} + \frac{k_{r2,B}}{\mu_2}\right)\frac{dP}{dx}, \qquad \text{velocity in region B} \tag{B.2}$$

$$u_{I,x} = -k\left(\frac{k_{r1,I}}{\mu_1} + \frac{k_{r2,I}}{\mu_2}\right)\frac{dP}{dx}, \qquad \text{velocity in region I} \tag{B.3}$$

where *k* is the absolute permeability at the given point and *x* denotes the flow direction. Integrating these velocities along the cross section shown in Figure 4.5 will give the total flowrates per unit width of the reservoir for each region.

$$U_J = \int_0^{h_J}\left(-k\left(\frac{k_{r1,J}}{\mu_1} + \frac{k_{r3,J}}{\mu_3}\right)\frac{dP}{dx}\right)\mathrm{dh} \tag{B.4}$$

$$U_B = \int_{h_J}^{h_J+h_B}\left(-k\left(\frac{k_{r1,B}}{\mu_1} + \frac{k_{r2,B}}{\mu_2}\right)\frac{dP}{dx}\right)dh \tag{B.5}$$

$$U_I = \int_{h_J+h_B}^{H}\left(-k\left(\frac{k_{r1,I}}{\mu_1} + \frac{k_{r2,I}}{\mu_2}\right)\frac{dP}{dx}\right)dh \tag{B.6}$$

where, h_J is the height of region J flooded with solvent, h_B is the height of region B occupied by oil bank and h_I is the height of region I occupied with resident oil and water. The total flowrate per unit width (superficial velocity) is given by:

$$U_t = U_J + U_B + U_I \tag{B.7}$$

Let's define total fluid mobility in each region as:

$$\lambda_J = \frac{k_{r1,J}}{\mu_1} + \frac{k_{r3,J}}{\mu_3}, \quad \text{Total fluid mobility in Region J} \tag{B.8}$$

$$\lambda_B = \frac{k_{r1,B}}{\mu_1} + \frac{k_{r2,B}}{\mu_2}, \quad \text{Total fluid mobility in Region B} \tag{B.9}$$

$$\lambda_I = \frac{k_{r1,I}}{\mu_1} + \frac{k_{r2,I}}{\mu_2}, \quad \text{Total fluid mobility in Region I} \tag{B.10}$$

Assuming vertical equilibrium in the absence of gravity segregation, the pressure gradient along the cross section would be the same (Lake, 1989).

$$\frac{\partial}{\partial y}\left(\frac{\partial P}{\partial x}\right) = 0 \tag{B.11}$$

Thus the total fractional flow in Region J, (F_J) would then be given by:

$$F_J = \frac{U_J}{U_t} = \frac{\int_0^{h_J} k\lambda_J dh}{\int_0^{h_J} k\lambda_J dh + \int_{h_J}^{h_J+h_B} k\lambda_B dh + \int_{h_J+h_B}^{H} k\lambda_I dh} = \frac{\lambda_J \int_0^{h_J} kdh}{\lambda_J \int_0^{h_J} kdh + \lambda_B \int_{h_J}^{h_J+h_B} kdh + \lambda_I \int_{h_J+h_B}^{H} kdh} \tag{B.12}$$

The total fluid mobilities in each region are constant because saturations within the regions are invariable. Thus, the heterogeneity representative of the window scale is decoupled from the pixel scale mobility ratios unlike the original Koval model (1963). The individual integrals in the equation B.12 are related to the cumulative flow capacity as defined as follows (Chapter 4, equation 4.17):

$$\int_0^{h_J} k\,dh = \frac{\int_0^{H} k\,dh}{1+\frac{1-C_J}{H_k C_J}} \tag{B.13}$$

$$\int_{h_J}^{h_J+h_B} k\,dh = \int_0^{H} k\,dh \left(\frac{1}{1+\frac{1-(C_J+C_B)}{H_k(C_J+C_B)}} - \frac{1}{1+\frac{1-C_J}{H_k C_J}} \right) \tag{B.14}$$

$$\int_{h_B}^{H} k\,dh = \int_0^{H} k\,dh \left(1 - \frac{1}{1+\frac{1-(C_J+C_B)}{H_k(C_J+C_B)}} \right) \tag{B.15}$$

Substituting equations B.13 to B.15 in equation B.12 would give:

$$F_J = \frac{C_J}{C_J + \left[\frac{\lambda_B}{\lambda_J}\right]\left[\frac{1}{1+(H_k-1)(C_J+C_B)}\right]C_B + \left[\frac{\lambda_I}{\lambda_J}\right]\left[\frac{1+(H_k-1)C_J}{1+(H_k-1)(C_J+C_B)}\right]\left[\frac{1}{H_k}\right]C_I} \tag{B.16}$$

Similarly, the total fractional flow in Region *B* (F_B) and Region *I* (F_I) would be given by:

$$F_B = \frac{C_B}{\left[\frac{\lambda_J}{\lambda_B}\right]\left[1+(H_k-1)(C_J+C_B)\right]C_J + C_B + \left[\frac{\lambda_I}{\lambda_B}\right]\left[\frac{1+(H_k-1)C_J}{H_k}\right]C_I} \tag{B.17}$$

$$F_I = \frac{C_I}{\left[\frac{\lambda_J}{\lambda_I}\right]\left[\frac{1+(H_k-1)(C_J+C_B)}{1+(H_k-1)C_J}\right]\left[H_k\right]C_J + \left[\frac{\lambda_B}{\lambda_I}\right]\left[\frac{H_k}{1+(H_k-1)C_J}\right]C_B + C_I} \tag{B.18}$$

and,

$$F_J + F_B + F_I = 1 \tag{B.19}$$

$$C_J + C_B + C_I = 1 \tag{B.20}$$

The mobility ratio at the front of the oil bank is given by:

$$MR_f = \frac{\lambda_B}{\lambda_I} \tag{B.21}$$

The mobility ratio at the back of the oil bank is given by:

$$MR_b = \frac{\lambda_J}{\lambda_B} \tag{B.22}$$

Using the mobility ratio definition, we rewrite equations B.16 to B.18 as follows:

$$F_J = \frac{C_J}{C_J + \left[\frac{1}{MR_b}\right]\left[\frac{1}{1+(H_k-1)(C_J+C_B)}\right]C_B + \left[\frac{1}{MR_f MR_b}\right]\left[\frac{1+(H_k-1)C_J}{1+(H_k-1)(C_J+C_B)}\right]\left[\frac{1}{H_k}\right]C_I} \tag{B.23}$$

$$F_B = \frac{C_B}{\left[MR_b\right]\left[1+(H_k-1)(C_J+C_B)\right]C_J + C_B + \left[MR_f\right]\left[\frac{1+(H_k-1)C_J}{H_k}\right]C_I} \tag{B.24}$$

$$F_I = \frac{C_I}{\left[MR_f MR_b\right]\left[\frac{1+(H_k-1)(C_J+C_B)}{1+(H_k-1)C_J}\right]\left[H_k\right]C_J + \left[MR_f\right]\left[\frac{H_k}{1+(H_k-1)C_J}\right]C_B + C_I} \tag{B.25}$$

Appendix C

AUTOMATIC HISTORY MATCHING ALGORITHM

The tertiary displacements model defined in Chapter 5 is a six parameter model. The standard optimization algorithms available in Microsoft excel or MATLAB such as simplex and reduced gradient methods cannot be used for this problem. The problem involves a set of differential equations that cannot be solved to obtain a closed form analytical solution. The optimization problem is also non-linear.

The set of equations to be solved for the optimization are

$$v_{f,OB}\frac{\partial F_I}{\partial x_D}+\frac{\partial C_I}{\partial t_D}=0 \tag{C.1}$$

$$v_{b,OB}\frac{\partial F_J}{\partial x_D}+\frac{\partial C_J}{\partial t_D}=0 \tag{C.2}$$

$$F_J=\frac{C_J}{C_J+\dfrac{C_B}{K_b}+\dfrac{C_I}{K_f a}} \tag{C.3}$$

$$F_I=\frac{C_I}{K_f a C_J+\dfrac{K_f a}{K_b}C_B+C_I} \tag{C.4}$$

$$C_J+C_B+C_I=a \tag{C.5}$$

Miscible WAG floods

$$v_{f,OB}=\frac{f_{1,I}-f_{1,B}}{S_{1,I}-S_{1,B}} \tag{C.6}$$

$$v_{b,OB}=\frac{f_{1,J}-f_{1,B}}{S_{1,J}-S_{1,B}}=\frac{1-f_{1,J}}{1-S_{1,J}-S_{ORM}}=\frac{1-f_{1,B}}{1-S_{1,B}-S_{ORM}} \tag{C.7}$$

Equations C.6 and C.7 are solved for $f_{1,B}$ (Equation C.7) in terms of all the input/history matched parameters for miscible WAG floods.

$$f_{1,B}=\frac{v_{f,OB}-v_{b,OB}f_{1,I}-v_{f,OB}v_{b,OB}(1-\mathrm{S}_{1,I}-\mathrm{S}_{ORM})}{v_{f,OB}-v_{b,OB}} \tag{C.8}$$

Polymer floods

$$v_{f,OB} = \frac{f_{1,I} - f_{1,B}}{S_{1,I} - S_{1,B}} \qquad \text{(C.9)}$$

$$v_{b,OB} = \frac{f_{1,B}}{S_{1,B}} = \frac{1}{1 - S_{OF}} \qquad \text{(C.10)}$$

Equations C.9 and C.10 are solved for $f_{1,B}$ (Equation C.11) in terms of all the input/history matched parameters for polymer floods.

$$f_{1,B} = \frac{v_{b,OB} v_{f,OB} S_{1,I} - f_{1,I} v_{b,OB}}{v_{f,OB} - v_{b,OB}} \qquad \text{(C.11)}$$

The boundary conditions are

$$C_J(x_D = 0, t_D) = a \quad \text{and} \quad C_I(x_D = 0, t_D) = 0 \qquad \text{(C.12)}$$

The initial conditions are

$$C_I(x_D, t_D = 0) = a \quad \text{and} \quad C_J(x_D, t_D = 0) = 0 \qquad \text{(C.13)}$$

The equations can be solved using the method of characteristics (MOC), but the MOC poses the following problems for automatic history matching:

1. Equations C.1 and C.2 pose as a two component MOC problem. The solution to such a problem is shown in Chapter 4 on a ternary plot Figure 5-6. The physical solution must be identified manually on the ternary plot because of the discontinuity in the solution where the slow path meets the fast path. Identifying the discontinuity manually is the first problem for automatic history matching. The insights obtained from MOC have been discussed in Chapter 4.
2. If the solution to the above problem is a shock then the shock placement depends on a discrete material balance across the shock while satisfying the Lax's conditions. Thus using MOC shock poses another problem for automatic history matching because shock placement has to be done manually.

Thus, the differential equations are solved numerically using finite differences. Equations C.1 and C.2 are further simplified for application of finite difference numerical solution.

$$v_{f,OB}\frac{\partial F_I}{\partial C_I}\frac{\partial C_I}{\partial x_D}+v_{f,OB}\frac{\partial F_I}{\partial C_J}\frac{\partial C_J}{\partial x_D}+\frac{\partial C_I}{\partial t_D}=0 \tag{C.14}$$

$$v_{b,OB}\frac{\partial F_J}{\partial C_I}\frac{\partial C_I}{\partial x_D}+v_{b,OB}\frac{\partial F_J}{\partial C_J}\frac{\partial C_J}{\partial x_D}+\frac{\partial C_J}{\partial t_D}=0 \tag{C.15}$$

The above set of equations is solved using explicit scheme

$$C_{\mathrm{I},i}^{n+1}=C_{\mathrm{I},i}^{n}-\left(\frac{t_D^{n+1}-t_D^{n}}{x_{D_{i+1}}-x_{D_i}}\right)\left[v_{f,OB}\left(\frac{\partial F_I}{\partial C_I}\right)_i^n\left(C_{I,i+1}^{n}-C_{I,i}^{n}\right)+v_{f,OB}\left(\frac{\partial F_I}{\partial C_J}\right)_i^n\left(C_{\mathrm{J},i+1}^{n}-C_{\mathrm{J},i}^{n}\right)\right] \tag{C.16}$$

$$C_{J,i}^{n+1}=C_{J,i}^{n}-\left(\frac{t_D^{n+1}-t_D^{n}}{x_{D_{i+1}}-x_{D_i}}\right)\left[v_{b,OB}\left(\frac{\partial F_J}{\partial C_I}\right)_i^n\left(C_{I,i+1}^{n}-C_{I,i}^{n}\right)+v_{b,OB}\left(\frac{\partial F_J}{\partial C_J}\right)_i^n\left(C_{\mathrm{J},i+1}^{n}-C_{\mathrm{J},i}^{n}\right)\right] \tag{C.17}$$

$$C_{B,i}^{n+1}=a-C_{J,i}^{n+1}-C_{I,i}^{n+1} \tag{C.18}$$

where, *n* refers to the n^{th} time step from the beginning (n=0) and *i* refers to the spatial location of the i^{th} gridblock from the injection face. The total number of gridblocks in *x* the direction is N_{gird}. The F_J and F_I at n+1 timestep are

$$F_{J,N_{grid}}^{n+1}=\frac{C_{J,N_{grid}}^{n+1}}{C_{J,N_{grid}}^{n+1}+\dfrac{C_{B,N_{grid}}^{n+1}}{K_b}+\dfrac{C_{I,N_{grid}}^{n+1}}{K_f a}} \tag{C.19}$$

$$F_{I,N_{grid}}^{n+1}=\frac{C_{I,N_{grid}}^{n+1}}{K_f a C_{J,N_{grid}}^{n+1}+\dfrac{K_f a}{K_b}C_{B,N_{grid}}^{n+1}+C_{I,N_{grid}}^{n+1}} \tag{C.20}$$

$$F_{B,N_{grid}}^{n+1}=1-F_{J,N_{grid}}^{n+1}-F_{I,N_{grid}}^{n+1} \tag{C.21}$$

The oil cut at n+1 timestep is

$$Oilcut(t_D^{n+1})=(1-f_{1,B})F_{B,N_{grid}}^{n+1}+(1-f_{1,\mathrm{I}})F_{\mathrm{I},N_{grid}}^{n+1} \tag{C.22}$$

The history matching algorithm has been adapted from Coats and Dempsy, (1970) work on the subject. Their work lies on the premise of developing a linear error surface for oil cut at each timestep.

Algorithm steps

1.) Set an upper and lower bound for each of the six history match parameter.

$$f_o(t_D)\big|_{x_D=1} = f(K_b, K_f, v_{\mathrm{b},OB}, v_{f,OB}, a, Vp) \qquad \text{(C.23)}$$

2.) Assume a uniform distribution for each parameter between the lower and upper bound.

3.) Prepare N_{set} number of sets with each set comprising of all the six history match parameter chosen randomly from the distributions. The number N_{set} for all the history matches was chosen to be 100 because it provided reasonable oil cut history matches. The total number of sets chosen can be varied depending upon the quality of the history match.

$$y_l = \begin{bmatrix} K_{b,l} \\ K_{f,l} \\ v_{b,OB,l} \\ v_{f,OB,l} \\ a_l \\ Vp_l \end{bmatrix} \qquad l \text{ refers to the } l^{\text{th}} \text{ set of parameters from } N_{set} \qquad \text{(C.24)}$$

4.) Calculate the oil cut for each of the N_{set} at all given times.

5.) Calculate the error between the calculated oil cut and the field oil cut for each of the N_{set}'s at all the given times.

$$error, e_l^n = f_{o,\mathrm{model}}(t_D^n) - f_{o,true}(t_D^n) \qquad \text{(C.25)}$$

where, n refers to the time step and l refers to the parameter set used for oil cut calculation.

6.) Fit the linear function defining the error at each timestep.

$$e_l^n = b_1^n + b_2^n K_{b,l} + b_3^n K_{f,l} + b_4^n v_{b,OB,l} + b_5^n v_{f,OB,l} + b_6^n a_l + b_7^n PV_l \tag{C.26}$$

or

$$e_l^n = \begin{bmatrix} 1 & y_l^T \end{bmatrix} \begin{bmatrix} b_1^n \\ b_2^n \\ b_3^n \\ b_4^n \\ b_5^n \\ b_6^n \\ b_7^n \end{bmatrix} = \begin{bmatrix} 1 & y_l^T \end{bmatrix} B^n \tag{C.27}$$

where,

$$B^n = \begin{bmatrix} b_1^n \\ b_2^n \\ b_3^n \\ b_4^n \\ b_5^n \\ b_6^n \\ b_7^n \end{bmatrix} \tag{C.28}$$

7.) Perform linear regression at each timestep to generate the error surface

$$E^n = \begin{bmatrix} e_1^n \\ e_2^n \\ e_3^n \\ . \\ . \\ . \\ e_{N_{set}}^n \end{bmatrix} = \begin{bmatrix} 1 & y_1^T \\ 1 & y_2^T \\ 1 & y_3^T \\ . & \\ . & \\ . & \\ 1 & y_{N_{set}}^T \end{bmatrix} B^n = YB^n \tag{C.29}$$

$$B^n = \left(Y^T Y\right)^{-1} Y^T E^n \tag{C.30}$$

The coefficients for the error surface at each time step are calculated using equation (C.30).

8.) Repeat steps 5 to 8 for each time.

9.) Obtain the optimum history match parameters by minimizing the total error

$$Min \quad (\sum_{n=1}^{I}\left|e^n\right|) = Min \quad \left(\sum_{n=1}^{I}\left|\begin{bmatrix}1 & y^T\end{bmatrix}B^n\right|\right) \tag{C.31}$$

Constraints:

$$\begin{array}{lll} v_{f,OB} > v_{b,OB} & f_{1,B} < f_{1,I} & f_{1,B} > 0 \\ S_{1,B} < S_{1,I} & S_{1,B} > 0 & \end{array} \tag{C.32}$$

where, I is the total number of time steps. The optimal parameter set $y_{optimal}$ is obtained after minimizing the error over all the time steps.

Appendix D

WATERFLOOD HISTORY MATCHES

Reservoir Sand C4

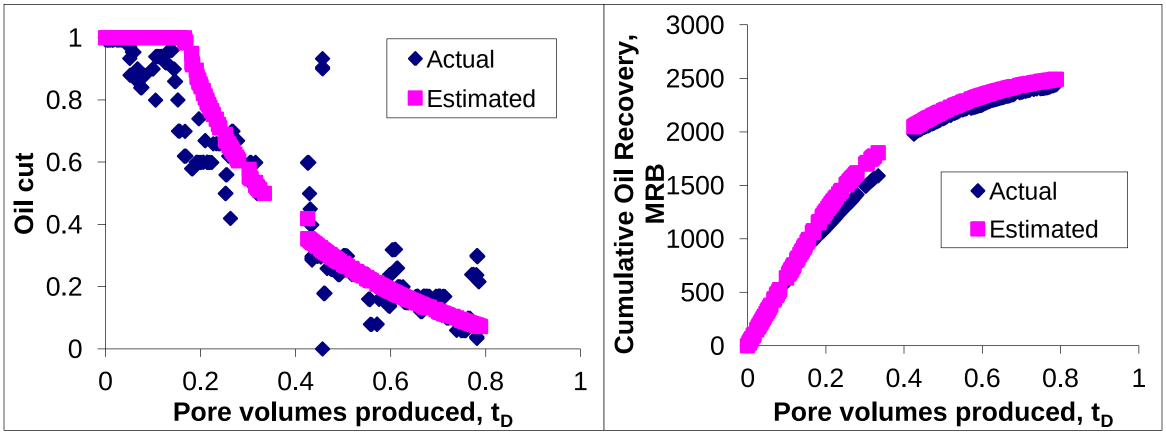

Figure D.1. Waterflood history match for a single well (Well 2) in the reservoir (Sand-C4)

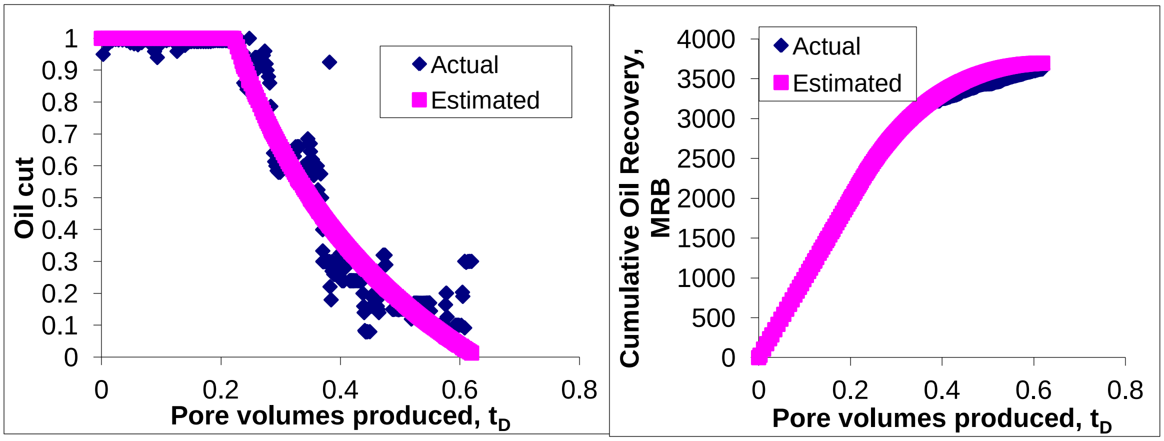

Figure D.2. Waterflood history match for a single well (Well 3) in the reservoir (Sand-C4).

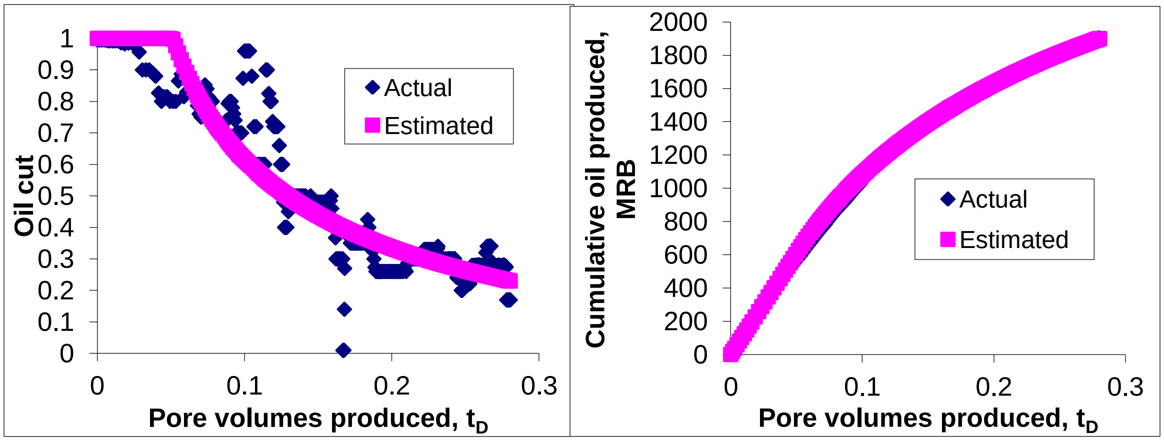

Figure D.3. Waterflood history match for a single well (Well 4) in the reservoir (Sand-C4).

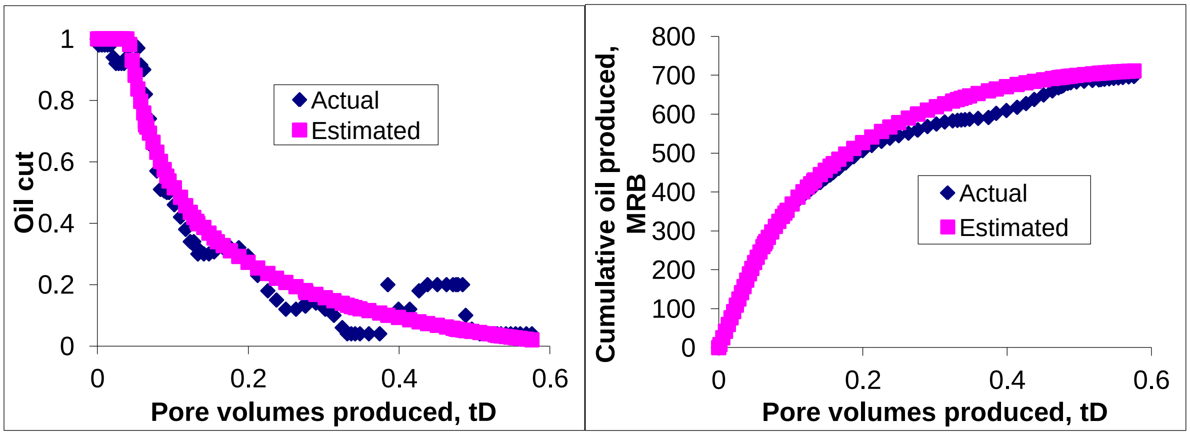

Figure D.4. Waterflood history match for a single well (Well 5) in the reservoir (Sand-C4).

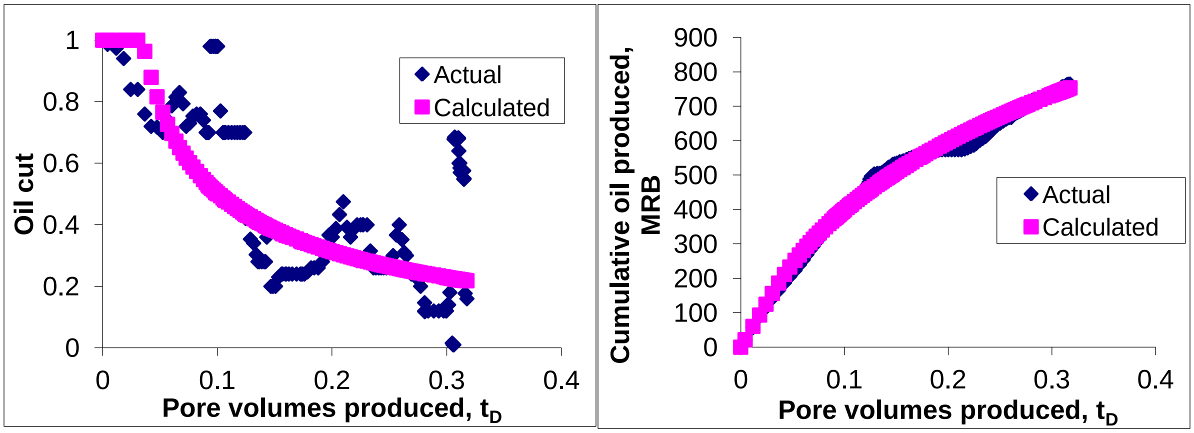

Figure D.5. Water lood history match for a single well (Well 6) in the reservoir (Sand-C4).

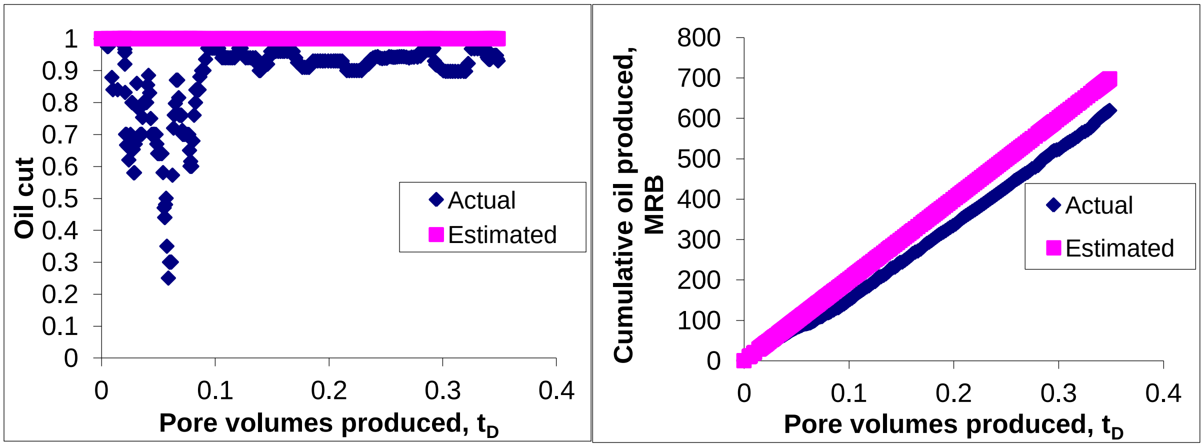

Figure D.6. Waterflood history match for a single well (Well 7) in the reservoir (Sand-C4). The oil cut never starts to decline after the plateau for this well so the parameters estimated from history matching are unreliable.

Reservoir Sand C5

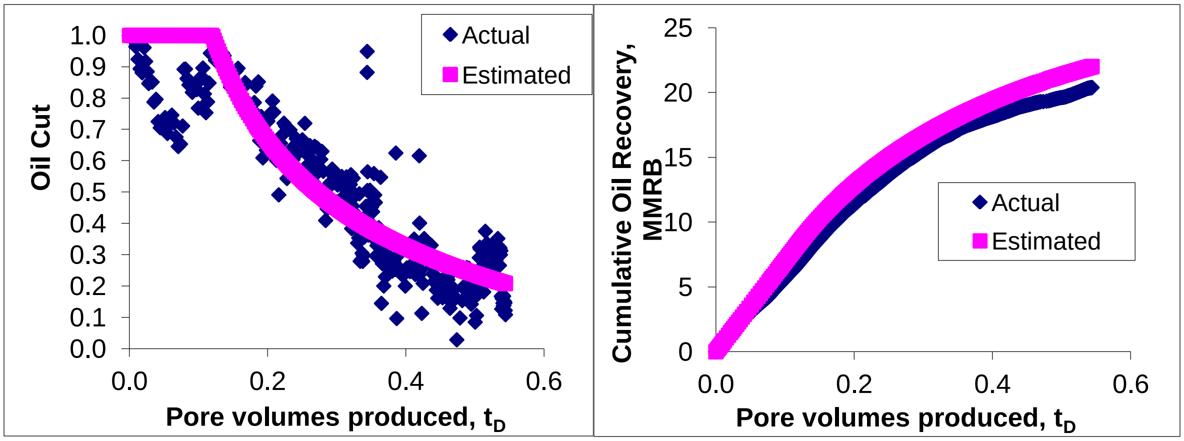

Figure D.7. Waterflood history match for the whole reservoir sand C5.

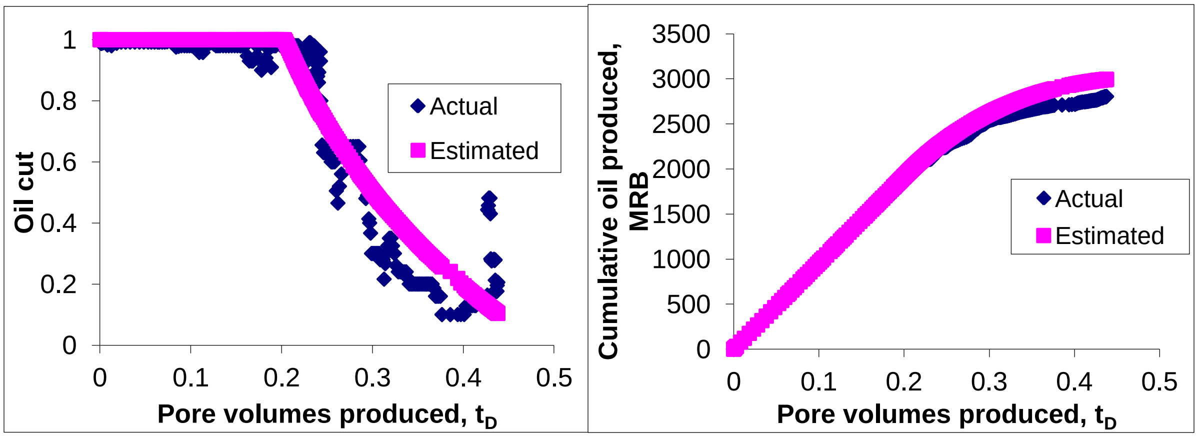

Figure D.8. Waterflood history match for a single well (Well 1) in the reservoir (Sand C5).

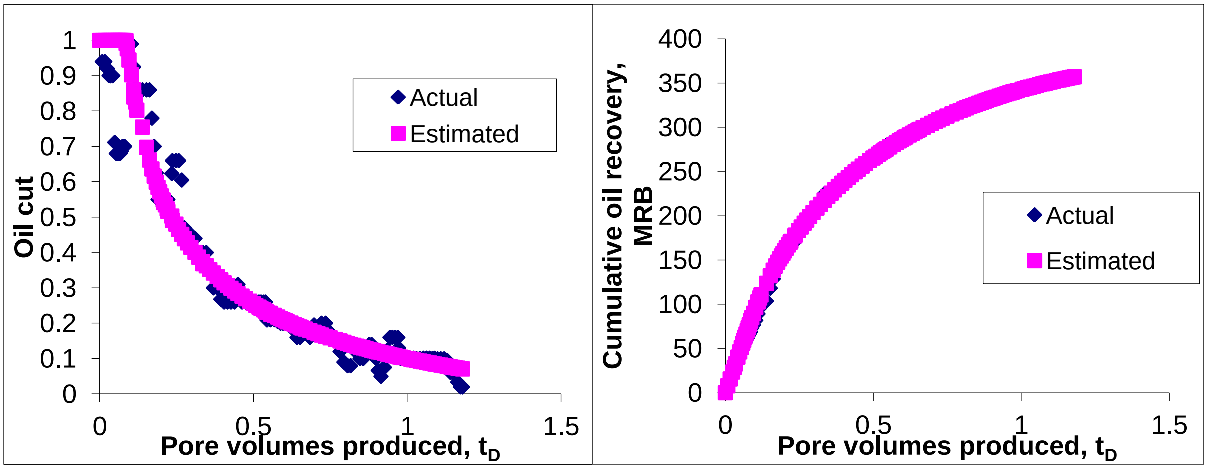

Figure D.9. Waterflood history match for a single well (Well 2) in the reservoir (Sand C5).

Reservoir Sand C6

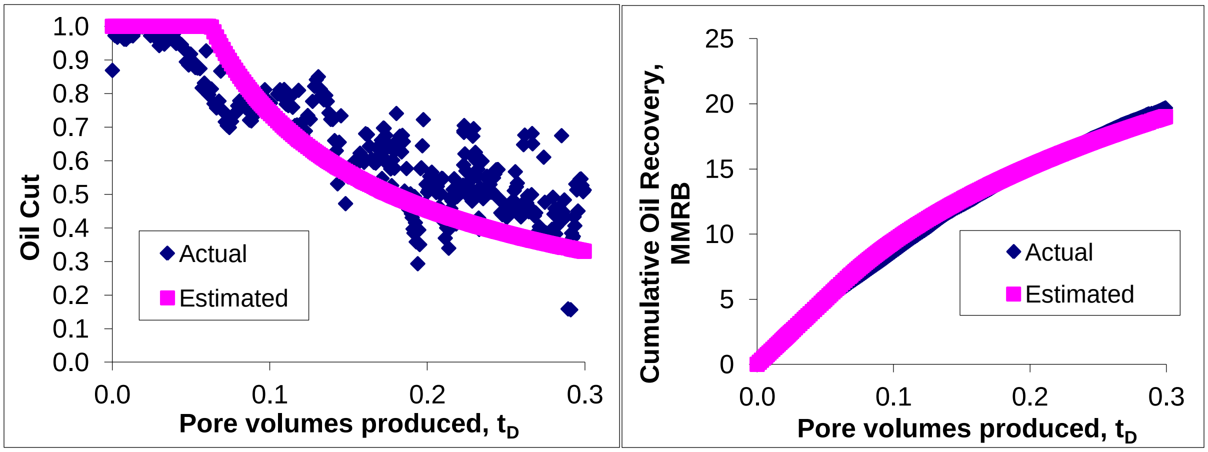

Figure D.10. Waterflood history match for the whole reservoir sand C6.

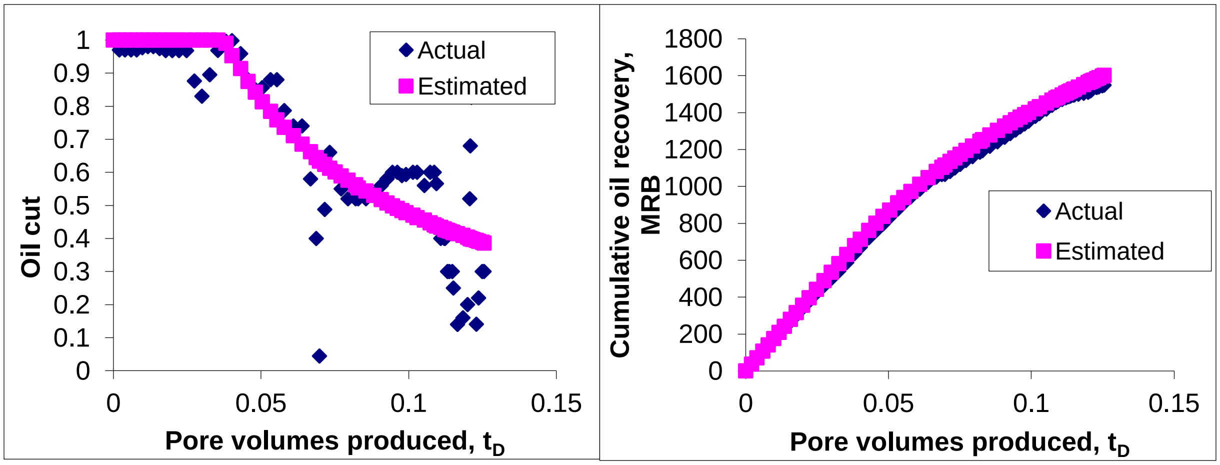

Figure D.11. Waterflood history match for a single well (Well 1) in the reservoir (Sand C6).

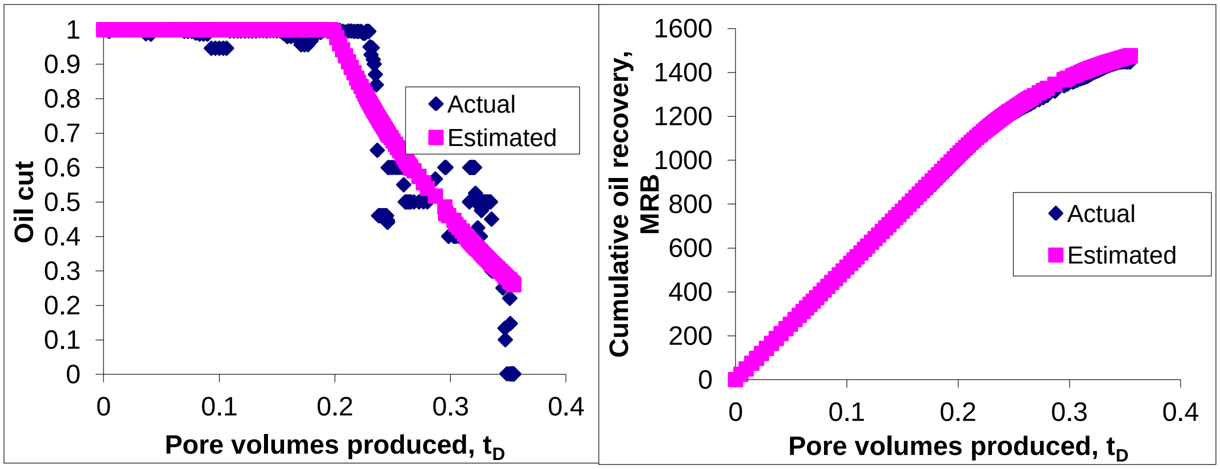

Figure D.12. Waterflood history match for a single well (Well 2) in the reservoir (Sand C6).

Reservoir Sand C7

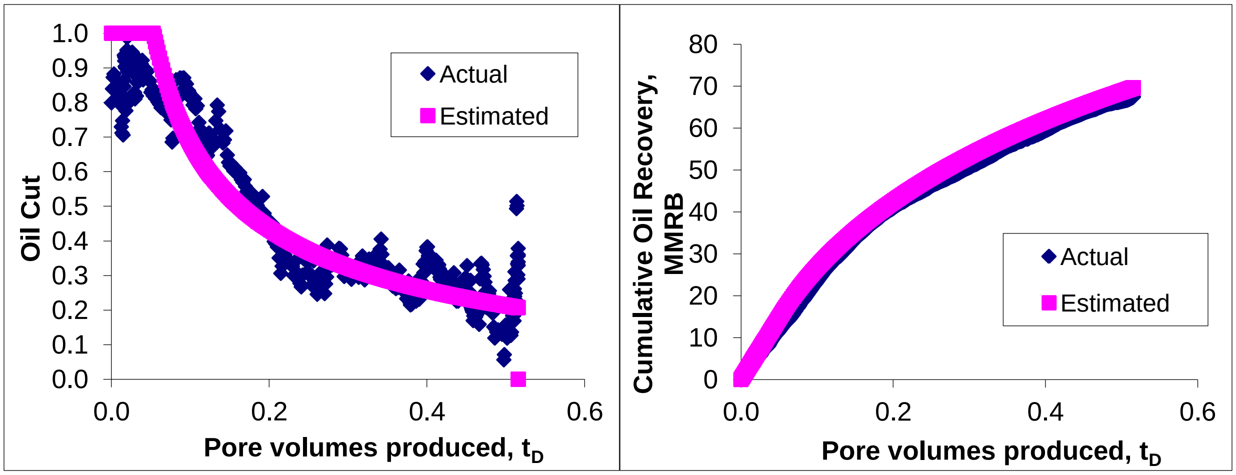

Figure D.13. Waterflood history match for the whole reservoir sand C7.

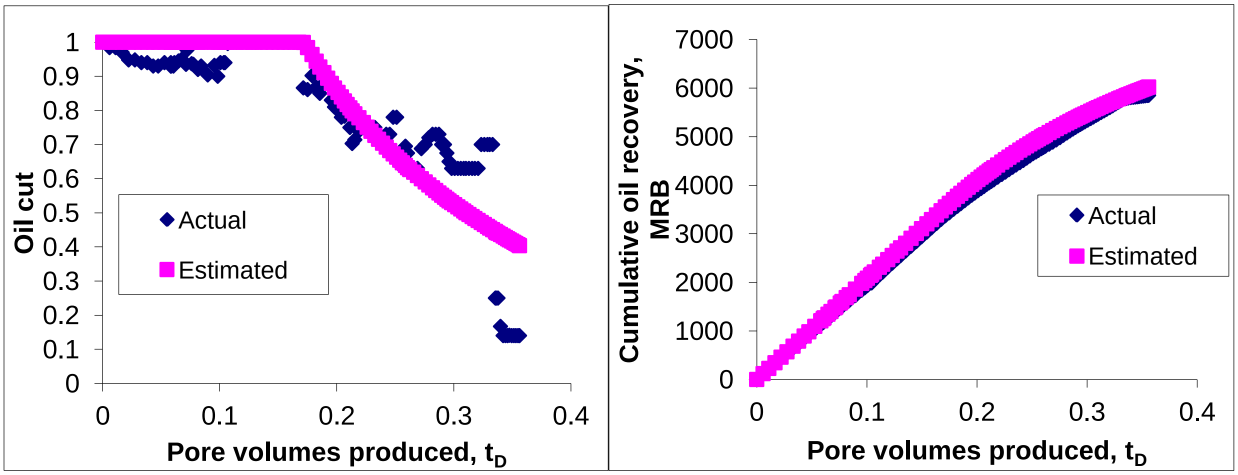

Figure D.14. Waterflood history match for a single well (Well 1) in the reservoir (Sand C7).

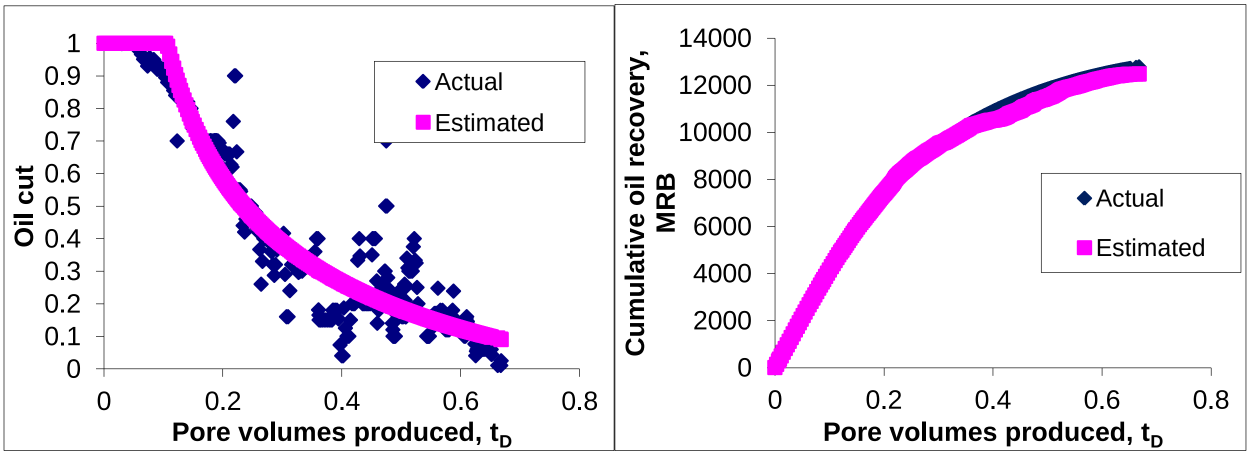

Figure D.15. Waterflood history match for a single well (Well 2) in the reservoir (Sand C7).

POLYMER FLOOD HISTORY MATCHES

Chateaurenard field pilot

Chateaurenard field is part of the Neocomian (Lower Cretaceous) oil reservoirs located in the southern part of the Paris Basin (France). The reservoir sand is unconsolidated with clay at 2 to 15%. The average total reservoir thickness of the reservoir is 15 ft with a porosity of 30%. The average permeability of the reservoir sand is high at 1000 md on account of channel type sedimentation and unconsolidated sands. The oil viscosity is 40 cp at reservoir temperature of 86 F. The field was discovered in 1958. The field started producing in 1960. The initial drive mechanism was edge water drive but low dip along with adverse mobility ratio caused early water production. The polymer injection in the first pilot began in 1977. Until 1979 the water cut was at 90% but after that the water cut dropped by 20% in the pilot area. The improvement in mobility ratio had a significant impact on the oil recovery. The results of the pilot with the history match are shown in Figure D.16.

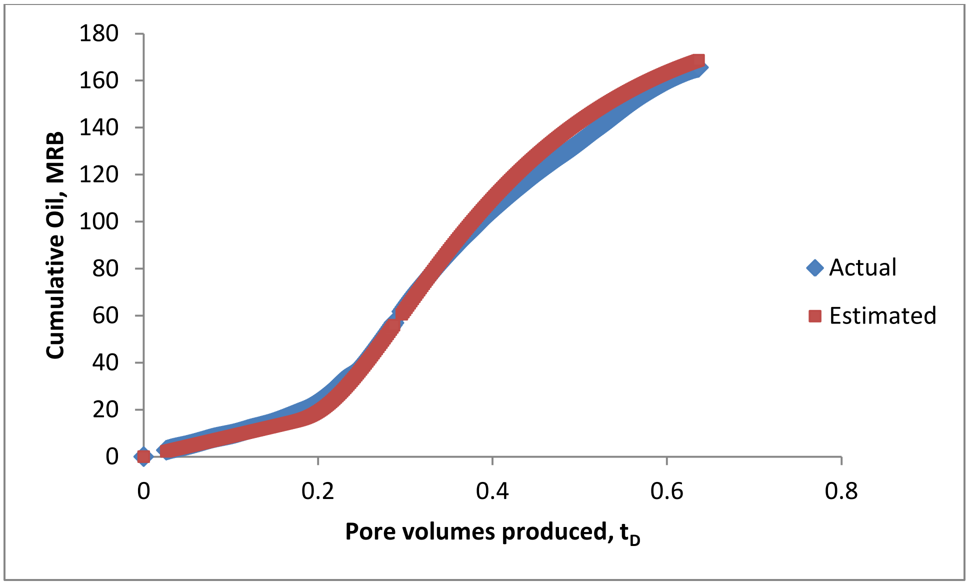

Figure D.16. Polymer flooding history match of Chateaurenard polymer flood (Takaqi et al., 1992)

Marmul field pilot

Marmul field is located in the southern part of Oman. The field was discovered in 1956 but only stated production in 1980. The geologic formation called Al Khlata is composed of sequence of glacial deposits and contains over 60% of the total oil in place. Al Khlata formation is a very high peameability reservoir (1-20 Darcy) with oil viscosity of 80 cp. The unfavorable water-oil mobility ratio (M=45) was recognized as the reason for the polymer flood pilot performance. The aim was to improve oil recovery by improving volumetric sweep efficiency in the pilot area. The polymer injection was preceded by a water preflush for five months. Oil cut declined steadily during the water preflush. Polymer injection followed the water preflush for 12 months during which time the oil cut increased significantly (by 30%). The pilot history match for Marmul field is shown in Figure D.17.

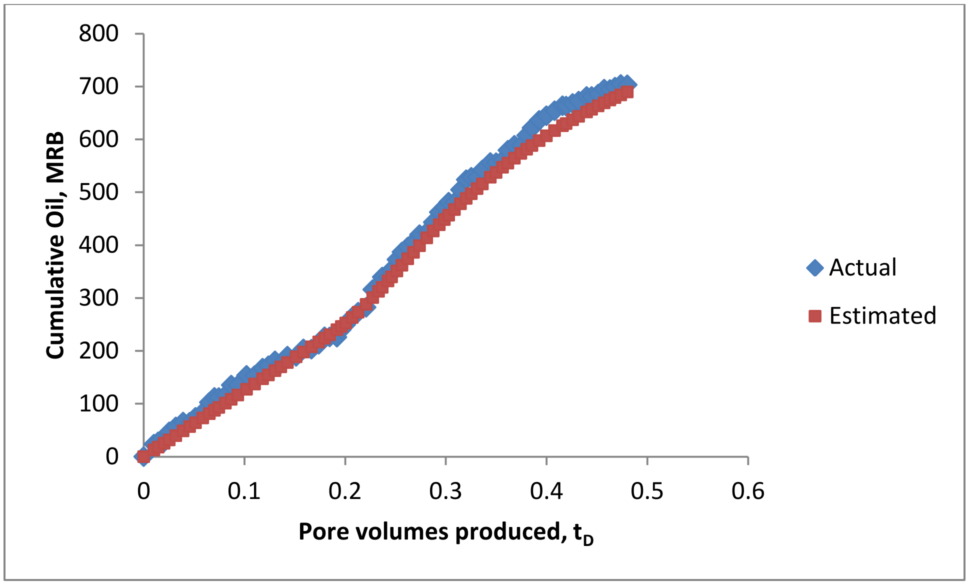

Figure D.17. Polymer flooding history match of Marmul polymer flood. (Koning et al., 1988)

North Burbank unit pilot

The North Burbank Unit is located in Osage county, Oklahoma. The Burbank sandstone formation is of fluvial origin, with river channels superimposed on each other. The field was discovered in 1920 and production started in 1923. The net formation thickness in the field varies from 37 to 50 ft. The average permeability in the field is 500 md with porosity varying between 11 to 32%. The waterflood in the unit started in 1949. The waterflood history suggests that water is channeling through the fractures and high permeability zones. Polymer flood is expected to improve vertical and areal conformance. The water cut in the high permeability zones went down from 60 to 50%. The fractured areas shows early polymer breakthrough as was seen with water. The polymer pilot history match is shown in Figure D.18.

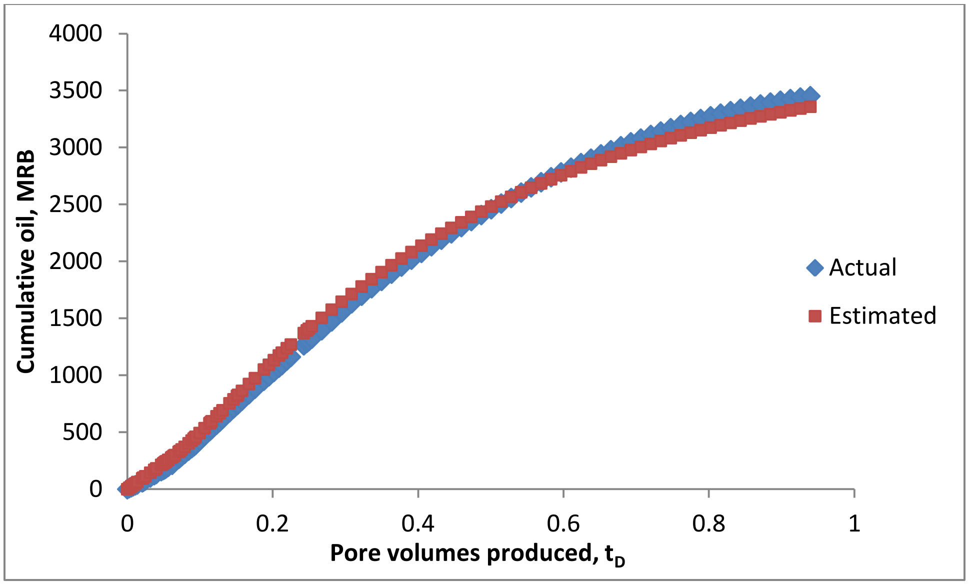

Figure D.18.Polymer flooding history match of North Burbank polymer flood. (Zornes et al., 1986)

Sleepy Hollow pilot

The Sleepy Hollow Reagan unit is located in Nebraska. The field was discovered in 1960 and started production in 1962. The average reservoir net thickness is 11.3 ft. The average porosity of the reservoir is 24% with the permeability of 2.5 Darcy. The oil in the formation is stratified in two zones. The upper oil zone has viscosity of 24 cp and the lower zone heavy oil viscosity can vary from 72 cp to 10000 cp. Peripheral water injection in the field began in 1966. Water injection in the interior part of the field started in 1983. Polymer injection started in 1985. The water cut in the polymer injection area decreased from 33% to 16%. The field polymer pilot history match is shown Figure D.1 9.

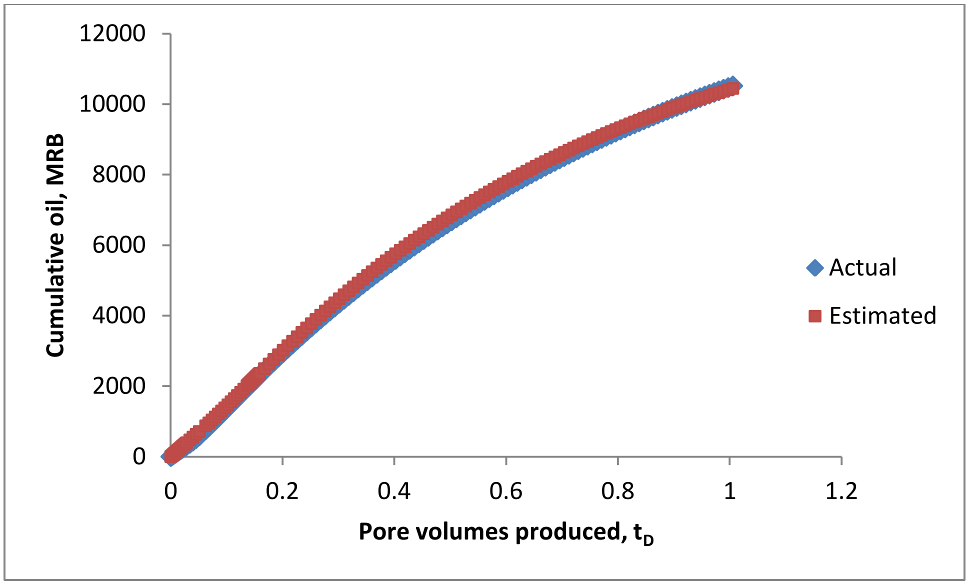

Figure D.19. Polymer flooding history match of Sleepy Hollow polymer flood.(Christopher et al., 1988)

Courtenay field

Courtenay field is a hydro-dynamically isolated compartment of Chateanurenard field. The Courtenay reservoir lies at the depth of 2000 ft. The net average reservoir thickness is 11 ft. The reservoir sands are unconsolidated and the average permeability is 2 Darcys. The oil is paraffinic with the viscosity at 40 cp. The production from the field began in 1965. The primary recovery was from edge water drive. Water flooding was not considered for the field due to adverse mobility ratio, close well spacing and high permeability channels. Early water breakthrough was expected so polymer flood was considered as an alternative. The full field polymer injection started in 1989. The edge water drive has resulted in high water cut in the production wells. Polymer injection has improved oil recovery as water cuts decreased from 92 % to 50 %. The Courtenay field history match is shown in Figure D.20.

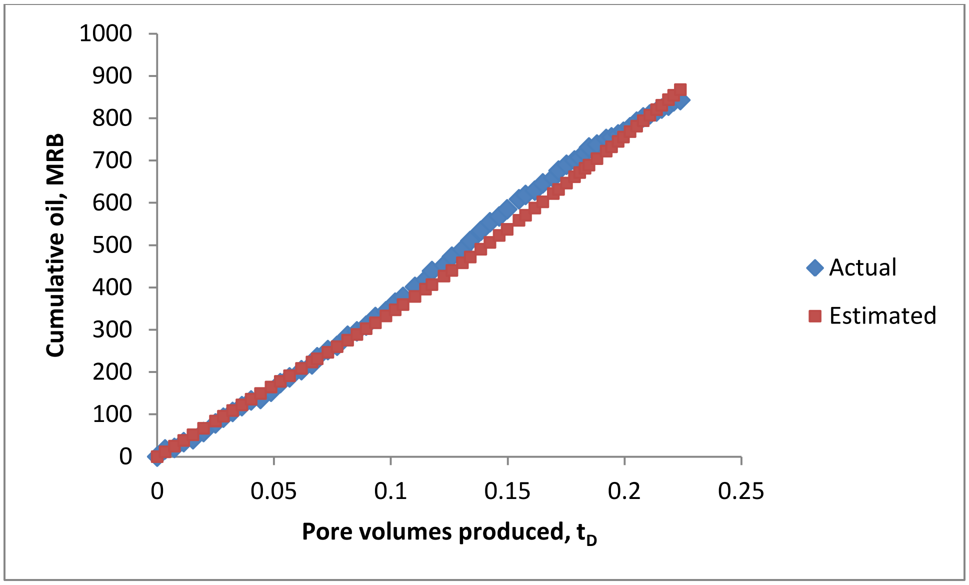

Figure D.20. Polymer flooding history match of Courtenay polymer flood. (Putz et al., 1994)

MISCIBLE WAG/CO_2 HISTORY MATCHES

Twofreds WAG project

The Twofreds field is located in Loving, Reeves and Ward counties of west Texas. The reservoir sand is very well sorted and fine grained with light cementation. The sand is moderately homogeneous. The average depth of the formation is 4800 ft. The average formation permeability and porosity is 27.7 md and 0.20 respectively. The formation temperature is 104 F with oil gravity of 36 API. Primary recovery from the field commenced in 1957. The water flood in the field started in 1963 and continued for ten years until Twofreds became a field scale CO_2 injection project. The recovery attributed to water flood is 4% of OOIP thus an inadequate response to secondary flood was observed. The tertiary flood incremental oil recovery is estimated at 10% of OOIP. The Twofreds field history match is shown in Figure D.21.

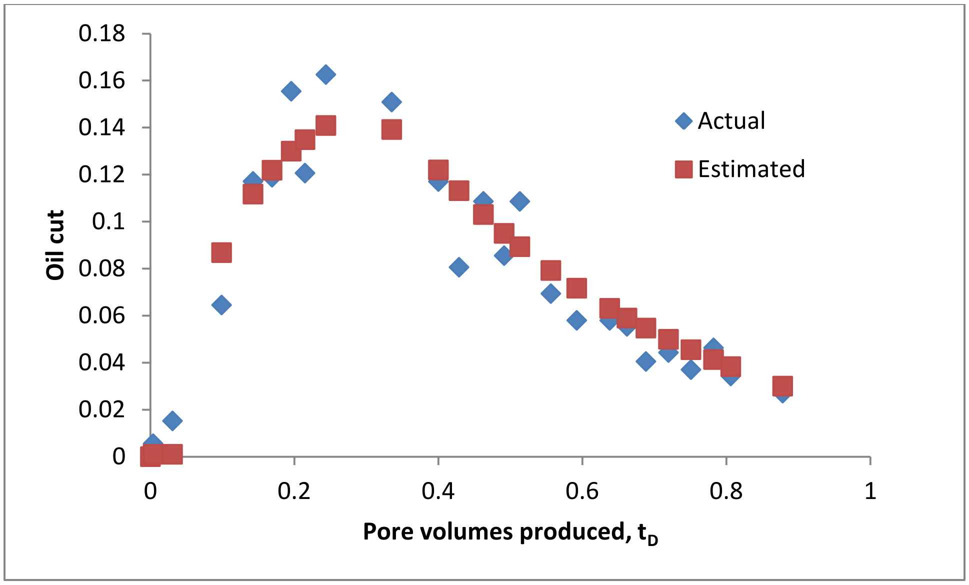

Figure D.21. CO_2 WAG flood history match for Twofreds pilot (Flanders et al., 1993).

Lost Soldier pilot

The Lost Soldier Field was discovered in 1916 and is located in south central Wyoming. The average depth of the Tensleep sandstone is 5000 ft. Tensleep is an eolian sandstone with an average net thickness of 210 ft. The average porosity and permeability of the net pay is 0.1 and 31 md, respectively. The reservoir oil has the stock tank gravity of 35 API. Primary production started in early 1940's with fluid expansion, water influx and gravity drainage as the main driving forces. The peripheral water injection began in 1962 and pattern water flood was initiated in 1976. The wells are laid out in north to south line drive pattern. CO_2/WAG injection started from 1989, prior to which reservoir was producing 2500 bopd at 97% watercut. Within a year, oil production exceeded 10,000 bopd. The tertiary oil recovery through 1995 reached over 10% of OOIP. The Lost Soldier field history match is shown in Figure D.22.

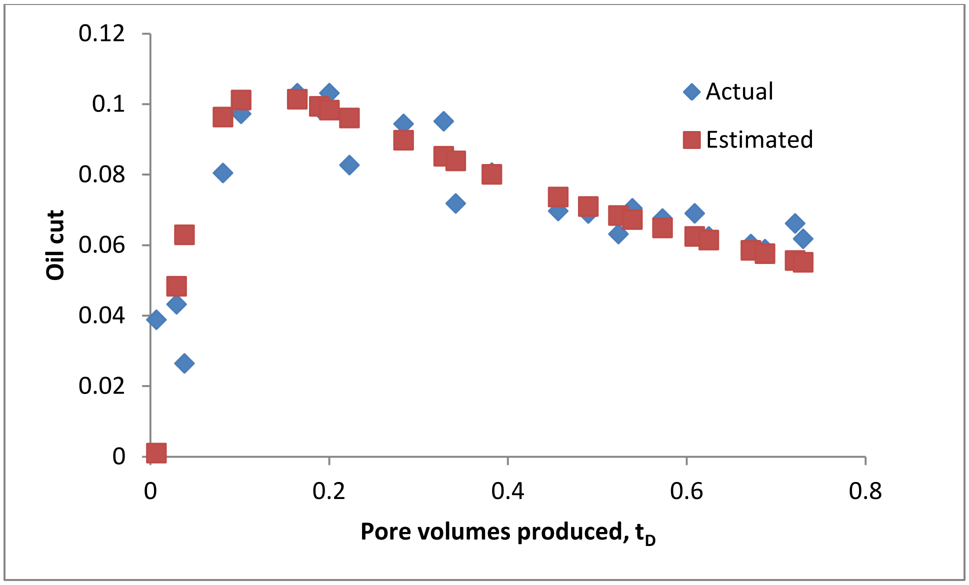

Figure D.22. CO_2 WAG flood history match for Lost Soldier pilot (Brokmeyer et al., 1996).

Rangely Field

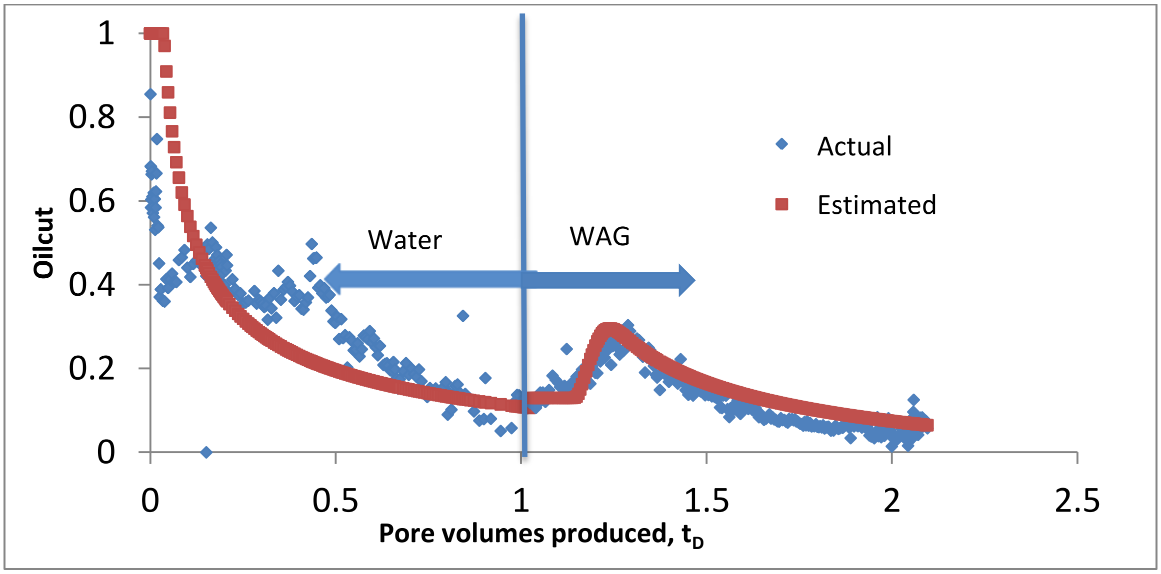

Figure D.23. Waterflood and CO_2/WAG flood history matches for Well 2 in Rangely field.

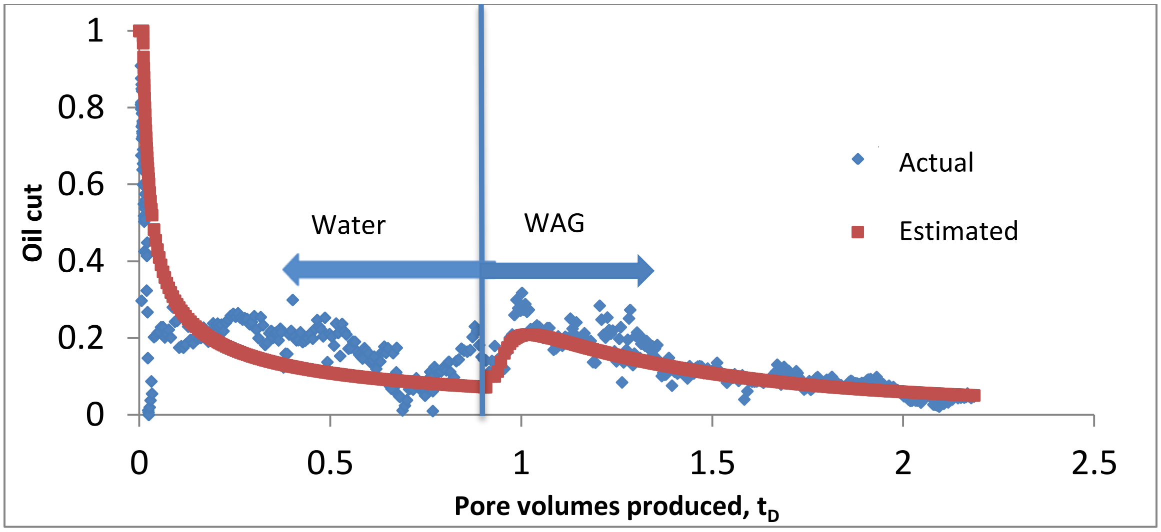

Figure D.24. Waterflood and CO2/WAG flood history matches for Well 3 in Rangely field.

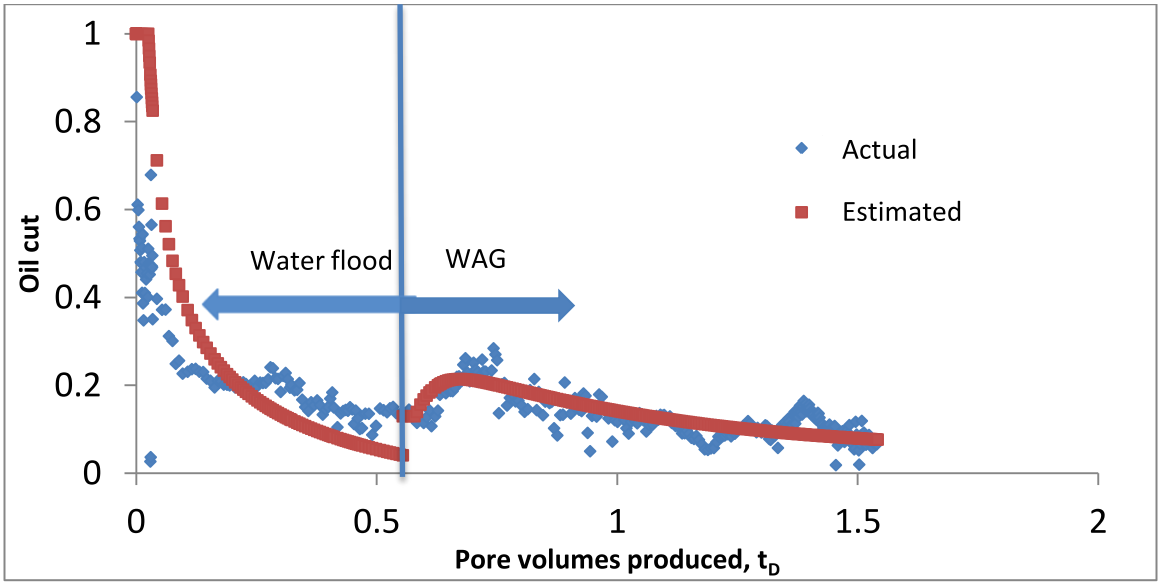

Figure D.25. Waterflood and CO_2/WAG flood history matches for Well 4 in Rangely field.

Nomenclature

a = Ultimate volumetric sweep, fraction

C = Storage capacity, fraction

C_J = Total fraction of cross-section swept by injectant, fraction

C_B = Total fraction of cross-section swept by oil bank, fraction

C_I = Total fraction of cross-section occupied by initial oil, fraction

F = Flow capacity, fraction

F_S = Average cross-sectional fractional for solvent flow, fraction

F_J = Total fractional flow contained in the injected fluid region, fraction

F_B = Total fractional flow contained in the oil bank region, fraction

F_I = Total fractional flow contained in the initial oil region, fraction

$f_{j,J}$ = Local fractional flow of phase j in the injected fluid region, fraction

$f_{j,B}$ = Local fractional flow of phase j in the oil bank region, fraction

$f_{j,I}$ = Local fractional flow of phase j in initial oil region, fraction

h = Layer thickness, ft

H = Reservoir thickness, ft

H_k = Heterogeneity factor

K = Koval factor for secondary floods (gas and waterfloods)

K_b = Koval factor for the tertiary bank front

K_f = Koval factor for the oil bank front

k_H = Average horizontal permeability, md

k_v = Average vertical permeability, md

$k_{rj,J}$ = Relative permeability of phase j in injected fluid region

$k_{rj,B}$ = Relative permeability of phase j in oil bank region

$k_{rj,I}$ = Relative permeability of phase *j* in initial region

L = Reservoir length, ft

MR = Mobility ratio

N_C = Total number of components

N_{CD} = Dimensionless capillary number

$N_{Di,x}$ = Dimensionless flux of component *i* in the x direction

$N_{Di,\mathrm{y}}$ = Dimensionless flux of component *i* in the y direction

N_g = Gravity number

N_{LD} = Dimensionless longitudinal dispersion number

N_{TD} = Dimensionless transverse dispersion number

P_c = Capillary pressure, psi

P_{jD} = Dimensionless pressure of phase j

P_{cD} = Dimensionless capillary pressure

q = Total injection flux, ft/day

r = Interstitial velocity, ft/day

R_L = Dimensionless parameter that controls viscous cross-flow

S = Saturation, fraction

$S_{j,J}$ = Local saturation of phase *j* in the injected fluid region, fraction

$S_{j,B}$ = Local saturation of phase *j* in the oil bank region, fraction

$S_{j,I}$ = Local saturation of phase *j* in the initial oil region, fraction

S_{2RM} = Residual oil to miscible floods, fraction

S_{OF} = Residual oil to polymer floods, fraction

t_D = Dimensionless time

u = Superficial injection velocity, ft/day

u_{jx_D} = Dimensionless flux of phase j in x direction

u_{jy_D} = Dimensionless flux of phase j in y direction

$v_{f,OB}$ = Local fractional flow velocity of the oil bank front

$v_{b,OB}$ = Local fractional flow velocity of the tertiary bank front

$v_{\Delta S}$ = Local fractional flow velocity for secondary floods

V_p = Total pore volume, Barrels

w = mass fraction

x_D = Dimensionless spatial location in x-direction

y_D = Dimensionless spatial location in y-direction

Greek symbols

μ = Viscosity of displacing fluid, cp

μ_2^o = Viscosity of phase 2 at standard conditions, cp

σ = Interfacial tension between flowing phases, lb/ft

$\wedge$ = Fraction of cross-section occupied by solvent finger

α_T = Transverse dispersivity, ft

α_L = Longitudinal dispersivity, ft

ρ = Density, lb/ft^3

$\overline{\rho}$ = Dimensionless density

λ = Fluid mobility

ϕ = Porosity, fraction

Subscripts

oe = Effective oil (viscosity)

og = Effective gas (viscosity)

o = Oil (viscosity)

g = Gas (viscosity)

m = mixture (viscosity)

n = Layer

i = Component

j = phase

1 = Brine

2 = Oil

3 = Solvent

J = Injected fluid region

B = Oil bank region

I = Initial fluid region

References

AIAA. 1998, Guide for the verification and validation of computational fluid dynamics simulations, AIAA-G-077.

Albertoni, A and Lake, L.W. 2003, Inferring interwell connectivity only from well-rate fluctuations in waterfloods, SPE Reservoir Evaluation & Engineering, 6 (1): 6-16

Araktingi, U.G. and Orr, F.M. 1993, Viscous fingering in heterogeneous porous media, SPE advanced technology series, v.I: 71-80.

Aris, R. 1956, On the dispersion of a solute in a fluid flowing through a tube, Proc. R. Soc. Lond 235 (1200): 67-77.

Arya, A. and Hewett, T.A. and Lake, L.W. 1988, Dispersion and reservoir heterogeneity, SPERE 3 (1): 139-148.

Barker, J.W. and Fayers, F.J. 1994, Transport coefficients for compositional simulation with coarse grids in heterogeneous media, SPE Advance Technology series 2 (2): 103-112.

Barker, J.W. and Thibeau, S. 1997, A critical review of the use of pseudorelative permeabilities for upscaling, SPERE 12 (2): 138-143.

Bear, J. 1972, Dynamics of fluid flow in porous media, New York: American Elsevier Publishing Company.

Beckers, H.L., 1965, The deformation of an interface between two fluids in a porous medium, Appl. Science Res. Annual, 14: 101.

Blackwell, R.J., Rayne, J.R. and Terry, W.M. 1959, Factors influencing the efficiency of miscible displacement, Petroleum Transactions, AIME, v. 217: 1-8.

Brokmeyer, S.E., Borling, D.C. and Pierson, W.T. 1996, Lost Soldier Tensleep CO_2 tertiary project, performance case history; Bairoil, Wyoming, SPE Paper 35191, Permian Basin Oil and gas Recovery Conference, Midland, March 27-29.

Buckley, S.E. and Leverett, M.C. 1942, Mechanism of fluid displacement in sands, SPE Journal 146 (1): 107-116.

Chen, G., Han, P., Shao, Z., Zhang, X., Ma, M., Lu, K., and Wei, C. 2011, History matching method for high concentration viscoelasticity polymer flood pilot flood in Daqing oilfield, SPE Paper 144538, Presented at Enhanced Oil Recovery Conference, Kuala Lumpur, July 19-21.

Christie, M.A. and Bond, D.J. 1987, Detailed simulation of unstable process in miscible flooding, SPERE 2 (4): 514-522.

Christie, M.A. and Blunt, M.J. 2001, Tenth SPE comparative solution project: A comparison of upscaling techniques, Paper SPE 66599, Reservoir Engineering Symposium, Houston, February, 11-14.

Christopher, C.A., Clark, T.J. and Gibson, D.H. 1988, Performance and operation of a successful polymer flood in the Sleepy Hollow Reagan unit, SPE Paper 17395, Enhanced Oil Recovery Symposium, Tulsa, April 17-20.

Claridge, E.L. 1972, Prediction of recovery in unstable miscible flooding, SPEJ 12(2): 143-155.

Coats, K.H., Dempsey, J.R. and Henderson, J.H. 1971, The use of vertical equilibrium in two-dimensional simulation of three dimensional reservoir performance, SPEJ 11(1): 63-71.

Coats, K.H., Dempsey, J.R. and Henderson, J.R. 1970, A new technique for determining reservoir description from field performance data, SPEJ, 10(1): 66-74.

Coats, K.H., Thomas, L.K. and Pierson, R.G. 2007, Simulation of miscible flow including bypassed oil and dispersion control, Society of Petroleum Engineers Reservoir Evaluation and Engineering 10 (5): 500-507.

Courant, R. and Hilbert, D. 1962, Methods of mathematical physics, Volume 1, Interscience Publishers Inc., New York.

Craig, F.F., Geffen, T.M. and Morse, R.A., Oil recovery performance of pattern gas or water injection operations from model tests, AIME, Petroleum Transactions 204, 7-15.

Craig, F.F 1971, The reservoir engineering aspects of waterflooding, SPE Monograph Series, Volume 3.

Crump, J.G. 1988, Detailed simulations of the effects of process parameters on adverse mobility ratio displacements, Paper SPE 17337 presented at SPE Enhanced Oil Recovery Symposium, Tulsa, 16-21 April.

Dake, L. P. 1983, Fundamentals of reservoir engineering, Elsevier Science.

Dai, K.K. and Orr, F.M. Jr. 1987, Prediction of CO_2 flood performance: Interaction of phase behavior with microscopic pore structure heterogeneity, SPEJ, 2(4): 531-542.

Dietz, D.N. 1954, A theoretical approach to the problem of encroaching and by-passing edge water, Akad. Van Wetenschappen, Amsterdam, Proc. 56-B, 83.

Dao, E.K., Lewis, E. and Mohanty, K.K. 2005, Multicontact miscible flooding in a high pressure quarter five-spot model. SPE Paper 97198, Annual Technical Conference and Exhibition, Dallas, October 9-12.

Doughtry, E.L. 1963, Mathematical model of an unstable miscible displacement, SPE Journal 3(2): 155-163.

Durlofsky, L.J., Gerritsen, M. and Wen, X.H. 2003, A coupled local-global upscaling approach for simulating flow in highly heterogeneous formations, Advances in Water Resources 26: 1041-1060.

Durlofsky, L.J., Behrens, R.A., Jones, R.C. and Bernath, A. 1996, Scale up of heterogeneous three dimensional reservoir descriptions, SPE Journal, 1 (3): 313-326.

Dykstra, H. and Parsons, R.L. 1950, The prediction of oil recovery by waterflooding, Secondary recovery of oil in the United States , 2nd ed. API: 160-174.

Evans, L.C. 2010, Partial Differential Equations, Graduate Studies in Mathematics, American Mathematical Society.

Fayers, F.J. 1988, An approximate model with physically interpretable parameters for representing miscible viscous fingering, SPE Reservoir Engineering 3(2): 551-558.

Fayers, F.J., Barker, J.W. and Newely, T.M.J. 1992, Effects of heterogeneities on phase behavior in enhanced oil recovery, The Mathematics of oil recovery, pp. 115-150.

Fayers, F.J. and Jouaux, F. 1995, An improved macroscopic model for viscous fingering and its validation for 2D and 3D flows III. inclusion of effects of heterogeneities, Department of Petroleum Engineering-Stanford University, Marcel Dekker, Inc., pp. 393-425.

Fayers, F.J., Jouaux, F. and Tchelepi, H.A. 1994, An improved macroscopic model for viscous fingering and its validation for 2D and 3D flows I, non-gravity flows, Department of Petroleum Engineering, Stanford University, Marcel Dekker, pp. 43-78.

Fayers, F.J. and Muggeridge, A.H. 1990, Extensions to Dietz theory and behavior of gravity tongues in slightly tilted reservoirs, SPEJ, 3: 145-155.

Fayers, F.J. and Newley, M.J. T. 1988, Detailed validation of an empirical model for viscous fingering with gravity effects, SPERE 3 (2): 542-550.

Flanders, W.A. and DePauw, R.M. 1993, Update case history: Performance of the Twofreds tertiary CO_2 project, SPE Paper 26614, Annual Technical Conference and Exhibition, Houston, October 3-6.

Gardner, J.W., Orr, F.M. and Patel, P.D. 1981, The effect of phase behavior on CO2-flood displacement efficiency, Journal of Petroleum technology 33 (11): 2067-2081.

Gardner J.W and Ypma, J.G.J. 1984, An investigation of phase-behavior/macroscopic-bypassing interaction in CO2 flooding, SPE Journal 24 (5): 508-520.

Genrich, J.F. and Sommer, F.S. 1989, Novel approach to sensitivity analysis, Journal of Petroleum Technology, 41(9): 930-985.

Giordano, W.B. and Surkalo, H. 1987, Estimating field-scale miscellar/polymer performance, SPE Paper 16731, Annual Technical Conference and Exhibition, Dallas, September 27-30.

Haberman, B. 1960, The efficiency of miscible displacement as function of mobility ratio, Petroleum Transactions AIME, v.I 219: 264-272.

Helfferich, F.G. 1981, Theory of multicomponent, multiphase displacement in porous media, SPEJ 21(1): 51-62.

Helfferich, F.G. and Klein, G. 1970, Theory of interference, Marcel Dekker Inc., New York.

Hirasaki, G.J. 1981, Application of the theory of multicomponent, multiphase displacement to three-component, two-phase surfactant flooding, SPEJ 21(2):191-204.

Homsy, G.M. 1987, Viscous fingering in porous media, Annual reviews of fluid mechanics, v.I 19, pp. 271-311.

Jennings, J.W., Ruppel, S.C., and Ward, W.B. 2000, Geostatistical analysis of permeability data and modeling of fluid flow effects in carbonate outcrops, SPE Reservoir Evaluation and Engineering, 3 (4), 292-303.

Jones, R.S., Pope, G.A., Ford, H.J. and Lake, L.W. 1984, A predictive model for water and polymer flooding, SPE Paper 12653, Enhance Oil Recovery Symposium, Tulsa, April 15-18.

Kirkpatrick, S. 1973, Percolation and conduction, Reviews of Modern Physics, 45 (4): 574-588.

Kirkpatrick, S. 1971, Classical transport in disordered media: Scaling and effective medium theories, Physical review letters, 27(25): 1722-1725.

Koning, E.J.L., Mentzer, E. and Heemskerk, J. 1988, Evaluation of a pilot polymer flood in the Marmul field, Oman, SPE Paper 18092, Annual Technical Conference and Exhibition, Houston, October 2-5.

Koval, E.J. 1963, A method for predicting the performance of unstable miscible displacements in heterogeneous media, SPE Journal 3 (2): 145-154.

Lake, L.W., Stock, L.G. and Lawson, J.B. 1978, Screening estimation of recovery efficiency and chemical requirements for chemical flooding, SPE Paper 7069, Improved Oil Reocvery Sumposium, Tulsa, April, 16-19.

Lake, L.W. 1989, Enhanced oil recovery, available through Society of Petroleum Engineers.

Lake, L.W. and Hirasaki, G.J. 1981, Taylor's dispersion in stratified porous media, SPE Journal 21 (4): 459-468.

Lantz, R.B. 1970, Rigorous calculation of miscible displacement using immiscible reservoir simulators, SPE Journal, 10 (2): 192-202.

Le Fur, B. and Sourieau, P. 1963, Etude de l’ecoulement diphasique dans une couche incline et dans un modele rectangulaire de milieu poreux, Rev. Inst. Fr. Petrol. 18: 325-343.

Lee, K. S., and Claridge, E. L. 1968, Areal sweep efficiency of pseudoplastic fluids in a five-spot Hele-Shaw model, SPE Journal 8 (1): 52–62

Li, D. and Lake, L. W. 1995, Scaling fluid flow through heterogeneous permeable media, SPE Advanced Technology Series 3 (1): 188-197.

Miller, M.C. Jr. 1966, Gravity effects in miscible displacements, SPE Paper 1531, Fall Meeting, AIME, Dallas, October 2-5.

Molleai, A., and Delshad, M. 2011, A novel forcasteing tool for water alternating gas (WAG) floods, Paper SPE 148742 presented at SPE eastern regional meeting, Columbus, 17-19 August.

Mollaei, A. 2011, Forecasting of isothermal enhanced oil recovery (EOR) and waterflood process, PhD Dissertation, The University of Texas at Austin.

Nghiem, L.X. 1989, A method for modeling incomplete mixing in compositional simulation of unstable displacements, Paper SPE 18439 presented at Reservoir Simulation Symposium, Houston, 6-8 Feburary.

Pande, K.K. and Orr, F.M. Jr. 1989, Interaction of phase behavior, reservoir heterogeneity and crossflow in CO_2 floods, SPE Paper 19668, Fall Technical Conference and Exhibition, San Antonio.

Paul, W., Lake, L.W., Pope, G.A. and Young, G.G. 1982, A simplified predictive model for micellar-polymer flooding, SPE Paper 10733, Regional meeting for SPE engineers, California, March 24-26.

Paul, W., Lake, L.W. and Gould, T.L. 1984, A simplified predictive model for CO_2 flooding, SPE Paper 13238, Annual Technical Exhibition and Conference, Houston, September 16-19.

Patton, J.T., Coats, K.H., and Colegrove, G.T. 1971, Prediction of polymer flood performance, SPE Journal, 11 (1): 72-84.

Peaceman, D.W. and Rachford, H.H. 1962, Numerical calculation of multidimensional miscible displacement, SPE Journal 2 (4): 327-339.

Perkins, T.K. and Johnson, O.C. 1963, A review of diffusion and dispersion in porous media, SPE Journal 3 (1): 70-84.

Perrine, R.L. 1961, Stability theory and its use to optimize solvent recovery of oil, SPEJ, 1(1): 9-16.

Popper, K. 1935, The logic of scientific discovery, Routledge, London

Putz, A.G., Bazin, B. and Pedron, B.M. 1994, Commercial polymer injection in the Courtenay field, 1994 update, SPE Paper 28601, Annual Technical Conference and Exhibition, New Orleans, September 25028.

Rowe, H.G., York, D.S. and Ader, J.C. 1982, Slaughter Estate unit tertiary pilot performance, JPT, 34(3):613-620.

Sayarpour, M. 2008, Development and application of capacitance-resistive models to water/CO_2 floods, PhD Dissertation, The University of Texas at Austin.

Sayarpour, M., Kabir, C.S. and Lake, L.W., Field applications of capacitance-resistive models in waterfloods, Paper SPE 114983, Annual Technical Conference and Exhibition, Denver, September, 21-24.

Shook, G. M., Li, D. and Lake, L.W. 1992, Scaling immiscible flow through permeable media by inspectional analysis, In-Situ 4: 311-349.

Shook, G. M. and Mitchell, K. M. 2009, A robust measure of heterogeneity for ranking earth models: The F-Phi curve and dynamic lorenz coefficient, Paper SPE 124625 presented at Annual Technical Conference and Exhibition, New Orleans, 4-7 October.

Sorbie, K. 1991, Polymer improved oil recovery, Blackie and Son Ltd, Glasgow

Stiles, W.E. 1949, Use of permeability distribution in waterflood calculations, Petroleum Transcripts, AIME.

Takaqi, S., Pope, G.A. and Sepehrnoori, K. 1992, Simulation of a successful polymer flood in the Chateaurenard field, SPE Paper 24931, Annual Technical Conference and Exhibition, Washington, October 4-7.

Taylor, G.I. 1953, Dispersion of soluble matter in solvent flowing through a tube, Proceedings of the Royal Society, 219: 186-203.

Taylor, G.I. 1954, The dispersion of matter in turbulent flow through a pipe, Proceedings of the Royal Society, 223: 446-468.

Taylor, G.I. 1954, Conditions under which dispersion of a solute in a stream of solvent can be used to measure molecular diffusion, Proceedings of the Royal Society, 225: 473-477.

Todd, M.R. and Chase, C.A. 1979, A numerical simulator for predicting chemical flood performance, SPE Reservoir Simulation Symposium, Denver, January 31-February 2.

Todd, M.R. and Longstaff, W.J. 1972, The development, testing, and application of a numerical simulator for predicting miscible flood performance, JPT 24 (7): 874-882.

U.S. Energy Information Administration, Annual Energy Outlook, April 2013.

U.S. Enhanced Oil Recovery Survey, Oil & Gas Journal, 2013.

Wang, D. and Hao, Y. 1993, Results of two polymer flooding pilots in the central area of Daqing oil field, SPE Paper 26401, Annual Technical Conference and Exhibition, Houston, October 3-6.

Walsh, M and Lake, L.W. 2003, A generalized approach to primary hydrocarbon recovery of petroleum exploration and production, Elsevier Science.

Yokoyama, Y. and Larry, L.W. 1981, The effects of capillary pressure on immiscible displacements in stratified porous media, Annual Technical Conference and Exhibition, San Antonio, October 4-7.

Yortsos, Y.C. 1995, A theoretical analysis of vertical flow equilibrium, Transport in Porous Media, 18: 107-129

Zapata, V.J. and Larry, L.W. 1981, A theoretical analysis of viscous crossflow, Annual Technical Conference and Exhibition, San Antonio, October 4-7.

Zornes, D.R., Cornelius, A.J. and Long, H.Q., An overview and evaluation of the North Burbank unit block, A polymer flood project, Osage county, Oklahoma, SPE Paper 14113, SPE International Meeting on Petroleum Engineering, Beijing, March 17-20.